

# Study of properties enhancement of Magnesium Diboride (MgB<sub>2</sub>) by TaB<sub>2</sub> doping via High Energy Ball Milling

by

**Richard Pérez Moyet**

A thesis submitted in partial fulfillment of the requirements for the degree of

**MASTER OF SCIENCE**

**in**

**PHYSICS**

UNIVERSITY OF PUERTO RICO

MAYAGÜEZ CAMPUS

2008

Approved by:

\_\_\_\_\_  
Oswald N C Uwakweh, PhD  
President, Graduate Committee

\_\_\_\_\_  
Date

\_\_\_\_\_  
Yong Jihn Kim, PhD  
Member, Graduate Committee

\_\_\_\_\_  
Date

\_\_\_\_\_  
Eric E. Hellstrom, PhD  
Member, Graduate Committee

\_\_\_\_\_  
Date

\_\_\_\_\_  
Hector J. Jiménez González, PhD  
Member, Graduate Committee

\_\_\_\_\_  
Date

\_\_\_\_\_  
Oscar Perales Pérez, PhD  
Representative of Graduate Studies

\_\_\_\_\_  
Date

\_\_\_\_\_  
Hector Jiménez González, PhD  
Chairperson of the Department

\_\_\_\_\_  
Date

© Copyright by Richard Pérez Moyet 2008

All Right Reserved

## ABSTRACT

The study of superconductivity properties enhancement on  $\text{MgB}_2$  due to  $\text{TaB}_2$  doping at 2 and 5 at.% levels were carried out, in addition to the effect of atmospheric exposure on  $\text{MgB}_2$ . High energy ball milling was used for the purposes of fostering mechanical alloying, generation of nanometer sized particles, and strain inducements respectively. Atmospheric exposures at the University of Puerto Rico-Mayagüez and University of Wisconsin-Madison, revealed critical temperature of 37.5 K and 38 K based on resistivity measurements, while the lower critical field,  $H_{c2}$  were 7.9 T and 7.0 T correspondingly. The formation of MgO during processing resulted in the variable grain connectivity and hence, the measured properties differences. SPEX 8000D processed materials revealed smaller particle size and higher strains in comparison to the Pulverisette-4 processed ones. The 5 at.%  $\text{TaB}_2$  doped  $\text{MgB}_2$  yielded the highest critical current density ( $J_c$ ) corresponding to 474.1  $\text{kA/cm}^2$  at 2 T, while 344.4  $\text{kA/cm}^2$  for SPEX 8000D and Pulverisette-4 materials. Correspondingly, the values of the flux pinning ( $F_p$ ) deduced for the 5t.%  $\text{TaB}_2$  doped  $\text{MgB}_2$  processed with the SPEX-8000D mill was 7.58  $\text{GN/m}^3$  while for same level of doping processed with the Pulverisette-4 processed material was 6.90  $\text{GN/m}^3$ . The irreversibility field ( $H_{irr}$ ) corresponding to the field associated with the maximization of the magnetization of the materials was 8.50 T for the 5 at.% doped  $\text{MgB}_2$ , while for the same level of doping processed with Pulverisette-4 was 7.11 T.

## Summary

In this research work, the superconducting and physical properties relation will be fundamental for the behavior of the material studied. MgB<sub>2</sub>, main material in this research, were studied under environmental, mechanical induced disorder and TaB<sub>2</sub> doping condition in way to improve its superconducting properties. In chapter 1 “Introduction” a brief discussion about previous works on MgB<sub>2</sub> research works was developed. Chapter 2, “Theoretical Background” give physical and superconducting properties information of MgB<sub>2</sub> and TaB<sub>2</sub>. The experimental process and characterization of the material were detail explained on Chapter 3. All results obtained on Chapters 4, 5 and 6 are related with Chapter 3.

In Chapter 4, atmospheric conditions were studied to found the level of oxidation of MgB<sub>2</sub> comparing the handling of the material at ambient atmosphere and on high Nitrogen, N<sub>2</sub>, concentration atmosphere condition. In Chapter 5, structural disorder induced by high energy ball milling was studied under the milling condition stipulated of SPEX-8000D and Pulverisette-4 ball milling machines. Milling condition from SPEX milling machine, short milling time and the use of BPR = 3:1 were the major contributions of this chapter, which were standardized in Chapter 6. TaB<sub>2</sub> doped MgB<sub>2</sub> was the main objective in Chapter 6, with 2 and 5 at.% doping levels. The last chapter, Chapter 7, resume important results and observations which lead to the enhancement of the superconducting properties of MgB<sub>2</sub>.

## Acknowledgment

During the period of my master studies, I would like to say THANK YOU to all those people that helped me to improve my personality as a good person in the society and as a scientific in the science world. Many steps were done to reach to this level of preparation in which I feel comfortable and able to continue. It could not be possible without I get with these beautiful people.

First, I would like to say thank you to our creator, God. Thank you my Lord to help me with my goals, especially my master degree. Believe in you make me understand and with conviction go through any obstacle in the life. Thank for you help and to create in me patient, constancy and a successful person.

My parents, Billy Pérez Figueroa and Clara Moyet de Leon, and my Brothers, Clarivette, Charon and Bill Perez Moyet. Thank you for always be there and be my inspiration to my goals. Have all of you as my family, makes me feel grateful and enviable to know that in anyplace and any situation I can count with all of you.

To Yenny P. Cardona Quintero. Thank for you unconditional help, especially the time spent in the laboratory, to accomplish this goals. Thank you to be part of my life and give me the opportunity to know, a beautiful person.

To my friends: Neida M, Santacruz Sarmiento, Carlos A. Flores Bustos, Segundo Jauregui Rosas y Angel L. Villalain García. Thank to all of you help, understanding and comprehension that I received from each of you. Thank you for be in the pages of the big book of my life.

To Dr. Oswald N C Uwakweh. Thank you professor for everything you have done with me and for me. Thank you for believe in me from the first day and just believe in my interest. Thank you for teach me material science and life science. Thank you for the friendship and to let me know that I can really count with you. Thanks professor for the patient and unconditional time. Professor Gracias.

To Dr. Eric E. Hellstrom and Dr. Durval Rodrigues Jr. Thanks for receive me in the University of Wisconsin and be my friends and my mentors for this work. Thank you for help me with the experimental big part of the thesis and the analysis of results. Thanks professors for you unconditional time in Wisconsin.

To Dr. Yong Jihn Kim. Thank you for all the classes of superconductivity theory. Thank you for let me know you as a friend.

Thank you to all persons that in some way help me and are part of this research work. Aracelis Thank you, Carlos and Carlos worker (Ricky, Miguel, Kary, Cintron), Luis... Thank you, and my entire partners from the master degree.

Thank to PREM that support me for all period of my research work and to everything I could learned, which will be valuable as my feature scientist life.

This research is based upon work supported by the National Science Foundation under Grant No. 0351449.

## Table of Content

ABSTRACT .....	i
Summary .....	ii
Acknowledgements .....	iii
Table of Content .....	v
Table List .....	viii
List of Figures.....	x
<b>1. INTRODUCTION.....</b>	<b>1</b>
1.1 Motivation.....	2
1.2 Literature Review.....	3
<b>2. THEORETICAL BACKGROUND.....</b>	<b>7</b>
2.1 Basic Physical Properties.....	7
2.1.1 <i>Structure and Bonding of MgB<sub>2</sub></i> .....	7
2.1.2 <i>Structure and Bonding of TaB<sub>2</sub></i> .....	9
2.2 Basic Superconducting Properties.....	10
2.3 Bulk Processing.....	15
<b>3. EXPERIMENTAL PROCEDURES.....</b>	<b>16</b>
3.1 Sample preparation synthesis.....	16
3.1.1 <i>Atmospheric conditions and their effects on Ball milled Magnesium Diboride</i> .....	16
3.1.1.1 <i>Experimental detail</i> .....	17
3.1.2 <i>Study of Ball Milling Induced Strain Disorder on MgB<sub>2</sub> Material</i> .....	19
3.1.2.1 <i>Experimetal detail</i> .....	20
3.1.3 <i>Critical Current Density Enhancement of TaB<sub>2</sub> Doped MgB<sub>2</sub></i> .....	22
3.1.3.1 <i>Experimental detail</i> .....	23

<b>3.1.4 High Energy Ball Milling process</b> .....	26
3.1.4.1 Pulverisette – 4.....	27
3.1.4.2 SPEX 8000D.....	30
3.1.4.3 General milling parameters.....	32
<b>3.1.5 Cold Isostatic Pressing and sealing methods</b> .....	34
<b>3.1.6 Hot Isostatic Pressing</b> .....	36
<b>3.1.7 Sintered sample preparation</b> .....	38
<b>3.2 Characterization Techniques</b> .....	39
<b>3.2.1 Superconducting characterization of the samples</b> .....	40
3.2.1.1 Magnetometry (PPMS).....	40
<b>3.2.2 Microstructure characterization of the samples</b> .....	47
3.2.2.1 Powder X-ray diffraction (XRD).....	47
3.2.2.2 Scanning Electron Microscope ( SEM).....	50
<b>4. ATMOSPHERIC CONDITIONS AND THEIR EFFECTS ON BALL MILLED MAGNESIUM DIBORIDE</b> .....	51
4.1 Results.....	52
4.2 Discussion.....	57
4.3 Conclusions.....	59
<b>5. STUDY OF BALL MILLING INDUCED STRAIN DISORDER ON MgB<sub>2</sub> MATERIAL</b> .....	60
5.1 Results and Discussion.....	60
5.2 Conclusion.....	88
<b>6. CRITICAL CURRENT DENSITY ENHANCEMENT OF TaB<sub>2</sub> DOPED MgB<sub>2</sub></b> .....	90
6.1 Results and Discussion.....	90
6.2 Conclusion.....	152

<b>7. CONCLUSIONS AND SUGGESTIONS FOR FUTURE WORKS.....</b>	<b>152</b>
References.....	156

## Table List

<u>Table</u>	<u>Description</u>	<u>Page</u>
<b>Chapter 3</b>		
Table 3.1	Processing Parameters	17
Table 3.2	Experimental runs and relevant processing conditions	21
Table 3.3	Milling condition and TaB <sub>2</sub> at. % for Pulverisette-4	25
Table 3.4	Milling condition and TaB <sub>2</sub> at. % for SPEX-8000D	25
Table 3.5	Relationships between M and J <sub>c</sub> for different sample geometries and orientations. M is in A/m, d and a are in m, and J <sub>c</sub> is in A/m <sup>2</sup> .	42
<b>Chapter 4</b>		
Table 4.1	Processing parameters, designations, and properties.	57
<b>Chapter 5</b>		
Table 5.1	Physical properties of Post-HIP processed MgB <sub>2</sub> from Rietveld's analyses.	61
Table 5.2	Normalized magnetic susceptibility ( $\chi$ ) for the different parameters	79
Table 5.3	Physical properties measurements for Post-HIP processed "pure MgB <sub>2</sub> " material. Data derived from the Beam model.	87
<b>Chapter 6</b>		
Table 6.1	Lattice constants, particle-size and strain analyses based on Rietveld Analyses using Power Cell Program for the SPEX-8000D at 2 at.% TaB <sub>2</sub> doped MgB <sub>2</sub> . Note: All physical parameters shown were obtained for the post-HIP samples.	112
Table 6.2	Lattice constants, particle-size and strain analyses based on Rietveld Analyses using Power Cell Program for the SPEX-8000D at 5 at.% TaB <sub>2</sub> doped MgB <sub>2</sub> . Note: All physical parameters shown were obtained for the post-HIP samples.	112
Table 6.3	Lattice constants, particle-size and strain analyses based on Rietveld Analyses using Power Cell Program for the Pulverisette-4 processed material at 800 rpm using 2 at.% TaB <sub>2</sub> doped MgB <sub>2</sub> . Note: All physical parameters shown were obtained for the post-HIP samples.	113
Table 6.4	Lattice constants, particle-size and strain analyses based on Rietveld Analyses using Power Cell Program for the Pulverisette-4 processed material at 1200 rpm using 2 at.% TaB <sub>2</sub> doped MgB <sub>2</sub> .	113

	Note: All physical parameters shown were obtained for the post-HIP samples.	
Table 6.5	Lattice constants, particle-size and strain analyses based on Rietveld Analyses using Power Cell Program for the Pulverisette-4 processed material at 800 rpm using 5 at.% TaB <sub>2</sub> doped MgB <sub>2</sub> . Note: All physical parameters shown were obtained for the post-HIP samples.	114
Table 6.6	Lattice constants, particle-size and strain analyses based on Rietveld Analyses using Power Cell Program for the Pulverisette-4 processed material at 1200rpm using 5 at.% TaB <sub>2</sub> doped MgB <sub>2</sub> . Note: All physical parameters shown were obtained for the post-HIP samples.	114
Table 6.7	Lattice constants, particle-size and strain analyses based on Rietveld Analyses using Power Cell Program for MgB <sub>2</sub> and TaB <sub>2</sub> raw no milling material, respectively. Note: All physical parameters shown were obtained for the post-HIP samples.	115
Table 6.8	Superconducting properties of the TaB <sub>2</sub> doped MgB <sub>2</sub> in the 2 at.% for the post HIP processed material in the SPEX-8000D.	149
Table 6.9	Superconducting properties of the TaB <sub>2</sub> doped MgB <sub>2</sub> in the 5 at.% for the post HIP processed material in the SPEX-8000D.	150
Table 6.10	Superconducting properties of the TaB <sub>2</sub> doped MgB <sub>2</sub> in the 2 at.% for the post HIP processed material milled in the Pulverisette -4.	150
Table 6.11	Superconducting properties of the TaB <sub>2</sub> doped MgB <sub>2</sub> in the 5 at.% for the post HIP processed material milled in the Pulverisette-4.	151

## List of Figures

<u>Figure</u>	<u>Description</u>	<u>Page</u>
<b>Chapter 2</b>		
Figure 2.1	MgB <sub>2</sub> single lattice structure	7
Figure 2.2	Fermi surface of MgB <sub>2</sub>	8
Figure 2.3	TaB <sub>2</sub> (0001) crystal structure representation of the transition metal diborides MeB <sub>2</sub> of the AlB <sub>2</sub> prototype. Red circles represent the metal atom of Ta and blue circles represent B atoms.	9
Figure 2.4	a. Triple phase diagram, b. Type I and Type II superconducting transition, c. cooper pair and the electron-phonon interaction	10
<b>Chapter 3</b>		
Figure 3.1	Schematic of the experimental procedure of Chapter 4	16
Figure 3.2	Schematic of the experimental procedure of Chapter 5	19
Figure 3.3	Schematic of the experimental procedure of Chapter 6	22
Figure 3.4	Fritch Pulverisette-4 with the two special made brass can	27
Figure 3.5	Milling ball action on grinding powder	28
Figure 3.6	SPEX 8000D mill machine with jars placed on the sample holders	30
Figure 3.7	Milling jar action on the SPEX 8000D. The red arrow shown the motion direction of the SPEX sample holders that is related to the milling ball motion inside the milling jar.	31
Figure 3.8	WC-Milling jars, control atmosphere container, milling balls and O-rings used in this work	32
Figure 3.9	a. Rubber setup and post-CIP setting for the CIP process. b. Stainless steel tube, with the post-CIP sample inside, and the vacuum setting to uses in the hot isostatic press (HIP) process, at the right.	34
Figure 3.10	Cold Isostatic Press use in this research work	35
Figure 3.11	Hot Isostatic Press use in this work and Hoskins furnace, at the right.	36
Figure 3.12	Process in the HIP treatment use in this work	37
Figure 3.13	(a) Transversal position from the pellet used in the SEM measurement. (b) Transversal surface from post-HIP pellet sectioned from the stainless steel tube.	39
Figure 3.14	Physical Properties Measurement System	40

Figure 3.15	(a) Hysteresis loop for superconducting material. (b) Isolated flux line (schematic). The distribution of magnetic field $B(r)$ (thick line) and of the density of Cooper pairs $n(r)$ (dotted line).	41
Figure 3.16	Rectangular section bar, representation of the sample, as field oriented for the PPMS measurements. Applied magnetic field is represented as dash arrow lines.	43
Figure 3.17	Representation of $T_c$ values determined at 10% $T_c$ criterion. ( $TaB_2$ doped $MgB_2$ as example).	45
Figure 3.18	STOE X-ray diffractometer. University of Wisconsin-Madison, ERB - 1128	47
Figure 3.19	A fully digital LEO GEMINI 1530 SEM with field emission electron gun, full orientation imaging based on backscattered electron Kikuchi patterns, and full EDS and control . University of Wisconsin-Madison, Material Science and Engineering Building MS&E – 171.	50
<b>Chapter 4</b>		
Figure 4.1	X-ray diffraction of heat treated samples ( $cu-K_\alpha$ ). Patterns have been offset.	52
Figure 4.2	Magnetic $T_c$ traces normalized to the magnetic moment 5K.	53
Figure 4.3	$H_{c2}(T)$ using 90% of normal state resistivity criterion. Also included for comparison is data taken from Wilke et al [30] using the same criterion.	54
Figure 4.4	$\rho(T)$ from 5 mA, 4-point measurement.	55
Figure 4.5	$J_c(H)$ at 4.2K determined from MH loops	56
<b>Chapter 5</b>		
Figure 5.1	X-ray diffraction (XRD) pattern from $MgB_2$ powdered mill material by high energy ball mill (HEBM) in the SPEX 8000D using Ball to BPR of 3:1.	62
Figure 5.2	XRD pattern from $MgB_2$ powdered mill material HEBM in the Pulverisette-4 using BPR of 10:1.	63
Figure 5.3	XRD pattern from $MgB_2$ powdered mill material HEBM in the Pulverisette-4 using BPR of 3:1.	64
Figure 5.4	Weight percent values of the $MgB_2$ and secondary phases of post-HIP processed milled material at different milling condition on the SPEX 8000D and Pulverisette-4 (P-4). Contamination by $MgO$ coming during the post-HIP no milling $MgB_2$ material is leveled at 1.6 wt.%.	66
Figure 5.5	Particle size for different milling conditions. (a) BPR = 3:1 at 300 minutes, (b) BPR = 3:1 at 4000 minutes and (c) BPR = 10:1 for 300 and 600 minutes.	68
Figure 5.6	Strain of post-HIP processed material using different milling condition shown in Table 5.1.	71

Figure 5.7	Lattice parameters of post-HIP processed $MgB_2$ using different milling condition showed in Table 5.1.	72
Figure 5.8	Tetragonality of post-HIP processed $MgB_2$ using different milling condition showed in Table 5.1.	74
Figure 5.9	Scanning electron microscope of Post HIP $MgB_2$ processed material in the Pulverisette-4 at 800 and 1200 rpm using BPR of 3:1 and 10:1 during 300 minutes.	76
Figure 5.10	Field Cooled (FC) and Zero Field Cooled (ZFC) curve normalized at 7.0K. (a) SPEX 8000D and (b) Pulverisette-4 samples are shown.	78
Figure 5.11	Superconducting critical temperature as a function of particle size of post-HIP samples. Note: The line connecting the points in the graph was traced manually in the computer. The numbers are associated with the sample number.	81
Figure 5.12	Critical current density as a function of magnetic field of the pre-reacted $MgB_2$ at 4.2 K. $J_c$ derived from the Bean model.	83
Figure 5.13	$F_p$ as a function of magnetic field at 4.2K.	85
 <b>Chapter 6</b>		
Figure 6.1	X-ray diffraction (XRD) measurement for the SPEX-8000D processed materials: 60, 120, 300, 600 and 2400 minutes corresponding to the 2 at.% $TaB_2$ doped $MgB_2$ .	91
Figure 6.2	XRD measurements for the Pulverisette-4 on the 2 at.% $TaB_2$ doped $MgB_2$ for the 800 rpm speed at 60, 120, 300, 600 and 2400 minutes.	91
Figure 6.3	XRD measurements for the SPEX-8000D for the 5 at.% $TaB_2$ doped $MgB_2$ : 60, 120, 300, 600 and 2400 minutes.	92
Figure 6.4	XRD measurements for the SPEX-8000D for the 5 at.% $TaB_2$ doped $MgB_2$ : 60, 120, 300, 600 and 2400 minutes.	92
Figure 6.5	XRD measurements for the SPEX-8000D for the 5 at.% $TaB_2$ doped $MgB_2$ : 60, 120, 300, 600 and 2400 minutes.	93
Figure 6.6	XRD measurements for the SPEX-8000D for the 5 at.% $TaB_2$ doped $MgB_2$ : 60, 120, 300, 600 and 2400 minutes.	93
Figure 6.7	MgO wt. % phase of processed material at different milling times.	94
Figure 6.8	$MgB_4$ wt. % phase of processed material at different milling times.	96
Figure 6.9	Particle size of post HIP SPEX processed $MgB_2$ phases at different milling times. Data plot at 2 at. % and 5 at. % $MgB_2$ doped $TaB_2$ .	97
Figure 6.10	Particle size of post HIP SPEX processed $TaB_2$ phase at different milling times. Data plot at 2 at. % and 5 at. % $MgB_2$ doped $TaB_2$ .	97
Figure 6.11	Tetragonality (c/a) of SPEX processed material, for $MgB_2$ and $TaB_2$ phases, at different milling times. Data plot at 2 at. % and 5 at. % $MgB_2$ doped $TaB_2$ .	99
Figure 6.12	Strain of SPEX processed material, for $MgB_2$ phase, at different milling times. Data plot at 2 at. % and 5 at. % $MgB_2$ doped $TaB_2$ .	100

Figure 6.13	Strain of SPEX processed material, TaB <sub>2</sub> phase, at different milling times. Data plot at 2 at. % and 5 at. % MgB <sub>2</sub> doped TaB <sub>2</sub> .	101
Figure 6.14	Particle size of Pulverisette-4 processed material, MgB <sub>2</sub> phase, at 800 and 1200 rpm for different milling times. Data plot at 2 at. % and 5 at. % MgB <sub>2</sub> doped TaB <sub>2</sub> .	103
Figure 6.15	Particle size of processed material, TaB <sub>2</sub> phase, in the pulverisette-4 at 800 and 1200 rpm for different milling times. Data plot at 2 at. % and 5 at.% MgB <sub>2</sub> doped TaB <sub>2</sub> .	104
Figure 6.16	Tetragonality (c/a) of Pulverisette-4 at 800 rpm processed material, for MgB <sub>2</sub> and TaB <sub>2</sub> phases, at different milling times. Data plot at 2 at. % and 5 at. % MgB <sub>2</sub> doped TaB <sub>2</sub> .	105
Figure 6.17	Tetragonality (c/a) of Pulverisette-4 at 1200 rpm processed material, for MgB <sub>2</sub> and TaB <sub>2</sub> phases, at different milling times. Data plot at 2 at. % and 5 at. % MgB <sub>2</sub> doped TaB <sub>2</sub> .	106
Figure 6.18	Strain of Pulverisette-4 processed material at 800 and 1200 rpm, for MgB <sub>2</sub> phase, at different milling times. Data plot at 2 at. % MgB <sub>2</sub> doped TaB <sub>2</sub> .	108
Figure 6.19	Strain of Pulverisette-4 processed material at 800 and 1200 rpm for MgB <sub>2</sub> phase and 800 rpm for TaB <sub>2</sub> phase at different milling times. Data plot at 5 at. % MgB <sub>2</sub> doped TaB <sub>2</sub> .	109
Figure 6.20	TaB <sub>2</sub> wt. % phase of processed material at different milling times.	111
Figure 6.21.a	Scanning Electron Microscope (SEM) of TaB <sub>2</sub> doped MgB <sub>2</sub> post HIP processed material. All micrographs belong to 60 minutes ball milled material at 2 at.% and 5 at.%.	116
Figure 6.21.b	Electron diffraction scattering (EDS) of the micrograph for SPEX processed material at 5 at.% during 60 minutes. Micrograph shown in Figure 6.21. a.	117
Figure 6.22	Critical current density (J <sub>c</sub> ) as a function of applied magnetic field (μ <sub>0</sub> H) post HIP Pulverisette-4 processed material at 800 rpm. a. 2 at.% and b 5 at.% TaB <sub>2</sub> doped MgB <sub>2</sub> .	119
Figure 6.23	Critical current density (J <sub>c</sub> ) as a function of applied magnetic field (μ <sub>0</sub> H) post HIP Pulverisette-4 processed material at 1200 rpm. a. 2 at.% and b 5 at.% TaB <sub>2</sub> doped MgB <sub>2</sub> .	120
Figure 6.24	Critical current density (J <sub>c</sub> ) as a function of applied magnetic field (μ <sub>0</sub> H) post HIP SPEX processed material. a. 2 at.% and b 5 at.% TaB <sub>2</sub> doped MgB <sub>2</sub> .	121
Figure 6.25	Overall comparison of critical current density (J <sub>c</sub> ) as a function of applied magnetic field (μ <sub>0</sub> H) for post HIP TaB <sub>2</sub> doped MgB <sub>2</sub> SPEX and Pulverisette-4 ball millings for (a) 2 at.% and (b) 5 at.% doped levels.	122
Figure 6.26	J <sub>c</sub> as a function of TaB <sub>2</sub> wt.% in the MgB <sub>2</sub> matrix. Data are extracted from J <sub>c</sub> (4.2 K) at 2 and 5 T from 2 and 5 at.% SPEX processed material.	124
Figure 6.27	J <sub>c</sub> as a function of TaB <sub>2</sub> wt.% in the MgB <sub>2</sub> matrix. Data are extracted from J <sub>c</sub> (4.2 K) at 2 and 5 T from 2 and 5 at.% of Pulverisette-4 processed material at 800 rpm.	125
Figure 6.28	J <sub>c</sub> as a function of TaB <sub>2</sub> wt.% in the MgB <sub>2</sub> matrix from Rietveld analyses. Data are extracted from J <sub>c</sub> (4.2 K) at 2 and 5 T from 2 and 5 at.% of Pulverisette-4 processed material at 1200 rpm.	125

Figure 6.29	TaB <sub>2</sub> wt. % as a function of the TaB <sub>2</sub> particle size. Data plot for 2 and 5 at.% for SPEX and Pulverisette-4 at 800 rpm processed material.	126
Figure 6.30	TaB <sub>2</sub> wt. % as a function of the TaB <sub>2</sub> particle size. Data plot for 2 and 5 at.% for Pulverisette-4 at 1200 rpm processed material.	127
Figure 6.31	Pinning force ( $F_p$ ) values as a function of applied magnetic field ( $\mu_0H$ ) for post HIP TaB <sub>2</sub> doped MgB <sub>2</sub> (a) 2 at.% and (b) 5 at.% based on Pulverisette-4 ball mill operated at 800 rpm for the times indicate in the in-set.	129
Figure 6.32	Pinning force ( $F_p$ ) values as a function of applied magnetic field ( $\mu_0H$ ) for post HIP TaB <sub>2</sub> doped MgB <sub>2</sub> (a) 2 at.% and (b) 5 at.% based on Pulverisette-4 ball mill operated at 1200 rpm for the times indicate in the in-set.	130
Figure 6.33	Pinning force ( $F_p$ ) values as a function of applied magnetic field ( $\mu_0H$ ) for post HIP TaB <sub>2</sub> doped MgB <sub>2</sub> (a) 2 at.% and (b) 5 at.% based on SPEX-8000D ball mill for the times indicate in the in-set.	131
Figure 6.34	Pinning force ( $F_p$ ) values as a function of applied magnetic field ( $\mu_0H$ ) for post HIP TaB <sub>2</sub> doped MgB <sub>2</sub> (a) 2 at.% and (b) 5 at.% based on Pulverisette-4, operated at 800 rpm and 1200 rpm, and SPEX-8000D ball mills for the times indicate in the in-set.	132
Figure 6.35	$F_p$ as a function of TaB <sub>2</sub> wt.% in the MgB <sub>2</sub> matrix. Data are extracted from $F_p$ (4.2 K) at 2 and 5 T from 2 and 5 at.% of SPEX processed material.	134
Figure 6.36	$F_p$ as a function of TaB <sub>2</sub> wt.% in the MgB <sub>2</sub> matrix. Data are extracted from $F_p$ (4.2 K) at 2 and 5 T from 2 and 5 at.% of Pulverisette-4 processed material at 800 rpm.	135
Figure 6.37	$F_p$ as a function of TaB <sub>2</sub> wt.% in the MgB <sub>2</sub> matrix. Data are extracted from $F_p$ (4.2 K) at 2 and 5 T from 2 and 5 at.% of Pulverisette-4 processed material at 1200 rpm.	135
Figure 6.38	$F_p$ as a function of TaB <sub>2</sub> wt.% in the MgB <sub>2</sub> matrix. Data are extracted from $F_p$ (4.2 K) at 2 and 5 T from 2 and 5 at.% of Pulverisette-4 processed material at 1200 rpm.	138
Figure 6.39	$T_c$ behavior at different milling time extract from 10% criterion.	139
Figure 6.40	$T_c$ as a function of MgO wt. % for SPEX processed material at 2 and 5 at. % TaB <sub>2</sub> doped MgB <sub>2</sub> . $T_c$ extract from the 10 % criterion	140
Figure 6.41	$T_c$ as a function of MgO wt. % for SPEX processed material at 2 and 5 at.% TaB <sub>2</sub> doped MgB <sub>2</sub> . $T_c$ extract from the 10 % criterion	141
Figure 6.42	$J_c$ as a function of superconducting transition slope (m) for SPEX processed material at 2 at.% and 5 at.%. $J_c$ (4.2 K) values at (a) 2 T and (b) 5 T.	142
Figure 6.43	Normalized Kramer Function ( $F_k = J_c^{0.5} H^{0.25}$ ) as a function of applied field H at 4.2 K. Pulverisette-4 at 800 rpm processed material. a. 2 at. % and b. 5 at. % TaB <sub>2</sub> doped MgB <sub>2</sub> .	145
Figure 6.44	Normalized Kramer Function ( $F_k = J_c^{0.5} H^{0.25}$ ) as a function of applied field H at 4.2 K. Pulverisette-4 at 1200 rpm processed material. a. 2 at. % and b. 5 at. % TaB <sub>2</sub> doped MgB <sub>2</sub> .	146
Figure 6.45	Normalized Kramer Function ( $F_k = J_c^{0.5} H^{0.25}$ ) as a function of applied field H at 4.2 K. SPEX processed material. a. 2 at. % and b. 5 at. % TaB <sub>2</sub> doped MgB <sub>2</sub> .	147

Figure 6.46 Irreversibility field ( $H^*$ ) as a function of  $TaB_2$  wt.% for the 2 and 5 at.%  $TaB_2$  doped  $MgB_2$ . Data plot for the material processed in the SPEX and Pulverisette-4 at 800 rpm, 1200 rpm at different milling time. 148

# 1 INTRODUCTION

Superconductivity is a phenomenon of some materials or elements where at specific temperature, the transition temperature, they suffer a change in the flow of electron through the lattice, due to the electron phonon interaction [7]. One electron collides with the ion and loses the energy, while the other electron absorbs the energy from the ion having a net energy loss equal to zero. Therefore, zero resistivity is found in superconducting materials. As functional materials and for viable applications, the main pursuit of this fascinating superconductors material is the interest in the increase of critical superconducting properties as  $J_c$  (critical current density),  $H_{c2}$  (upper critical field) and  $T_c$  (critical temperature), introducing changes at the different structural levels. One of the major applications of superconductor materials is the manufacture of high-performance superconducting magnets used in the magnetic resonance imaging (MRI) and the Superconducting Quantum Interference Device (SQUIDS). For example, Nb based superconductors as  $Nb_3Sn$  and Nb-Ti, was primary use as tape or multifilamentary cable in this magnet, but the need to use large amounts of expensive liquid helium as refrigerant was the major obstacle. Then ceramics based on copper oxide called high-temperature superconductors (HTS) as YBCO permit wide practical application allowing helium to be replaced by liquid nitrogen due to the high temperature,  $T_c$ , values. But the difficulty to obtain in a single crystal and the tendency to degrade by the weak links from the high crystalline anisotropy, the misoriented granular structure and the probable presence of lattice defects are a big problem for high temperature superconductors (HTS).”[9].

## 1.1 Motivation

This research work was motivated by the need to obtain superconducting material with high critical temperature ( $T_c$ ), critical current density ( $J_c$ ) and upper critical field ( $H_{c2}$ ), inter-grain connectivity and intra-grain pinning. Among the candidate materials used for superconducting magnets, magnesium diboride ( $MgB_2$ )-based materials appears promising because they have relatively high  $J_c$ ,  $H_{c2}$ , lower field anisotropy compared with the cuprates based ones, and also, lower material cost vis-à-vis Nb-Sn<sub>3</sub> and Nb-Ti magnets. For cuprates based superconductors {(Y,Ca)Ba<sub>2</sub>Cu<sub>3</sub>O<sub>7- $\delta$</sub>  single crystal with  $H_{c2}^{\parallel a} = 130T$ ,  $H_{c2}^{\parallel c} = 38T$  having a  $\gamma = H_{c2}^{\parallel ab} / H_{c2}^{\parallel c} = 3.4$  [57], as an example} the field anisotropy is higher than single crystal  $MgB_2$  ( $\gamma$  between 1.7 and 2.7 [58, 59, 60]). In the case of Nb<sub>3</sub>Sn ( $T_c = 18K$ ) and NbTi ( $T_c = 9.5K$ ) the cost/performance, or the price for any conductor to take electricity for one place to another, is of \$10.00/kAxm and \$0.90/kAxm for a wire at 4.2K in 10T and 2T respectively. Comparing with  $MgB_2$  the cost/performance is of 2.64/kAxm but at 25K in 1T [61]. Meaning that advances in cryocoolers, many electric utilities, fusion and high-energy physics applications may be best optimized at temperatures of 10 to 35K, a domain for which  $MgB_2$  could provide the cheapest superconducting wires. In addition, the relatively simple crystal structure, the low cost and the lack of complications arising from spin-dependent interactions or strong electron-electron correlations made accurate ab initio calculations of the electronic structure [14, 4] and of the lattice dynamics [16, 17] possible.  $MgB_2$  is characterized by relatively large coherence lengths ( $\xi$ ) compared with other metal based superconductors. NbTi ( $\xi = 4nm$ ) and Nb<sub>3</sub>Sn ( $\xi = 3nm$ ) [62], the most common metal-based superconductors used today for wires used in strong magnetic field magnets, have a coherence lengths higher than  $MgB_2$  ( $\xi = 3.7 - 12nm$ ) [2]. And an important characteristic

of MgB<sub>2</sub> superconductor is the absence of weak links in relation to the transparency of grain boundaries to current flow [3] making it a good candidate for practical applications.

On the above base, the present research is focused on the enhancement of the superconducting properties of MgB<sub>2</sub>, especially the critical current density of this material, in way to use for practical application as mention before.

## 1.2 Literature Review

After the discovery of superconducting properties of MgB<sub>2</sub> [1] many studies to the understanding of the behavior of this material have been made specially in 2001, as resume C. Busea et al. In particular, the granular type two superconductor showed strong link to the current flow due to the high current density from the large numbers of high-angle grain boundaries and blocking insulating phases within strongly shielding regions [3], with the lack of texture consisting on untextured two-phase nanomixture of MgB<sub>2</sub>, MgO, pores and some amorphous B-rich phase. This flow of electrons through the lattice is highly consistent with the Bardeen-Cooper-Schiffer (BCS) theory, due to the formation of Cooper pair by the electron-phonon interaction. The BCS theory is strongly supported by experimental study and simulation, as was demonstrated by Bud'ko et al., 2001[11] and Kortus et al., 2001 [4], respectively. Increasing neutron mass on Boron from MgB<sub>2</sub>, as MgB<sub>4</sub>, MgB<sub>11</sub>, Bud'ko et al., shown how the superconducting critical temperature change having an effects on the boron phone mode. Kortus et al, theoretically, shown that this phonon mode was due by the strong covalent B-B and ionic B-Mg bonding which induce strong electron scattering and hence strong electron-phonon coupling.

As the understanding of MgB<sub>2</sub> superconductor, increase its critical properties, manipulating the material, is the main pursuit. High Energy Ball Milling (HEBM), corresponding to this research work, is one of the techniques used to the improving of the material properties. Senkowicz et al. doping MgB<sub>2</sub> with carbon, Y.F. Wu et al. ex-situ behavior of MgB<sub>2</sub> and Bathia et al. doping MgB<sub>2</sub> with ZrB<sub>2</sub> are some of the recent study to improve superconducting properties of MgB<sub>2</sub> by HEBM. Using HEBM process, the oxidation effect, as MgO is a new phase transformation from the ex-situ MgB<sub>2</sub> reaction. Having this problem, Senkowicz, R. Perez Moyet et al., studied the effect of HEBM process on MgB<sub>2</sub> under N<sub>2</sub> atmosphere condition founding electron scattering from higher MgO composition [42]. The HEBM process is used to induce defects on the lattice structure of the material, MgB<sub>2</sub> in our case.

Due to the brittle behavior of MgB<sub>2</sub> as bulk material, a treatment to obtain dense material had been done. These have included uniaxial pressing of mixtures of Mg and B [3, 48, 49], sintering at high pressure [50, 51] and hot isostatic press (HIP) [5, 6, 32, 38, 39, 42, 52]. Senkowicz et al., had recently report higher values for J<sub>c</sub> with C doped MgB<sub>2</sub> using 1000°C at ~30kpsi for 200 min. Serquis et al., could develop 6-layer coil able to generate field of 1T at self-field. The HIP process is used in this research work with the purpose of measure physical and superconducting properties from a compact material.

MgB<sub>2</sub>, as compact material, is better known as a granular superconductor. Refinement of the grain boundaries, connection between grains and inter-grain and intra-grain superconducting or non-superconducting phases are of major importance for the improvement of this type of superconductor. Intra-granular pinning and the inter-granular connectivity, to improve the critical current density J<sub>c</sub> of MgB<sub>2</sub> especially in high applied magnetic field, is of determination for practical application [38]. In the inter-granular connectivity, the apparent lack of granularity and the low degree of texture to dominate on

high- $T_c$  materials [3], take  $MgB_2$  to a new compound based system with significant important values of  $J_c$ . In addition, superconducting homogeneity of the sample and the presence of strong inter-granular current flow having the sample as a whole [28,29], had been reported. The current on  $MgB_2$  is not limited by weak-links at the grain boundaries as cuprate high temperature superconductor (HTS) materials which require highly oriented microstructures and very small grain boundary angle in order to achieve a good inter-granular connectivity [10]. For good inter-grain connectivity is require precluding excessive porosity and microcraks, and the formation of large non-superconducting precipitates, such as  $MgO$ , at grain boundaries [42, 52].

For intra-granular pinning, is necessary to identify the effective vortex pinning centers as dislocation networks, impurities, precipitates etc. Intra-grain improved by precipitates of (e.g.  $Mg(B,O)_2$  [54],  $TiB$  [31]) has been reported. Daboried studies by D. Rodrigues Jr. showed that the critical current density,  $J_c$ , of  $MgB_2$  could be substantially enhanced by Ta doping [34].

These values of  $J_c$  are proportional related to the flux pinning of the sample which is in inter or intra grain position. Due to the granular behavior of  $MgB_2$ , shown as a double transition on resistivity ( $\rho$ ) Vs temperature (T) [56], is necessary to introduce more pinning centers and also overcome the poor connectivity between grains to increase  $J_c$  [55]. Both, pinning center and connectivity is the major deal for the superconducting properties  $MgB_2$  enhancement.

Based on the above, this study, in the pursuit for the superconducting properties enhancement, will be conducted by the following experiment: 1. Atmospheric exposure condition effects in which the handling of the material, related to atmospheric condition, will reflect drastically changes the current flow behavior through the material, 2. Strain

inducement disorder in which milling parameters will result in superconducting properties changes, especially for  $J_c$ , and 3. TaB<sub>2</sub> doped MgB<sub>2</sub> at 2 and 5 at.% in which by the decomposition of TaB<sub>2</sub> during the ball milling process is expected to have Ta substitution in the MgB<sub>2</sub> matrix as well as TaB<sub>2</sub> nanoparticles around grain boundaries.

## 2 THEORETICAL BACKGROUND

In this chapter, basic physical properties, superconducting properties and bulk processing will be discussed, as well as the understanding of magnesium (and tantalum) diborides superconductors.

### 2.1 Basic Physical Properties

#### 2.1.1 Structure and Bonding of $MgB_2$

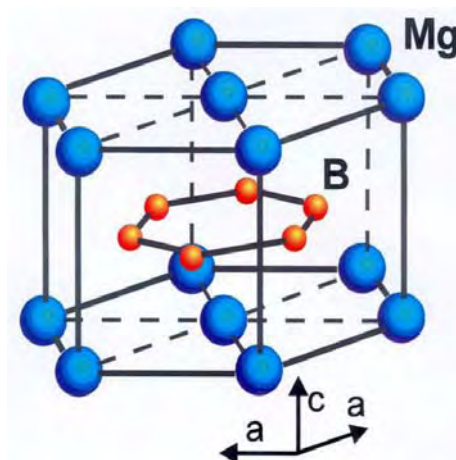


**Figure: 2.1**  $MgB_2$  single lattice structure [C. Buzea et al., 2001] [2]

Magnesium diboride  $MgB_2$ , atomic mass of 24.305 g/mol, a binary inter-metallic compound [13], shown in Figure 2.1 contains graphite-type boron layers which are separated by hexagonal close-packed layers of magnesium, as the simple hexagonal  $AlB_2$ -type structure (space group  $P6/mmm$ ) with lattice parameters  $a = 0.3085\text{nm}$  and  $c = 0.3523\text{nm}$  [21]. In this structure, the magnesium atoms are located at the center of hexagons formed by boron atoms and donate their electrons to the boron planes [2]. Metallic boron bonding, due to the delocalized metallic-type bonding between boron sheets [14], held together by covalent B-B and ionic B-Mg bonding is essentially holding  $MgB_2$ . Strong bonding induces strong electron-ion scattering and hence strong electron-phonon coupling

[4]. Due to the isotope effect, isotopic disorder on the boron phonon modes, detected in this material [11,12], the electron-phonon interactions play an important role which is consistent with the conventional BCS theory, suggested to explain the superconductivity in this material. Similar to graphite,  $\text{MgB}_2$  exhibits a strong anisotropy in the B-B lengths: the distance between the boron planes is significantly longer than the in-plane B-B distance. This anisotropy is not too strong as compared with HTS such as YBCO or BiSCCO where  $c$  is much larger than  $a$ . Theoretical study [15] found that there should be two superconducting gaps. One of them is associated with the in-plane boron phonons that are strongly coupled to the  $p_{x,y}$ -orbital ( $\sigma$ -bands) with high  $a/c$  anisotropy, and the other gap, associated to the Boron  $p_z$  orbital and Mg ( $\pi$ -bands) which is essentially three dimensional [18]. State wavefunction  $p$  is related to the outer shell orbital of Boron  $2s^2 2p^1$  in the horizontal ( $xy$ ) and vertical ( $z$ ) orientation.

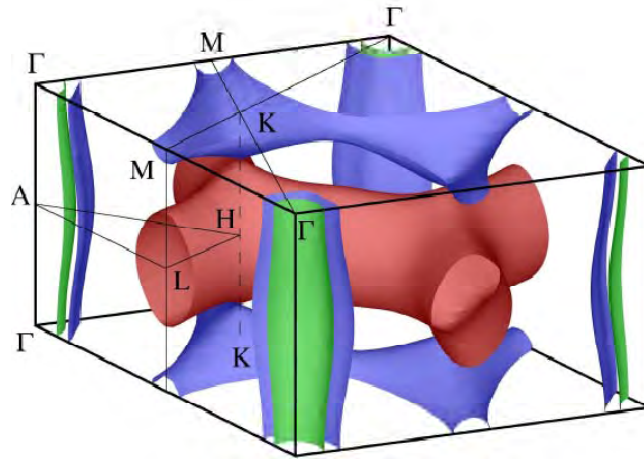


**Figure 2.2 Fermi surface of  $\text{MgB}_2$**  [Kortus et al., 2001] [4]

The Fermi surface of  $\text{MgB}_2$  is shown in Figure 2.2. In the  $\sigma$ -band, the green and blue cylinders (hole-like) come from the bonding  $p_{x,y}$  bands and in the  $\pi$ -band the blue tubular network (hole-like) from the bonding  $p_z$  bands and the red (electron-like) tubular network from the antibonding  $p_z$  band [4]. Boron atoms are  $sp^2$  hybridized, with three of the four

valence electrons tied up in strong covalent  $\sigma$  ( $p_{x,y}$ ) bonds lying in-plane, while the fourth electron is in nonbonding  $\pi$  ( $p_z$ ) states, which are delocalized. In the case of  $Mg^{2+}$ , attractive potential is felt more strongly by the electrons in the  $\pi$  states than by the ones in the  $\sigma$  states. Alloying can strain the lattice, altering the band structure.

In the case of  $TaB_2$ , c-lattice parameter is reduced as will be show in chapter 6.  $MgB_2$  is brittle and oxidezes easily.

### 2.1.2 Structure and Bonding of $TaB_2$

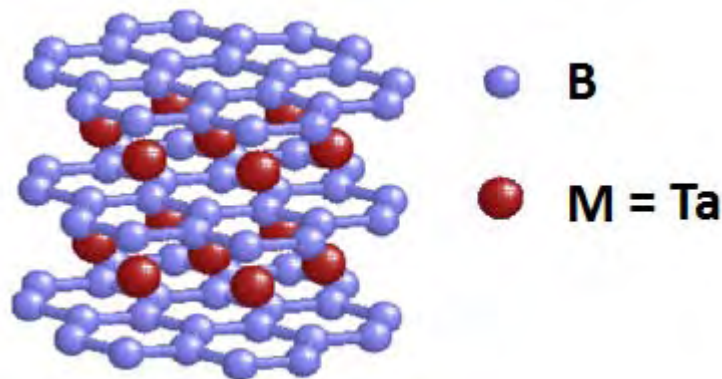


**Figure 2.3**  $TaB_2$  (0001) crystal structure representation of the transition metal diborides  $MeB_2$  of the  $AlB_2$  prototype. Red circles represent the metal atom of Ta and blue circles represent B atoms. [S. Kumashiro et al., 2006] [19]

Tantalum diboride, atomic mass of 202.57 g/mol, transition metal diborides, contain the same  $AlB_2$  prototype (space group  $p6/mmm$ ) as  $MgB_2$  with Ta as  $M_v$  from  $MB_2$  structures prototype, where  $M_v$  mean the metal atoms group V in the periodic table [19]. The boron layer are like graphite-type separated by hexagonal close-packed layers of Tantalum with  $a = 0.3098nm$  and  $c = 0.3225nm$  lattice parameters [20]. On the basis of the band structure the superconducting properties of  $TaB_2$  ( $T_c = 9.5K$ ) [22] is essentially different from  $MgB_2$  ( $T_c = 40K$ ) [1] due to the strong hybridization effects of the  $Ta(5d)-B(2d)$  states [23,24], corresponding to the outer orbital shell, with a dominating contribution (70%) of Ta 5d

states to the density of state (DOS) at Fermi level. As  $\text{MgB}_2$ ,  $\sigma$ -band belong to  $p_{x,y}$ -band while  $\pi$ -band to  $p_z$ -band. The difference between its electronic configurations is constituted on the amount of valence electrons from M atoms of the  $\text{MB}_2$  prototype. For  $\text{TaB}_2$ , three additional valence electrons of Ta with respect to Mg results in a shift from the bonding B states below the hybridization gap in  $\text{MgB}_2$  to the anti-bonding states above this gap in  $\text{TaB}_2$  at the Fermi level [23].

## 2.2 Basic Superconducting Properties

The behavior of superconducting materials is reveal in its electrical and magnetic properties. Next figure, Figure 2.4, shows important superconducting characteristics which describe that phenomenon at different structural levels.

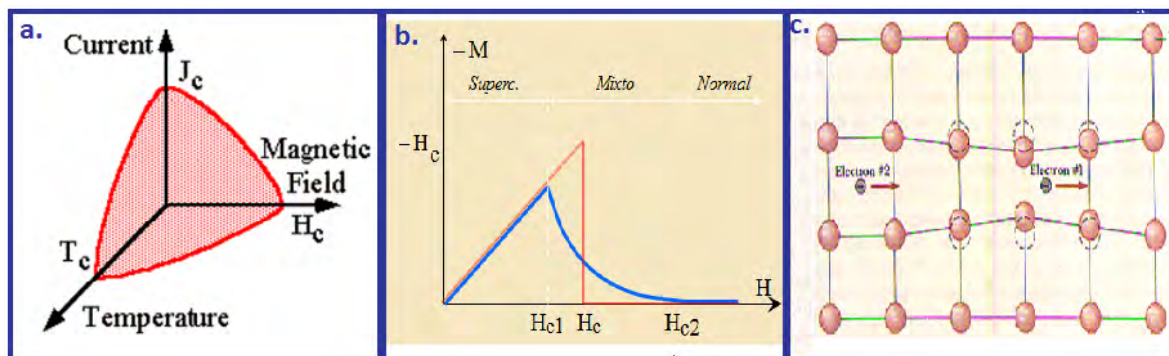


Figure 2.4 a. Triple phase diagram, b. Type I and Type II superconducting transition c. cooper pair and the electron-phonon interaction.

As shown in figure 2.4-a, an increase in any axis direction of a critical limit will destroy the superconducting state. In type II superconductor, such as  $\text{MgB}_2$  or  $\text{Nb}_3\text{Sn}$ , lower critical field ( $H_{c1}$ ) describes the area where the field can't penetrate the material, Figure 2.4-b left, and the upper critical field ( $H_{c2}$ ) where a mixed state persists with magnetic field penetrating the material creating pinning flux known as vortices, Figure 2.4-b right. These vortices will be pinned near the defects or in the grain boundaries and the pairs of electrons, known as Cooper pairs, will rotate around the vortices leading to quantized flux. If the magnetic flux moves transversely through the material, the Cooper pair can be destroyed and a resistance or scattering of electrons will be reflected in  $J_c$ . In Figure 2.4-c, the pairing of two electrons is shown by the interaction with the structure. One electron collides with the ion and loses the energy, while the other electron absorbs the energy from the ion. Therefore, the net energy loss of the Cooper pair is zero: i.e. no energy dissipation! [25]

Between metallic superconductors,  $\text{Nb}_3\text{Sn}$  is being used on commercial. It was defined as one of the superconductor to be used in the International thermonuclear experimental reactor (ITER) project in France and the Large Hadron Collider (LHC) for particles acceleration in Geneva, Suiza.  $\text{MgB}_2$  is a high field superconductor with potential interest in the future. Due to the low cost of  $\text{MgB}_2$ , and its high  $H_{c2}$  ( $H_{c2}^{\perp}(0) \approx 40\text{T}$  to  $T_c \approx 35\text{-}40$ ) it is able to substitute  $\text{Nb}_3\text{Sn}$  ( $H_{c2}(0) \approx 30\text{T}$  to  $T_c \approx 18\text{K}$ ) for high magnetic field application. Application as the ITER,  $\text{Nb}_3\text{Sn}$  is too expensive compared with  $\text{MgB}_2$  and for NMR (Nuclear Magnetic Resonance) application, with 1GHz magnets needed, will be not possible with the  $\text{Nb}_3\text{Sn}$  technology.

The critical current density ( $J_c$ ) in a material is defined as the maximum current that a superconductor can support or the maximum applied magnetic field a material where the magnetic flux lines are pinned in the material. Above  $J_c$ , the dc current breaks the Cooper pairs, and thus, destroys the superconducting state. This magnetic flux line pinning in the

material is due to the defects in the material such as grain boundaries or second phase precipitations from the same or different superconducting composition. The intensity ( $\vec{F}_p = \vec{J}_c \times \vec{B}$ ) of the flux line, different from  $J_c$  that depend on the flux line center, comes from different source of the superconducting material. As an example, in NbTi,  $F_p$  arise from normal superconducting phases of Ti- $\alpha$  created from mechanical deformation and heat treatment sequences. In Nb<sub>3</sub>Sn,  $F_p$  originates from the grain boundaries generated during the heat treatment of the superconducting phase formation and by the compositional variation of the phases close to the grain boundaries [26]. This situation is similar to MgB<sub>2</sub> and granular superconductor ceramics [27].

Another way to increase the magnetic flux line by introducing normal or superconducting phase to the superconducting material known as artificial pinning center (APC). The introduction of normal or superconducting phase in the intra-grain or inter-grain region can be compared with the coherent length  $\xi$  of the material. The coherence length is a key parameter for the performance of superconductors for applications, because this parameter determines the size of the normally conducting core of the flux lines. In order to control the motion of flux lines one needs a microstructure with defects as small as the coherence length [43]. When the thickness and/or spacing of the different phases are of the order of  $\xi$ , the proximity effect will induce superconductivity in those regions which will transform in internal defects as superconducting phases. This generates magnetic flux pinning highly efficient at increasing the critical current density. [34]

In the inter-granular connectivity, respect to the apparent lack of granularity and the low degree of texture is said to dominate on high- $T_c$  materials [27], superconductivity on MgB<sub>2</sub> is improved it by its weak links behavior in the grain boundaries. In addition, superconducting homogeneity of the sample, due to the uniformly trapped magnetic field

by the sample, and well connected grain, by the presence of strong inter-granular current flow, in the whole of the sample [28,29], had been reported by Magneto Optical image study up to 30K. For intra-granular pinning, it is necessary to identify the effective vortex pinning centers such as dislocation networks, impurities, precipitates etc. For example, intra-grain pinning improved by precipitates had been reported, (e.g. Mg(B,O)<sub>2</sub> [30], TiB [31]).

MgB<sub>2</sub> is a special superconductor because of its two superconducting gaps [4]. The superconductivity in this material occurs in the boron layers. There are two bands at the Fermi surface in this material. The first one is a narrow band, built up of boron  $\sigma$  orbital and with the larger energy gap  $\Delta_{\sigma}$ , while the second one is a broader band with a smaller effective mass. Both energy gaps have a s-wave symmetry. The larger gap is highly anisotropic, while the smaller one is either isotropic or slightly anisotropic, [33]. It means that  $T_c$  and  $H_{c2}$  must be controlled by  $\sigma$  band properties in a randomly oriented bulk. Because the bands are only weakly coupled, it is possible to exploit differential scattering rates within each band to alter the properties, especially to improve  $H_{c2}(T)$  without significant  $T_c$  reduction. For each band acting separately,  $H_{c2}$  is determined by the coherence length, and for a total  $H_{c2}$  is therefore determined by the dirtier band. Decrease on  $T_c$  with no  $H_{c2}$  benefit is causing by an interband scattering [32]. In the interband scattering  $T_c$  decrease with no  $H_{c2}$  benefit.

In practice, the electron scattering can be the result of defects, disorder (such as neutron scattering [35]), strain, or alloying. The electron scattering can be improved by good grain boundaries connectivity that is the main issue in order to achieve high  $J_c$ . In the case of MgB<sub>2</sub>, weak link behavior at grain boundaries [3] indicates less electron scattering. As we discussed before, artificial introduction of flux pinning centers such as Si compounds [36]

has resulted in increased  $J_c$ , but  $MgB_2$  is primarily a grain boundary flux pinner, as demonstrated by Kitaguchi et al. [37].

The improvement of grain connectivity had been done by the use of the hot isostatic pressing (HIP), on  $MgB_2$ . The hot isostatic pressing allows the application of pressure during the heat treatment in the material. High  $J_c$  values ( $10^6$  A/cm<sup>2</sup>) had been obtained by this process on the ex-situ  $MgB_2$  [38]. Heat treatment of bulk sample at ambient pressure lead to unsatisfactory results [39].

Moreover, the introduction of inter-grain and intra-grain of superconducting phases will have an important contribution on the magnetic flux pinning for granular materials in practical applications. [40]. In the case of  $MgB_2$ , which shows granular behavior, the manipulation of its superconductivity properties, magnetic flux pinning mainly, had been arise by compound-element doped  $MgB_2$ . This methodology attempt to improve the poor capacity of intrinsic pinning flux in  $MgB_2$ , increasing the  $J_c$  values without negatively influencing the  $T_c$  in the material but positively influencing the grain connectivity. In order to have the superconducting phase via doping well mixture, the use of high energy mechanical alloying had been used specially on intermetallic superconductors [41, 39 and 42]. One of the interesting aspects of this technique is that no change of the physical and chemical compound characteristic in the final results. Metastable compound can be obtained as a result of the milling process.

After high energy ball mill process the hot isostatic press process will be used for sintering, and pressing small particles from a metastable state, to an equilibrium state. These small particles will have different responses, compared with the starting material, by the amount of defects induced in the process. Therefore, the mixed state might increase and the superconducting properties will be enhanced by the material processing, especially the critical current density. In that way, the atomic configuration for  $MgB_2$  and  $TaB_2$  must

respond to a new electron flow action through the lattice using TaB<sub>2</sub> doped MgB<sub>2</sub> to improve the magnetic flux pinning.

## 2.3 Bulk Processing

The processing of MgB<sub>2</sub> bulk material, starts from two different routes. One route is the *ex-situ* process and the other is the *in-situ* process. In both route, the main goal is to find the balance between grain connectivity and the intra-grain pinning by enhancement of inter-grain and intra-grain phases which can improve the critical current density through the superconducting material. The in-situ method involves the formation of MgB<sub>2</sub> by the reaction of Mg and B, while the ex-situ involves the processing of the pre-reacted material. Because the melting temperature  $T_m$  of Mg is 650 °C, good grain connectivity is difficult to obtain. The advantage of the ex-situ method is that it allows working directly with processing variables as mechanical work. Some mechanical works, such as the reduction of particles size, inducing of strain, and alloying can be induced by high energy ball milling. Additionally, sintering and grain growth is obtained by the HIP treatment.

TaB<sub>2</sub> as doped material, in this research work, can be found, after processed the material, at the grain boundaries, inter-intra grain boundaries, as well as interstitial or substitutional defects by the decomposition of its constituent. As a result, superconducting properties on MgB<sub>2</sub> will be improved, especially  $J_c$ , an important superconducting parameter in view of application.

### 3 EXPERIMENTAL PROCEDURES

#### 3.1 Sample preparation Synthesis

##### *3.1.1 Atmospheric conditions and their effects on Ball Milled Magnesium Diboride [Senkowicz B.J., Pérez Moyet R., et al., 2006]*

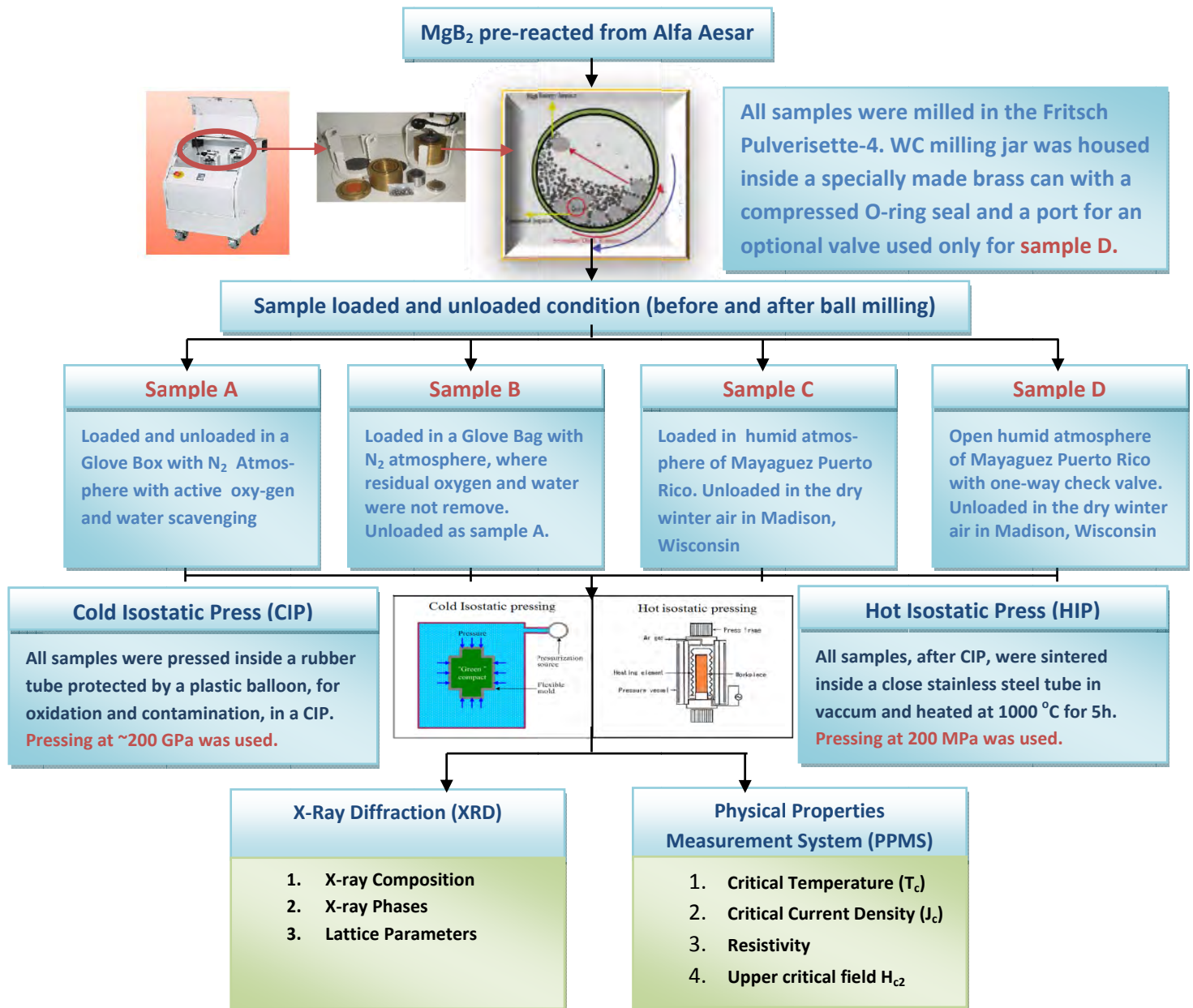


Figure 3.1 Schematic of the experimental procedure of **Chapter 4**

### 3.1.1.1 Experimental detail

All four samples were made from Alfa-Aesar pre-reacted  $\text{MgB}_2$ . We milled for 10 hours in a Fritsch Pulverisette-4 ball mill both to promote compositional homogeneity and in order to facilitate interaction with gas in the milling jar. For all samples, the WC milling jar was housed inside a specially made brass can with a compressed O-ring seal and a port for an optional valve used only for sample D. Milling was carried out with hardened steel balls. Although there is a possibility of contamination by the milling apparatus, the jar and balls did not show any visible wear, and there was no evidence for iron or WC contamination based on x-ray diffraction patterns. Moreover the milling procedure was identical for each sample.

The four samples were handled and milled under slightly different atmospheric conditions. For sample A, the milling jar was loaded and sealed into the brass can in a glove box filled with dry nitrogen and equipped with active oxygen and water scavenging. After milling, the jar was opened and the powder was handled in the same glove box. For sample B, a similar milling jar was loaded and sealed in the brass can in a nitrogen filled glove bag filled with flowing  $\text{N}_2$  gas from which residual oxygen and water were not removed. Unsealing and post-milling handling were done in the glove box, as for A. For samples C and D, the milling jars were loaded and sealed in the brass can in the typically humid atmosphere of Mayaguez, Puerto Rico and, after milling, were unsealed and handled in the dry winter air in Madison, Wisconsin. The brass can was hermetically sealed for sample C, whereas for sample D the brass can was fitted with a one-way check valve that could open to vent excess pressure from the milling can. The handling atmospheres and property summary are listed in Table 3.1.

**Table 3.1 Processing Parameters**

Sample	Atmosphere
A	Glove Box
B	Glove Bag
C	Air (sealed)
D	Air (valve)

The milled powders were pressed into pellets and sealed in evacuated stainless steel tubes, then hot isostatic pressed (HIP) at 1000°C and ~200 MPa for 5 hours. The pellets were sufficiently dense after sintering that they had hardness > 10 GPa and needed to be sectioned with a diamond saw before measurement.

### 3.1.2 Disorder (Strain) Experimental on Pure $MgB_2$ : Pulverisette-4 Vs SPEX 8000D

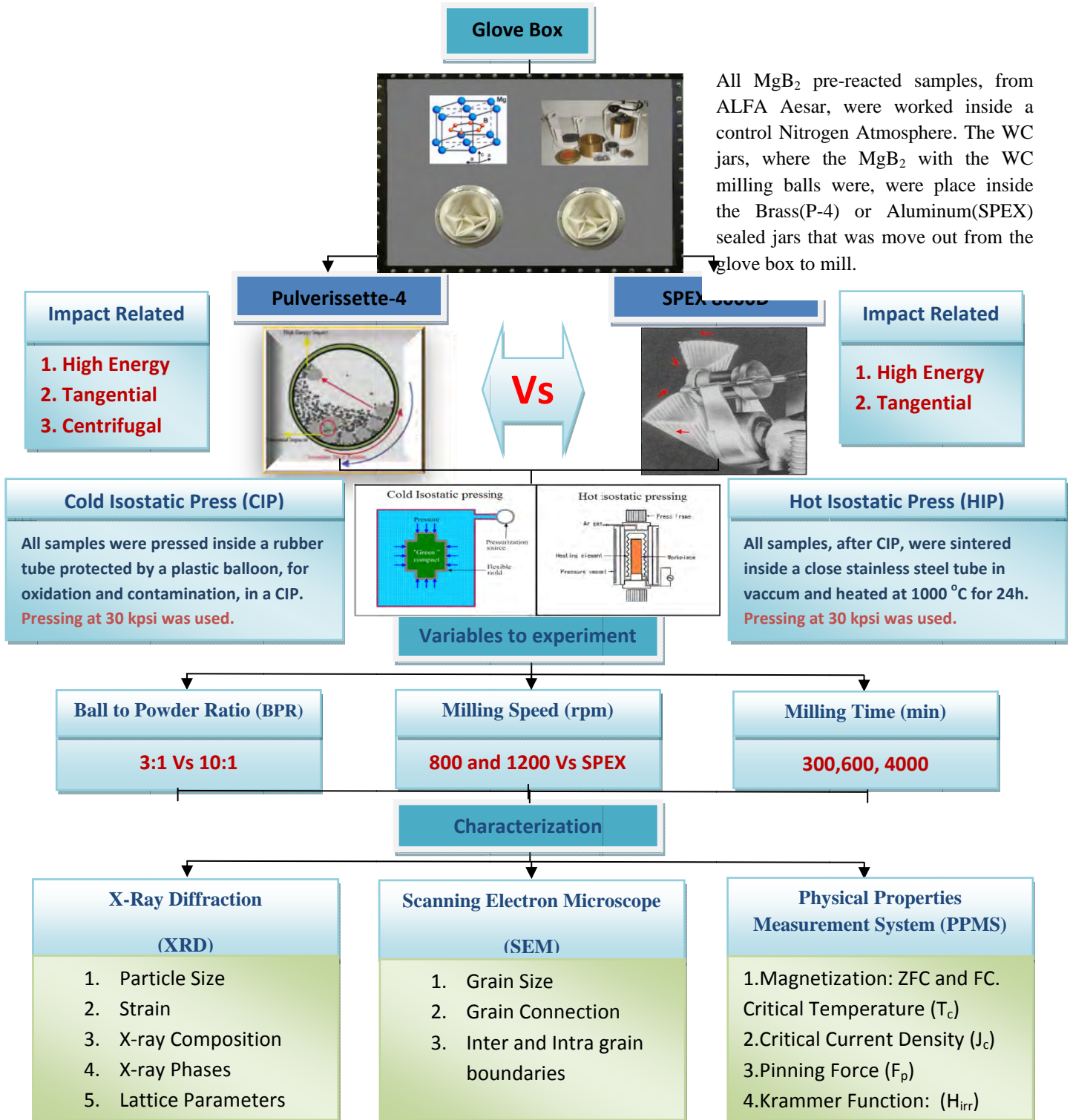


Figure 3.2 Schematic of the experimental procedure of Chapter 5

### *3.1.2.1 Experimental detail*

The starting material for this study was ALFA-Aesar supplied pre-reacted MgB<sub>2</sub> of -325 corresponding mesh. All material handling, including weighing and loading in grinding jars were carried out under tightly controlled atmospheres in a glove box purged with both nitrogen and forming gas in order to eliminate or minimize oxidation and humidity getting during material handling. Special containers were constructed to enable ball milling in the SPEX 8000D and Pulverisette mills without exposure of the materials to humidity and possible oxidation.

The SPEX 8000D mill was operated with a WC lined jar and WC milling balls. The number and sizes of the WC balls were of ½”, two of 3/8” and one of ¼” balls. The total amount of powder used were to achieve Ball-to-powder ratios (BPR) of 10:1 and 3:1 respectively. For the Pulverisette-4 (P-4) mill, the two rotational speeds employed were 800rpm, and 1200rpm using a -2.0 R-ratio setting respectively. The milling times were 60min, 300min, 600min and 2,400min in the two milling machines.

Following ball milling, the powders were pressed in a Cold Isostatic Press (CIP) at 30,000psi into pellets by placing the powders in a rubber tube with rubber taps inside a close rubber balloon under N<sub>2</sub> atmosphere which was followed by sealing in evacuated stainless steel tubes. Next, the samples were sintered at 1000 °C for 24h at 29,500psi in a hot isostatic press (HIP). The samples were sectioned with a diamond saw after sintering in order to undertake structural characterization and superconducting properties measurements.

**Table 3.2 Experimental runs and relevant processing conditions**

Processing Conditions		Ball milling conditions			
		Sample	Time (min)	BPR	
SPEX 8000D		1	300	3:1	
		2	4000	3:1	
Pulverisette-4	800 rpm	3	300	3:1	
		4	4000	3:1	
		5	300	10:1	
		6	600	10:1	
	1200 rpm	7	300	3:1	
		8	4000	3:1	
		9	300	10:1	
		10	600	10:1	
	Un-milled		11	MgB <sub>2</sub> Raw after CIP and HIP process	

All high energy ball milled samples and sample 11, in Table 3.2, were CIP and HIP processed after milling process.

### 3.1.3 Critical Current Density Enhancement of TaB<sub>2</sub> Doped MgB<sub>2</sub>: High Energy Ball Milling Process

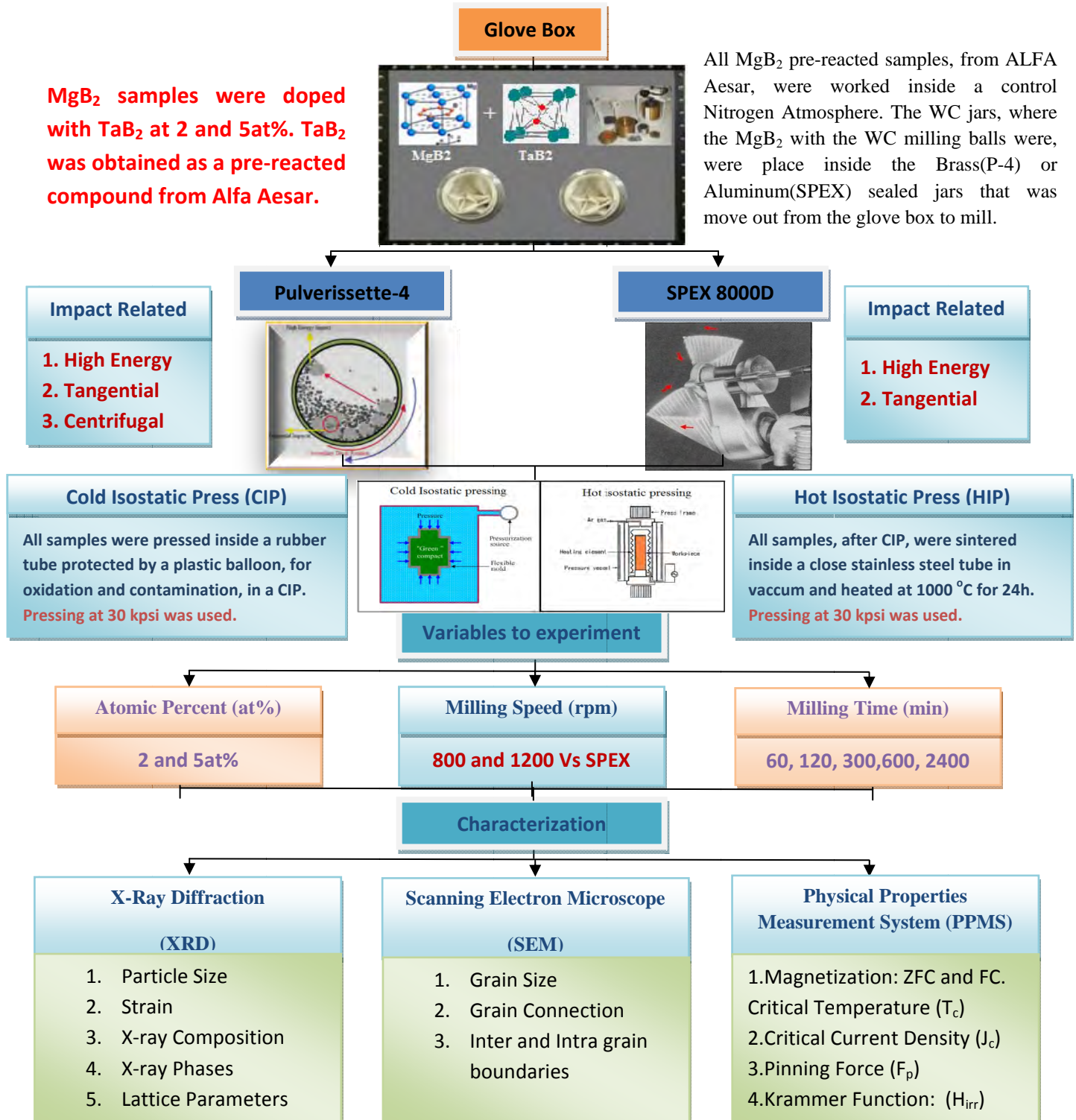
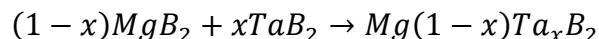


Figure 3.3 Schematic of the experimental procedure of Chapter 6

### 3.1.3.1 Experimental detail

Alfa-Aesar supplied prereacted  $MgB_2$  powders, corresponding to -325 mesh were weighed out in appropriate amounts together with Sigma Aldrich supplied pre-reacted  $TaB_2$  powders (product # 336173) to reflect 2 at.% and 5 at.% of  $TaB_2$ , with the  $MgB_2$ , in a tightly controlled inert nitrogen atmosphere. The two powder materials were loaded in vials for SPEX-8000D and Pulverisette-4 mills respectively in order to achieve the following reaction:



The WC lined jars were operated with WC balls in order to achieve a ball-to-powder ratio (BPR) of 3:1 in all the ball milling operations.

For the SPEX-8000D mill, a total of four WC balls were used. Two of the balls measured 3/8" in diameter, while the other remaining ones measured 1/2" and 1/4" in diameter respectively. Since the milling speed of the SPEX-8000D was fixed, therefore the only parameters that could be adjusted with this mill were the milling time, and the BPR. The vials were housed in a specially constructed container to permit tightly controlled handling and processing of the powdered materials

In the case of Ball milling with Pulverisette-4, the rotation speed and the BPR were varied. In this study two rotation speeds of 800rpm and 1200rpm were used, using the -2.0 R-ratio setting for the two cases respectively. The milling times were 60, 120, 300, 600, and 2400min in both the SPEX-8000D and Pulverisette-4 millings. Following the ball milling operations, the powders were removed from the milling jars housed in the specially constructed containers inside a glove box back filled with nitrogen. The powders were pressed in a cold isostatic press (CIP) into pellets at 30,000 psi by placing them in a rubber

tube equipped with rubber taps enclosed in a close rubber balloon under N<sub>2</sub> atmosphere. The pellets were subsequently sintered at 1000 °C for 24 hours on a hot isostatic press (HIP) at 29,500 psi after sealing them in evacuated stainless steel tubes.

Lastly, the superconducting wires were characterized using a Siemens-STOE X-ray diffract meter and scanning electron microscopy (LEO Gemini 1530 field emission). X-ray diffraction measurement was used to determine the lattice parameters while the strain analyses was carried out with the aid of the Power Cell program. The magnetization measurements were undertaken with a physical property measurement system (PPMS-Quantum Design). Magnetization-Field [M-H] at 4.2K and Magnetization-Temperature [M-T] at 50 Oe were carried out. The current density (J<sub>c</sub>), pinning force (F<sub>p</sub>) and irreversibility field extrapolation (H\*) were derived from the width of the magnetization loop using the Bean's model [44], while critical temperature (T<sub>c</sub>) was determined from zero field cooled (ZFC) and field cooled (FC) curves.

Following equations were used to change at.% to wt.% from 2 and 5 at.% TaB<sub>2</sub> doped MgB<sub>2</sub>.

$$A_1 = \text{atomic weight MgB}_2 = 45.925 \text{ g/mol} \quad = \frac{C_1 = \text{MgB}_2 \text{ wt. \%}}{(\text{MgB}_2 \text{ at. \%})x A_1 + (\text{TaB}_2 \text{ at. \%})x A_2} \times 100$$

$$A_2 = \text{atomic weight TaB}_2 = 202.57 \text{ g/mol} \quad = \frac{C_2 = \text{TaB}_2 \text{ wt. \%}}{(\text{MgB}_2 \text{ at. \%})x A_1 + (\text{TaB}_2 \text{ at. \%})x A_2} \times 100$$

TaB<sub>2</sub> wt.% for 2 at.% is 8.26 wt.% and TaB<sub>2</sub> wt.% for 5 at.% is 18.84 wt.% equal C<sub>2</sub>, respectively.

To verified:

$$C'_1 = \frac{C_1 A_2}{C_1 A_2 + C_2 A_1} \times 100 = \text{at. \% for MgB}_2$$

$$C'_1 = \frac{C_2 A_1}{C_1 A_2 + C_2 A_1} \times 100 = \text{at. \% for TaB}_2$$

Table 3.3 Milling condition and TaB<sub>2</sub> at. % for **Pulverisette-4**

Equipment	Rotational Speed (rpm)	Time (min)	at. %
<b>Pulverisette-4</b>	800	60	2
	800	120	2
	800	300	2
	800	600	2
	800	2400	2
	1200	60	2
	1200	120	2
	1200	300	2
	1200	600	2
	1200	2400	2
	800	60	5
	800	120	5
	800	300	5
	800	600	5
	800	2400	5
	1200	60	5
	1200	120	5
	1200	300	5
	1200	600	5
	1200	2400	5

Table 3.4 Milling condition and TaB<sub>2</sub> at. % for **SPEX-8000D**  
Note: **SPEX** milling machine has a constant speed.

Equipment	Time (min)	at. %
<b>SPEX-8000D</b>	60	2
	120	2
	300	2
	600	2
	2400	2
	60	5
	120	5
	300	5
	600	5
	2400	5

### ***3.1.4 High Energy Ball Milling Process***

In the processing of milling materials, in the High Energy Ball Milling, the numbers of mechanical parameters came relevant. Parameters that, at the end, you can make constant for the specific material or a group of materials. Materials to mill, amount of milling balls and the different size, the revolution of milling, the milling time are some of the parameters we can find in the milling process. In this case, we use two different milling media: Pulverisette-4 (P-4) and SPEX-8000D (SPEX)

These two mill machines, using just prepared material, help us to reduce the particles and grains size of the compound we have interest. But the way they mill is not the same. The mechanical parameters and the way they mill, send us for two different ways in the big matrix of variables in try to reach to optimal conditions of processing. The metastable state after milling is always present in both mill Ball Mill, where is necessary to sintering them close to the melting point of the material. In this case, we used a Hot Isostatic Press in which pressing and sintering the material at the same time. But let try first to understand how mill machine work.

### 3.1.4.1 Pulverisette – 4



**Figure 3.4 Fritsch Pulverisette-4 with the two special made brass can.**

Three different impacts are responsible for the milling process in the P-4: high energy impact, tangential impact and centrifugal impact. These three impacts are related to the motion of the two different plates in which the jar, containing the sample, is placed. The secondary plate or disk, rotate as a function of the rate of the main disk that always rotate clockwise. This rate is known as R-ratio. These parameters allow that the secondary disk rotates clockwise, counter clockwise or just free rotation manipulated by the main disk.

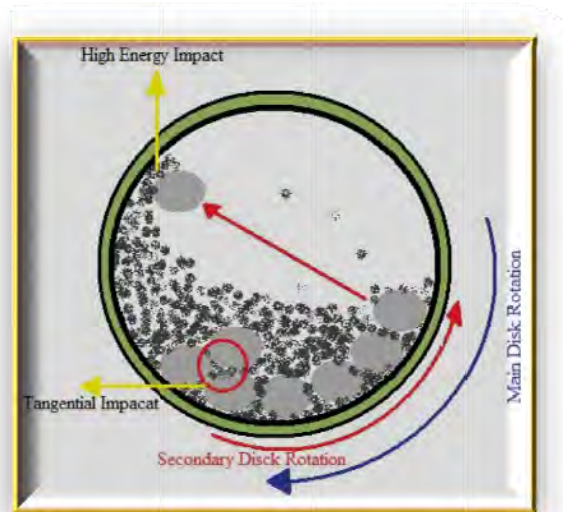


**Figure 3.5 Milling ball action on grinding powder.**

When the motion of the secondary disk is counter clockwise the ball moves around the inner walls of the jar and in some critical point, jump side to side the jar creating the high energy impact. If the motion is clockwise most of the balls stay around the inner walls by the centrifugal force and might overlap each other. For the clockwise motion, the predominant impact of the ball is the centrifugal impact. The tangential impact always occurs in the milling process creating a friction between ball-particle-ball or ball-particle-inner wall.

Understanding these three important impacts in the P-4, it is clear to realize how the momentum between particles, balls and the inner walls depended on the material, size of the balls and the revolution per minute (rpm) can be set. In a conservative system the momentum of a particle that drops from a determinate high will have the same kinetic energy seconds before stop, that is associated to the impact force in that system. The same in the ball milling process when the balls collide with the wall and between them. If the revolution of the main disk and the R-ratio parameters are constant, the mass of the ball, related to the material being made, and the size of the ball, will be the two parameters that

come to play. Three important range sizes of the balls are 5mm or ¼", 10mm or 3/8" and 15mm or ½". The homogenization of the particles is facilitated by reduced ball size. Parallely, the reduction of the particle size leads to the increase of the energy of the material, defects density, and subsequently increased metastable state. This metastable state is a state in which the overall sample is out of equilibrium and the microstructure and the atomic properties are affected due to the defects at the atomic and microscopic length scale.

If the parameter to evaluate is the change of the rotation speed, revolution per minute (rpm), the energy will increase inside the jar while increase the speed of the main disk. In this case the energy inside the jar will depend on the velocity of the balls that will define the impact force between the wall-particle-ball. Another way to manipulate the speed of the ball is changing the r-ratio parameter. It might reduce or increase the speed depends of the direction and the rate is set.

### 3.1.4.2 SPEX 8000D

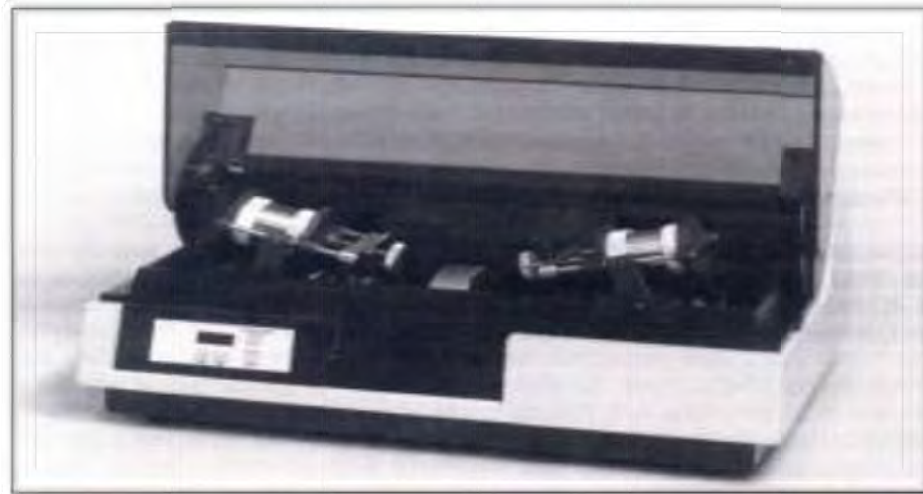


**Figure 3.6 SPEX 8000D mill machine with jars placed on the sample holders.**

The SPEX machine, specifically SPEX 8000D, does not too many parameters as the P-4. The only variables that could be manipulated in the SPEX are the milling time, and ball to powder ratio and the variation of the ball sizes. The two sample holders of the SPEX can support one samples in each, which helps to reduce the amount of milling work, with respect to the samples. Instead of rotation, as the Pulverisette-4, the motion of the SPEX 8000D is violent shaking and rocking of the balls with the material charge in a horizontal motion of the plate, that support the two sample holders, letting the ball to move side to side inside the milling jar. As the container is swung, the inertia of the grinding elements causes them to move independently, into each other and against the container wall, grinding the sample. This type of motion is too aggressive putting too many defects on the lattice structure.

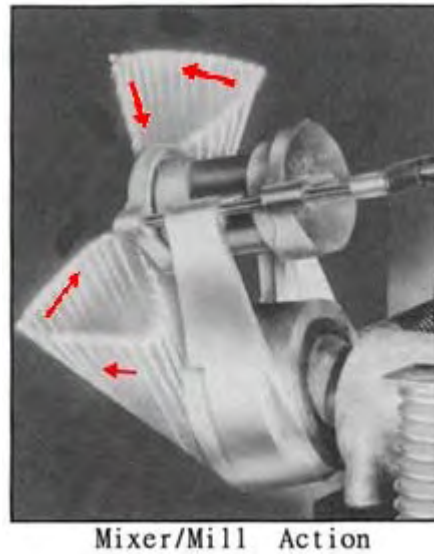


**Figure 3.7** Milling jar action on the SPEX 8000D. The red arrow shown the motion direction of the SPEX sample holders that is related to the milling ball motion inside the milling jar.

Tangential impacts in the SPEX 8000D is the most probably impact when compared with Pulverisette-4, because the horizontal and vertical movement. This is one of the reasons why the particle size of materials milled in this machine decrease so drastically to 10nm while the particle size on P-4 was for about ~30nm, based on the milling conditions discussed in the experimental section of this document. Tungsten Carbide (WC) contamination on SPEX was found, in addition to its contribution to the  $T_c$  reduction discussed in subsequent chapters.

### 3.1.4.3 General milling parameters

The grain refinement and the mechanical alloy, TaB<sub>2</sub> doped MgB<sub>2</sub>, were carry out for both milling machines. More drastically for SPEX 800D which particle size reduction was ~10nm before the hot isostatic press (HIP) treatment. Due to the many parameters in Pulverisette-4 the comparison with SPEX was not easy. However, in way to make experimental analyses in the disorder experiment and TaB<sub>2</sub> dope MgB<sub>2</sub> effect experiment, slightly changes on the milling parameters were took. To control the contamination by humidity or oxidation [Senkowicz and R. Perez Moyet et al., 2006] an especial brass container for Pulverisette-4 and aluminum container for SPEX 8000D was made shown in Figure 3.8.



Figure 3.8 WC-Milling jars, control atmosphere container, milling balls and O-rings used in this work.

An O-ring seal was need to have an hermetical brass and aluminum container. Because the heavily weight of the brass material, an aluminum brass container was necessary in the SPEX 8000D with the same specification of the brass container for the pulverisette-4. A silicon rubber was at the bottom and top of the inside brass container to eliminate vibration on the tungsten carbide (WC) milling jar, with the inside wall of the container. Because the WC jar of the SPEX can screw it, no rubber was used.

Milling jar used in both milling machine were WC jar with an internal volume of 45mL (pulverisette-4) and 49.5mL (SPEX). The milling balls were of the same material using BPR of 10:1 Vs 3:1 in the disorder experiment and just 3:1 in the TaB<sub>2</sub> experiment and in the atmospheric condition as well. After the first part of the process (load the sample in the milling jar inside the glove box, seal it in the brass can, mill for several time and unload in the glove box) the milling jar should have the same condition before start the new sample process. The first step for clean the jars is put some water and soap in the jar with the balls and let it in the pulverisette-4 or in the SPEX, depend from which milling jar belong (if a shaker is available will be better), for 15min. Repeat the same process two times more. After it, the material will come out. Is necessary use a sand paper or a soft stone with a “dremer” and clean carefully all area inside until eliminate particles that not come out in the first step. Then, the internal area of the milling jar must be clean well with water and soap again. To do this, the use of the shaker or the milling machine for 15min will help. The next step is wash and clean well the milling jar with water and dry it with hot air. To eliminate the particles of H<sub>2</sub>O inside the jar and around the balls is necessary to use Isopropanol 99.99% and shake well as in the previous steps with water. Two times this process is enough to eliminate the contamination with water. Hot air was use again to dry the milling jar. After all this process the milling jars were ready to use again for the next sample. Is important to never let the material in water for many time, some white surface is created on the balls and the inner wall of the milling jars. The O-rings was clean with water and soap and then isopropanol 99.99% as with the milling jars. Silicon rubber O-ring was more useful.

### 3.1.5 Cold Isostatic Pressing and sealing methods

The compressed milled powder was first performance by the cold isostatic press (CIP). CIP is a powder compaction method involving applying pressure from multiple directions through a liquid or gaseous medium surrounding the compacted part. In this work, liquid medium was used. The sample to the CIP process must have a contamination protection setup. In that way, the sample preparation before the CIP process consisted on load the powder in short (2.5”) sections of rubber tubing sealed at the ends with rubber plugs, as shown in Figure 3.9-a.

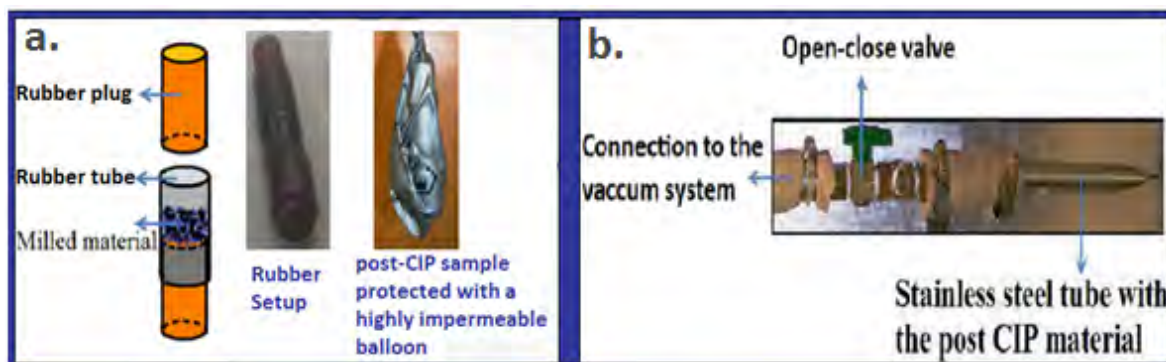


**Figure 3.9** a. Rubber setup and post-CIP setting for the CIP process. b. Stainless steel tube, with the post-CIP sample inside, and the vacuum setting to uses in the hot isostatic press (HIP) process, at the right.

This rubber setup is done in inside the glove box. The glove box used was the from Dr. Hellstrom E.E lab in Engineering Research Building (ERB) in Madison-Wisconsin, now in Tallahassee-Florida. The rubber setup was covered by a highly impermeable balloon closed. The balloon is placed in the CIP machine and pressed at 30,000 psi (~200 MPa). An amorphous cylindrical pellet is obtained. The CIP used was fabricated by Autoclave Engineers Inc., de Erie, PA, EUA, Brand “IP3-22-60 (WP-60000PSI, shown in Figure 3.10.



**Figure 3.10** Cold Isostatic Press use in this research work ,from D. Rodrigues Jr. [26]

After the CIP process the post-CIP sample was loaded in a 304 stainless steel tube with one end of the tube already closed and welded. The starting tube length was ~6". Then, the tube with the pellet inside was connected to the vacuum setup shown in Figure 3.9-b. The valve was opened while connected to the tube to the vacuum setup inside the glove box, and closed before removal from the glove box. After vacuuming, the open side of the tube was closed with an air pressure press and flattened with a hammer. The side close to the vacuum setup in Figure 3.9-b was cut with the scissors and welded to preserve the vacuum inside.

The totally closed stainless steel tube was put back again in the CIP unit and pressed further in order to verify if the tube was well closed. This is necessary to ensure that unwanted chemical reaction does not occur due to  $MgB_2$  reacting with the stainless steel due to the high pressure of the CIP unit, during the heat treatment stage of the CIP process. This process was handling involving the sample to an inert gas or vacuum.

Next, the sample will be heat treated on the HIP unit. There is a reasonable possibility of direct air exposure during the welding stage of the material, hence the suggestion of spot welding by Senkowicz [32] during this step.

### ***3.1.6 Hot Isostatic Pressing***

Hot isostatic pressing (HIP) involves isostatic pressing conducted at increased temperature. It combines pressing and sintering, causing consolidation of powder particles, reducing amount of healing voids and pores. The HIP unit used in this project was fabricated by American Isostatic Presses Inc. (International Pressure Service, Inc.), of Columbus, OH, USA, model HIP6-45H (Eagle HIP), shown in Figure 3.11.



**Figure 3.11** Hot Isostatic Press use in this work ,from D. Rodrigues Jr [26].  
Hoskins furnace, at the right.

The heat treatment allowed the formation of superconducting phases of  $\text{MgB}_2$  with the inter-grain and intra-grain segregation of  $\text{TaB}_2$  (magnetic flux pinning centers) while a high

sample densification and thereby ensuring optimal condition to increase the grain connectivity of the superconducting phase.

After CIP process, explained in section 3.1.5, the post-CIP sample was placed inside the Hoskins furnace shown in Figure 3.11. This furnace is loaded inside the HIP chamber as identified with the arrow. The heat on this furnace is more concentrated at the middle. Because the sample was not exactly in the center of the stainless steel tube, the tube was placed in the furnace so as to have the closes proximity between the sample and the heat concentration area. The amount of samples for HIP treatment was around 15 samples. In the HIP process the temperature used was 1000°C for 24 hours and the pressure was 29,500 psi (~200MPa). This time is enough to obtain samples with highly homogeneous and dense, structure thereby increasing the granular connectivity and the superconducting properties optimization. The temperature and pressure was increased as describe in Figure 3.12.

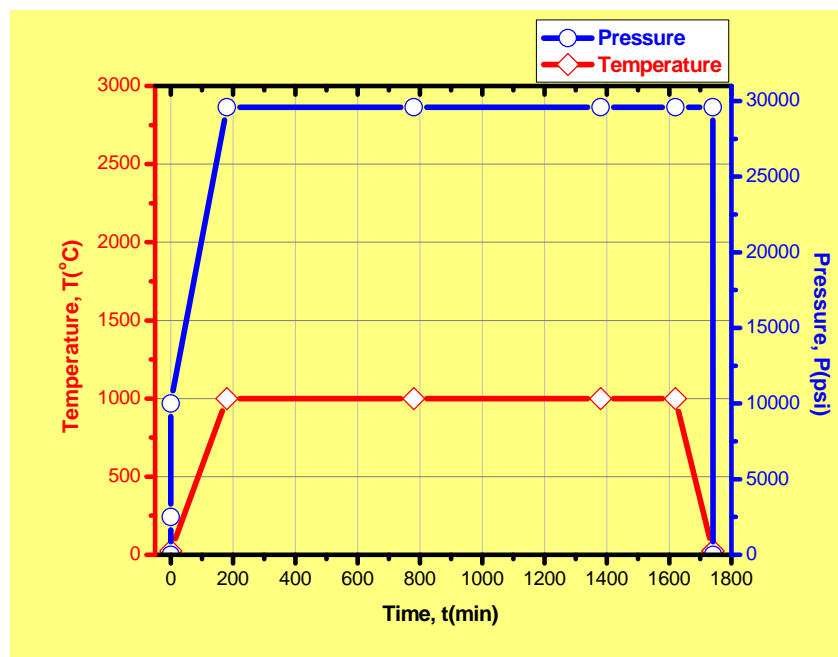


Figure 3.12 Process in the HIP treatment use in this work.

In the first four stage the pressure increases while the temperature remain at 25<sup>0</sup>C. With increase in pressure due to increase of temperature, eventually both attend values in which was considered the heat treatment for 24 hours. This is subsequently fallowed the temperature decrease and, after which the pressure decrease to its original stage.

### ***3.1.7 Sintered sample preparation***

After the HIP process the sample must be removed from the post-HIP stainless steel tube to make possible its characterization. An isomer of Buehler with a diamond blade (4”diametro and 0.0012”thick) was used to transversally section the tube making deformed cylindrical pellets with thickness of ~0.9 to 1.0 mm. the lubricant use was the typically water-based. Although water oxidizes MgB<sub>2</sub>, those samples that required lubricant were dense enough that oxidation was limited to a surface layer typically a few microns thick [32]. An advantage of the diamond blades thickness was less sample loss. The piece of stainless steel around the pellet was cut with a pliers and removed with hand.

## 3.2 Characterization Technique

The characterizations of the samples investigated were carried out by subjecting the samples to the following measurements:

- Powder X-ray diffraction measurements were made on the milled powders and the hot isostatically pressed superconducting pellet, at the facilities of the University of Wisconsin-Madison in the STOE diffractometer system.
- In the case of SEM measurement, the transversal surface of the pellet was used. Figure 3.13 shows the position of the pellets in the SEM measurement. Carbon tape was used to paste the sample.
- For the physical properties measurement system (PPMS) measurement, the pellets were cut, using pliers and sand paper, in small rectangular shapes. With this shape it was possible to determine the magnetic transition temperatures  $T_c$ , the critical current density  $J_c$  and magnetic flux pinning using the Bean Model [44]

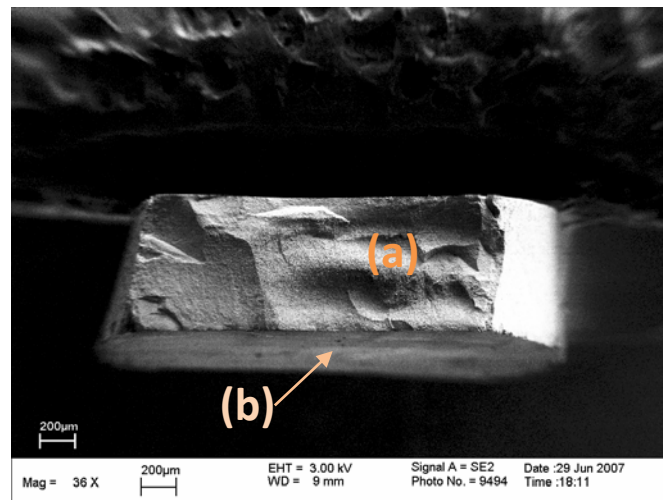


**Figure 3.13** (a) Transversal position from the pellet used in the SEM measurement. (b) Transversal surface from post-HIP pellet sectioned from the stainless steel tube, used in the X-ray diffraction measurements.

### 3.2.1 Superconducting characterization of the samples

#### 3.2.1.1 Magnetometry

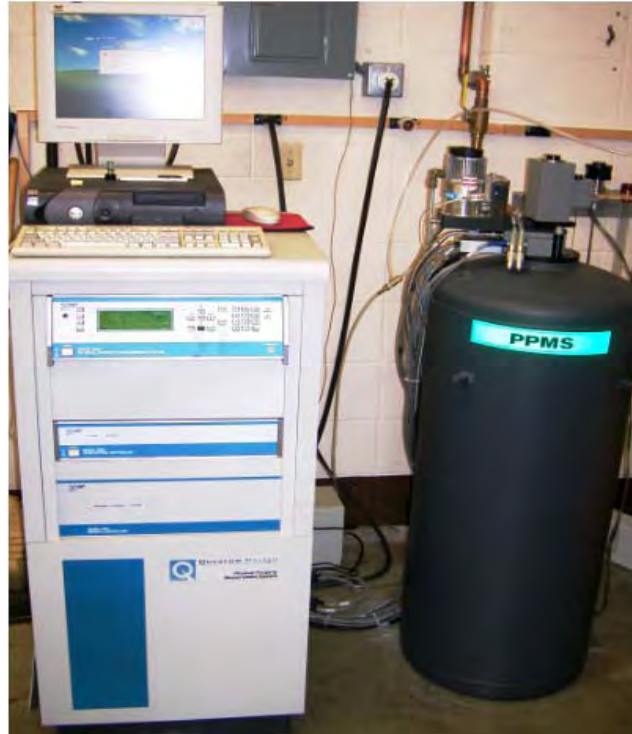


**Figure 3.14 Physical Properties Measurement System (PPMS)**

The Physical Properties Measurement System (PPMS) of Quantum Design model 6000, using small densities of transport current of the order of  $0.3 \text{ A/cm}^2$  at the ASC-University of Wisconsin-Madison, was used to measure the magnetic properties of the post-HIP sample  $\text{MgB}_2$  and the alloy with  $\text{TaB}_2$ . This system consisted of a pair of pick-up coils with opposite winding directions connected in series. The sample was placed at the end of a probe which moved the sample vertically from one coil to the other. Magnetic moment ( $m$ , expressed in  $\text{A} \cdot \text{m}^2$ ) was generated on the sample when a magnetic field was applied. The reaction of the sample to the applied magnetic field was evaluated as the volumetric magnetization ( $M = m/\text{Volume}$ , expressed in  $\text{A/m}$ ).

For type II superconductors, the magnetization behavior will be the contribution between the clean area, where the magnetic field can't penetrate the sample (before the lower critical field  $H_{c2}$ ), and mix state, where the applied magnetic field penetrates the sample creating magnetic flux pinning surrounded by superconducting phases. Then, a Hysteresis loop by vortex pinning is the result of induced current by the applied magnetic field.

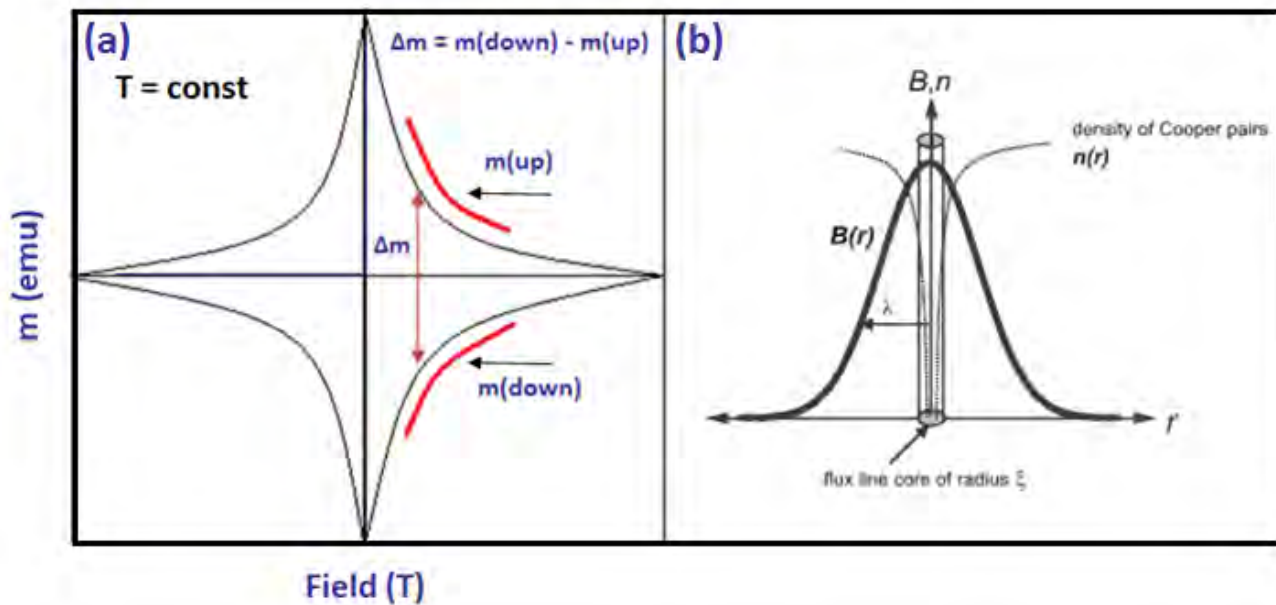


Figure 3.15 (a) Hysteresis loop for superconducting material. (b) Isolated flux line (schematic). The distribution of magnetic field  $B(r)$  (thick line) and of the density of Cooper pairs  $n(r)$  (dotted line). [Picture (b) from reference 43]

As shows in Figure 3.15-a,b, the density of the Cooper pair,  $n(r)$ , disappears within the flux line core of radio  $\xi$  (coherence length). At the same time,  $B(r)$ , decays exponentially, becoming very small for  $r \gg \lambda$  (penetration depth) [43]. This is the situation of type-II superconductors, in which the most important elementary interaction between vortices and pinning centers are the magnetic interaction and the core interaction [8]. The magnetic interaction arises from the interaction of surfaces between superconducting and non-superconducting material parallel to the applied magnetic field and the core interaction is

due to the short coherence length and the large penetration depth. In the non-superconducting surface, or when superconductivity is suppressed, the magnetic flux are well pinned, as for example superconducting second phase, pores, or grain boundaries. The magnetic flux has two possibilities to pass through the sample: first, increasing the penetration depth ( $\lambda$ ), around the material, while the temperature increase, as in Type I superconductors, or second, increasing  $\lambda$  from flux pinning center created for non superconducting regions in the material, as in granular type superconductors. This association of flux vortices with pinning centers gives rise to the pinning force density ( $F_p$ ):

$$F_p = -F_L \cdot J_c = -(J_c \times \mu_0 H) \cdot J_c$$

Where  $F_L$  is the Lorentz force associated with electrical conduction in a magnetic field and  $\mu_0 H$  is the applied magnetic field. Using the critical state model, known as the Bean model [44], it is possible to extract  $F_p$  from the hysteresis loops shown in Figure 3.15.a. In order to determine  $J_c$ , based on this model, it is necessary to use the sample geometry according to he expressions given in Table 3.5.

**Table 3.5 Relationships between M and  $J_c$  for different sample geometries and orientations. M is in A/m, d and a are in m, and  $J_c$  is in A/m<sup>2</sup>. [32]**

Sample shape	Orientation	M(A/m) =
Cylinder (diameter 2a)	B // axis	$\frac{J_c a}{3}$
	B $\perp$ axis	$\frac{4J_c a}{3\pi}$
Infinite slab (thickness d)	B // face	$\frac{J_c d}{2}$
Square section bar (d x d)	B // axis	$\frac{J_c d}{6}$
	B $\perp$ face	$\frac{J_c d}{4}$
Sphere (radius a)		$\frac{3\pi J_c a}{32}$
Disk (2a, thickness d)	B $\perp$ face	$\frac{J_c a}{3}$
Rectangular section bar (b x d with b > d)	B // axis	$\frac{3b-d}{12b} J_c d$

In this research work, the rectangular geometry was used, with  $l$  (m), the length of the sample, parallel to the applied magnetic field.

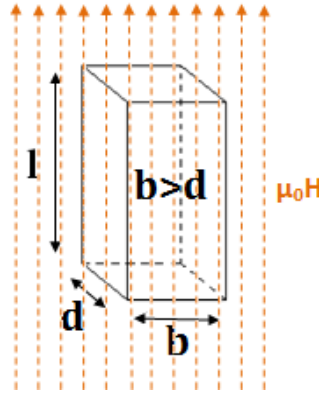


**Figure 3.16** Rectangular section bar, representation of the sample, as field oriented for the PPMS measurements. Applied magnetic field is represented as dash arrow lines.

In this way  $J_c$  is:

$$J_c(A/m^2) = \left(\frac{\Delta M}{2}\right) (GF) = \left(\frac{m(\text{down}) - m(\text{up})}{2}\right) \left(\frac{12b}{3bd - d^2}\right)$$

Where GF is the geometrical factor from Table 3.5.a and  $\Delta M/2$  is to have the best average curve. From the  $J_c$  measurement is possible to determine the force pinning  $F_p$  is given by:

$$F_p(N/m^3) = J_c(A/m^2) * \mu_0 H(T)$$

in which will be possible to observe the efficiency of pinning present in the samples.

For the irreversibility field ( $H^*(T)$ ) it is necessary to make an extrapolation of the  $J_c$  values to the x-axis. This field is the applied magnetic field at which the pinning force goes to zero (or the Cooper pair are destroyed) and the sample cannot sustain any current without vortex

motion. Respect to the hysteresis loop is shown in Figure 3.15.a, where  $H^*$  is defined as the field in which the hysteresis loop closes. Another way to find  $H^*$  is by the Kramer function extrapolation. The extrapolation of this function is a straight line which approximates  $H^*$ . This line is obtained by plotting  $J_c^\alpha H^\beta$  against  $H$ . For  $MgB_2$ ,  $\alpha = 0.5$  and  $\beta = 0.25$  in which Kramer function is quite linear.

The error bar is a reflection of the measurements due to the caliper calibration in the measurements of the dimensions sizes of the shape selected from Table 3.5, rectangular shape for this research measured with a caliper, and from eye error. The smallest division of the caliper is 0.05 mm. The caliper error was taken as the half of those divisions, 0.025 mm. If the sample is not regular the eye error must take it account. To eliminate this error the polished of the sample must be as well as possible. Good parallel faces, getting from the polishing of the sample, can help to eliminate those errors. In this experiment, just the caliper error was used.

Another magnetometry characterization is the M-T curve in the zero field cooled (ZFC) and field cooled (FC) process.

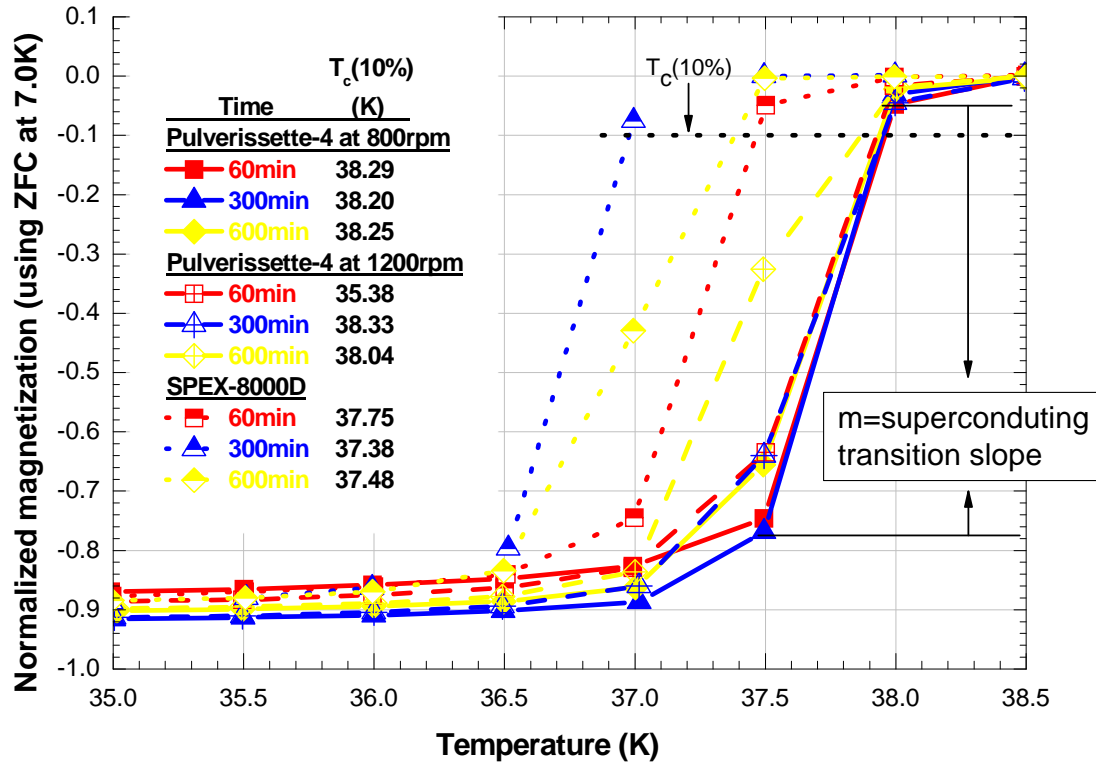


Figure 3.17 Representation of  $T_c$  values determined at 10%  $T_c$  criterion. ( $TaB_2$  doped  $MgB_2$  as example).

Figure 3.17 allows to observe the critical temperature ( $T_c$ ) in which the material loose or gain superconductivity, depending in the temperature direction. In the ZFC process, the temperature in the system go to the minimum temperature it can reach, which was in this research work 4.2K with zero applied magnetic field. Then, the magnetic field is applied and the sample produced a negative moment, superconductor responds as a diamagnetic material, due to induced screening currents which flow on the superconductor surface. This measurement is due not too far, after  $T_c(K) < T(K)$ . In the FC process, the reducing of

temperature is with an applied magnetic field. In this situation, the applied magnetic field is inside the superconductor material before reaching  $T_c$  and the weak induced magnetic field in the sample is not enough to totally repeal the magnetic field as in the ZFC. As  $T$  approach  $T_c$ , the diamagnetic response weakens until superconductivity breaks down at  $T_c$ . The broad transition, after  $T_c$ , to reach the maximum negative moment of the sample is related to inhomogeneity and non-superconducting phases. Because of this it is a necessary criterion to get the most accurate values of  $T_c$ . The criterion used in this research work was  $T_c(K)$  at 10%.

Next, the transition to the lower magnetization can reveal information about the impurities, from secondary phases, and grain connectivity in the material. In Figure 3.17 this transition is leveled as a slope  $m$ . This superconducting transition slope is different from each material processing due to the wt. % composition amount of difference phases. In Chapter 6, TaB<sub>2</sub> doping effect, this transition is generated by the amount of TaB<sub>2</sub> wt. % phases in addition to the other contribution as MgO and MgB<sub>4</sub>. Then, low and high slopes were observed for different material processed. The difference between the slopes can shows levels of inhomogeneity in the sample.

### ***3.2.2 Microstructure characterization of the samples***

#### ***3.2.2.1 Powder X-ray diffraction (XRD)***



**Figure 3.18** STOE X-ray diffractometer. University of Wisconsin-Madison, ERB - 1128

The basic principle for XRD is better understood by the Bragg diffraction. Bragg diffraction is a consequence of interference between waves reflecting from different crystal planes. The condition of constructive interference is given by:

$$m\lambda = 2d\sin(\theta) \quad (\text{Bragg's law})$$

where  $\theta$  is the diffraction angle,  $d$ , is the distance between crystal planes,  $\lambda$ , is the wavelength of the x-ray radiation, and  $m$  is an integer called the order of the interference. Because, as is clear in the Bragg's law,  $d$  is dependent of  $\theta$ , referred to peak position  $2\theta$ , XRD can be used to determine the lattice parameter. In the case of the peak broadening, due to the inhomogeneity, disorder, strain, grain size and instrument factor as the slit width. The grain size, using small grain condition, can be to determined by:

$$t = \frac{0.9\lambda}{B \cos \theta_B} \quad (\text{Scherrer's formula})$$

where,  $t$ , is the calculated grain size,  $B$  is the peak breath in radians and  $\theta_B$  is the peak position.

X-ray diffraction pattern allows the phase analyses associated with composition and structural transformation from the original material. By XRD technique it is possible to have information about the structure of solids, and the arrangement of atoms that compose the solid. The diffractometer used in this work was Siemes-STOE of high resolution with Bragg-Brentano geometry. Defects on the crystal lattice were precisely analyzed, with the STOE, reflected as strain on the structure from the lattice parameters. Using a Powder Cell program for the X-ray analyses, and not the traditional method of the Scherrer's formula, it was possible to study the structural properties changes on  $\text{MgB}_2$ .

This program is to translate, rotate, change, add or clip atoms, molecules or components of the structures, in order to manipulate the resulting XRD pattern, thus obtaining a better correspondence with experiments [46]. Powder Cell is based in the Rietveld Analyses [45] which allows the determination of the lattice parameters, particle size and strain of the sample. The Rietveld's analysis, by Hugo M. Rietveld, is an introduction of the least-squares refinement of structure, especially for a polycrystalline sample where certain information is lost as a result of the random orientation of the crystallites. This refinement method is applicable for nuclear and magnetic structures. Rietveld divide in two groups the least-squares parameters. The first group defines the positions, the half widths, and the possible asymmetry of the diffraction peaks in addition to a property of the powder sample preferred orientation. The second group, the structure parameters, defines the contents of the asymmetric unit cell. Because these parameters are not linear, the first refinement cycle, in the program, is an approximation of all parameters. Refinement cycles continuing until a

certain convergence criterion have been reached. Others tools are necessary to be able to use employ Rietveld analyses using Powder Cell program.

The Pearson's Handbook of crystallography is a crucial tool to set the original parameters that will be compared with the XRD pattern of the samples. In the initial data, getting from the Pearson's Handbook, the space group number, lattice parameters  $a_0$ ,  $b_0$ ,  $c_0$ ,  $\alpha$ ,  $\beta$ ,  $\gamma$  and all atoms of the asymmetric unit (atomic number and the coordinates of all atoms), is necessary to set. Data as  $2\theta$  range, step size, diffraction geometry and many other parameters are necessary, too.

Those physical properties, by XRD analyses will contribute in the understanding of the magnetic properties as changes in the critical current density and critical temperature are recorded. Relations as "lattice parameters Vs  $J_c$ " are shown in the following chapters.

### 3.2.2.2 Scanning Electron Microscope (SEM)



**Figure 3.19** A fully digital LEO GEMINI 1530 SEM with field emission electron gun, full orientation imaging based on backscattered electron Kikuchi patterns, and full EDS and control . University of Wisconsin-Madison, Material Science and Engineering Building MS&E – 171.

The SEM technique is used for qualitative analyses of average particle size and grain size, and identifies phase composition and microstructures defects. The SEM is a type of electron microscope that creates images by focusing a high energy beam of electrons onto the surface of a sample and detecting signals from the interaction of the incident electrons with the sample's surface. The type of signals in SEM can include secondary electrons, characteristic x-rays, and back scattered electrons. The SEM technique was used in this work to indentify secondary phases and to observe the internal surface o the sample.

## 4 ATMOSPHERIC CONDITIONS AND THEIR EFFECT ON BALL-MILLED MAGNESIUM DIBORIDE

In this chapter atmospheric condition effect was studied in way to understand the change of superconductivity properties of  $MgB_2$ . Pure  $MgB_2$  was milled in the Pulverisette-4 at different exposure condition to the atmosphere. This chapter was a contribution of the University of Wisconsin-Madison (UW-Madison) and the University of Puerto Rico - Mayaguez Campus (UPRM). Our major contribution to the atmospheric condition effect study was experimental. The synthesis and the handling of the material outside and inside of a glove bag, with nitrogen atmosphere, and the milling of the materials in the Pulverisette-4 milling machine, at different milling parameters, was our major contribution, done in UPRM laboratories facilities. It was compared with the synthesis and the handling of the material outside and inside a glove box with Nitrogen atmosphere and regeneration system, at UW-Madison, to control the oxygen amount that can react with the sample. The results and discussion of this chapter was carryout by Ben Senkowicz at the UW-Madison. The publication of this chapter corresponds to reference [64].

## 4.1 Results

X-ray diffraction patterns are shown in Figure 4.1. Experimental detail and description for each sample was discussed in Chapter 3. All material processed has similar XRD patterns and all contained small amount of MgO and MgB<sub>4</sub>. The observed peak at ~63° is a composite between MgB<sub>2</sub> peak at 63.27° and MgO peak at 62.22°. The shift in this peak from sample A to sample D indicated that the amount of MgO contained in those samples is high compared with samples A and B, which were milled in an inert atmosphere. These peaks were also observed in the disorder experiment in chapter 4 and in chapter 6, TaB<sub>2</sub> doped MgB<sub>2</sub>. Higher amount of MgO peaks was found for SPEX processed material compared with the Pulverisette-4 processed samples. MgB<sub>4</sub> was also observed in the next two chapters, must prominent to material processed in the SPEX.

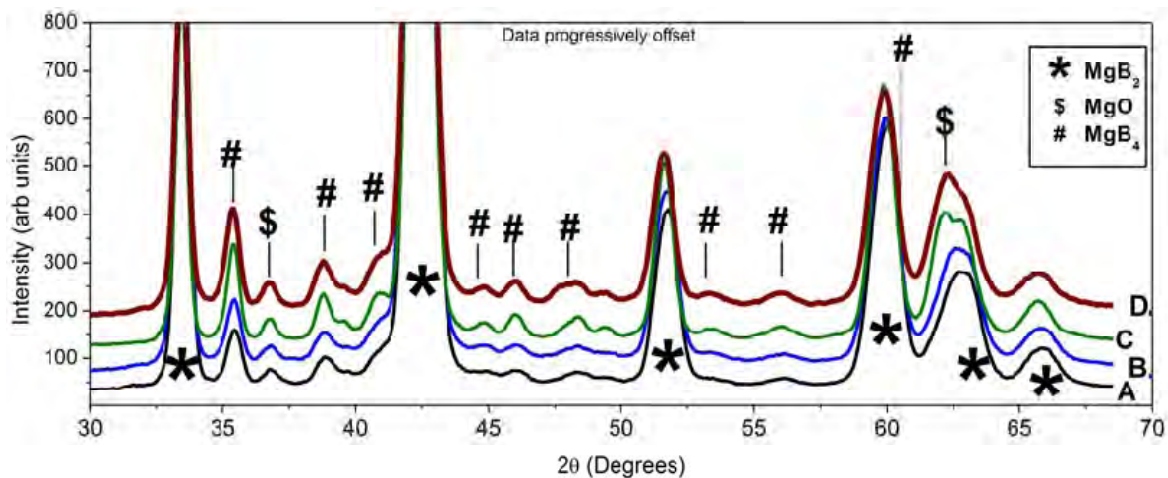


Figure 4.1 X-ray diffraction of heat treated samples. Patterns have been offset. [32]

Figure 5.2 shows the magnetic moment  $m$  as function of Temperature, normalized to the moment at 5 K. It was measured in the SQUID after increasing zero-field cooling. From sample A to sample D a depression in  $T_c$  is observed. The highest  $T_c$  is obtained for sample A while the lower  $T_c$  correspond to sample D. The transition to the lower magnetization is slightly different for each sample. Sample A have the sharpest transition while sample D had a fairly sharp transition, beginning  $\sim 0.5$  K below that of sample A. Sample B and C has a sharp transition but not as sharp as sample A. Fairly and sharps transition was also found for TaB<sub>2</sub> doped MgB<sub>2</sub> at 2 and 5 at.%.

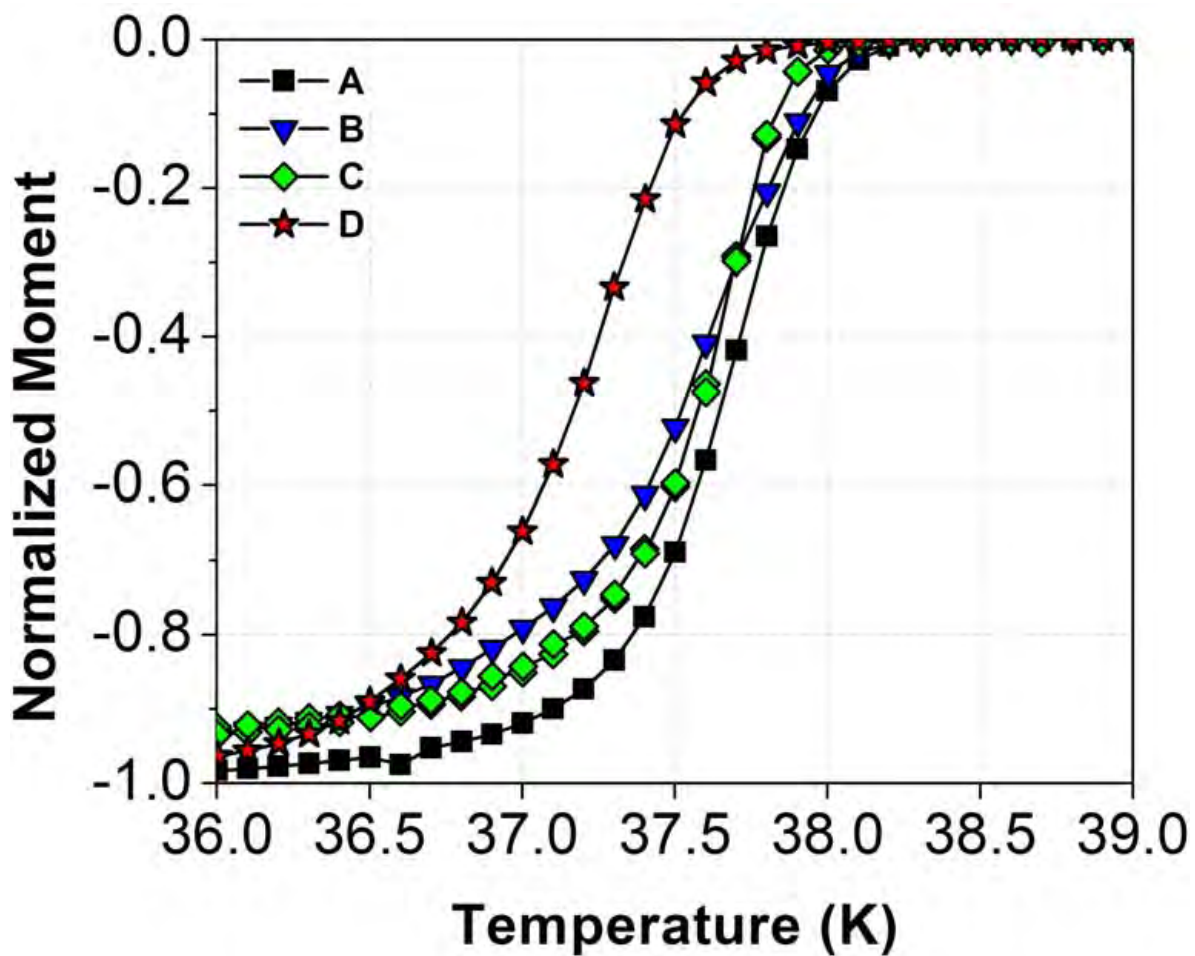


Figure 4.2 M-T properties 5 K. [32]

Figure 4.3 shows the dependence of the upper critical field,  $H_{c2}$ , on temperature, defined using 90% of the normal state resistivity.  $H_{c2}$  increase from 7.0 T from sample A to 7.9 T for sample D. This behavior was opposite to what was found for  $T_c$  in each sample. While  $T_c$  decrease from sample A to D,  $H_{c2}$  decrease.

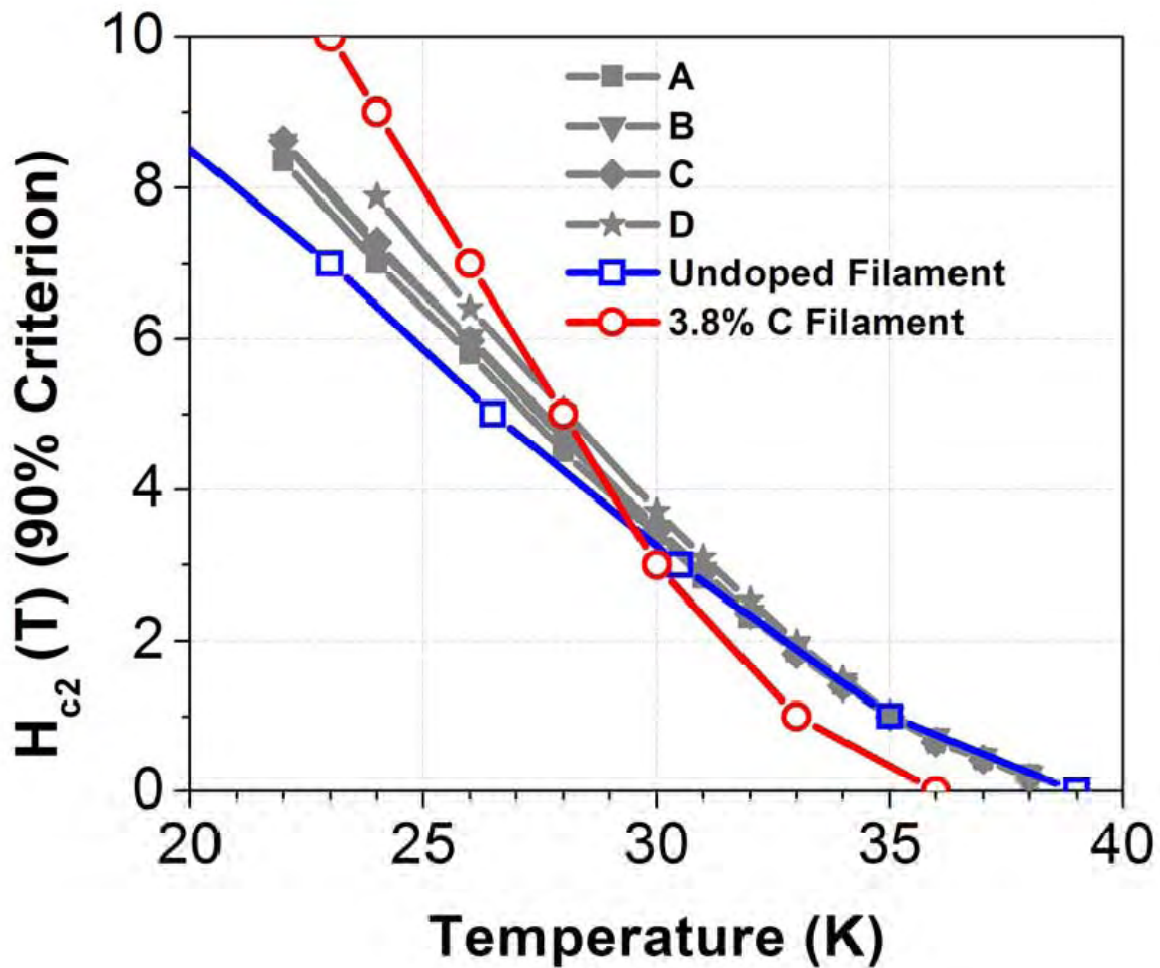


Figure 4.3  $H_{c2}(T)$  using 90% of normal state resistivity criterion. Also included for comparison is data taken from Wilke et al [65] using the same criterion. [32]

Figure 4.4 shows the temperature dependence of resistivity  $\rho$ . An increase in resistivity was observe, as well as an increase in  $\Delta\rho = \rho(300\text{ K}) - \rho(40\text{ K})$  from sample A to C while a decrease in the residual resistivity ration RRR. The resistivity of sample D fall between samples B and C and had the lowest RRR.

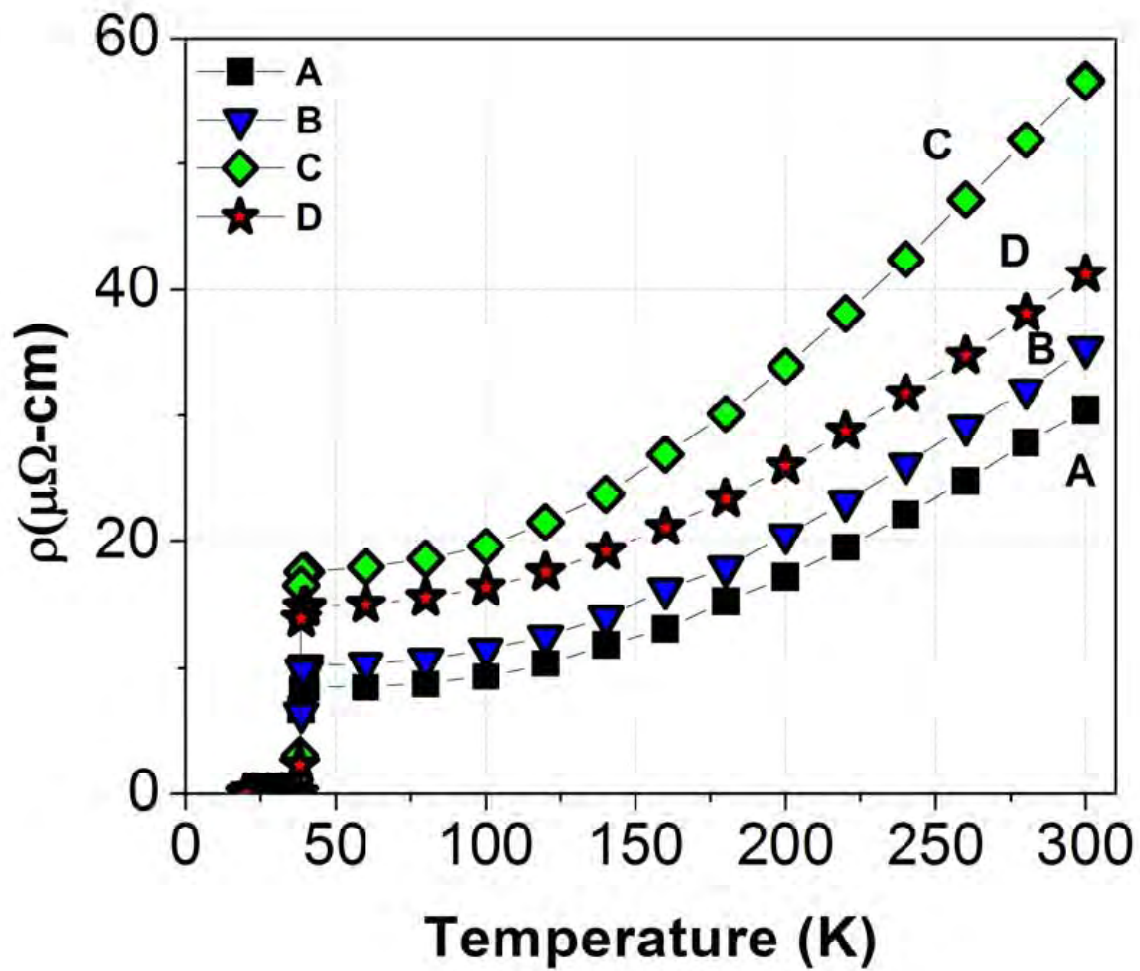


Figure 4.4  $\rho(T)$  from 5 mA, 4-point measurement.[32]

Figure 4.5 shows  $J_c$  at 4.2 K for each samples, as calculates form the Bean model using rectangular section bar.  $J_c$  is similar at the lower field for all the samples, as observed while a markable difference is observed at high field. An increase of  $J_c$  from sample A to D is observed in the high field. At the same time  $H^*$  ranged from close to 8 T for sample A to more than 9 T for sample D.

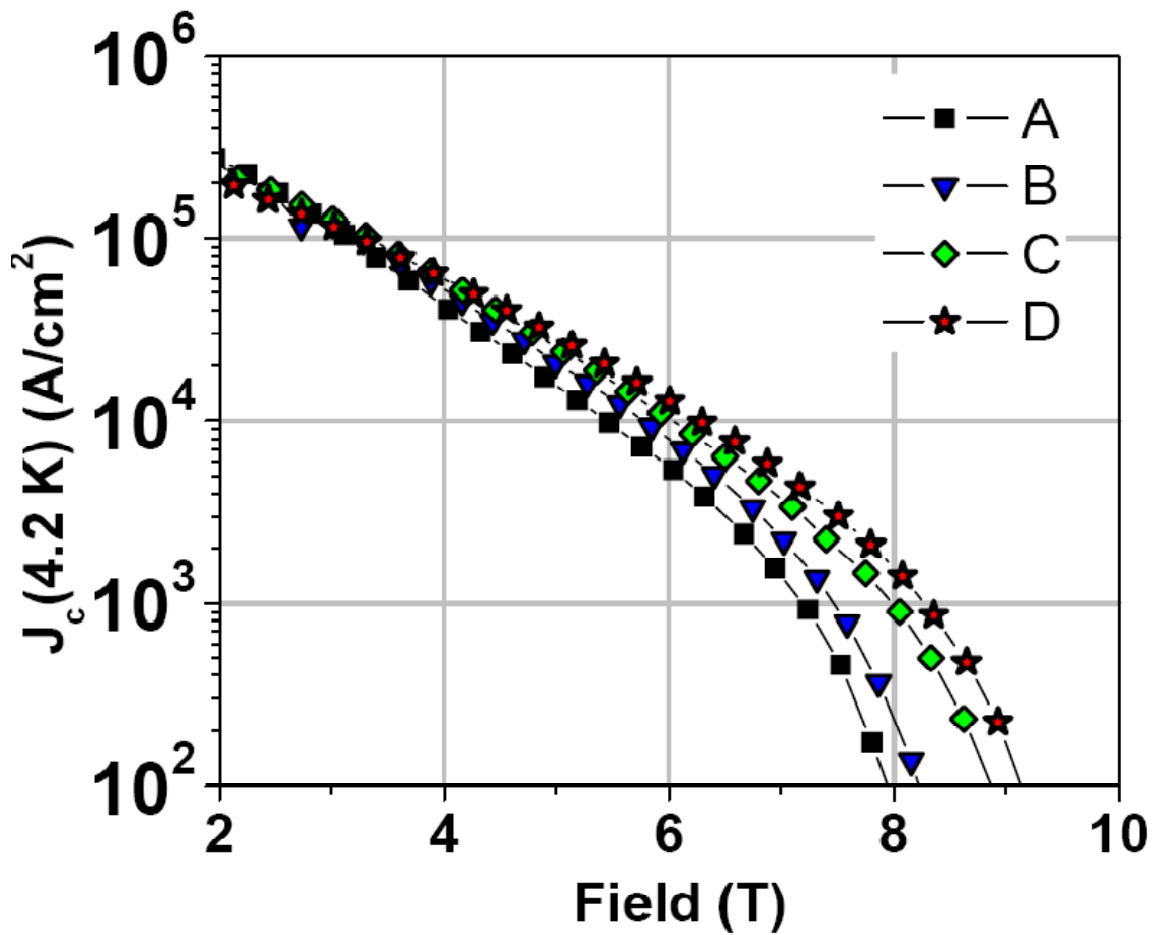
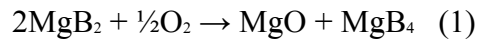


Figure 4.5  $J_c(H)$  at 4.2K determined from MH loops. [32]

## 4.2 Discussion

The x-ray diffraction shown in Figure 4.1 reveal higher concentration of MgO and MgB<sub>4</sub> in sample C and D and in sample A and B. H<sub>2</sub>O and O<sub>2</sub> atmosphere appears to have resulted in the reactions:



which is consistent with the milling atmospheres. This can explained the reduction of T<sub>c</sub>, observed for sample D, in Figure 5.2, by the small amount of oxygen or carbon present as CO<sub>2</sub> in air. These amounts of secondary phases are showing change in the superconducting properties of the material.

Table 4.1 Processing parameters, designations, and properties.

Sample	Atmosphere	T <sub>c</sub> (SQUID 90%) (K)	H <sub>c2</sub> (24K) (T)	ρ(40) μΩ-cm	ρ(300) μΩ-cm	RRR	Δρ μΩ-cm	A <sub>F</sub>	ρ <sub>A</sub> (40) μΩ-cm
<b>A</b>	Glove Box	38.0	7.0	8.44	30.53	3.62	22	0.33	2.8
<b>B</b>	Glove Bag	37.9	7.2	10.23	35.37	3.46	25	0.29	3.0
<b>C</b>	Air (sealed)	37.8	7.3	17.58	56.73	3.23	39	0.19	3.3
<b>D</b>	Air (valve)	37.5	7.9	14.91	41.26	2.77	26	0.28	4.1

Properties description: T<sub>c</sub> = critical Temperature, H<sub>c2</sub> = critical high magnetic field, ρ(40) = resistivity obtained at 40 K, ρ(300) = resistivity obtained at 300 K, RRR = residual resistivity ratio = ρ(300)/ρ(40), Δρ = ρ(300) – ρ(40), A<sub>F</sub> = active area fraction, ρ<sub>A</sub> = Adjusted resistivity.

Conducting properties of the material processed are showed in Table 4.1. Monotonic trend is consistent for  $T_c$  and  $H_{c2}$ , which is consistent with intragrain scattering effects. This  $T_c$  and  $H_{c2}$  trends are generally support by RRR and normal state resistivity which are controlled both scattering and by variable sample connectivity.

Ben Senkowicz used a modified formalism of the Rowell analysis, with  $\Delta\rho_{ideal} = 7.3 \mu\Omega\text{-cm}$  to calculated the active area fraction  $A_F$ , the fraction of the cross section carrying the measurements current, and the adjusted resistivity  $\rho_A(40 \text{ K})$ , the normal state resistivity of this fraction, finding that  $A_F$  ranged between 0.19 and 0.33. Sample A, milled under the cleanes conditions, shows the largest  $A_F$  and at the same time the lowest  $\rho_A(40 \text{ K})$ , indicating the smallest amount of electron scattering by defects and dopants.

In sample B, 12 % smaller  $A_F$  was observed compared with sample A. Sample C and D had lower  $A_F$  which as see in Figure 4.5 a link between current obstruction and exposure to air was observed. Despite sample D had greater  $A_F$  than sample C, not clear understanding, the analysis focus on the difference of atmosphere exposure between sample A and B with C and D.

Low field  $J_c(H)$  was found to be similar across our sample set, (samples A, B, C, and D had  $J_c(2 \text{ T}, 4.2 \text{ K})$  of 212, 244, 220, and 208 kA/cm<sup>2</sup> respectively) indicating no strong effect from varied connectivity. More significantly,  $J_c(H)$  decreased more slowly with increased magnetic field as the atmospheric exposure increased, with a difference in  $H^*(4.2\text{K})$  of more than 1 T which means that  $H^*(4.2\text{K})$  for sample D is about 12% greater than for sample A.

### 4.3 Conclusions

This experiment studied the effect of variable air exposure during processing on nominally undoped pre-reacted  $\text{MgB}_2$  subjected to ball milling. The following conclusions were observed:

1. On the effect of atmospheric condition: it was observed that the formation of  $\text{MgO}$  during ball milling and material handling resulted in the changes in  $T_c$  and  $H_{c2}$  values. The  $T_c$  for the materials of this study were 37.5 K, and 38 K compared to 39 K for pure  $\text{MgB}_2$ . Relative residual resistivity (RRR) measurements was the basis for this determination. The difference in  $T_c$  recorded for this study was attributed to variable sample connectivity with the distribution of  $\text{MgO}$  in the  $\text{MgB}_2$ .
2. The connectivity parameters,  $A_t$ , was determined to range from 0.19 to 0.33 from the sample studied.
3. The presence of atmospheric air exposure resulted in the formation of  $\text{MgO}$  and  $\text{MgB}_4$  while decomposition of  $\text{CO}_2$  resulted in the unintentional C-doping of the  $\text{MgB}_2$ .

## 5 STUDY OF BALL MILLING INDUCED STRAIN DISORDER ON MgB<sub>2</sub> MATERIAL

In this chapter, the ball milling effect, by Pulverisette-4 and SPEX-8000D ball milling machine, was investigated. The purpose of this study was to identify the optimum conditions, from the milling parameters selected, in way to improve the superconductivity properties of MgB<sub>2</sub>. The milling effect is mainly based on high energy impact inducement from the interaction between the milling material and the material to be studied. As a results of this interactions average crystallite size reduction, strain generated, change in lattice parameters and secondary phases in the material, focus on MgB<sub>2</sub> based superconductor, can be extracted by simply X-ray diffraction analysis. This analysis was done by Rietveld method.

### 5.1 Results and discussion

The discussion in this chapter is extracted from the X-ray diffraction and micrograph, from the scanning electron microscope, analyses. This analysis is based in the improvement of superconductivity properties of pure MgB<sub>2</sub> by varied the milling conditions. The milling parameters varied was the ball to powder ratio (BPR), milling rotational speed, for Pulverisette-4 (P-4), and the comparison of the high energy impact effect between P-4 and SPEX 8000D (SPEX) ball milling machines.

### 5.1.1 X-ray diffraction pattern

Structural composition is possible change by the high energy impacts in the ball milling machine. Rietveld analysis from the X-ray diffraction measurement can reveal the changes in the physical properties of MgB<sub>2</sub>

Table 5.1 Physical properties of Post-HIP processed MgB<sub>2</sub>. From Rietveld analyses.

SAMPLE	Mill	Milling Time	BPR	Composition	a (Å)	b (Å)	c (Å)	c/a post-HIP	Average crystallite size (nm) Pre- HIP	Average crystallite size (nm) Post- HIP	Strain Post-HIP
1	SPEX 8000D	300	3:1	90.5wt% MgB <sub>2</sub> 6.8wt.% MgO 2.7wt.% MgB <sub>4</sub>	3.0780 4.1787 4.4595	- - 4.3913	3.5219 - 7.4428	1.1464	6.18 - -	17.80 23.98 14.36	0.002815 0.001804 0.000054
		4000	3:1	92.0wt.%MgB <sub>2</sub> 7.0wt. % MgO 0.3wt. % WC 0.8wt. % MgB <sub>4</sub>	3.0806 4.2273 2.8434 5.3643	- - - 4.5283	3.5316 - 2.8434 7.5514	1.1412	5.07 - -	8.78 8.05 24.28 21.74	0.006634 0.006205 0.005983 0.002136
3	Pulverisette-4 at 800 rpm	300	3:1	99.3wt% MgB <sub>2</sub> 0.7wt.% MgO	3.0837 4.2145	- -	3.5191 -	1.1411 -	18.9 -	52.06 46.28	0.002583 0.002832
4		4000	3:1	97.7wt% MgB <sub>2</sub> 2.2wt.% MgO 0.1wt. %MgB <sub>4</sub>	3.0829 4.2299 5.4755	- - 4.4540	3.5177 - 7.4540	1.1410 - -	18.4 - -	54.14 23.79 31.29	0.002613 0.001806 0.001766
5		300	10:1	98.4wt% MgB <sub>2</sub> 1.6wt.% MgO	3.0837 4.2245	- -	3.5195 -	1.1413	16.6 -	36.86 62.41	0.002513 0.002671
6		600	10:1	86.7wt% MgB <sub>2</sub> 4.7wt.% MgO 8.6wt% MgB <sub>4</sub>	3.0804 4.2128 5.4337	- - 4.3978	3.5239 - 7.4730	1.1439 - -	24.7 - -	42.19 25.98 48.67	0.001682 0.000414 0.003596
7	Pulverisette-4 at 1200 rpm	300	3:1	89.7wt% MgB <sub>2</sub> 4.3wt.% MgO 6.0wt% MgB <sub>4</sub>	3.0822 4.2111 5.5643	- - 4.3283	3.5221 - 7.3723	1.1427	32.7 - -	48.10 37.48 7.78	0.001304 0.000599 0.005970
		4000	3:1	93.0wt% MgB <sub>2</sub> 3.2wt% MgO 3.8wt% MgB <sub>4</sub>	3.0822 4.2112 5.5643	- - 4.4332	3.5238 - 7.3723	1.1432 - -	25.9 - -	39.06 32.39 11.79	0.001281 0.001224 0.006226
9	Pulverisette-4 at 1200 rpm	300	10:1	97.8wt% MgB <sub>2</sub> 2.2wt.%MgO	3.0841 4.2124	- -	3.5251 -	1.1430	34.7 -	51.95 59.75	0.001465 0.000587
10		600	10:1	96.1wt% MgB <sub>2</sub> 3.9wt.% MgO	3.0821 4.2112	- -	3.5227 -	1.1429	33.5 -	46.01 37.77	0.001128 0.000592
11		MgB <sub>2</sub> raw Dr.Durval Rodrigues		98.4wt% MgB <sub>2</sub> 1.6wt.% MgO	3.0880 4.2342	- -	3.5241 -	1.1412	- -	97.01 -	0.001855 -

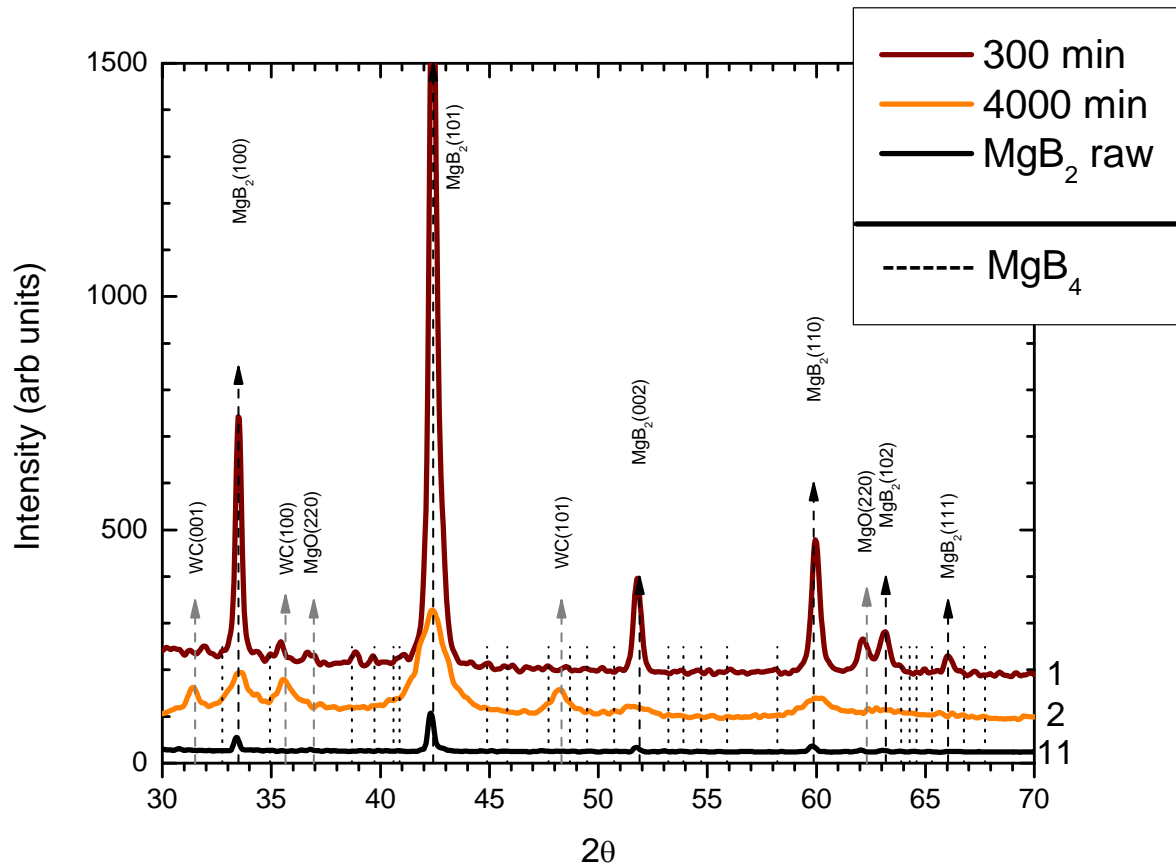


Figure 5.1 X-ray diffraction (XRD) pattern from  $\text{MgB}_2$  powdered mill material by high energy ball mill (HEBM) in the **SPEX 8000D** using Ball to BPR of **3:1**.

Figure 5.1 shows the X-ray diffraction spectra for SPEX-8000D processed materials, revealing the presence of MgO and WC contamination in comparison to the as-received  $\text{MgB}_2$ , sample 11. Tungsten carbide (WC) 0.3 wt.% is observed in sample 2, as revealed by the presence of more spectral peaks as compared to the case of sample 1. The lack of WC (101) peak on Figure 5.1 for sample 1 may suggest that some of the contamination may have segregated with MgO which appeared to be higher in amount in the milled materials. Or, the amount of high energy impacts was not enough to release tungsten carbide from the milling material. This is confirmed from the display of data in Table 5.1. The level of MgO observed in both samples reached about 7 wt.%. The present of  $\text{MgB}_4$  in sample 1 is higher than sample 2.

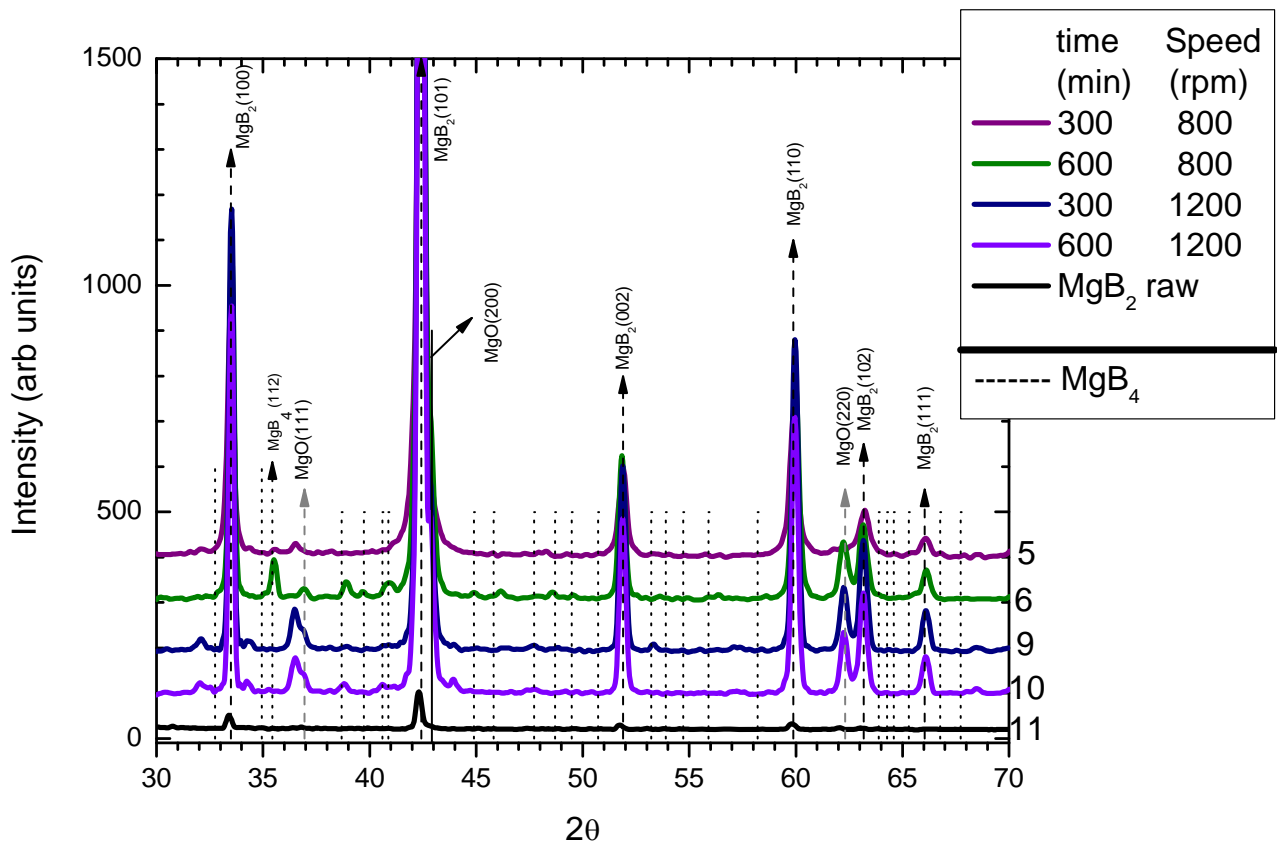


Figure 5.2 XRD pattern from MgB<sub>2</sub> powdered mill material HEBM in the Pulverisette-4 using BPR of 10:1.

Next, according to Figure 5.2, which showed the spectra for the 10:1 BPR ratio processed material ball milled in the Pulverisette-4 with a rotational speeds of 800 rpm corresponding to samples 5 and 6, and 1200 rpm for samples 9 and 10. The times of milling were varied between 300 minutes for samples 5 and 9, and 600 minutes for samples 6 and 10 shown in Figure 5.2. Sample 6, as we saw for sample 1 in Figure 5.1, show extra peak compared with the rest of the samples, 5, 9, 10 and 11, which corresponds to MgB<sub>4</sub> phase. Table 5.1 confirm the present of this phase just for sample 6 in Figure 5.2. The amount of MgO phase seems to be higher, as observed in reflection (220) for sample 9 and 10. It is due to an increment on the superficial area contact between average crystallites at the time they became small in size. Compared with SPEX processed samples, the MgB<sub>2</sub> peak are less

broadening for Pulverisette-4 processed material. It is confirm by the strain amount observed in Figure 5.6.

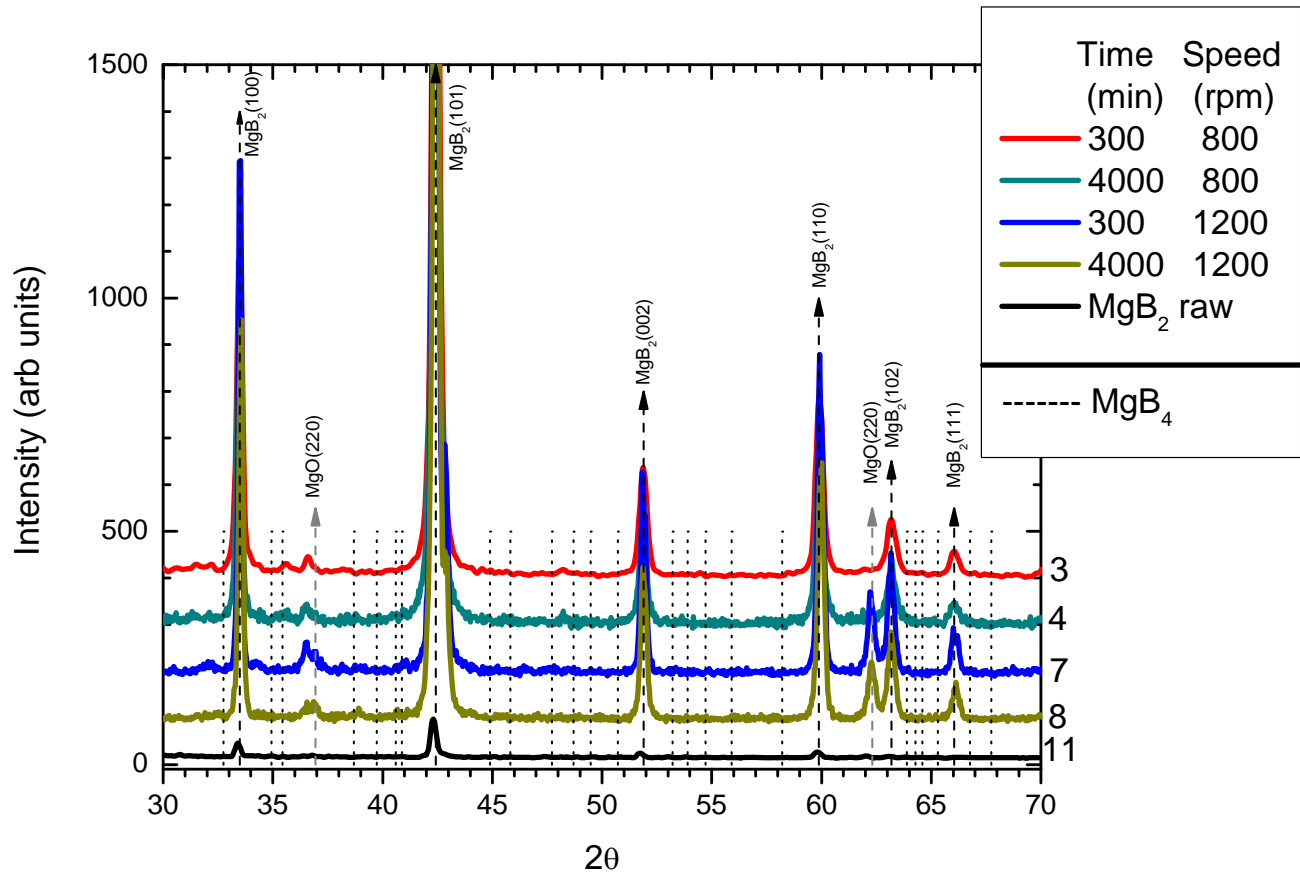
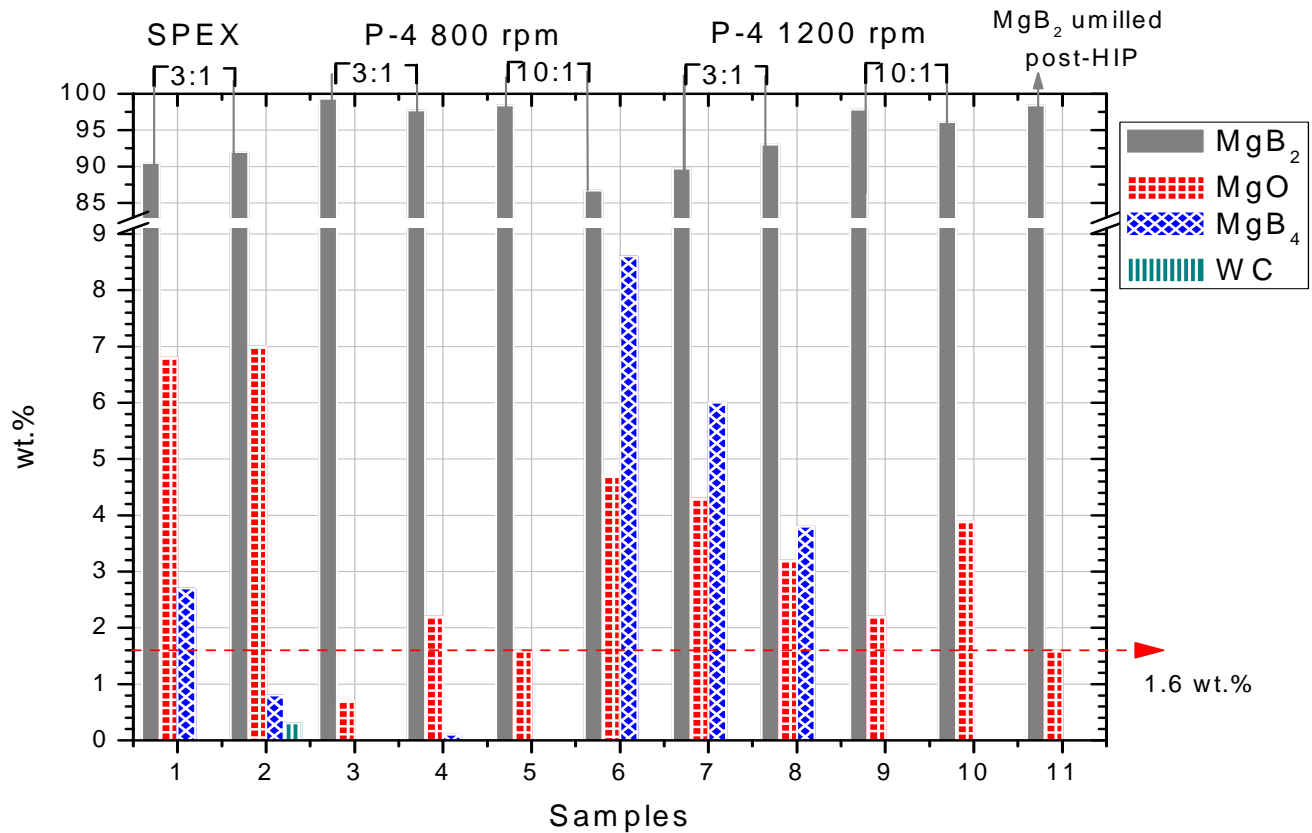


Figure 5.3 XRD pattern from MgB<sub>2</sub> powdered mill material HEBM in the Pulverisette-4 using BPR of 3:1.

Figure 5.3 shows the spectra for material processed at different milling time in the Pulverisette-4 using a rotational speed of 800 rpm and 1200 rpm and a BPR of 3:1. The difference between Figure 5.2 and Figure 5.3 is the BPR parameter 10:1 and 3:1, respectively. From the spectra in Figure 5.3 is possible to observe the lack of peaks for the MgB<sub>4</sub> phase. However, after the Rietveld analysis showed in Table 5.1, is observed MgB<sub>4</sub> phase for sample 4, 7 and 8. It confirms that the MgB<sub>4</sub> phase was hidden in the background or has low intensity peaks. MgO peaks are again present for all the samples with lower

peaks in sample 3. The broadening in the peaks is similar compared with samples in Figure 5.3. Comparing (101) reflection for  $\text{MgB}_2$ , sample 3 and 4 are broader than samples 7 and 8. It is confirmed in Figure 5.6 where sample processed at 1200 rpm in the Pulverisette-4 shows lower strain compared with samples milled at 800 rpm.

From careful examination of Figures 5.1, 5.2, and 5.3, it can be deduced that the combination of speed and time of milling had some effects on the strain of milled materials. The least energy transferred, strain, during ball milling seemed to correspond to the material of sample 5 (Figure 5.2), which showed least  $c/a$  ratio of 1.1410 for sample 4 compared to 1.1464 corresponding to SPEX processed sample 1. This gap of  $c/a$  between these two samples is similar to what is observed for the strain in Figure 5.6. As lower the strain an increase in average crystallite size is observed. However, the slight variation in average crystallite size, Figure 5.5, is observed for Pulverisette-4 processed material.



**Figure 5.4** Weight percent values of the MgB<sub>2</sub> and secondary phases of post-HIP processed milled material at different milling condition on the SPEX 8000D and Pulverisette-4 (P-4). Contamination by MgO coming during the post-HIP no milling MgB<sub>2</sub> material is leveled at 1.6 wt.%.

All the samples had trace of MgO contamination which varied from 0.8 wt.% for sample 3, to 4.7 wt.% for sample 6, as show Figure 5.4. The SPEX 8000D processed material, sample 1 and 2 had the most amount of MgO at 6.8 and 6.7 wt.%, respectively. Close examination of the materials analyses as shown from Table 5.1 revealed that the strain associated with the MgO phase milled materials had tendency to be lower in value than the main MgB<sub>2</sub> phases. In addition to the MgO phase, there were MgB<sub>4</sub> phases detected with the sample 6 at a level higher than the amount for the MgO (4.7 wt.% and 8.6 wt.%) respectively. The relationship between the formation of MgB<sub>4</sub> and the presence of MgO is not clear from the

milling carried out because, while MgO was observed in all the samples, MgB<sub>4</sub> was detected in some samples alone. It appears that the formation of MgB<sub>4</sub> phase was favored by prolonged milling time. However, for sample 2 while MgB<sub>4</sub> was not detected, 0.5 wt.% WC was detected which was correlated by examination of the WC grinding balls, which where decreased in size.

Next, the Rietveld's analyses of the ball milled materials shown from Table 5.1 revealed a major difference between the two milling techniques. The post HIP average crystallite size of the materials milled with the Pulverisette-4 for the MgB<sub>2</sub> phases were 39.06 nm to 48.10 nm, at 1200 rpm, much higher than the SPEX-8000D milled materials with their post HIP size of 9.10 nm to 17.80 nm, in the BPR of 3:1 respectively. In addition, the SPEX-8000D milled materials had higher strain than the Pulverisette-4 milled ones.

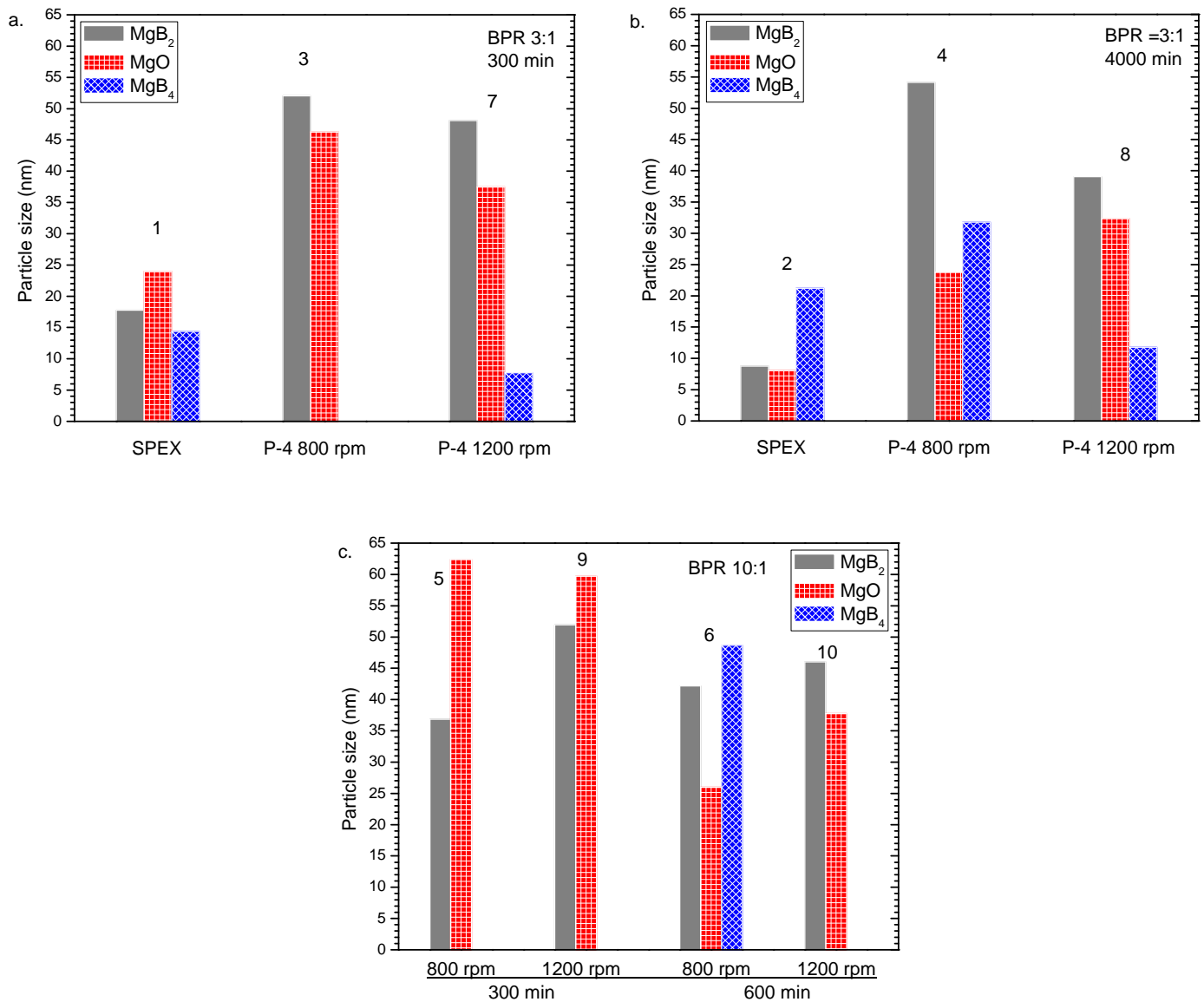


**Figure 5.5** Average crystallite size for different milling conditions. (a) BPR = 3:1 at 300 minutes, (b) BPR = 3:1 at 4000 minutes and (c) BPR = 10:1 for 300 and 600 minutes.

In Figure 5.5 the average crystallite size for the main, MgB<sub>2</sub>, and secondary, MgO and MgB<sub>4</sub>, phases are shown. In the case of SPEX ball mill, MgB<sub>2</sub>, as well MgO, have the smallest average crystallite size compared with the samples processed in the Pulverisette-4 (P-4) at 800 and 1200 rpm. In both, SPEX at 300 minutes, Figure 5.5 (a), and 4000

minutes, Figure 5.5 (b), the phase of  $\text{MgB}_4$  is obtained. In the case of Pulverisette-4 processed material, this phase is observed for the half of the sample studied, most prominent in material processing at higher rotational speed, 1200 rpm, and at longer milling time, 600 minutes and 4000 minutes. All samples at 4000 minutes, Figure 5.5 (b), showed  $\text{MgB}_4$  phase.

Samples processed in the Pulverisette-4, shown larger average crystallite size from a range of 36.86 nm (sample 5) to 54.14 nm (sample 4) for  $\text{MgB}_2$  compared with SPEX processed material. In the Pulverisette-4, as the rotational speed increase, a decrease in average crystallite size for  $\text{MgB}_2$  is observed for BPR 3:1, Figure 5.5 (a) and (b), in contrast with a BPR = 10:1, Figure 5.5 (c), which an increase in average crystallite size is observed. Additionally, the average crystallite size for  $\text{MgO}$  is higher using BPR of 10:1, Figure 5.5 (c), compared with average crystallite size using 3:1, Figure 5.5 (a) and (b).

For the milling time range used in this studied, 300, 600 and 4000 minutes, the reduction of average crystallite size from the no milling post-HIP material (sample 11) can be reached at the short period of time (300 minutes) as seen in Figure 5.5 (a). Mean that, for long period of time, the reduction in average crystallite size observed is similar to the ones ball milled at short period of time. Therefore, the reduction of average crystallite size, to at least half of its original size (97.01 nm – sample 11), is possible to obtain at short period of time for P-4 processed material. In the case of SPEX, the average crystallite size is half the size of the average crystallites for Pulverisette-4 processed material.

The average crystallite size of  $\text{MgO}$  tends to decrease with increased ball milling time for both the Pulverisette-4 and SPEX processed materials as was expected. In 3:1, the values ranged from sample 3 (46.28 nm) to sample 4 (23.79 nm) at 800 rpm, from sample 7 (37.48 nm) to sample 8 (32.39 nm) at 1200 rpm and from sample 1 (23.98 nm) to and 7.91 nm for

sample 2 corresponding to SPEX-8000D processing. At 10:1, the values varied 62.41 nm for sample 5 to 25.98 nm for sample 6 at 800 rpm, while 59.75 nm for sample 9 and 37.77 nm for sample 10 based on 1200 rpm processing speed.

Given the information displayed from Table 5.1, the combination of the milling time, speed of milling, and powder-to-ball ratios with the Pulverisette-4 processed materials indicated that the average crystallite size reduction process for SPEX-8000D processed materials were more significant than the Pulverisette-4 milled ones.

In general, the Pulverisette-4 processed materials depicted XRD peaks that were not as broad as the ones corresponding to the SPEX processed ones. Broadening peaks in the spectra give us the information of small average crystallite size distribution in the sample. In the similar manner, the intensities of the peaks for the Pulverisette-4 milled material spectra were higher than the SPEX-milled ones showing high amount contribution of high average crystallite size. This can be explained from the difference between the energies associated with the two milling processes. The SPEX milling machine has higher energy of milling than the Pulverisette-4 which is further supported by the average crystallite sizes reduction immediately after ball milling, the  $c/a$  ratio, and the strain in the milled materials. Looking at the Table 5.1 is possible to observe that the average crystallite size reduction from Pulverisette-4 to SPEX milling process, pre-HIP SPEX processed material is  $\sim 12$  nm less than Pulverisette-4 at 300 min in the BPR of 3:1. In the case of the  $c/a$  parameter, for the same sample post-HIP, is 0.0053 higher for SPEX than Pulverisette-4, the same for the strain which is 0.00023 in difference. SPEX milled powders had smaller average crystallite size and higher strain consistent with more aggressive milling than the Pulverisette-4 ball milled materials. As shown from Table 5.1, both the SPEX and Pulverisette-4 milled materials exhibited increase in average crystallite size with the HIP process. The SPEX milled materials showed average crystallite size increase of 6.18 nm to 17.80 nm (a

percentage increase of 65.2%) for sample 1, while an increase of 42.2% for sample 2. While sample 1 did not reveal the presence of WC phase, sample 2 showed the presence of WC phase, which came out from the tungsten carbide balls used during the ball milling process. It appears that the longer the milling time, the higher the chances of WC contamination for SPEX ball milling. On this note, the Pulverisette-4 milled materials did not reveal WC contamination, even when the milling was carried out at 1200 rpm for a BPR of 3:1 with 4000 minutes milling time (sample 8), using the same milling media.

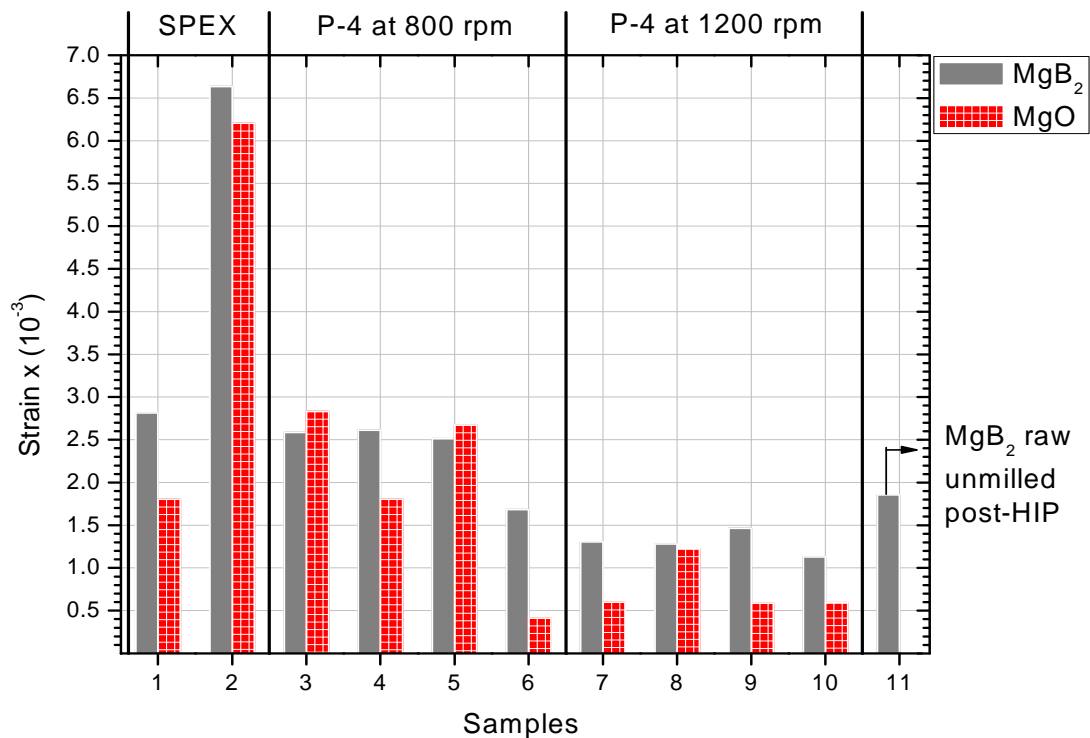


**Figure 5.6** Strain of post-HIP processed material using different milling condition showed in Table 5.1.

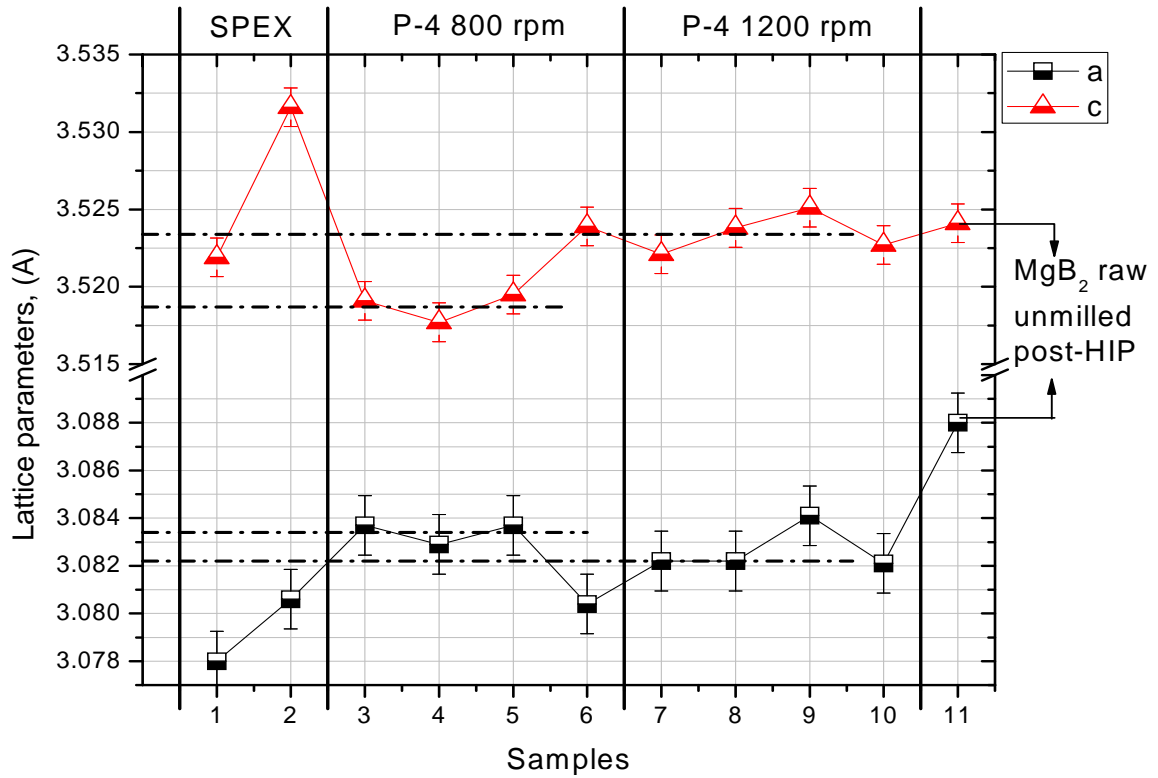


**Figure 5.7** Lattice parameters of post-HIP processed  $\text{MgB}_2$  using different milling condition showed in Table 5.1.

The severity of the SPEX milling is further demonstrated by comparing the strains associated with samples 2, 4 and 8, Figure 5.6, respectively. The strain was two to four times higher for sample 2, respectively. This increase of strain correlated with a decrease of a-lattice parameters from 3.088 nm (raw  $\text{MgB}_2$ ) to 3.078 nm. In contrast to SPEX milled materials, the strain in the Pulverisette-4 milled materials decreased from 0.002583 for sample 3, to half the value for sample 10. This decreasing can be correlated with a decrease of c-lattice parameters of about 0.0034 Å between materials processed at 800 rpm and 1200 rpm, as shown in Figure 5.7. As shown from Table 5.1, this strain is proportional to the average crystallite size reduction, with the smallest size obtained for the SPEX milled samples. The error bar are extracted from the Rietveld's analysis program which are equal to 0.00125 Å.

It suggest that, in the range of 300 to 4000 minutes, in the case of Pulverisette-4 where more of its physical properties have not a drastically change, an average of the physical parameters can reveal difference between ball mill at 800 rpm and 1200 rpm. The average of average crystallite sizes was 46.85 nm (Pulverisette-4) and 11.43 nm (SPEX) after HIP and 25.67 nm (Pulverisette-4) and 13.14 nm (SPEX) before it. The average strain values were 0.002036 (Pulverisette-4) and 0.004130 (SPEX), after HIP process.

Strain in SPEX was two times more than in Pulverisette-4 strain. In Pulverisette-4, the probability to induce defects in the atomic structure by strain was high for short period of time, implying that 300 minutes, or possible less, was enough to change the atomic or microstructure of the raw sample. After 300 minutes the reduction of average crystallite size was about 9% before HIP and in some case, as with samples 5 and 6 before and after HIP process, the average crystallite size increased. This increase was a result of average crystallite agglomeration.

The decrease in average crystallite size for the BPR of 3:1 was more than for the 10:1 ball mill material while there was no significant difference in the strain of the material. It is conceivable that higher impact occurred with the 3:1 processing than with the 10:1 case. The speed of milling seemed to play a more significant role than the BPR variable. Comparison of samples 7, 8, 9 and 10 showed that the average crystallite sizes remained constant, while the 800 rpm processed materials had smaller average crystallite sizes with range of strain from 0.02583 to 0.001682 for samples 3 and 6 respectively.

In the case of SPEX, using a BPR of 3:1, the high energy impact was higher than the Pulverisette-4 processed material, resulting in lower average crystallite size (8.78 nm) and higher strain value (0.006634), for sample 2 after HIP, decreasing and increasing about 22% the values of Pulverisette-4, respectively compared with sample 8. To achieve to this

result, as a suggestion for future studied, in the Pulverisette-4, the R-ratio (discussed in chapter 3), can be modified to try to understand the high energy impact induce to the average crystallites.

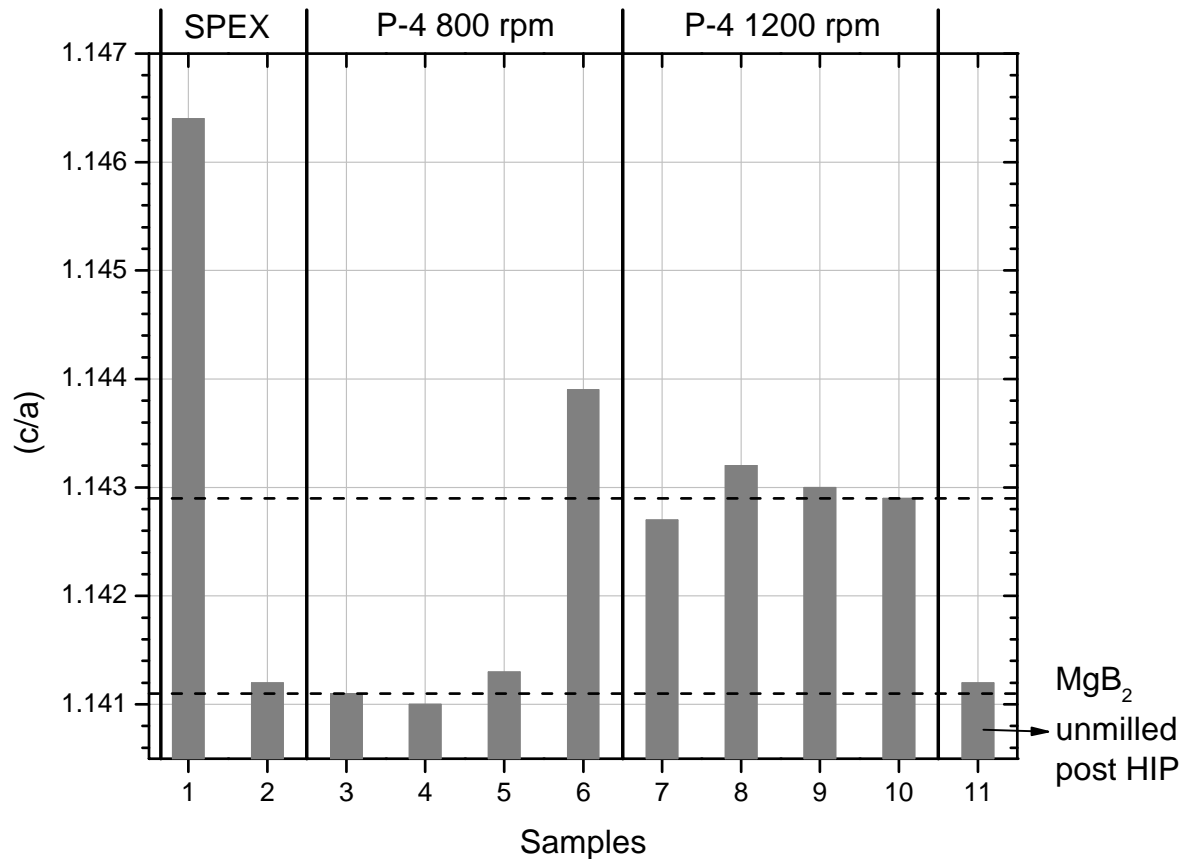


**Figure 5.8** Tetragonality of post-HIP processed  $\text{MgB}_2$  using different milling condition showed in Table 5.1.

The tetragonality is showed in Figure 5.8 as a function of the processed sample in the SPEX and Pulverisette-4 at 800 rpm and 1200 rpm. A clear different is observer for the tetragonality between material processed at 800 rpm and 1200 rpm in the Pulverisette-4 ball milling. Tetragonality for material processed at 1200 rpm is around 1.143 while for material processed at 800 rpm c/a remained at 1.141. There is no change in tetragonality for material processed at 800 rpm compared with no milled post-HIP  $\text{MgB}_2$ .

For SPEX processed material a noticeable difference is observed between 300 minutes and 4000 minutes milling time. This is inversely proportional to the strain shown in Figure 5.6 which shows lower strain values compared with 4000 minutes. It is consequence of the lower strain received in the lattice parameters as show Figure 5.8. The same was observed for Pulverisette-4 processed materials which show lower strain as the  $c/a$  increase.

### 5.1.2 Scanning Electron Microscope (SEM) measurements

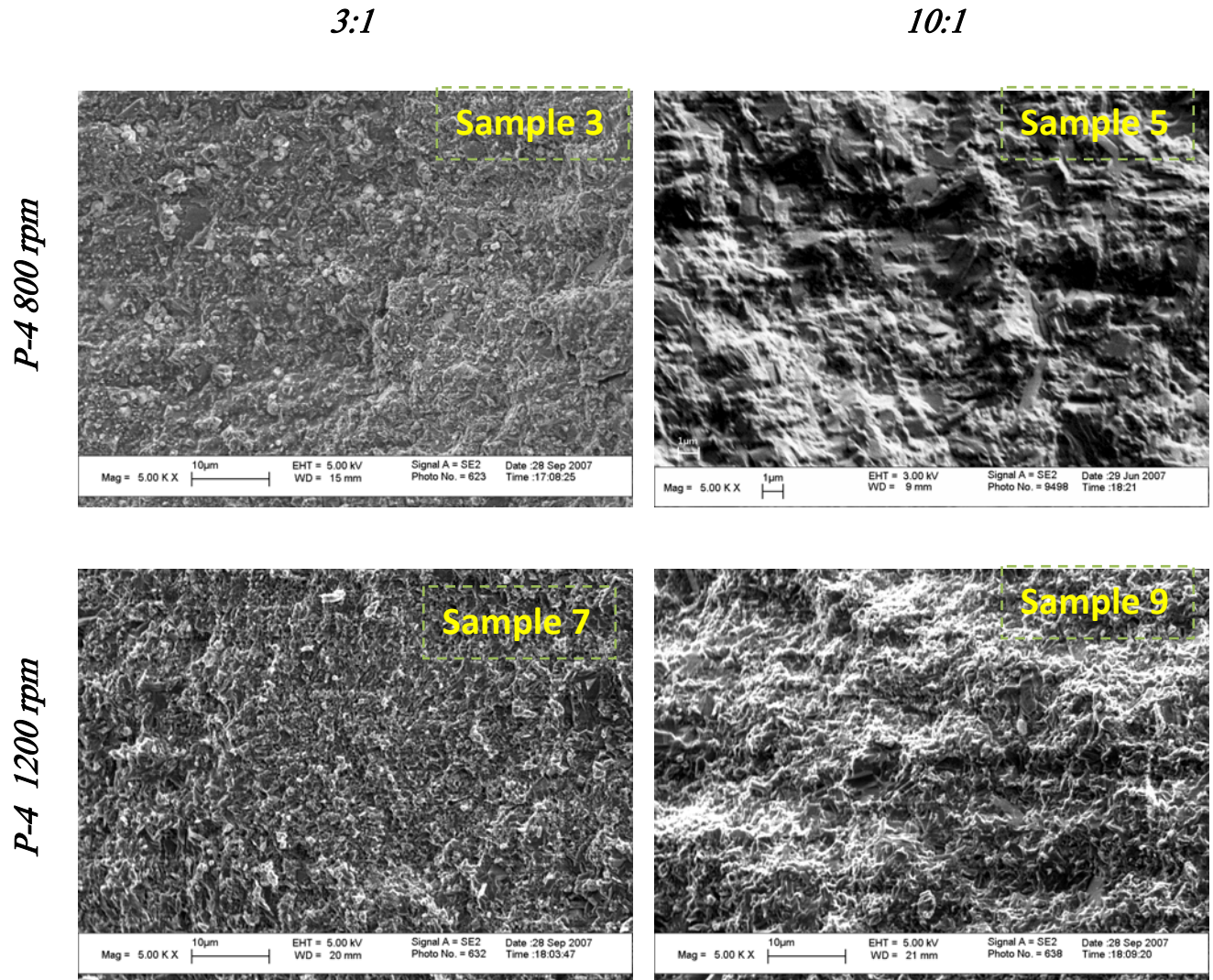


Figure 5.9 Scanning electron microscope of Post HIP  $MgB_2$  processed material in the **Pulverisette-4** at 800 and 1200 rpm using BPR of 3:1 and 10:1 during 300 minutes.

Figure 5.9 shows the micrograph of post-HIP superconducting pellets of samples 3, 5, 7 and 9 which were processed at 300 minutes in the Pulverisette-4. Sample 3 and 7, which shown a porous surface, were ball milled using a BPR of 3:1. In the other case, in samples 5 and 9 the surface in the micrograph seems to be smooth compared with sample 3 and 7. The BPR used for samples 5 and 9 was 10:1. At the same time, the rotational speed was change from 800 to 1200 rpm, for each BPR parameter. Changes in the surface, increasing the rotational speed, are not observed in the micrograph, as the BPR.

The average crystallite size in the micrograph seems to be in micron. No further analysis was done in the micrograph study due to the poor information is possible to get from them, at the magnification level was performs.

I suggest, in the continuation of this study, that analysis of the micrograph at high magnification in the SEM. Strong analysis using the Transmission Electron Microscope (TEM) could reveal the information around the grain. For the preparation of this sample to be used in the TEM, is necessary to crash the post-HIP pellet and suspend small particles in a solvent.

### 5.1.3 Magnetization measurement ( $T_c$ )

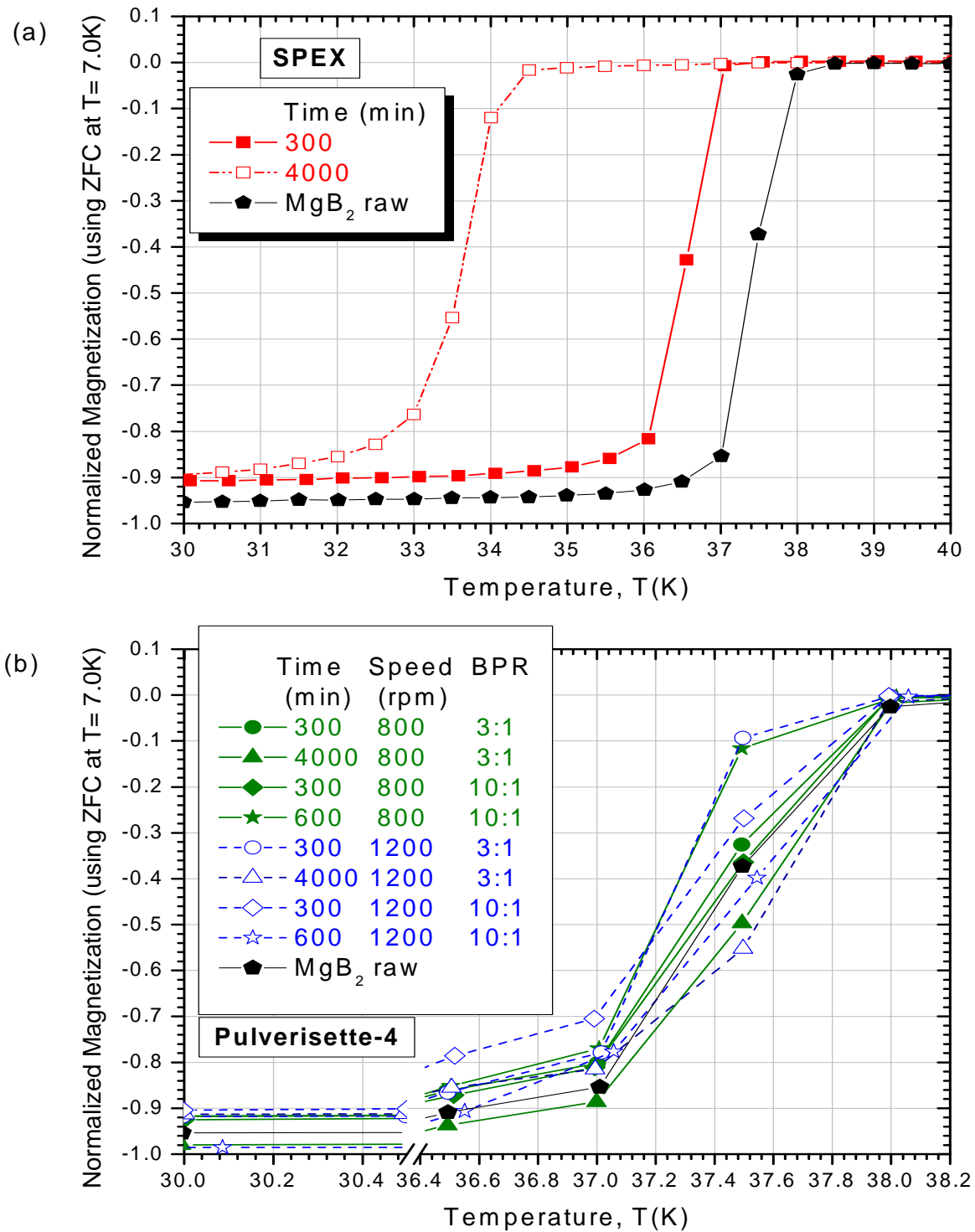


Figure 5.10 Field Cooled (FC) and Zero Field Cooled (ZFC) curve normalized at 7.0K. (a) SPEX 8000D at BPR = 3:1 and (b) Pulverisette-4 samples are shown.

The Zero Field Cooled (ZFC) curves corresponding to the SPEX 8000D and Pulverisette-4 processed materials are shown in Figure 5.10 (a) and Figure 5.10 (b) respectively. The magnetization measurements of SPEX-8000D processed material shown in Figure 5.10 (a), corresponding to 300 minutes and 4000 minutes milling times, revealed differences in their  $T_c$  values, and also in their transition behavior. However the transition behavior observed for the Pulverisette-4 processed materials were completely different in comparison to those of the SPEX-8000D processed ones.

From Table 5.3 and as shown in Figures 5.10 (a) and (b), the  $T_c$  values, as deduced from the measurements was practically the same for the 800 rpm and 1200 rpm processed materials. However, the induced magnetic field for the 800 rpm processed material was higher than the 1200 rpm ball milled material, as shown in Figure 5.10 (b) at 30.0 K. Table 5.2 show the normalize magnetization at 30 K.

**Table 5.2 Normalized magnetic susceptibility ( $\chi$ ) for the different milling parameters.**

Sample	Mill		BPR	Time	$\chi(\text{emu}/\text{cm}^3)$ at 30 K	
Sample 1	SPEX		3:1	300	-0.907	
Sample 2			3:1	4000	-0.893	
Sample 3	P-4	800 rpm	3:1	300	-0.917	
Sample 4			3:1	4000	-0.979	
Sample 5			10:1	300	-0.925	
Sample 6			10:1	600	-0.916	
Sample 7			1200 rpm	3:1	300	-0.918
Sample 8				3:1	4000	-0.913
Sample 9		10:1		300	-0.904	
Sample 10		10:1		600	-0.986	
Sample 11		MgB <sub>2</sub> as received no milled				-0.953

The magnetization ( $\chi$ ) decreased with the increase in revolution and with high impact as created in the SPEX-8000D ball milling. Figures 5.10 (a) and (b) showed that the  $\chi$  at 800 rpm and 1200 rpm, for all milling times, is greater than  $\chi$  values from SPEX. As the milling speed, rotational speed for Pulverisette-4, increase having an effect in the impacts of the balls, the ball to powder ration (BPR) as milling parameter showed an increase in the intensity of the impact, too. The comparison of induced magnetic field for the materials corresponding to samples 9 (i.e., a BPR = 10:1) is lower than samples 7 (a BPR = 3:1 at 1200 rpm in the Pulverisette-4) as the milling time increase. The induced magnetic field was determined increasing the temperature in the presence of a constant applied magnetic field, and so were trapped within the solid material.

The processing material act as a cushion to the high energy impacts of the milling ball interacting each other, or with the wall, in the milling process. This behavior decreases in intensity as the rotational speed increase in the case of the Puleverisette-4. This tendency is not possible to observe in the SPEX ball milling due to the impossibility to change its speeds.

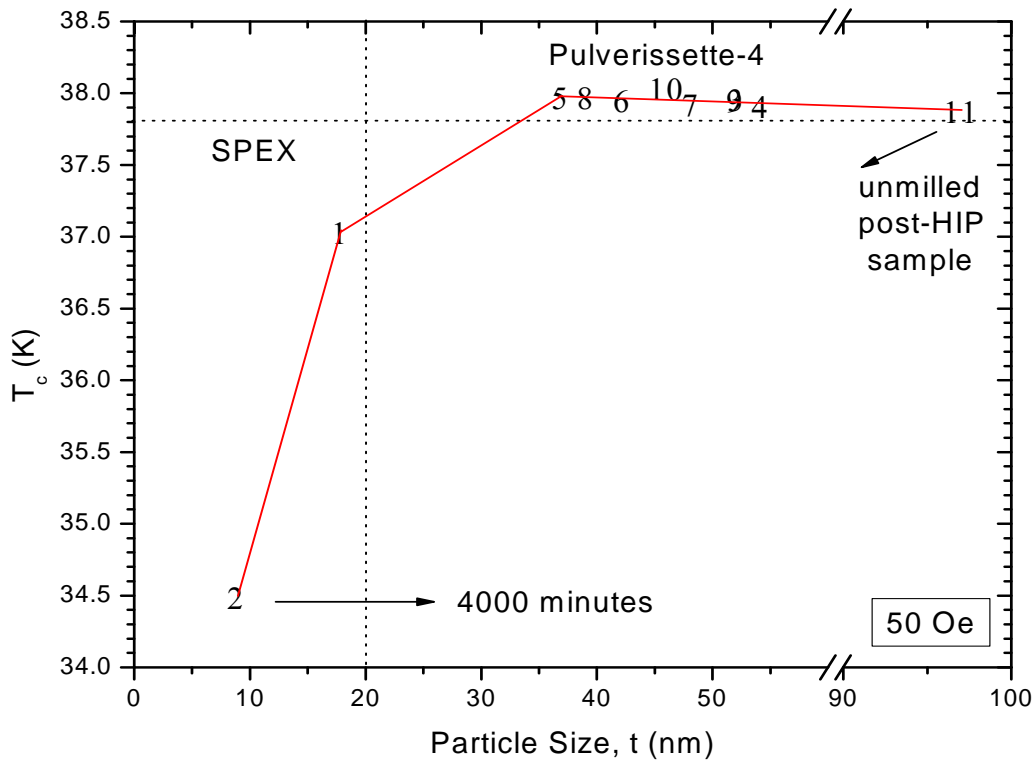


**Figure 5.11** Superconducting critical temperature as a function of average crystallite size of post-HIP samples. Note: The line connecting the points in the graph was traced manually in the computer. The numbers are associated with the sample number.

Figure 5.11 shows how  $T_c$  decreases with a decrease in average crystallite size. SPEX processed material has the lower average crystallite size and the lower  $T_c$ . The lower  $T_c$  was found for sample 11 which was milled for 4000 minutes. Additionally, this sample contains WC average crystallite as a phase shown in Figure 5.1 and Figure 5.4. The variation of average crystallite size in the Pulverisette-4 was not too high as the SPEX processed materials. Due to that variation, the change in  $T_c$  is observed to be small. However, from sample 4 to 5 and sample 9 to 8, a reduction in  $T_c$  was observed as increasing the BPR from 3:1 to 10:1.

Different perspective, compared with the BPR and the milling speed, is observed on the milling time parameter. As the milling time increased, the magnetization, using a BPR of

3:1, increased for SPEX and Pulverisette-4 at 1200 rpm material processed different for Pulverisette-4 at 800 rpm, which magnetization values decrease. Again, as in the evaluation of the other milling parameters, Pulversiette-4 processed material at 800 rpm and 1200 rpm shows different behavior. In the case of BPR equal to 10:1, the magnetization values decrease as the milling time increase in the case of Pulverisette-4 at 800 rpm, in contrast to 1200 rpm which magnetization increase as the milling time increase. For samples 9 to 10 and samples 3 to 4 a 10 % increase in magnetization occurs from 300 to 600 minutes and 300 to 4000 minutes, respectively. Average crystallite size reduction, for sample 9 and 10 in Table 5.1, could explain this change of magnetization as shown in Figure 5.10 (a).

### 5.1.4 Critical current density ( $J_c$ ) measurement

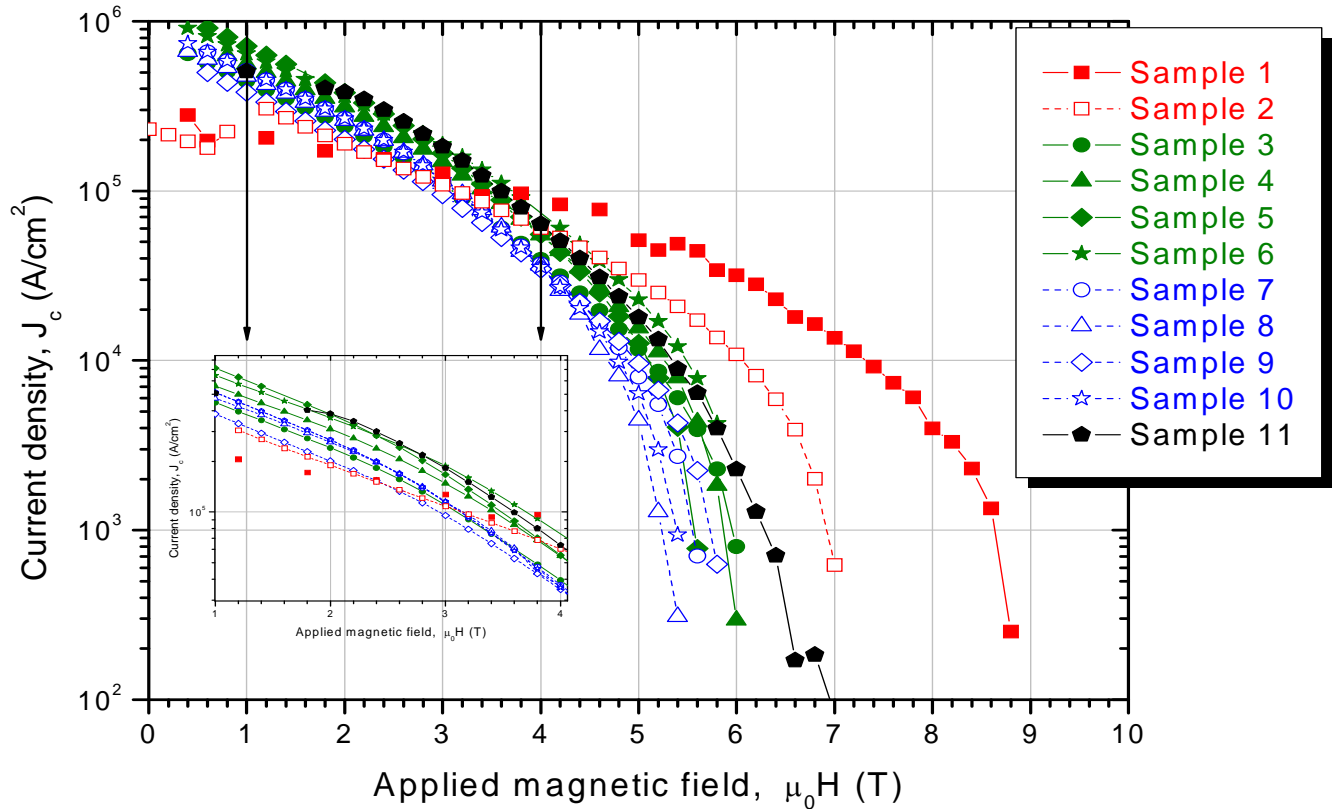


Figure 5.12 Critical current density as a function of magnetic field of the pre-reacted  $\text{MgB}_2$  superconducting post-HIP pellets at 4.2 K.  $J_c$  derived from the Bean model.

Table 5.3 shows  $J_c(2 \text{ T}, 4.2 \text{ K})$ , and  $J_c(5 \text{ T}, 4.2 \text{ K})$  values. In Figure 5.12,  $J_c$  values, in high applied magnetic field ( $> 5 \text{ T}$ ), are higher for SPEX milled samples than for Pulverisette-4 samples. Sample 1, milled for 300 minutes, has the higher values of  $J_c$  close to 9 T. In the speed range of 1200 rpm, the values of  $J_c$  are the lower ones. Increases in revolution per minute, in the Pulverisette-4, decrease the  $J_c$ . It is due by the introduction of strain in the sample as show Figure 5.6. Samples 4, 8 and 2 have the lower  $J_c(4.2\text{K}, 5 \text{ T})$  values in each

range of speed, 800 rpm, 1200 rpm and SPEX milled for 4000 minutes, respectively. As the same time, as in the SPEX, the increasing milling time decrease  $J_c$ . Amounts of impurities in the samples are increasing with the milling time as for the 300 minutes and 4000 minutes samples. From Table 5.1 the last parameter evaluated was the mass ratio between powder and milling balls (BPR). This parameter allows using more milling ball mass for less amount of powder or vice versa. Evaluating this parameter in samples 3 and 5, at 800 rpm for 300 minutes, is possible to observe that both curves in Figure 5.12, for the lower and higher applied magnetic field, overlap each other. The same is true at 1200 rpm, samples 7 and 9, and have a small difference in high applied magnetic field around 6 T, overlap again in the lower field. Therefore, the effects of BPR 3:1 against 10:1, is not shows high effect as the effects of speed and milling time. Possible in a short period of milling time, like 60 minutes, the effects of BPR came as an important parameter to play, due to the strain generate at short period of time. But in this experiment, about disorder, for long period of time as 4000 minutes, the BPR parameter comes invaluable compared with 300 and 600 minutes. As the milling time increase the amount of impact to the material, by the milling media, show a constant value to the particle size reduction. However, looking at low milling time, the grain refinement is better obtained at a high BPR.

### 5.1.5 Force pinning ( $F_p$ ) measurement

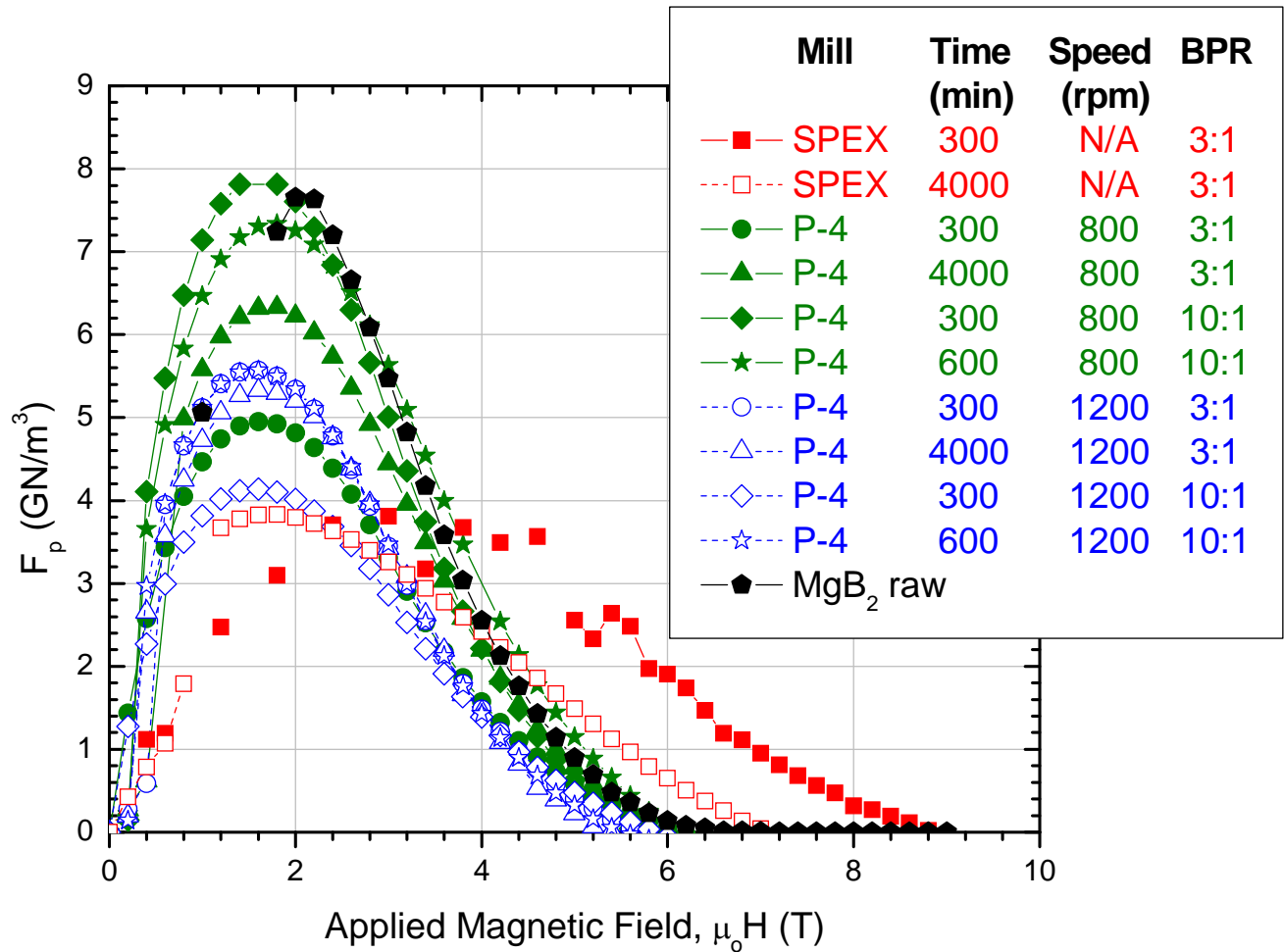


Figure 5.13  $F_p$  as a function of magnetic field at 4.2K.

Figure 5.13 show pinning force curves at 4.2 K. Sample 5 has the highest pinning force ( $F_p$ ) value ( $F_p = 7.81 \text{ GN/m}^3$ ). This samples, as shown in Figure 5.4 has the same level of MgO phase as the no milled material but the average crystallite size of this phase for this sample is the highest as observed in Figure 5.5. Sample ball milled in the Pulverisette-4 at 800 rpm have higher  $F_p$  compared with 1200 rpm and SPEX samples. As observed in Figure 5.6, the strain for sample ball milled at 800 rpm is higher than sample milled at 1200 rpm. The strain inducement in the material, by the high energy impact from the ball milling

machines, leads the structure in a non-equilibrium state or on a higher metastable state. This state is a consequence of the disorder implemented by the high energy impact.

Comparing the extent of these impacts from both milling machine, Pulverisette-4 Vs SPEX, sample 9, with milling parameters described in Table 5.1, has similar  $F_p$  values as SPEX milled samples in the range of 2 T. Apart from the tangential and centrifugal impact described in chapter 3 for Pulverisette-4, the impact from ball to ball or wall to ball was extremely aggressive in high rotational speed rang, 1200 rpm. This impact was related to the number of ball in the jar and the amount of powder. BPR of 10:1 for samples 5 and 6 milled samples, has the higher  $F_p$  values,  $7.81 \text{ GN/m}^3$  and  $7.33 \text{ GN/m}^3$  respectively, compared with BPR at 3:1 for sample 3 ( $4.95 \text{ GN/m}^3$ ) and sample 4 ( $6.32 \text{ GN/m}^3$ ), in the 800 rpm rotational speed range.

By the disorder in the atomic arrangement, by the amount of impact induced in the high energy ball milling, the electrons can be scatter. Then, in the HIP processes, a recrystallization is perform and the growing of the grains, creating interstitial area and pores in the material. From these areas, the presence of magnetic flux in the material will increase as the temperature increase until critical field and as well critical temperature is reached. The effect of this disorder by BPR decreased with an increase of speed. Furthermore, if SPEX showed a higher impact force reflected on the disorder, using the same milling parameters and heat treatment condition. SPEX samples showed similar  $F_p$  maximum values. More drastic was the change by the BPR, for the range speed of 800 rpm, than the effect of milling time. As Senkowicz et al. found that the milling time did not have a straight forward relationship with the pinning force curves, the same was observed in this study. After 4000 minutes of milling  $F_p$  reduced about 6 % of the maximum  $F_p$  value, while, by BPR effect,  $F_p$  reduce about 36 % from 10:1 to 3:1. The milling time exposure on

average crystallites by high energy impact might be determined in short period of time for the  $F_p$  effect. Values for 2 and 5 T are shown in Table 5.3.

### *Superconducting Properties*

Table 5.3 Physical properties measurements for post HIP processed “pure  $MgB_2$ ” material. Data derived from the Bean model.

Sample	Description			Deduced superconducting properties					
	Mill	Time	BPR	$J_c(2T,4.2K)$ kA/cm <sup>2</sup>	$J_c(5T,4.2K)$ kA/cm <sup>2</sup>	$F_p(2T,4.2K)$ GN/m <sup>3</sup>	$F_p(5T,4.K)$ GN/m <sup>3</sup>	$H^*(T)$ at 4.2K	$T_c(K)$ (10%)
1	SPEX 8000D	300	3:1	165.87	29.67	3.29	2.54	8.95	37.04
2		4000	3:1	189.48	51.71	3.79	1.49	7.25	34.50
3	P-4 800 rpm	300	3:1	240.65	11.52	4.81	0.58	6.29	37.97
4		4000	3:1	311.03	15.33	6.21	0.77	6.13	37.92
5		300	10:1	380.21	12.61	7.60	0.63	6.76	37.98
6		600	10:1	362.55	22.99	7.26	1.14	6.38	37.96
7	P-4 1200 rpm	300	3:1	266.87	8.04	5.33	0.40	5.81	37.93
8		4000	3:1	259.94	4.41	5.19	0.23	6.60	37.98
9		300	10:1	201.16	9.62	4.02	0.48	6.03	37.96
10		600	10:1	267.11	6.42	5.43	0.30	5.66	38.04
11	MgB <sub>2</sub> Raw received from ALFA Aesar Dr. Durval Rodrigues			382.72	17.91	7.66	0.89	6.80	37.88

## *5.2 Conclusions*

Different milling conditions parameters were studied in this chapter. These parameter correspond to the effect of the SPEX-8000D and Pulverisette-4 ball milling machine. The milling conditions were: the BPR of 3:1 and 10:1, the rotational speed 800 rpm and 1200 rpm and the milling time 300, 600 and 4000 minutes. Due to the lack of trend between these parameters, the purpose of this studied was to select parameters ranges, to be used in next studies. The effect of these parameters was observed in the superconductivity properties of MgB<sub>2</sub>.

- a. In general, the SPEX processed materials were smaller in particle size than the Pulverisette-4 processed ones.
- b. The SPEX processed materials in general showed distinct properties in comparison to the Pulverisette-4 processed ones because particle size reduction, and also defects introduction were higher in SPEX milling. The determined T<sub>c</sub> for SPEX milled materials varied from 37.89 K (5 at.%, 60 minutes ball milling) to 35.4 K (5 at.%, 2400 minutes). For the Pulverisette-4 processed materials displayed T<sub>c</sub> of 38.35 K (5 at.%, 120 minutes, at 800 rpm) to 37.29 K (2 at.%, 2400 minutes, 1200 rpm).
- c. For the Pulverisette-4, though smaller particle sizes were obtained with 1200 rpm processed materials, however, better superconducting properties were realized with the 800 rpm processed ones. Further, it was observed that amount of MgO increased in the materials as the rotational speed increased from 800 to 1200 rpm with a reduction on the T<sub>c</sub> from 37.92 to 37.29 K (milled samples at 2400 minutes at 2 at.%), respectively.

- d. Change in the BPR did not result in comparable changes to the superconductivity properties as was the rotational speed. However, the BPR of 10:1 shows better superconducting properties. For instance, material processed at 800 rpm for 300 minutes in the Pulverisette-4 using BPR of 3:1 and 10:1, Chapter 5, show the following superconducting properties, respectively:  $J_c(2 \text{ T}, 4.2 \text{ K}) = 240.65 \text{ to } 380.21 \text{ kA/cm}^2$ ,  $J_c(5 \text{ T}, 4.2\text{K}) = 11.52 \text{ to } 12.61 \text{ kA/cm}^2$ ,  $F_p(2 \text{ T}, 4.2 \text{ K}) = 4.81 \text{ to } 7.26 \text{ GN/m}^3$ ,  $H_{irr}(4.2 \text{ K}) = 6.29 \text{ to } 6.79 \text{ T}$  and  $T_c(50 \text{ Oe}) = 37.97 \text{ to } 37.96 \text{ K}$  from M-T curve.

## 6 TANTALUM DIBORIDE DOPPING EFFECTS

In this chapter, the effect of TaB<sub>2</sub> doped MgB<sub>2</sub> as a function of milling parameters and HIP processed material. TaB<sub>2</sub> average crystallites will interact with the MgB<sub>2</sub> matrix as well with its atomic configuration. At the end of this chapter the effect TaB<sub>2</sub> doped MgB<sub>2</sub> at 2 and 5 at.% will be observed on the enhancement of the superconducting properties of MgB<sub>2</sub>, especially the critical current density ( $J_c$ ) and the pinning force ( $F_p$ ) in the material.

### 6.1 Results and Discussion

#### *6.1.1 X-ray diffraction measurements*

Room temperature x-ray diffraction measurements were carried out to help evaluate the processed superconducting wires, and to help reconcile other measurements carried out. The X-ray diffraction spectra for the TaB<sub>2</sub> doped materials are shown in Figures 6.1 through 6.6. Diffraction peak from secondary phases, such as MgO and MgB<sub>4</sub> were observed in some of the X-ray diffraction spectra. Exposure of the starting materials, before ball milling, or during post ball milling operations, resulted in the formation of MgO.

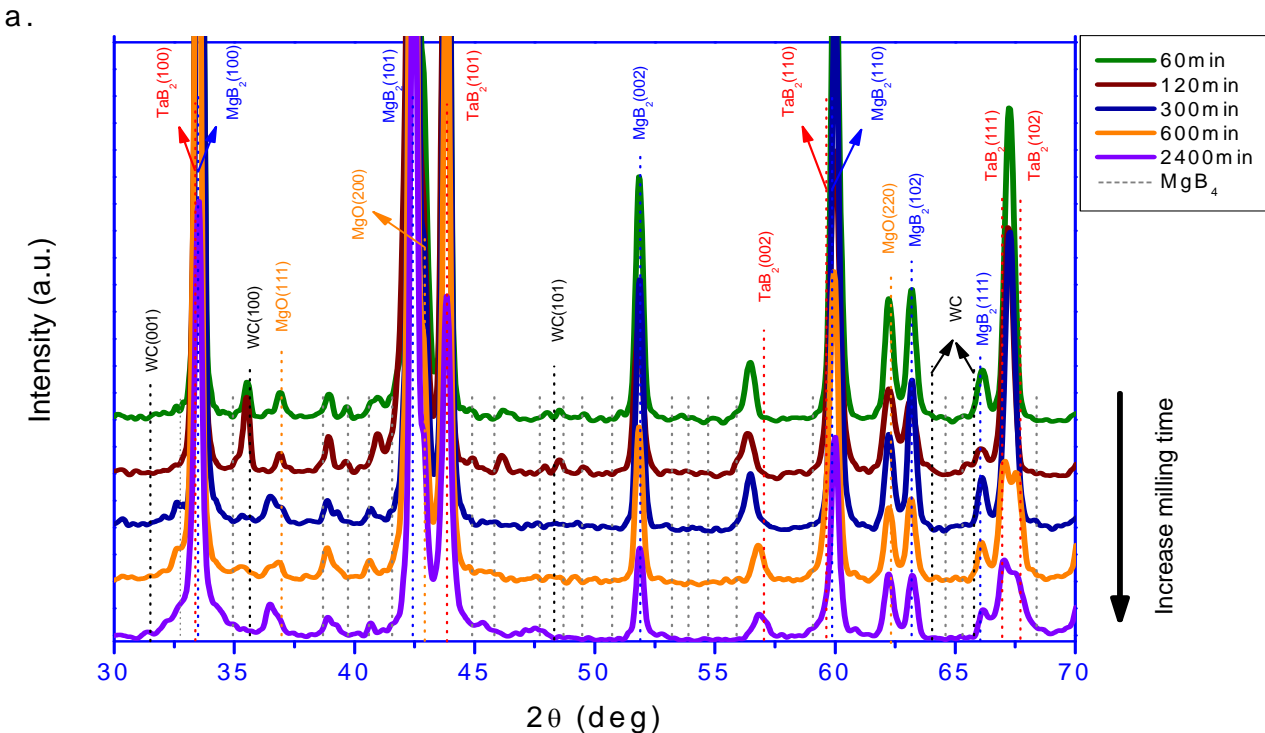


Figure 6.1 X-ray diffraction (XRD) measurement for the SPEX-8000D processed materials: 60, 120, 300, 600 and 2400 minutes corresponding to the 2 at.% TaB<sub>2</sub> doped MgB<sub>2</sub>. MgB<sub>4</sub> phase is identify by a dot line in the legend.

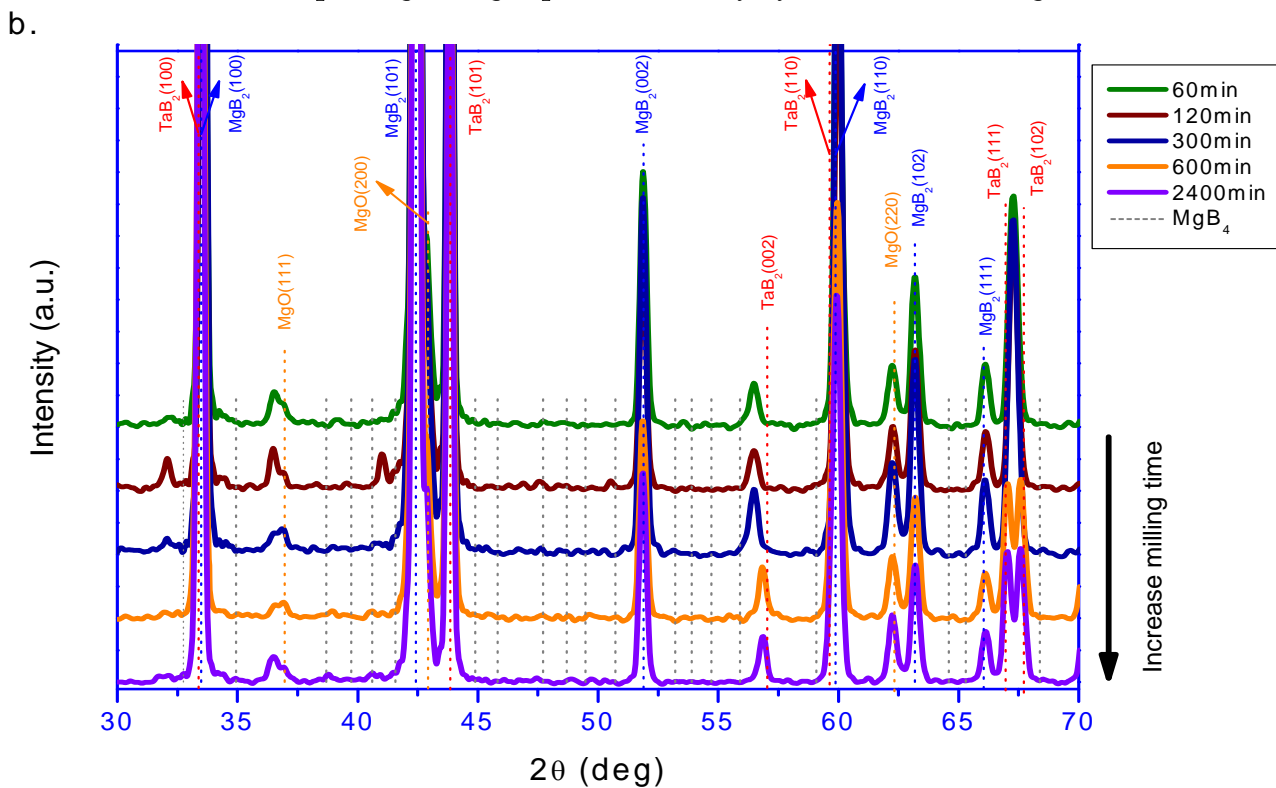


Figure 6.2 XRD measurements for the Pulverisette-4 on the 2 at.% TaB<sub>2</sub> doped MgB<sub>2</sub> for the 800 rpm speed at 60, 120, 300, 600 and 2400 minutes. MgB<sub>4</sub> phase is identify by a dot line in the legend.

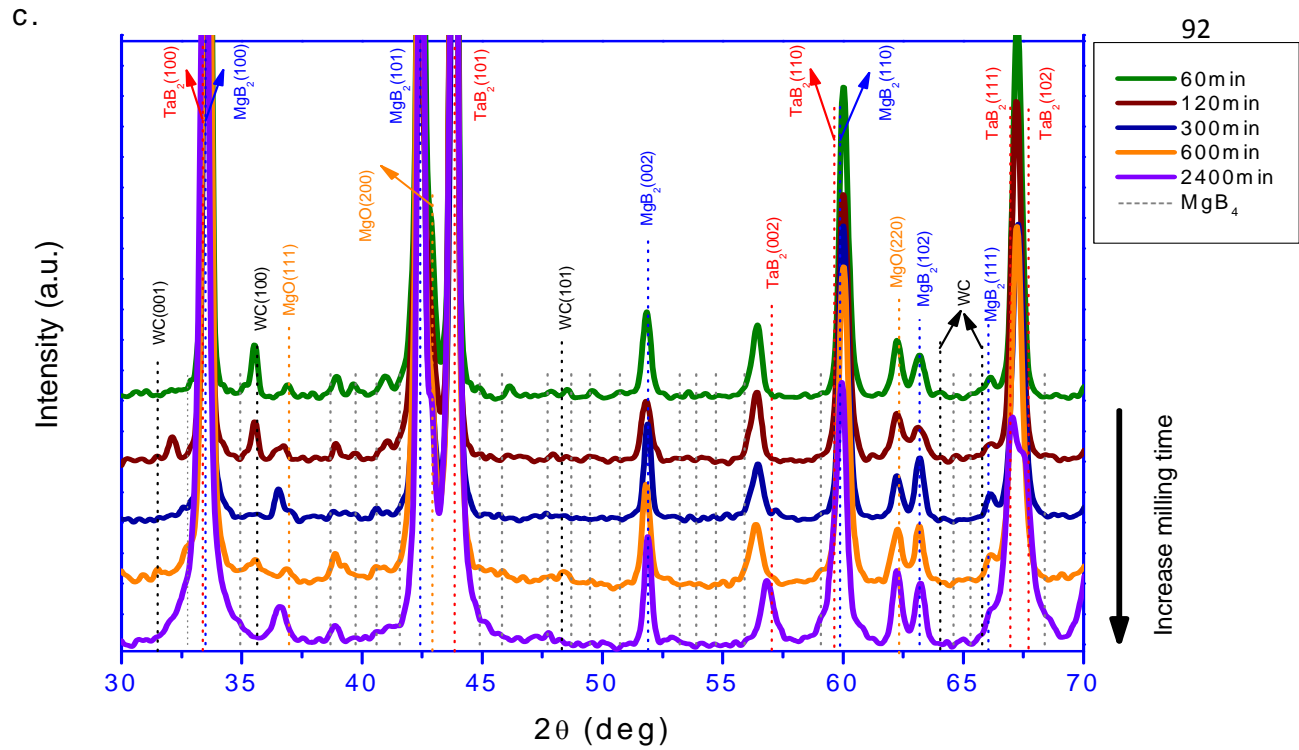


Figure 6.3 XRD measurements for the SPEX-8000D for the 5 at.% TaB<sub>2</sub> doped MgB<sub>2</sub>: 60, 120, 300, 600 and 2400 minutes. MgB<sub>4</sub> phase is identify by a dot line in the legend.

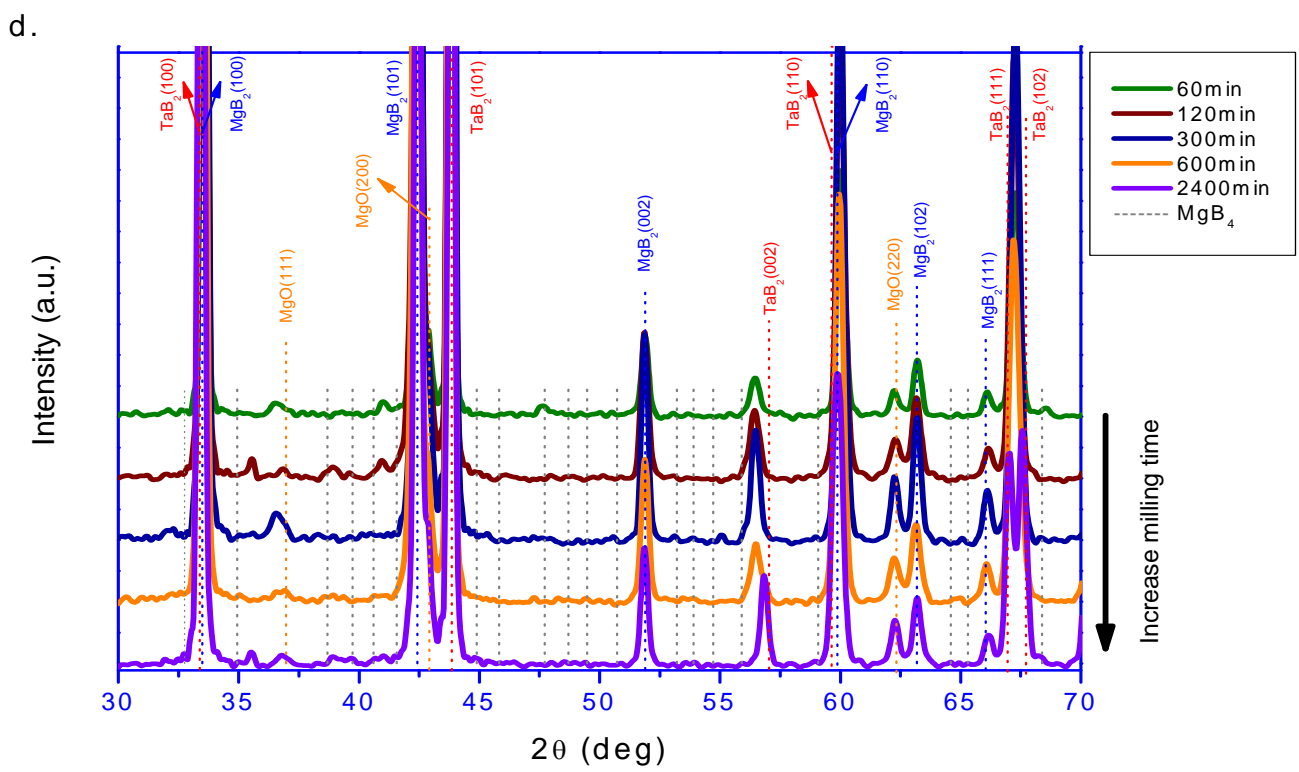


Figure 6.4 XRD measurements for the Pulverisette-4 at 800 rpm process at 5 at.% TaB<sub>2</sub> doped MgB<sub>2</sub>: 60, 120, 300, 600 and 2400 minutes. MgB<sub>4</sub> phase is identify by a dot line in the legend.

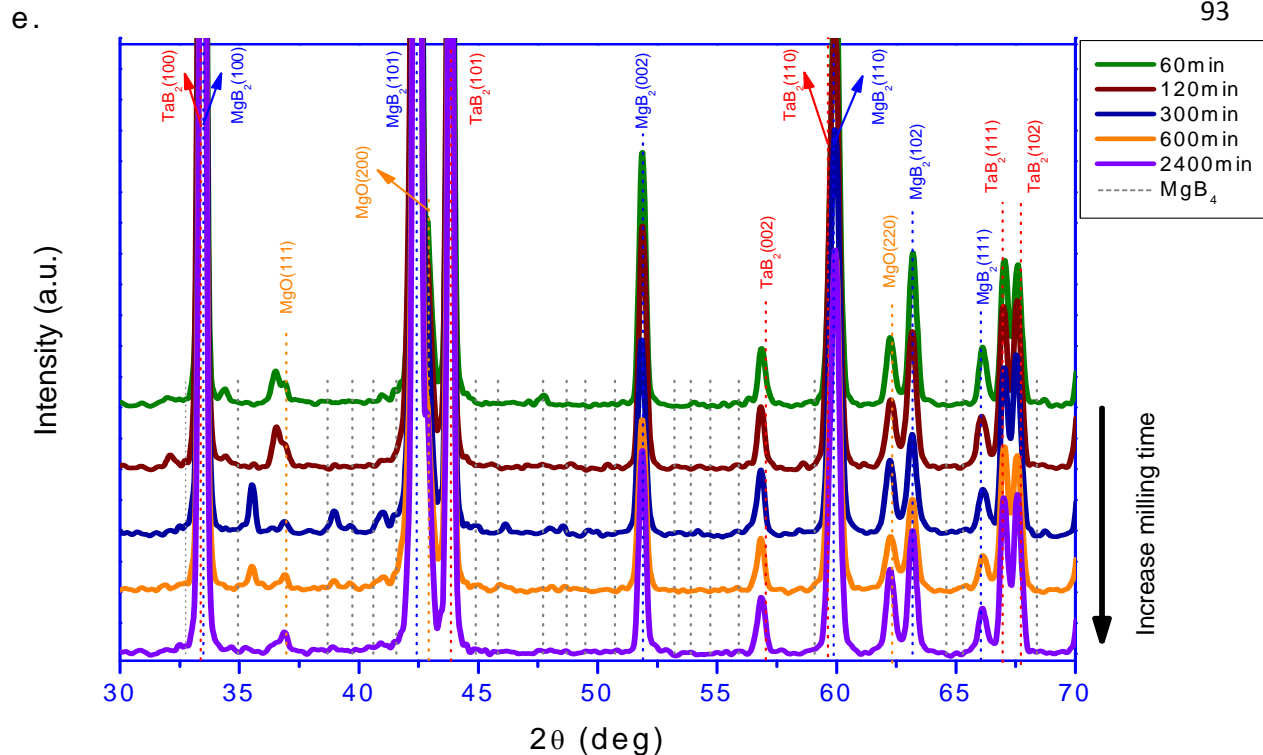


Figure 6.5 XRD measurements for the Pulverisette-4 at 1200 rpm processed material: 60, 120, 300, 600 and 2400 minutes at 2 at.% TaB<sub>2</sub> doped MgB<sub>2</sub>. MgB<sub>4</sub> phase is identify by a dot line in the legend.

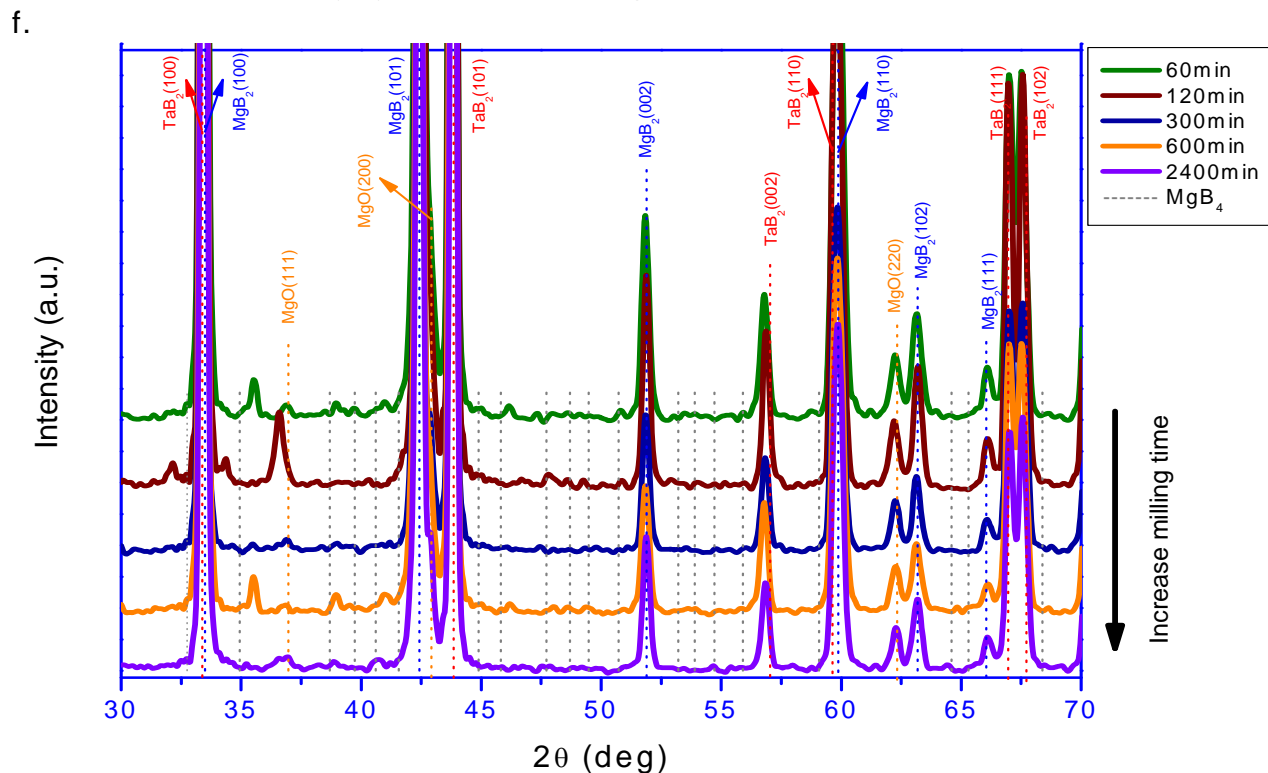


Figure 6.6 XRD measurements for the Pulverisette-4 at 1200 rpm process at 5 at.% TaB<sub>2</sub> doped MgB<sub>2</sub>: 60, 120, 300, 600 and 2400 minutes. MgB<sub>4</sub> phase is identify by a dot line in the legend.

The spectra peaks for the secondary phase,  $\text{MgB}_4$ , showed as a dot line in the spectra, were more prominent in material processed at 60 120 and 600 minutes ball milling time, with clear peak in the 35-40 range as in the 45-50° range. The presence of spectral peaks corresponding to the  $\text{TaB}_2$  phase demonstrated that independent of the doping level, there was some undissolved  $\text{TaB}_2$  in the milled material. For 2 and 5 at.%  $\text{TaB}_2$  and  $\text{MgB}_2$  phases are observed meaning that a large amount of the material for the substitution of Mg by Ta atoms in the structure was not completed. In Figures 6.3, 6.4 and 6.6 the intensity of  $\text{TaB}_2$  phase was higher than the intensity shown in Figures 6.1, 6.2 and 6.5, due to the higher density of  $\text{TaB}_2$ , corresponding to the 5 at.% as and 2 at.% doping levels respectively. Other secondary phases, notably  $\text{MgO}$ ,  $\text{MgB}_4$  (gray dotted lines) and  $\text{WC}$ , were indentified.

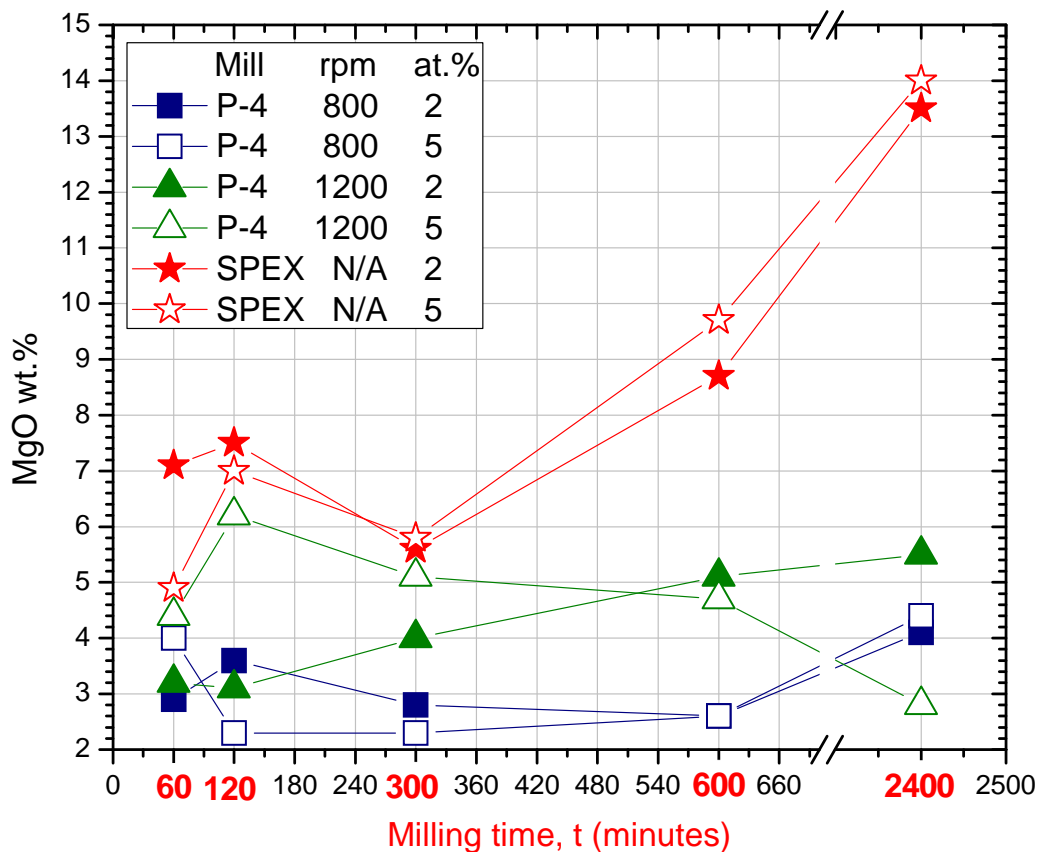
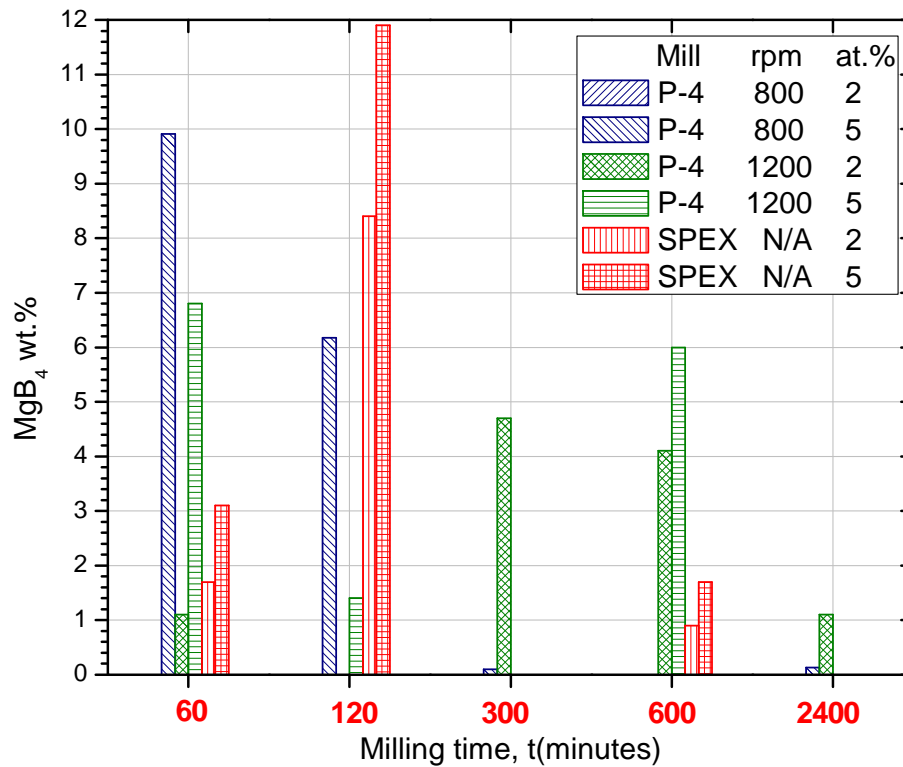


Figure 6.7 MgO wt. % phase of processed material at different milling times.

The Rietveld analyses of the X-ray diffraction measurements, as tabulated in Table 6.1 to 6.6, showed that MgO contamination levels, Figure 6.7, were higher in the SPEX processed materials than in the Pulverisette-4 processed materials. Further, MgO contamination was essentially continuously increasing from 60 minutes to 2400 minutes in the SPEX milled 2 at.% and 5 at.% TaB<sub>2</sub> doped MgB<sub>2</sub>, with highest level of 13.5 and 14 wt.% observed for the 2400 minutes ball milled material, respectively. In contrast to Pulverisette-4, MgO contamination was essentially practically constant having small wt. % variations. The highest level of 6.2 wt.% was observed for Pulverisette-4 processed material at 1200 rpm for 120min for the 5 at.% TaB<sub>2</sub> doped MgB<sub>2</sub>. Otherwise, as SPEX processed material, an increment in MgO wt.% is obtained for material processed for 2400 minutes in both rotational speed range, 800 and 1200 rpm, and for both doping levels. Different from material processed at 800 rpm, in both doping levels which MgO wt. % remain constant from 120 to 600 minutes, an unlike the MgO contaminant with a maximum content of 3.2 to 5.5 wt.% was observed for 1200 rpm corresponding to the 2 at.% TaB<sub>2</sub> doped MgB<sub>2</sub> (Tables 6.4). This behavior, for 1200 rpm at 5 at.%, is totally different for material processed in the rotational speed range at 5 at.%. A decrease in MgO wt.% is observed as the milling time increase from 6.2 to 2.8 wt.%.

Figure 6.8 show that the amount of MgB<sub>4</sub> decreased as the milling time increase. No peaks of MgB<sub>4</sub> phase were observed for material processed at in the Pulverisette-4 at 800 rpm for the 2 at.5 TaB<sub>2</sub> doped MgB<sub>2</sub>. The totally absent of MgB<sub>4</sub> phase for the 600 and 2400 minutes processed materials with the SPEX mill for the 2 at.% and 5 at.% TaB<sub>2</sub> doped MgB<sub>2</sub>, detected in the 60, 120 and 600 minutes SPEX processed, only. In these three cases, the amount of the unreacted MgB<sub>4</sub> for SPEX processed material at 5 at.% was higher than 2 at.% ones.



**Figure 6.8** MgB<sub>4</sub> wt. % phase of processed material at different milling times.

The higher value of MgB<sub>4</sub> recorded for SPEX at 2 at.% and 5 at.% processed material was 8.4 wt.% and 11.9 wt.%, respectively. For Pulverisette-4, the higher value, 9.9 wt.%, was obtained material ball milled at 800 rpm for 60 minutes using 5 at.% TaB<sub>2</sub> doped MgB<sub>2</sub>. At this parameter almost zero MgB<sub>4</sub> phase were observed after 300 minutes. At 1200 rpm, MgB<sub>4</sub> phase was obtained in most of the material processed. The levels of MgB<sub>4</sub> variation is not well defined at this rotational speed range. At this rotational speed range, the highest values, 6.8 wt.%, was observed for 5 at.% during 60 minutes ball milling. In the case of 2 at.%, for 1200 rpm ball milling, the highest wt.% level of MgB<sub>4</sub> was 4.7 wt.%. At this parameters, no MgB<sub>4</sub> wt.% values were obtained as well at 2400 minutes.

A predominant tendency at shorted milling time, 60 and 1200 minutes, is observed for the generation of MgB<sub>4</sub> phase. It is highly valid for SPEX processed material in the both atomic dopant levels.

### 6.1.1 X-ray-Diffraction of SPEX ball milled.

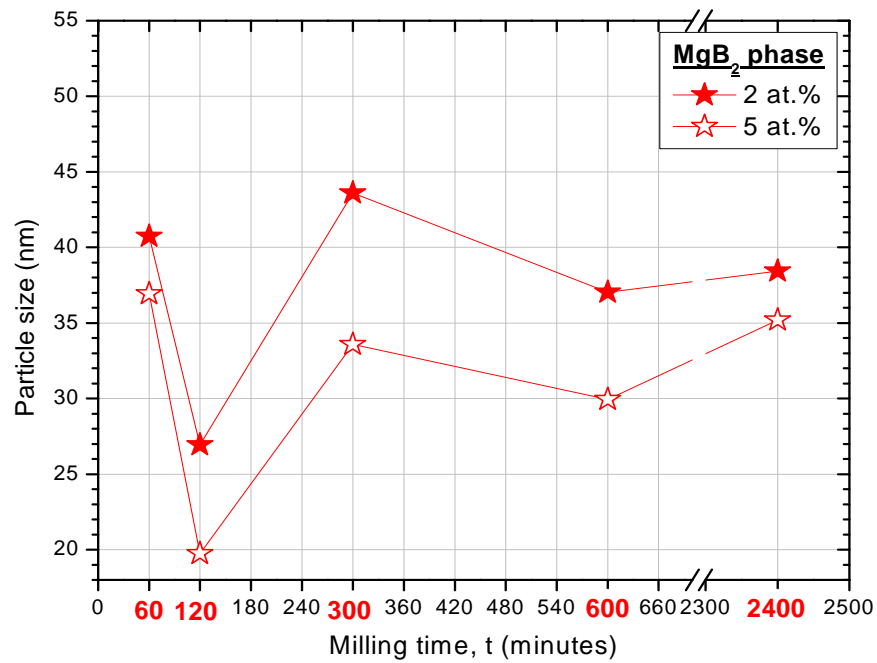


Figure 6.9 Average crystallite size, from Rietveld analysis, of post HIP SPEX processed MgB<sub>2</sub> phases at different milling times. Data plot at 2 at. % and 5 at. % TaB<sub>2</sub> doped MgB<sub>2</sub>.

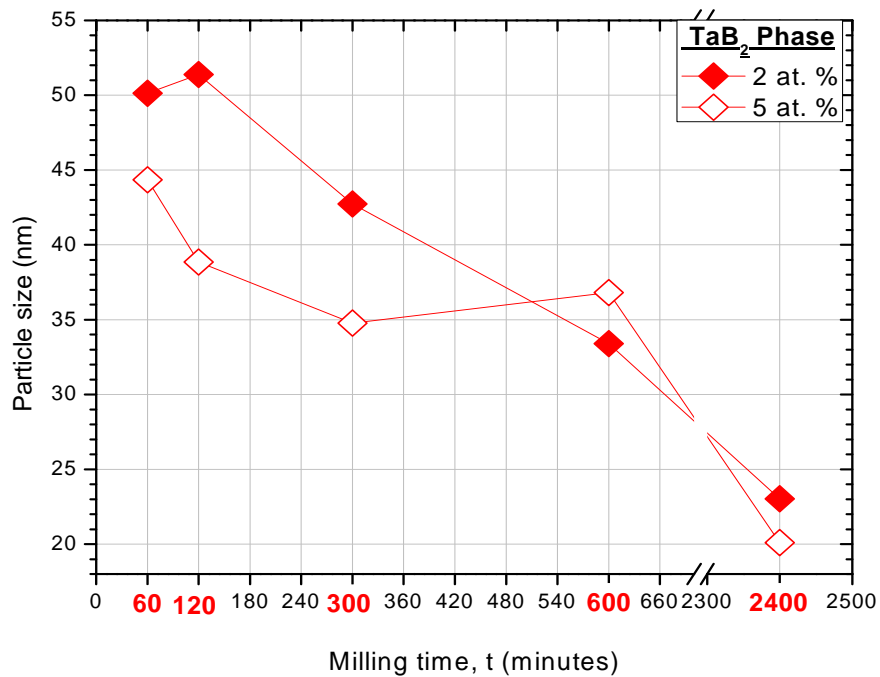


Figure 6.10 Average crystallite size, from Rietveld analysis, of post HIP SPEX processed TaB<sub>2</sub> phase at different milling times. Data plot at 2 at. % and 5 at. % TaB<sub>2</sub> doped MgB<sub>2</sub>.

As shown in Table 6.1, the amount of unreacted TaB<sub>2</sub> in the 2 at.% TaB<sub>2</sub> doped MgB<sub>2</sub> seemed to remain constant at 5.2-6.0 wt.% independent of ball milling time for the SPEX processed materials. A monotonically behavior of a reduction on average crystallite size is observed in Figure 6.10 for TaB<sub>2</sub> average crystallites as the milling time increase. The average crystallite size of TaB<sub>2</sub> at 5 at.% is, for all milling time except 600 minutes, lower than the average crystallite size at 2 at.% dopant level. At 2400 minutes, the lower average crystallite size was 23.03 and 20.11 nm for SPEX at 2 and 5 at. % doping level, respectively.

Diferent from TaB<sub>2</sub> average crystallites, the average crystallites of MgB<sub>2</sub> are decreasing and increasing as the milling time increase. This variation at longer milling time (300 - 2400 minutes) is less pronounced than at short milling time (60 – 120 minutes). The variation of average crystallites in longer milling time has the tendency to reach to a limit reduction of average crystallite size, which has is similar to the reduction of average crystallite size at 60 minutes ball milling. For short milling time, larger reduction of MgB<sub>2</sub> average crystallites is obtained especially at 120 minutes. In both cases, SPEX at 2 and 5 at.% ball milled at 120 minutes, 26.94 and 38.86 nm were the lower average crystallite size, respectively. Thus from the initial average crystallite size of 97.01 nm for the MgB<sub>2</sub> precursor powder, which reduced to 40.74 nm after 60 minutes and 26.94 after 120 minutes ball milling in the presence of 2 at.% TaB<sub>2</sub> doping, it seemed that initial average crystallite reduction was more pronounced within the first hours, short milling time, of ball milling.

Comparing Figure 6.9 and 6.10, the average crystallite size for MgB<sub>2</sub> remain larger than the average crystallite size for TaB<sub>2</sub> in most of the material processed. This is not valid for material processed at 2400 minutes in the SPEX. Average crystallite size of TaB<sub>2</sub> at 2 and 5 at. % is observed to be lower than average crystallite size forMgB<sub>2</sub> 38.43 nm to 23.03 nm

and 35.20 nm to 20.11 nm, respectively. The same situation was observed at 300 and 600 for 2 at. % in the SPEX processed materials.

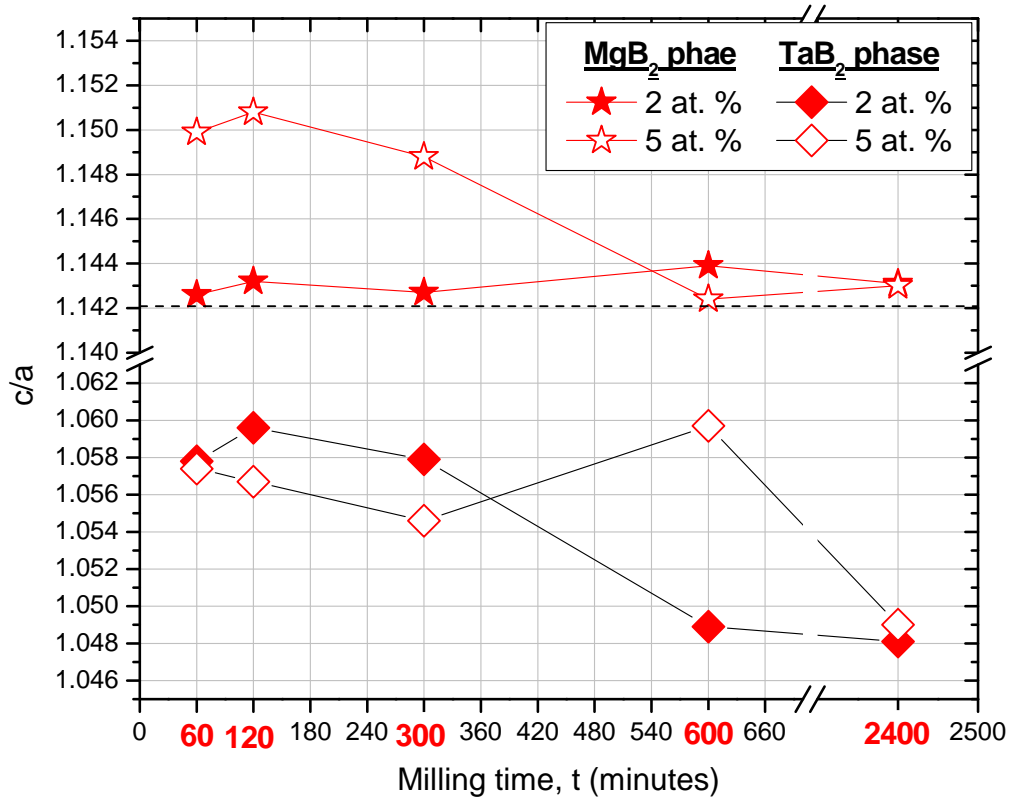


**Figure 6.11** Tetragonality ( $c/a$ ), from Rietveld's analysis, of SPEX processed material, for  $MgB_2$  and  $TaB_2$  phases, at different milling times. Data plot at 2 at. % and 5 at. %  $MgB_2$  doped  $TaB_2$ .

The tetragonality ratio,  $c/a$ , for the  $MgB_2$  and  $TaB_2$  phases decrease as the milling time increase. High values of  $c/a$  were observed of mostly at 120 minutes ball milling time. At 2400 minutes ball milling the lower  $c/a$  for both cases in the 2 and 5 at.% doping level is obtained. Respect to  $MgB_2$ , SPEX at 2 at. % shows higher tetragonality than SPEX at 5 at. %. The variation of  $c/a$  for 5 at. % for  $MgB_2$  is relatively constant as the milling time increase. In contrast with  $TaB_2$ , SPEX at 5 at. % revealed the higher  $c/a$  values compared with the 2 at. % for  $TaB_2$ . The tetragonality effect seems to be similar to the average

crystallite size reduction as the milling time increase for  $\text{MgB}_2$  and  $\text{TaB}_2$  in Figure 6.9 and Figure 6.10, respectively. All SPEX processed samples have an increase in  $c/a$ , for  $\text{MgB}_2$  phase, compared with the no milling material. It is larger for SPEX 5 at.% processed material than 2 at.%, as shown in Figure 6.11 for the  $\text{MgB}_2$  phase.

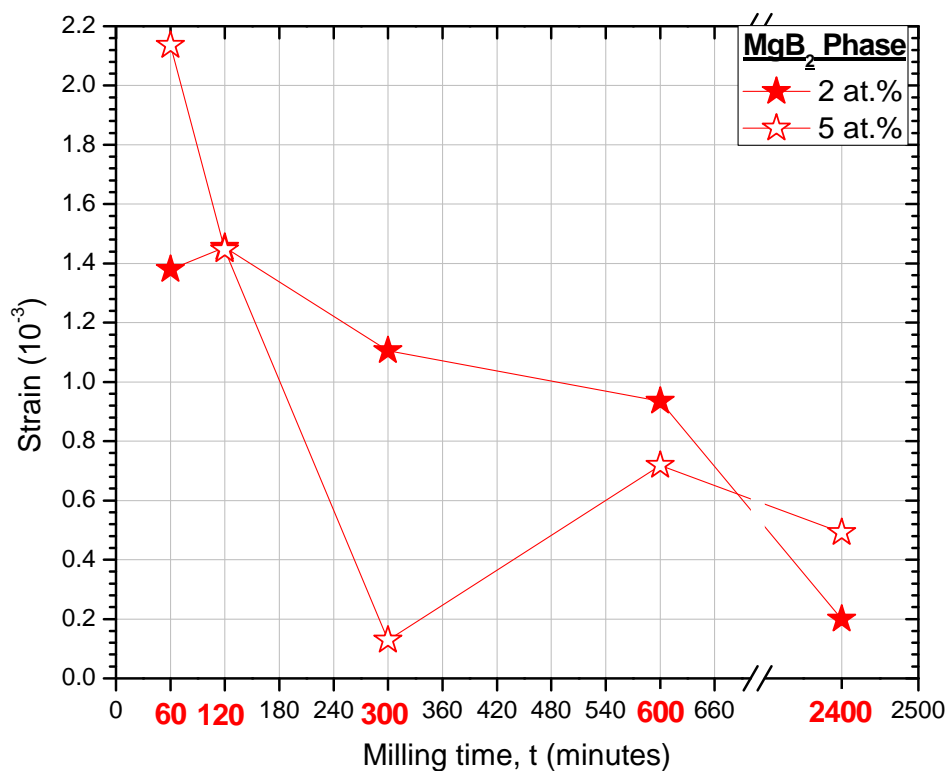
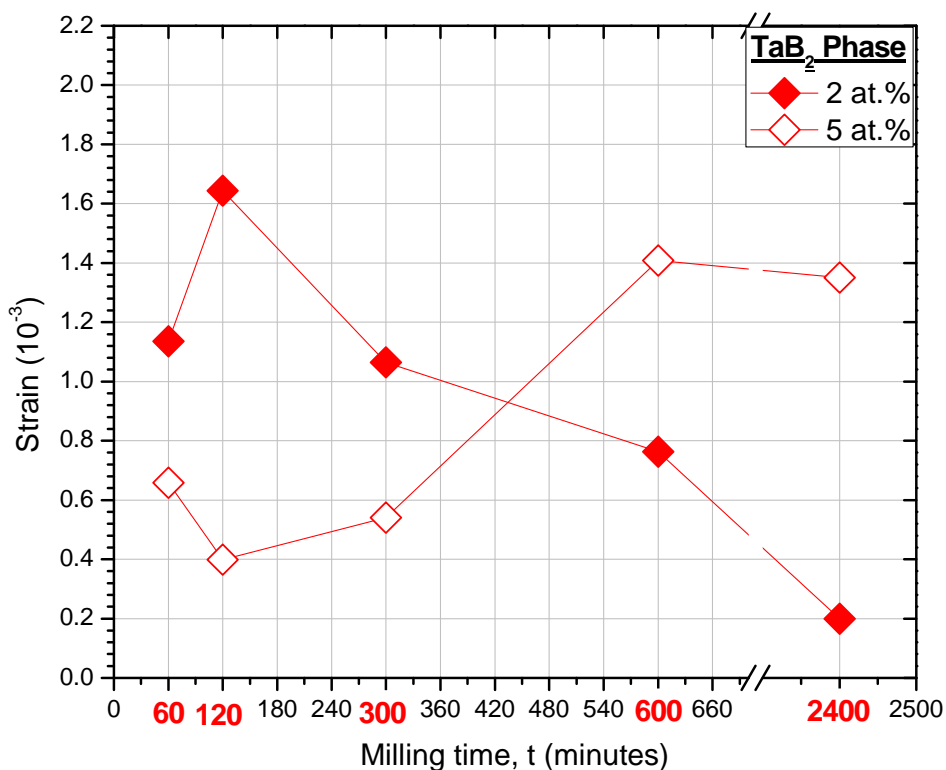


Figure 6.12 Strain, from Rietveld's analysis, of SPEX processed material, for  $\text{MgB}_2$  phase, at different milling times. Data plot at 2 at. % and 5 at. %  $\text{MgB}_2$  doped  $\text{TaB}_2$ .



**Figure 6.13** Strain, from Rietveld'analysis, of SPEX processed material,  $TaB_2$  phase, at different milling times. Data plot at 2 at. % and 5 at. %  $MgB_2$  doped  $TaB_2$ .

The variation deduced from the Rietveld analyses for the strain point to decrease as the milling time increase in the case for  $MgB_2$  phase show in Figure 6.12. The highest strain was 0.002135 for SPEX at 5 at. % processed material. The relation between 2 at. % and 5 at. % seems to be similar as the milling time increase. The lower strain is observed at 2400 milling time, in both cases, which average crystallite size, Figure 6.9, at this milling time range has the tendency to reach to a constant value. Due to that, the strain at longer milling time is lower than short milling time. It appeared that extensive milling time favored loss of strain, while average crystallite size refinement reach to a constant value.

The loss of strain for TaB<sub>2</sub> average crystallites at 2 at. % in the SPEX, Figure 6.13, seems to be similar as MgB<sub>2</sub> average crystallites, different from 5 at. % processed ones. SPEX sample at 2 and 5 at. % shows the same trend, losing strain as the milling time increase. The higher strain for SPEX at 2 at. % of TaB<sub>2</sub> average crystallites was observed at 120 minutes, 0.001644. In contrast, SPEX at 5 at. % shows a different trend. As the milling time increase, the strain of SPEX 5 at. % material increase. The highest strain for SPEX 2 at. % was observed for 600 minutes, 0.001408. This behavior is not well understanding compared with the other trends, but it has a similar tendency of the increase of tetragonality as shown in Figure 6.11 for TaB<sub>2</sub> phase processed in the SPEX at 5 at.%. This increase in tetragonality is due to an increase of c lattice parameter, as shown in Table 6.2.

### **6.1.2 X-ray diffraction analysis of Pulverisette-4 processed material.**

The X-ray diffraction measurements of the TaB<sub>2</sub> doped MgB<sub>2</sub> processed with Pulverisette-4 ball milling are shown in Figures 6.2, 6.4, 6.5 and 6.6 respectively. The capability of the Pulverisette-4 ball mill made it possible to select and combine processing parameters that were not possible with the SPEX-mill used in this study. As shown in Tables 6.3, 6.4, 6.5, and 6.6, the analyses of the x-ray-diffraction measurements reflected the same trends that distinguished the ball milling operations between the SPEX-8000D and the Pulverisette-4 mills for TaB<sub>2</sub> doped MgB<sub>2</sub> processed material.. This in turn reflected on the critical properties (such as critical current density, J<sub>c</sub>, critical temperature, T<sub>c</sub>, irreversibility field, H\*, flux pinning force, F<sub>p</sub>) of the differently processed TaB<sub>2</sub> doped MgB<sub>2</sub> materials.

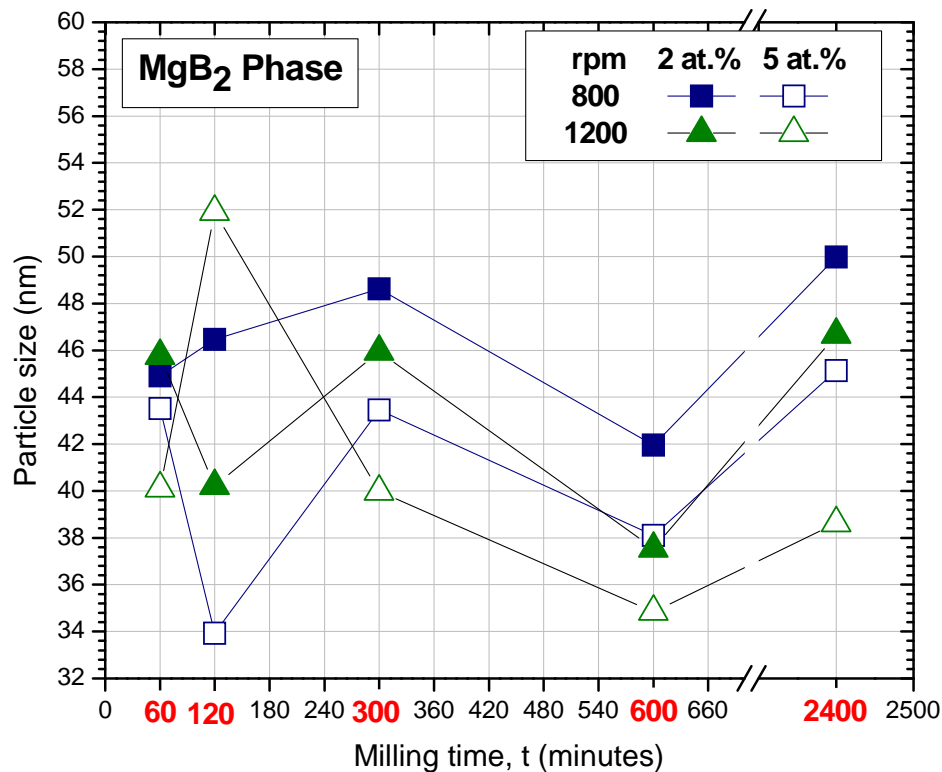


**Figure 6.14** Average crystallite size, from Rietveld Analysis, of Pulverisette-4 processed material,  $\text{MgB}_2$  phase, at 800 and 1200 rpm for different milling times. Data plot at 2 at. % and 5 at. %  $\text{MgB}_2$  doped  $\text{TaB}_2$ .

Similar trend of average crystallite size variation, for all material processed in the Pulverisette-4 at 800 rpm and 1200 rpm is showed in Figure 6.14. Average crystallite sizes for processed material in both rotational speed range at 2 at. % are smaller than material processed at 5 at. % in the Pulverisette-4. The trends showed that from the starting, post HIP no milling material (97.01 nm), average crystallite size is possible to reach to a average crystallite size reduction of most of the half of the initial values. At 60 minutes the lower average crystallite size is found for the 5 at.% material processed at 1200 rpm, 40.10 nm, following by 800 rpm, 43.52, at the same atomic doping level. At 120 minutes, further reduction of average crystallite size is observed for material processed at 800 rpm 5 at. % and 1200 rpm 2 at.%. A non understanding behavior is found for material processed 800 rpm 2 at.% and 1200 rpm 5 at.% during 120 minutes. It is possible, due to an increase in c lattice parameter as show Figure 6.16. Examination of Figure 6.2 and Table 6.3,

corresponding to the results of Pulverisette-4 (for 800 rpm) processed 2 at.% TaB<sub>2</sub> doped MgB<sub>2</sub> showed that average crystallite size reduction of MgB<sub>2</sub> from 97.01 nm to 35.27 nm occurred within the first 60 minutes of Ball Milling, while milling for 2400 minutes did not translate to further average crystallite reduction, as is observed in Figure 6.14.

As the milling time increased the average crystallite sizes increased. These behaviors is well understood by the conglomeration of average crystallites by cold working action or the stick in and stick off during the milling process. The highest average crystallite size was obtained for long period of time, 600 and 2400 minutes, by the post HIP sample milled in the Pulverisette-4 at 1200 rpm with 5 at.% TaB<sub>2</sub> doped MgB<sub>2</sub>.

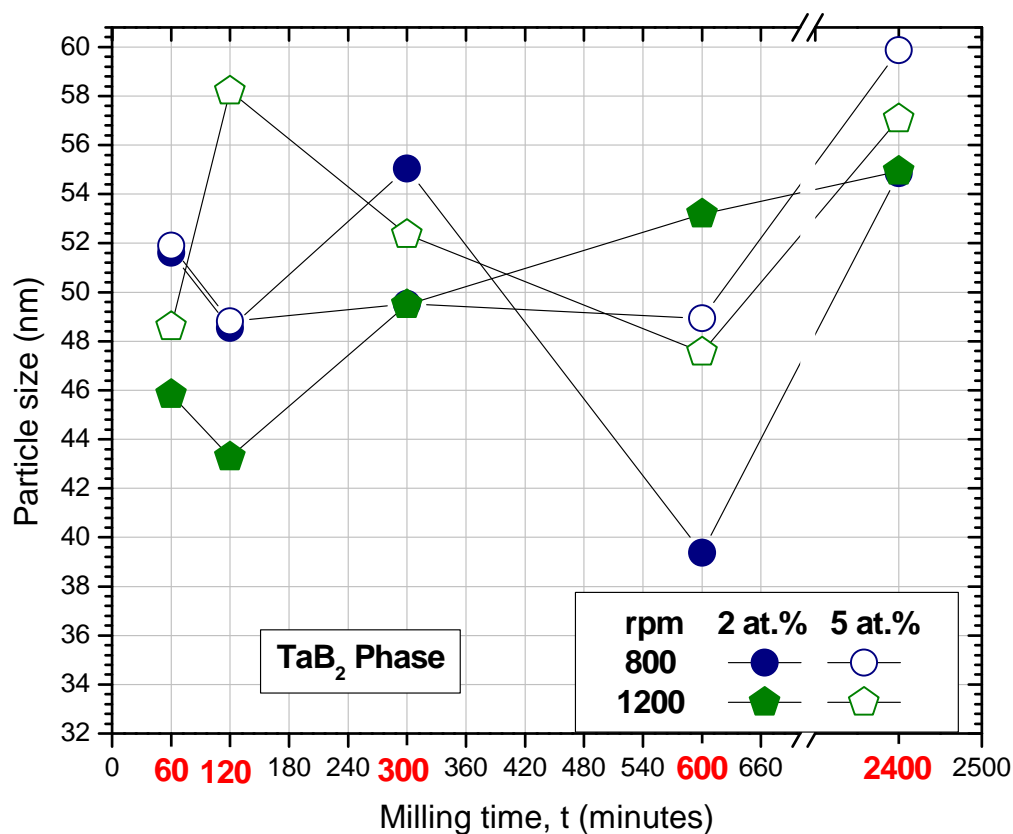


Figure 6.15 Average crystallite size, from Rietveld's analysis, of processed material, TaB<sub>2</sub> phase, in the Pulverisette-4 at 800 and 1200 rpm for different milling times. Data plot at 2 at. % and 5 at. % MgB<sub>2</sub> doped TaB<sub>2</sub>.

Average crystallite size reduction for TaB<sub>2</sub> phase is shown in Figure 6.15 for material processed at 800 and 1200 rpm in the 2 and 5 at.% doping levels. The average crystallite size for the TaB<sub>2</sub> phase remains higher than for MgB<sub>2</sub> average crystallite size in most of the cases. As the milling time increase the average crystallite size increase especially for material processed at 1200 rpm in the 2 at. %. The lower average crystallite size of TaB<sub>2</sub> observed was for 800 rpm at 2 at. % during 600 minutes. Different from SPEX material processed, just on this milling parameters, TaB<sub>2</sub> average crystallite size shows further reduction than MgB<sub>2</sub> average crystallites.

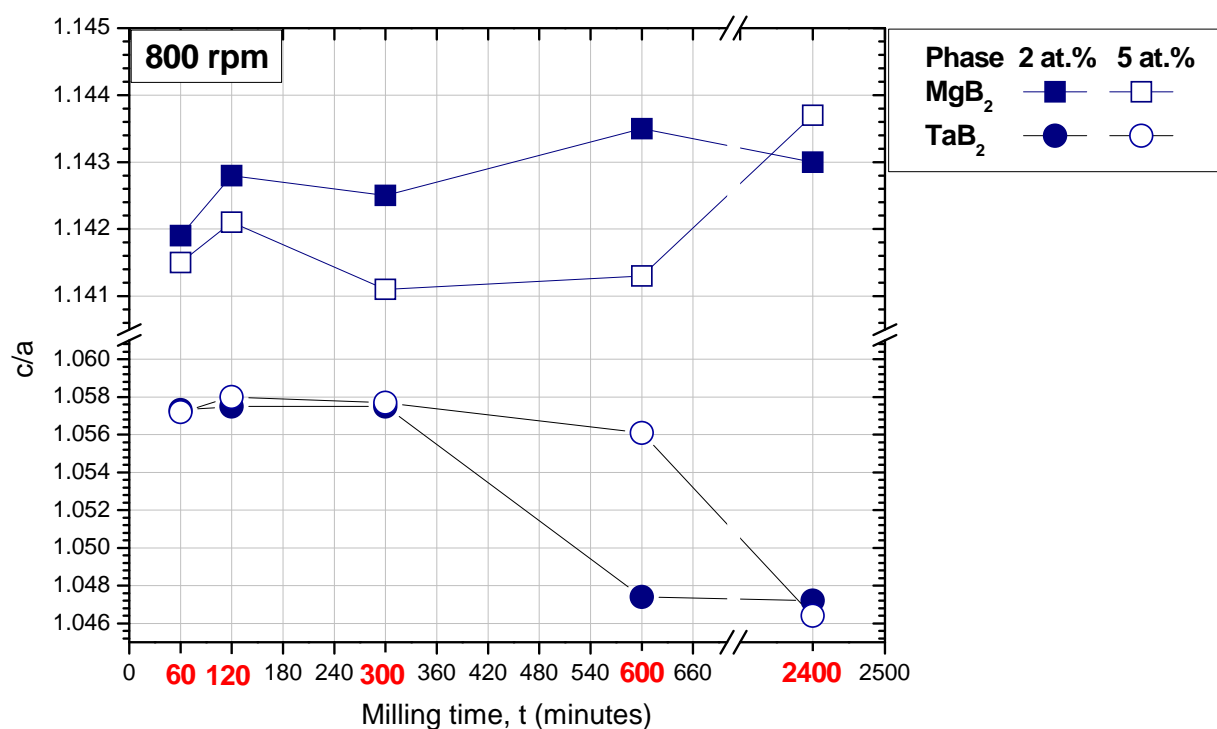
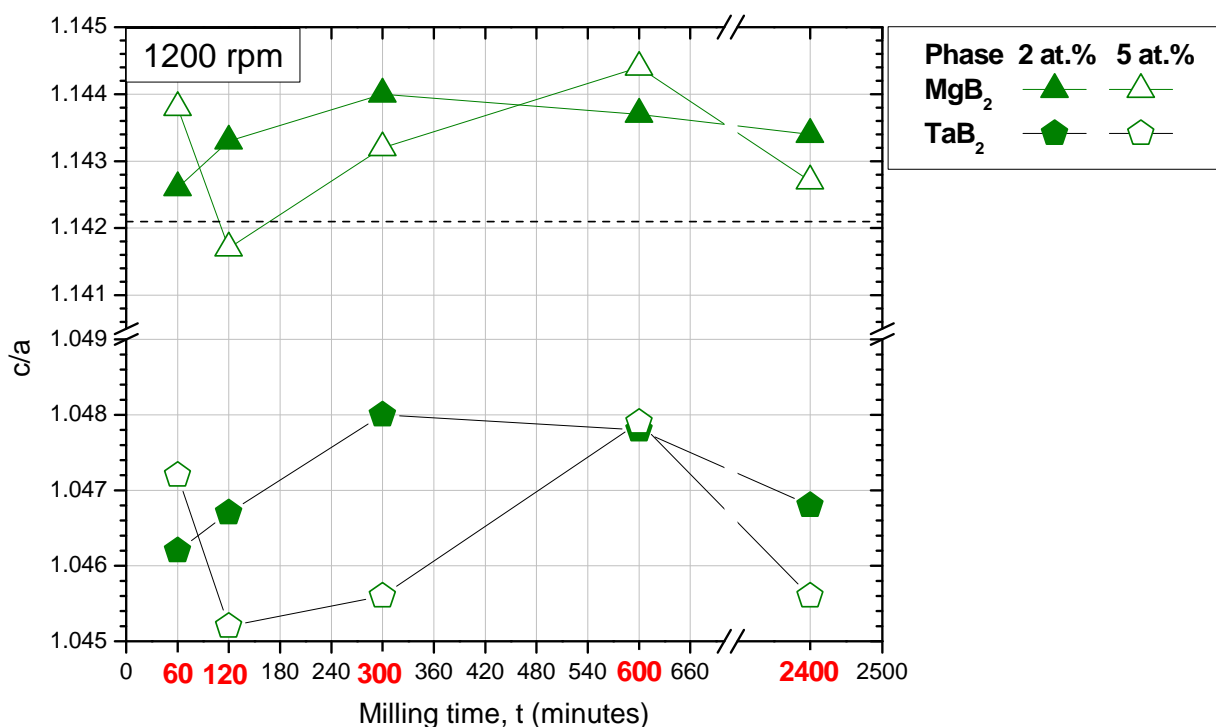


Figure 6.16 Tetragonality ( $c/a$ ), from Rietveld's analysis, of Pulverisette-4 at 800 rpm processed material, for MgB<sub>2</sub> and TaB<sub>2</sub> phases, at different milling times. Data plot at 2 at. % and 5 at. % MgB<sub>2</sub> doped TaB<sub>2</sub>.



**Figure 6.17** Tetragonality ( $c/a$ ), from Rietveld's analysis, of Pulverisette-4 at 1200 rpm processed material, for MgB<sub>2</sub> and TaB<sub>2</sub> phases, at different milling times. Data plot at 2 at. % and 5 at. % MgB<sub>2</sub> doped TaB<sub>2</sub>.

The material processed, either SPEX or Pulverisette-4, will reflect a change in the lattice parameters. It is due by the high energy impact in the, milling process, and the mechanical alloy as a result of the TaB<sub>2</sub> doped MgB<sub>2</sub> processed material. Because the atomic configuration of MgB<sub>2</sub> and TaB<sub>2</sub> lattice correspond to a hexagonal atomic arrangement, the tetragonality,  $c/a$ , reveals the change in the atomic structure. In Figure 6.16 and Figure 6.17, the tetragonality for MgB<sub>2</sub> and TaB<sub>2</sub> at 2 and 5 at. % TaB<sub>2</sub> doped MgB<sub>2</sub> and at 800 and 1200 rpm for different milling time is showed. Material processed at 800 rpm for MgB<sub>2</sub> at 2 and 5 at. % TaB<sub>2</sub> doped MgB<sub>2</sub> showed similar trend. At this rotational speed range, for material processed at 5 at. %,  $c/a$  values are lower than at 2 at. %. Further, the values of 5 at. % are below the tetragonality value for no milling post-HIP material, 1.1421, which is showed as dash line in the graph.

At 1200 rpm processed material, for 2 at.% TaB<sub>2</sub> doped MgB<sub>2</sub> tetragonality values are, in most of the case, higher than at 5 at. %. Different from 800 rpm, at 1200 rpm, both atomic doping level, c/a is higher than compared with the no milling post HIP material. the behavior is similar as 800 rpm. This is not valid for material processed for 120 minutes at 5 at. % in the Pulverisette-4 at 1200 rpm, which c/a values is 1.1417. This is consistent with the average crystallite size reduction, 51.91 nm, which value is out of the trend compared with all processed material milled at 120 minutes milling time. Similar comparison is observed in Figure 6.7, which the higher values of MgO wt.% is obtained for the material processed at 1200 rpm for 120 minutes in the 5 at.% TaB<sub>2</sub> doped MgB<sub>2</sub>.

Next, for TaB<sub>2</sub> at 800 rpm c/a has a reduction tendency as the milling time increase for both 2 and 5 at.%, as shown in Figure 6.16. Higher values, in the range of 1.0572 to 1.0580, were observed for 60, 120 and 300 minutes at 800 rpm in both atomic dopant levels. The tetragonality values for material processed at 1200 rpm is lower, in all cases, compared with 800 rpm ones. The lower value, 1.0452 was found for 120 minutes 5 at.% for the rotational speed range of 1200 rpm. The behavior of c/a as the milling time increase seems to be similar for 2 and 5 at.% at 1200 rpm for MgB<sub>2</sub> and TaB<sub>2</sub> phases, respectively. This trends are comparable with the strains as the milling time increase.

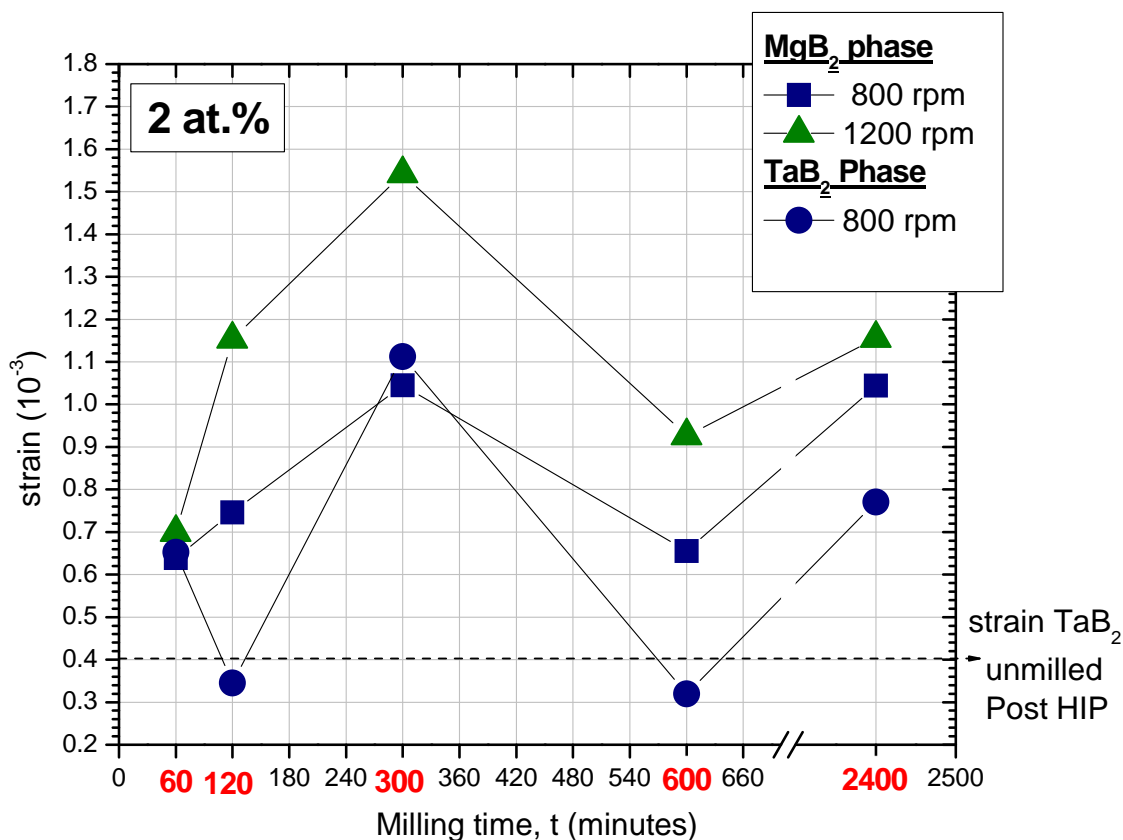


**Figure 6.18** Strain, from Rietveld's analysis, of Pulverisette-4 processed material at 800 and 1200 rpm, for  $\text{MgB}_2$  phase, at different milling times. Data plot at 2 at. %  $\text{MgB}_2$  doped  $\text{TaB}_2$ .

For 2 at.%  $\text{TaB}_2$  doped  $\text{MgB}_2$ , for the  $\text{MgB}_2$  phase, the strain increase as the milling time increases until 300 minutes, ball milling, as shown in Figure 6.18. After 300 minutes, a loss in strain is observed which reveal strains constants values for longer milling time. This behavior in strain is similar for rotational speed at 800 rpm and 1200 rpm. Figure 6.18 shows higher strain values for 1200 rpm compared with 800 rpm as the milling time increase. Strain values for Pulverisette-4 material processed at 60 minutes ball milling, 0.000639 and 0.000669, are close similar as the strain values at 2400 minutes, 0.001044 and 0.001155, for the rotational speed of 800 rpm and 1200 rpm, respectively. The same occurred for average crystallite size reduction in the  $\text{MgB}_2$  phase as shown in Figure 6.14.

A different behavior, for  $\text{MgB}_2$  phase, is observed for Pulverisett-4 material processed at 5 at.% in the 800 rpm and 1200 rpm.

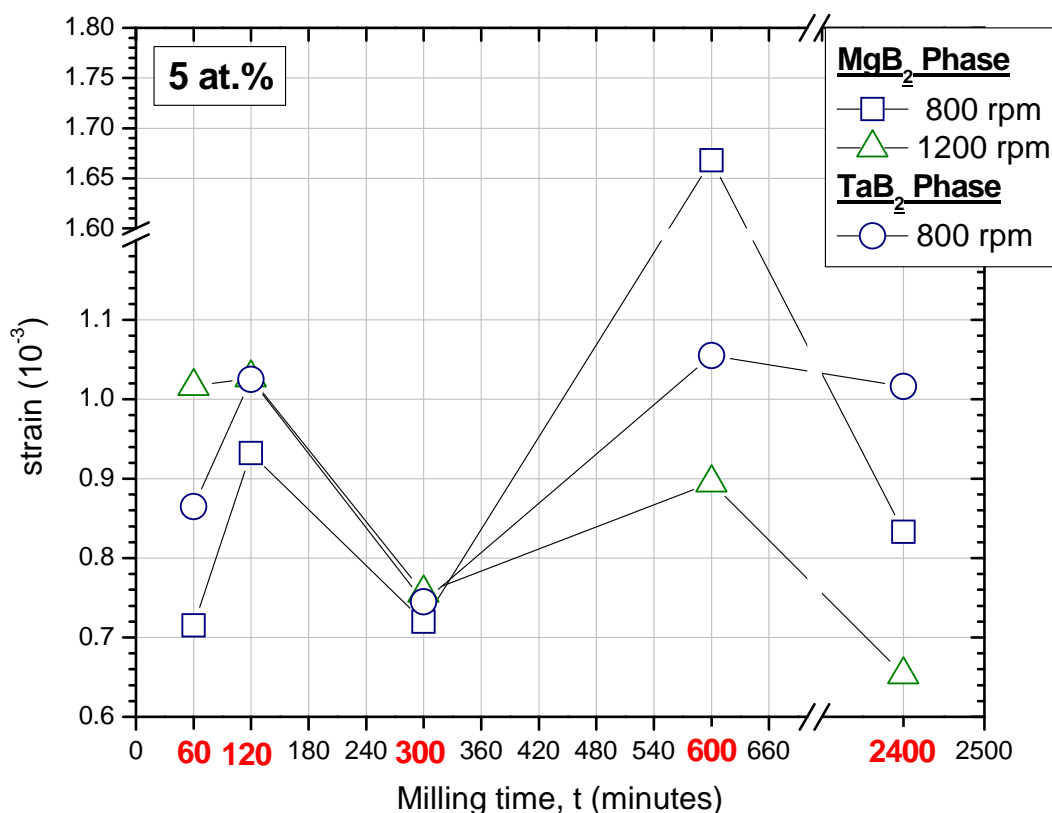


**Figure 6.19** Strain, from Rietveld analysis, of Pulverisette-4 processed material at 800 and 1200 rpm for  $\text{MgB}_2$  phase and 800 rpm for  $\text{TaB}_2$  phase at different milling times. Data plot at 5 at. %  $\text{MgB}_2$  doped  $\text{TaB}_2$ .

At 300 minutes ball milling, Figure 6.19, the strain decrease from 0.000932 and 0.001027 to 0.000720 and 0.000756 and increase again to 0.001668 and 0.000895 for 800 rpm and 1200 rpm, respectively. The behavior for longer milling time, compared with 2 at. % in the 1200 rpm rotational speed range has the tendency to decrease. With this clearly different in strain values, Figure 6.18 and Figure 6.19, and increase in at.% is having an effect in the mechanical alloy of  $\text{TaB}_2$  doped  $\text{MgB}_2$ .  $\text{TaB}_2$  phase at 800 rpm is show in Figure 6.18 and Figure 6.18 for 2 and 5 at.% respectively. The strain values for 5 at. % have higher values

compared with 2 at. %. It is not valid at 300 minutes ball milling in which TaB<sub>2</sub> strain values for 2 at.% is higher than 5 at. % processed material at 800 rpm, 0.001112 and 0.000745 respectively. This strain values is higher than material processed with the same parameters at 2 at.% for MgB<sub>2</sub> phase, 0.001045.

Next, in the 5 at.% TaB<sub>2</sub> doped MgB<sub>2</sub> in Figure 6.19, the strain values, in the MgB<sub>2</sub> phase, for 800 rpm are higher compared with 1200 rpm in the shorter milling time, 60 and 120 minutes. Inverse situation, but similar as in 2 at.%, is observed for longer milling time, 600 and 2400 minutes, for the same phase.

Apart of the 2 and 5 at.% trends for the strain values, which seems similar respect to each other in the 800 rpm and 1200 rpm rotational speed for both phases, MgB<sub>2</sub> and TaB<sub>2</sub>, the behavior promote statistical values for the different milling times and milling parameters. It is different compared with SPEX processed material which showed strain reduction tendency, Figure 6.12.

Otherwise, the amount of TaB<sub>2</sub> in MgB<sub>2</sub>, comparing 2 and 5 at.% is having an effect in the strain values, Figure 6.19 and Figure 6.18, as well in the tetragonality values, Figure 6.16 and Figure 6.17.

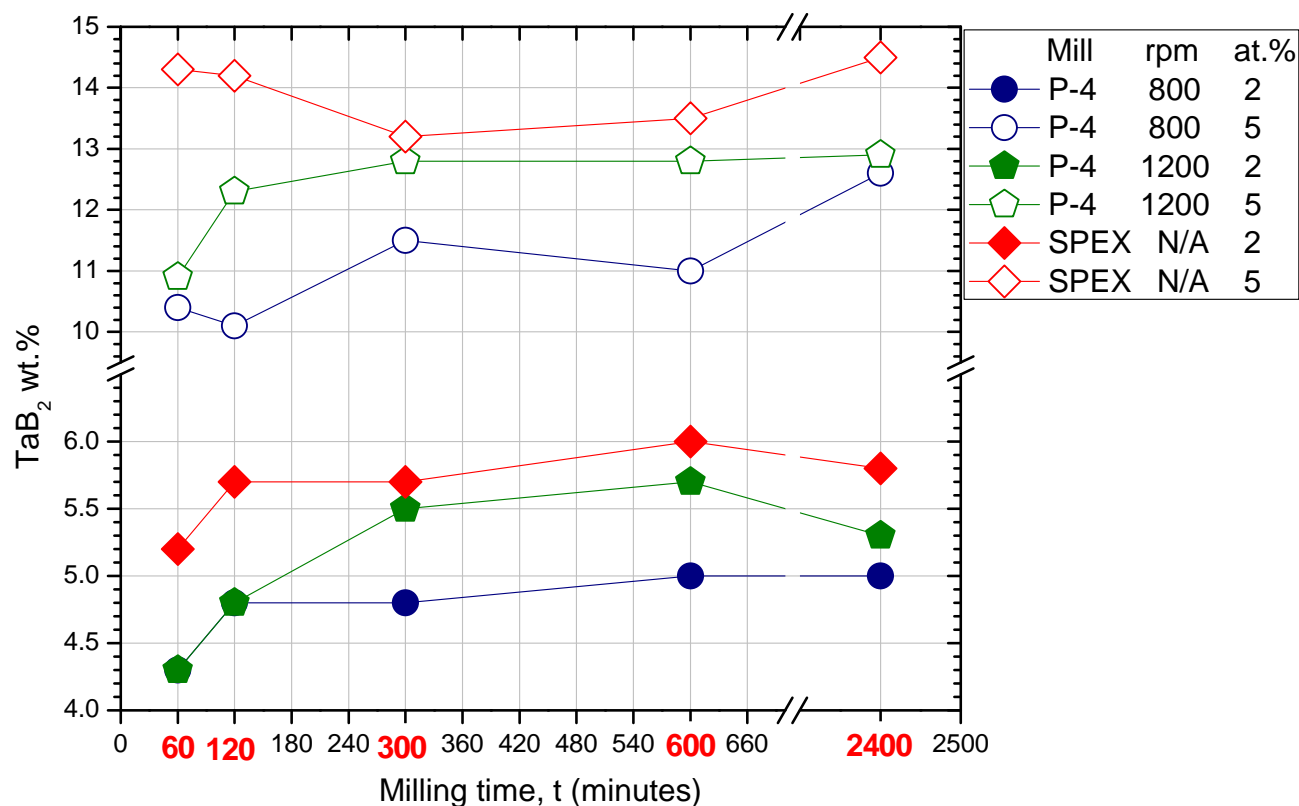


**Figure 6.20** TaB<sub>2</sub> wt. % phase, from Rietvel's analysis, of processed material at different milling times.

Figure 6.20 shows the TaB<sub>2</sub> wt.% of TaB<sub>2</sub> doped MgB<sub>2</sub> at 2 and 5 at.% as the milling time increase. As shown in chapter 3 section 3.1.3, 2 at.% is 8.26 wt.% while 5 at.% represent the 18.84 wt.%. In the 2 and 5 at.%, the amount of TaB<sub>2</sub>wt.% observed was higher for SPEX processed material compared with Pulverisette-4 ones. Respect to Pulverisette-4 processed material at 1200 rpm the amount of TaB<sub>2</sub> in the found was higher than at 800 rpm processed material in both atomic dopant levels. Due to the high amount used of TaB<sub>2</sub> wt.% before ball milling process, higher level amount of this phase was found for the 5 at.% TaB<sub>2</sub> doped MgB<sub>2</sub>. Comparing the different in TaB<sub>2</sub> wt.% with the tetragonality and the values, respect to Figure 6.16, 6.17 and Figure 6.18, 6.19, higher introduction of this phase is promoted changes on that parameters.

**Table 6.1** Lattice constants, average crystallite-size and strain analyses based on Rietveld Analyses using Power Cell Program for the **SPEX-8000D at 2 at.% TaB<sub>2</sub>** doped MgB<sub>2</sub>. Note: All physical parameters shown were obtained for the post-HIP samples.

Ball milling time (minutes)	Composition	Average crystallite size (nm)	Lattice constants (Å)			c/a	Strain Post-HIP
			A	B	c		
60	86.0 wt.% MgB <sub>2</sub>	40.74	3.0813	-	3.5209	1.1426	0.001379
	5.2 wt.% TaB <sub>2</sub>	50.14	3.0773	-	3.2554	1.0578	0.001136
	7.1 wt.% MgO	34.79	4.2118	-	-	-	0.001016
	1.7 wt.% MgB <sub>4</sub>	99.77	5.4639	4.4281	7.4722	-	0.000147
120	78.4 wt.% MgB <sub>2</sub>	26.94	3.0792	-	3.5203	1.1432	0.001454
	5.7 wt.% TaB <sub>2</sub>	51.38	3.0736	-	3.2569	1.0596	0.001644
	7.5 wt.% MgO	33.35	4.2090	-	-	-	0.001610
	8.4 wt.% MgB <sub>4</sub>	75.69	5.4534	4.3839	7.4372	-	0.000791
300	88.8 wt.% MgB <sub>2</sub>	43.65	3.0819	-	3.5218	1.1427	0.001106
	5.7 wt.% TaB <sub>2</sub>	42.74	3.0779	-	3.2563	1.0579	0.001065
	5.6 wt.% MgO	25.57	4.2136	-	-	-	0.001239
600	84.4 wt.% MgB <sub>2</sub>	37.03	3.0796	-	3.5229	1.1439	0.000935
	6.0 wt.% TaB <sub>2</sub>	33.39	3.0871	-	3.2383	1.0489	0.000763
	8.7 wt.% MgO	31.12	4.2121	-	-	-	0.001670
	0.9 wt.% MgB <sub>4</sub>	38.62	5.4187	4.4359	7.4831	-	0.001164
2400	80.7 wt.% MgB <sub>2</sub>	38.43	3.0803	-	3.5212	1.1431	0.000200
	5.8 wt.% TaB <sub>2</sub>	23.03	3.0899	-	3.2388	1.0481	0.001141
	13.5 MgO	34.73	4.2162	-	-	-	0.002776

**Table 6.2** Lattice constants, average crystallite-size and strain analyses based on Rietveld Analyses using Power Cell Program for the **SPEX-8000D at 5 at.% TaB<sub>2</sub>** doped MgB<sub>2</sub>. Note: All physical parameters shown were obtained for the post-HIP samples.

Ball milling time (minutes)	Composition	Average crystallite size (nm)	Lattice constants (Å)			c/a	Strain
			A	b	c		
60	77.7 wt.% MgB <sub>2</sub>	36.93	3.0737	-	3.5346	1.1499	0.002135
	14.3 wt.% TaB <sub>2</sub>	44.35	3.0782	-	3.2551	1.0574	0.000658
	4.9 wt.% MgO	56.95	4.2112	-	-	-	0.000978
	3.1 wt.% MgB <sub>4</sub>	63.78	5.4626	4.4219	7.4655	-	0.000432
120	66.9 wt.% MgB <sub>2</sub>	19.74	3.0769	-	3.5412	1.1508	0.001445
	14.2 wt.% TaB <sub>2</sub>	38.86	3.0833	-	3.2583	1.0567	0.000399
	7.0 wt.% MgO	35.46	4.2178	-	-	-	0.001670
	11.9 wt.% MgB <sub>4</sub>	3.21	7.3723	4.3283	7.3723	-	0.000769
300	81.0 wt.% MgB <sub>2</sub>	33.58	3.0813	-	3.5401	1.1488	0.000128
	13.2 wt.% TaB <sub>2</sub>	34.77	3.0866	-	3.2552	1.0546	0.000541
	5.8 wt.% MgO	20.07	4.2199	-	-	-	0.001836
600	75.1 wt.% Mg <sub>2</sub>	29.95	3.0813	-	3.5203	1.1424	0.000718
	13.5 wt.% TaB <sub>2</sub>	36.82	3.0746	-	3.2582	1.0597	0.001408
	9.7 wt.% MgO	61.88	4.2133	-	-	-	0.004367
	1.7 wt.% MgB <sub>4</sub>	47.21	5.4514	4.4460	7.4979	-	0.000835
2400	71.5 wt.% MgB <sub>2</sub>	35.20	3.0767	-	3.5168	1.1430	0.000491
	14.5 wt.% TaB <sub>2</sub>	20.11	3.0849	-	3.2363	1.0490	0.001351
	14.0 wt.% MgO	23.30	4.2088	-	-	-	0.002451

Table 6.3 Lattice constants, average crystallite-size and strain analyses based on Rietveld Analyses using Power Cell Program for the **Pulverisette-4 processed material at 800 rpm using 2 at.% TaB<sub>2</sub> doped MgB<sub>2</sub>**. Note: All physical parameters shown were obtained for the post-HIP samples.

Ball milling time (minutes)	Composition	Average crystallite size (nm)	Lattice constants (Å)			c/a	Strain
			A	B	c		
60	92.7 wt.% MgB <sub>2</sub>	44.91	3.0822	-	3.5198	1.1419	0.000639
	4.3 wt.% TaB <sub>2</sub>	51.62	3.0777	-	3.2542	1.0573	0.000653
	2.9 wt.% MgO	35.98	4.2103	-	-	-	0.000265
120	91.6 wt.% MgB <sub>2</sub>	46.46	3.0818	-	3.5219	1.1428	0.000746
	4.8 wt.% TaB <sub>2</sub>	48.55	3.0781	-	3.2551	1.0575	0.000345
	3.6 wt.% MgO	45.23	4.2119	-	-	-	0.000911
300	92.4 wt.% MgB <sub>2</sub>	48.63	3.0829	-	3.5223	1.1425	0.001045
	4.8 wt.% TaB <sub>2</sub>	55.05	3.0787	-	3.2560	1.0575	0.001112
	2.8 wt.% MgO	34.69	4.2123	-	-	-	0.000966
600	92.3 wt.% MgB <sub>2</sub>	41.96	3.0796	-	3.5217	1.1435	0.000655
	5.0 wt.% TaB <sub>2</sub>	39.37	3.0886	-	3.2352	1.0474	0.000320
	2.6 wt.% MgO	42.83	4.2109	-	-	-	0.000605
2400	90.9 wt.% MgB <sub>2</sub>	49.99	3.0818	-	3.5228	1.1430	0.001044
	5.0 wt.% TaB <sub>2</sub>	54.86	3.0913	-	3.2373	1.0472	0.000771
	4.1 wt.% MgO	40.78	4.2133	-	-	-	0.000377

Table 6.4 Lattice constants, average crystallite-size and strain analyses based on Rietveld Analyses using Power Cell Program for the **Pulverisette-4 processed material at 1200 rpm using 2 at.% TaB<sub>2</sub> doped MgB<sub>2</sub>**. Note: All physical parameters shown were obtained for the post-HIP samples.

Ball milling time (minutes)	Composition	Average crystallite size (nm)	Lattice constants (Å)			c/a	Strain
			A	B	c		
60	91.4 wt.% MgB <sub>2</sub>	45.76	3.0822	-	3.5220	1.1426	0.000669
	4.3 wt.% TaB <sub>2</sub>	45.83	3.0922	-	3.2351	1.0462	0.000561
	3.2 wt.% MgO	33.82	4.2119	-	-	-	0.000759
	1.1 wt.% MgB <sub>4</sub>	100.66	5.4690	4.4269	7.4731	-	0.000335
120	92.1 wt.% MgB <sub>2</sub>	40.21	3.0803	-	3.5218	1.1433	0.001153
	4.8 wt.% TaB <sub>2</sub>	43.27	3.0899	-	3.2342	1.0467	0.000334
	3.1 wt.% MgO	31.28	4.2068	-	-	-	0.001010
300	85.8 wt.% MgB <sub>2</sub>	45.95	3.0799	-	3.5236	1.1440	0.001542
	5.5 wt.% TaB <sub>2</sub>	49.49	3.0896	-	3.2380	1.0480	0.000611
	4.0 wt.% MgO	41.91	4.2120	-	-	-	0.000933
	4.7 wt.% MgB <sub>4</sub>	40.64	5.4645	4.3998	7.4460	-	0.000972
600	85.1 wt.% MgB <sub>2</sub>	37.53	3.0791	-	3.5216	1.1437	0.000926
	5.7 wt.% TaB <sub>2</sub>	53.19	3.0885	-	3.2363	1.0478	0.001181
	5.1 wt.% MgO	28.00	4.2104	-	-	-	0.001240
	4.1 wt.% MgB <sub>4</sub>	17.60	5.4580	4.4197	7.4198	-	0.001885
2400	88.0 wt.% MgB <sub>2</sub>	46.66	3.0812	-	3.5231	1.1434	0.001155
	5.3 wt.% TaB <sub>2</sub>	54.94	3.0911	-	3.2359	1.0468	0.000806
	5.5 wt.% MgO	32.97	4.2120	-	-	-	0.000710
	1.1 wt.% MgB <sub>4</sub>	30.90	5.4195	4.4649	7.4728	-	0.001546

**Table 6.5** Lattice constants, average crystallite-size and strain analyses based on Rietveld Analyses using Power Cell Program for the **Pulverisette-4 processed material at 800 rpm using 5 at.% TaB<sub>2</sub> doped MgB<sub>2</sub>**. Note: All physical parameters shown were obtained for the post-HIP samples.

Ball milling time (minutes)	Composition	Average crystallite size (nm)	Lattice constants (Å)			c/a	Strain
			A	B	c		
60	80.0 wt.% MgB <sub>2</sub>	43.52	3.0830	-	3.5195	1.1415	0.000715
	10.4 wt.% TaB <sub>2</sub>	51.90	3.0780	-	3.2542	1.0572	0.000865
	4.0 wt.% MgO	65.76	4.2117	-	-	-	0.001135
	6.6 wt.% MgB <sub>4</sub>	7.12	5.5641	4.3283	7.3723	-	0.006715
120	79.7 wt.% MgB <sub>2</sub>	33.93	3.0821	-	3.5202	1.1421	0.000932
	10.1 wt.% TaB <sub>2</sub>	48.81	3.0777	-	3.2565	1.0580	0.001025
	2.3 wt.% MgO	28.35	4.2089	-	-	-	0.001155
	7.9 wt.% MgB <sub>4</sub>	14.14	5.4589	4.4137	7.4276	-	0.002864
300	85.9 wt.% MgB <sub>2</sub>	43.45	3.0833	-	3.5184	1.1411	0.000720
	11.5 wt.% TaB <sub>2</sub>	49.52	3.0769	-	3.2547	1.0577	0.000745
	2.3 wt.% MgO	87.31	4.2116	-	-	-	0.000408
	0.3 wt.% MgB <sub>4</sub>	43.08	5.5055	4.3729	7.5723	-	0.001580
600	86.4 wt.% MgB <sub>2</sub>	38.10	3.0833	-	3.5191	1.1413	0.001668
	11.0 wt.% TaB <sub>2</sub>	48.94	3.0785	-	3.2514	1.0561	0.001055
	2.6 wt.% MgO	62.08	4.2092	-	-	-	0.001187
2400	79.9wt.% MgB <sub>2</sub>	45.13	3.0831	-	3.5262	1.1437	0.000833
	12.6 wt.% TaB <sub>2</sub>	59.87	3.0946	-	3.2383	1.0464	0.001016
	4.4 wt.% MgO	45.61	4.2155	-	-	-	0.000967
	3.1 wt.% MgB <sub>4</sub>	40.05	5.4916	4.4279	7.4475	-	0.001110

**Table 6.6** Lattice constants, average crystallite-size and strain analyses based on Rietveld Analyses using Power Cell Program for the **Pulverisette-4 processed material at 1200rpm using 5 at.% TaB<sub>2</sub> doped MgB<sub>2</sub>**. Note: All physical parameters shown were obtained for the post-HIP samples.

Ball milling time (minutes)	Composition	Average crystallite size (nm)	Lattice constants (Å)			c/a	Strain
			A	B	c		
60	77.9 wt.% MgB <sub>2</sub>	40.10	3.0821	-	3.5256	1.1438	0.001016
	10.9 wt.% TaB <sub>2</sub>	48.60	3.0926	-	3.2386	1.0472	0.000932
	4.4 wt.% MgO	21.96	4.2195	-	-	-	0.000969
	6.8 wt.% MgB <sub>4</sub>	28.58	5.5062	4.4022	7.4265	-	0.001424
120	80.1 wt.% MgB <sub>2</sub>	51.91	3.0858	-	3.5231	1.1417	0.001027
	12.3 wt.% TaB <sub>2</sub>	58.20	3.0971	-	3.2371	1.0452	0.000761
	6.2 wt.% MgO	26.18	4.2266	-	-	-	0.002304
	1.4 wt.% MgB <sub>4</sub>	19.94	5.5506	4.4388	7.3723	-	0.002909
300	82.1 wt.% MgB <sub>2</sub>	39.96	3.0854	-	3.5273	1.1432	0.000756
	12.8 wt.% TaB <sub>2</sub>	52.35	3.0957	-	3.2371	1.0456	0.000948
	5.1 wt.% MgO	20.40	4.2207	-	-	-	0.001035
600	76.5 wt.% MgB <sub>2</sub>	34.85	3.0799	-	3.5249	1.1444	0.000895
	12.8 wt.% TaB <sub>2</sub>	47.55	3.0898	-	3.2381	1.0479	0.000725
	4.7wt.% MgO	27.91	4.2140	-	-	-	0.000323
	6.0 wt.% MgB <sub>4</sub>	74.54	5.4563	4.4189	7.4365	-	0.002400
2400	84.4 wt.% MgB <sub>2</sub>	38.62	3.0870	-	3.5278	1.1427	0.000653
	12.9 wt.% TaB <sub>2</sub>	57.08	3.0972	-	3.2386	1.0456	0.001019
	2.8 wt.% MgO	53.94	4.2159	-	-	-	0.000479

**Table 6.7** Lattice constants, average crystallite-size and strain analyses based on Rietveld Analyses using Power Cell Program for MgB<sub>2</sub> and TaB<sub>2</sub> raw no milling material, respectively. Note: All physical parameters shown were obtained for the post-HIP samples.

Ball milling condition & TaB <sub>2</sub> at. %	Composition	Average crystallite size (nm)	Lattice constants (Å)			c/a	Strain
			a	b	c		
MgB <sub>2</sub> raw (Durval)	98.4wt. % MgB <sub>2</sub> 1.6wt. % MgO	97.01	3.0880 4.2342	- -	3.5241	1.1421	0.001855
TaB <sub>2</sub> raw (Durval)	100wt TaB <sub>2</sub>	73.90	3.1006	-	3.2294	1.0415	0.000403

### 6.1.2 Scanning Electron Microscope (SEM) measurements

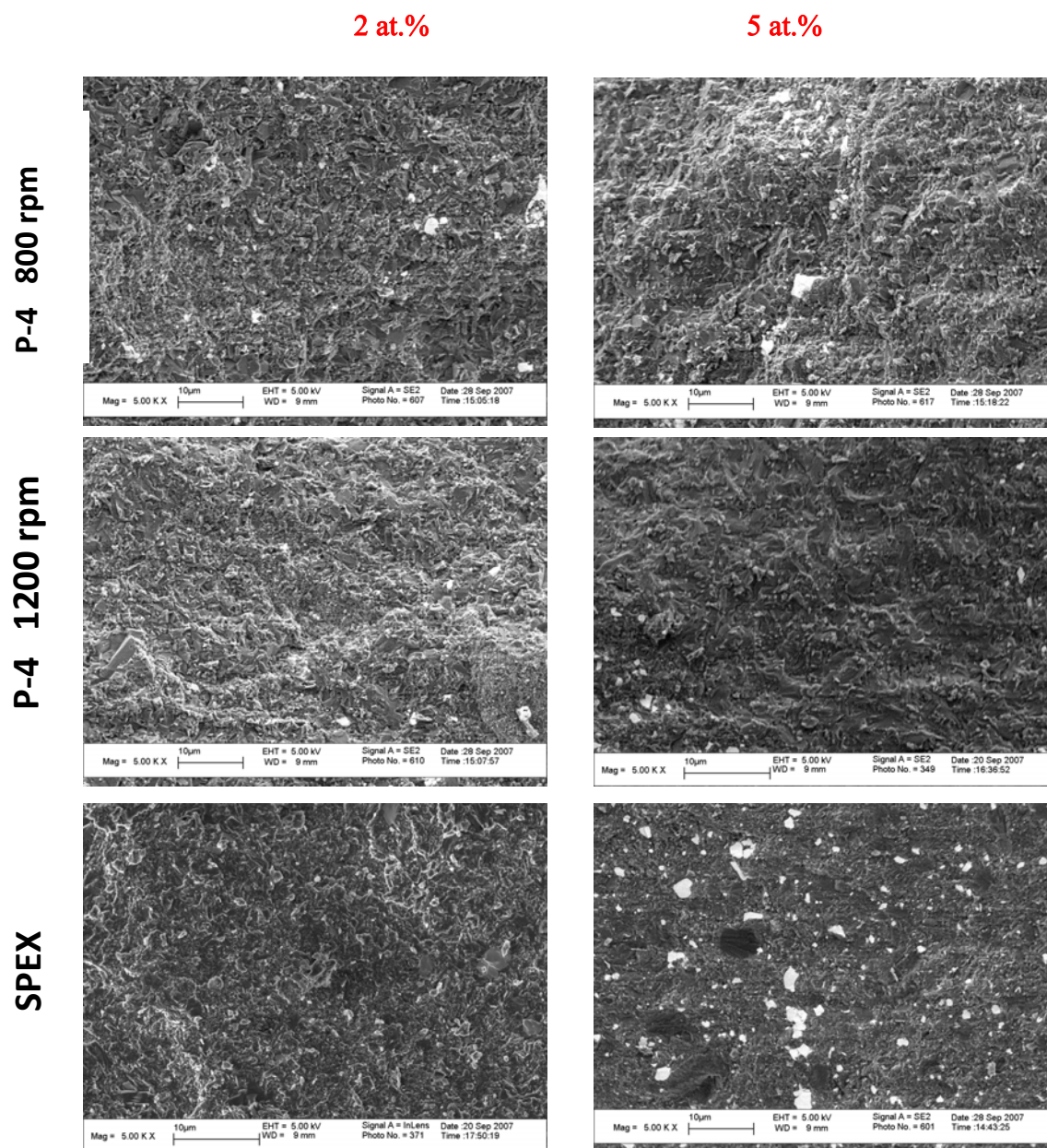


Figure 6.21.a Scanning Electron Microscope (SEM) of TaB<sub>2</sub> doped MgB<sub>2</sub> post HIP processed material. All micrographs belong to 60 minutes ball milled material at 2 at.% and 5 at.%.

Figure 6.21.a shows SEM micrographs of 60 minutes milling for  $\text{MgB}_2 + \text{XTaB}_2$ .  $X = 2$  and 5 at.%. The surface in the micrograph seems to be similar for all the samples except for SPEX processed at 5 at.%  $\text{TaB}_2$  doped  $\text{MgB}_2$ , lower right corner. In this micrograph is possible to distinguish between white, black and grain zones.

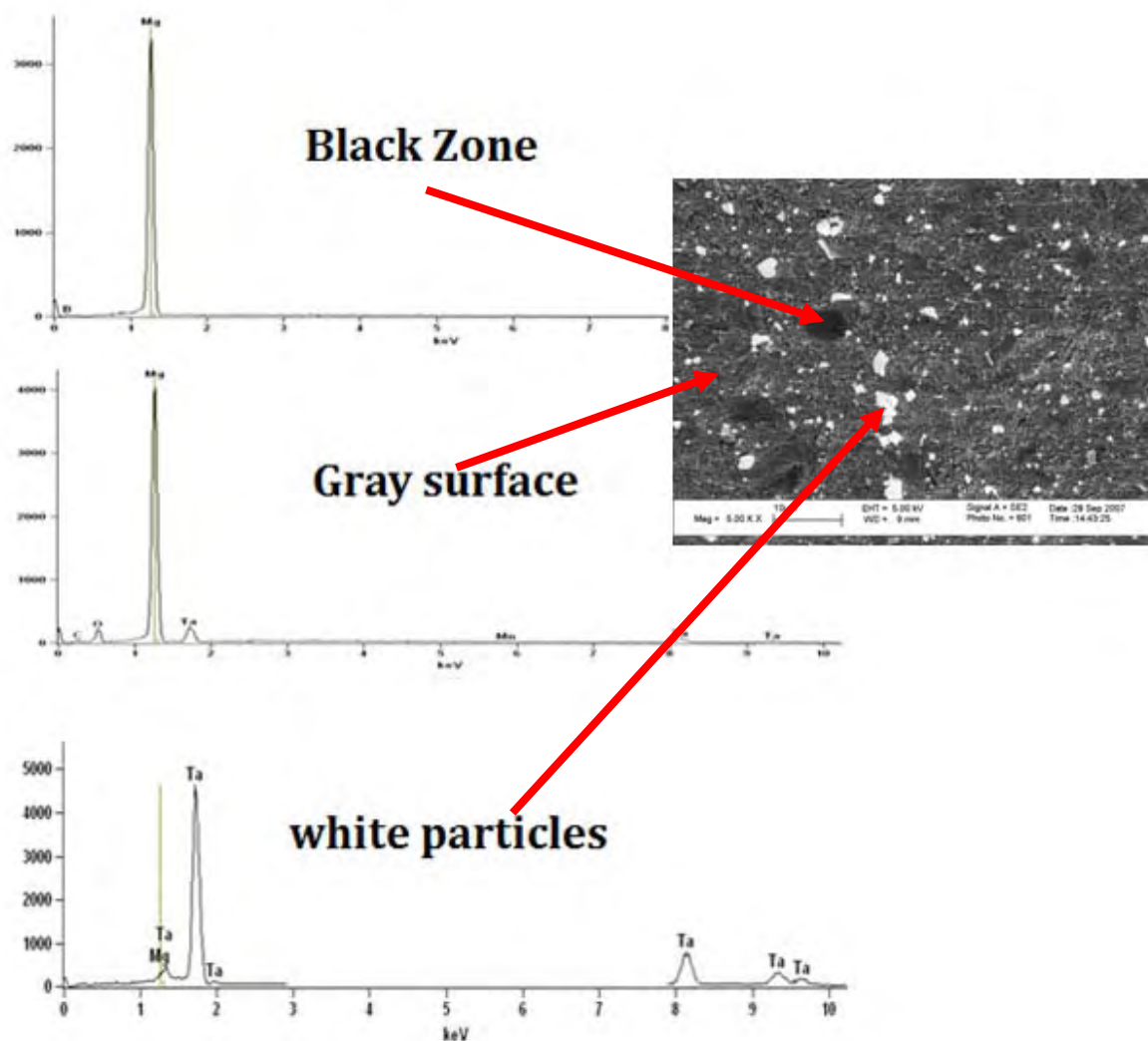


Figure 6.21.b Electelectron diffraction scattering (EDS) of the micrograph for SPEX processed material at 5 at.% during 60 minutes. Micrograph shown in Figure 6.21. a.

In Figure 6.21.b, is possible to identify different phases in the micrograph. Gray region, represent the matrix of  $\text{MgB}_2$ . Some  $\text{MgO}$  and Carbon content are present. Black regions correspond to a high concentration of Magnesium. White average crystallites are  $\text{TaB}_2$  phases in the material. Apart of the secondary phases in the material, not to many information, as intra and inter grain  $\text{TaB}_2$  positions, were obtained from the micrograph. Further investigation on the SEM, at higher magnification, need to be address as well as a transmission electron micrograph analysis.

### *6.1.3 Critical current density ( $J_c$ ) measurements as a function of applied magnetic field.*

The critical current density in a material is derived from the magnetization loops. This magnetization is generated from the applied magnetic field ( $\mu_0 H$ ) variation at 4.2 K for this work. Higher  $J_c$  values can be observed at the lower  $\mu_0 H$  and lower ones as  $\mu_0 H$  increase. A geometrical shape of the sample is needed, in way to extract  $J_c$  values. The electrons confined in the geometrical shape sample must responses to  $\mu_0 H$ . The response of electrons to the  $\mu_0 H$ , generates current loops in the sample. This current loop must generate an induce magnetic field opposite to the  $\mu_0 H$  in way to remain it superconducting properties. This is better explained in Chapter 3 section 3.2.1.

In granular superconductors, such as  $\text{MgB}_2$  and  $\text{Nb}_3\text{Sn}$ , the magnitude of the current loop will depend on the grain connectivity. In this way higher current density shows higher amount of grain connection.

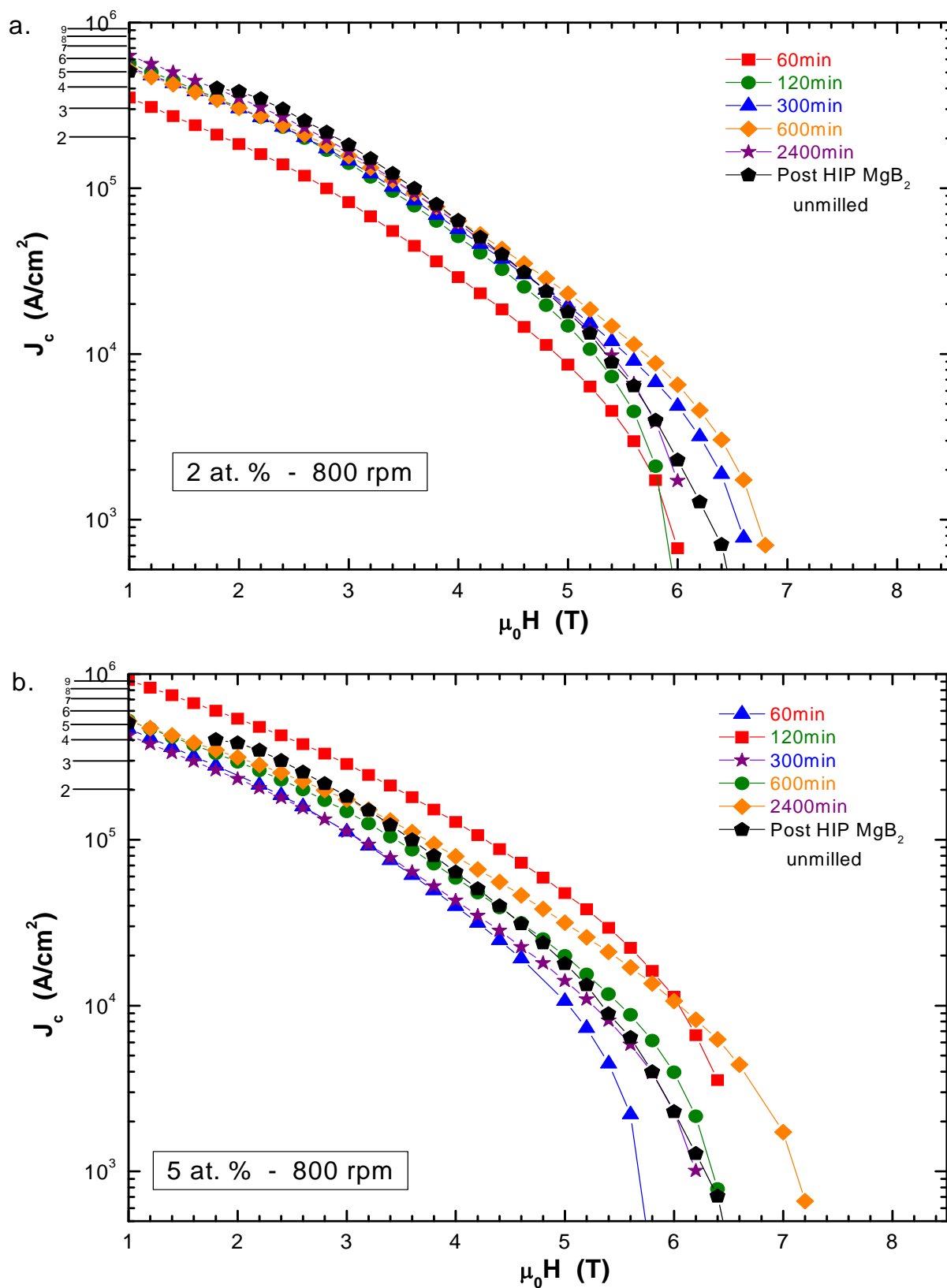


Figure 6.22 Critical current density ( $J_c$ ) as a function of applied magnetic field ( $\mu_0 H$ ) post HIP Pulverisette-4 processed material at 800 rpm. **a. 2 at.% and b 5 at.% TaB<sub>2</sub> doped MgB<sub>2</sub>.**

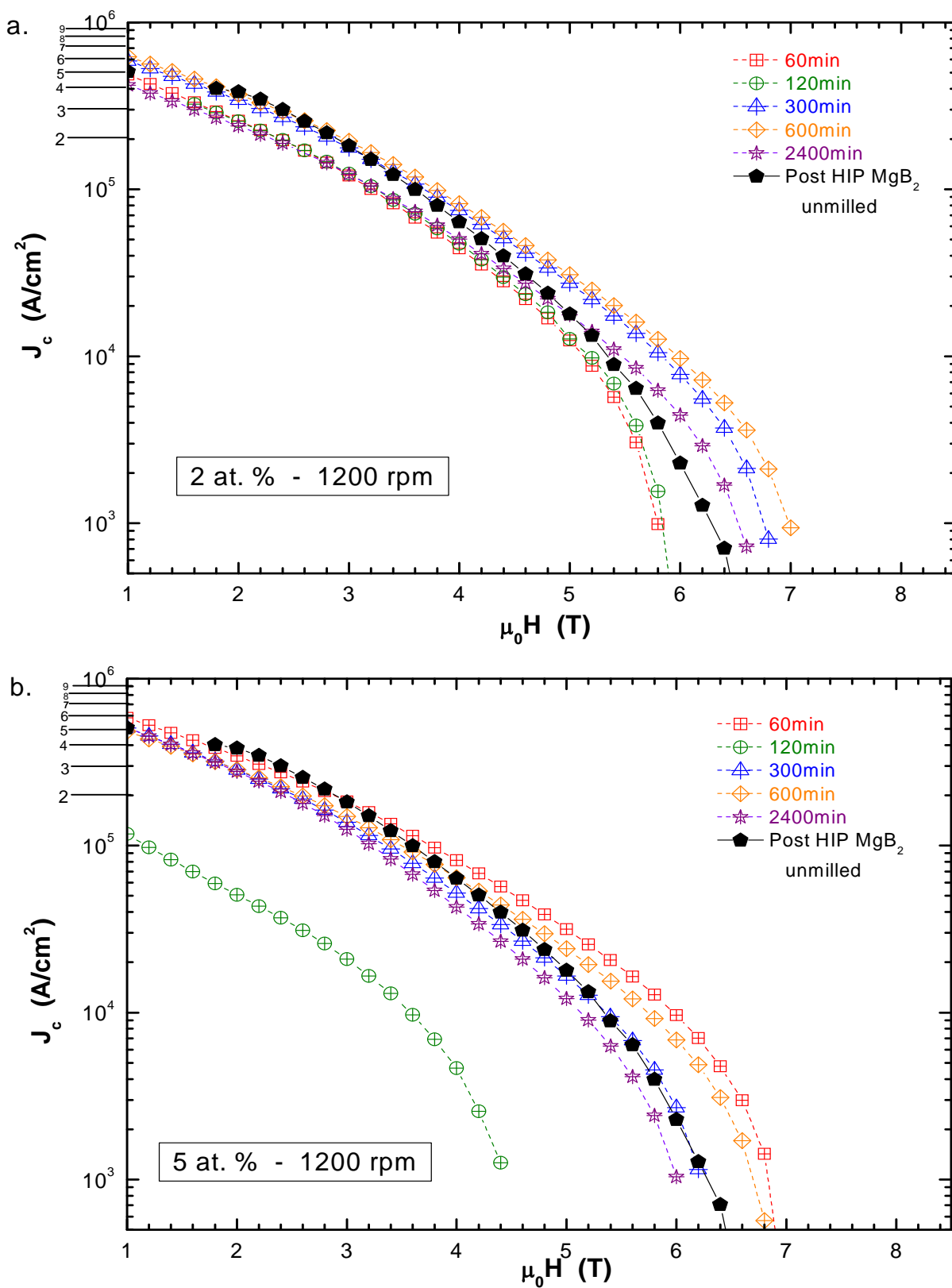


Figure 6.23 Critical current density ( $J_c$ ) as a function of applied magnetic field ( $\mu_0 H$ ) post HIP Pulverisette-4 processed material at 1200 rpm. **a. 2 at.% and b 5 at.% TaB<sub>2</sub> doped MgB<sub>2</sub>.**

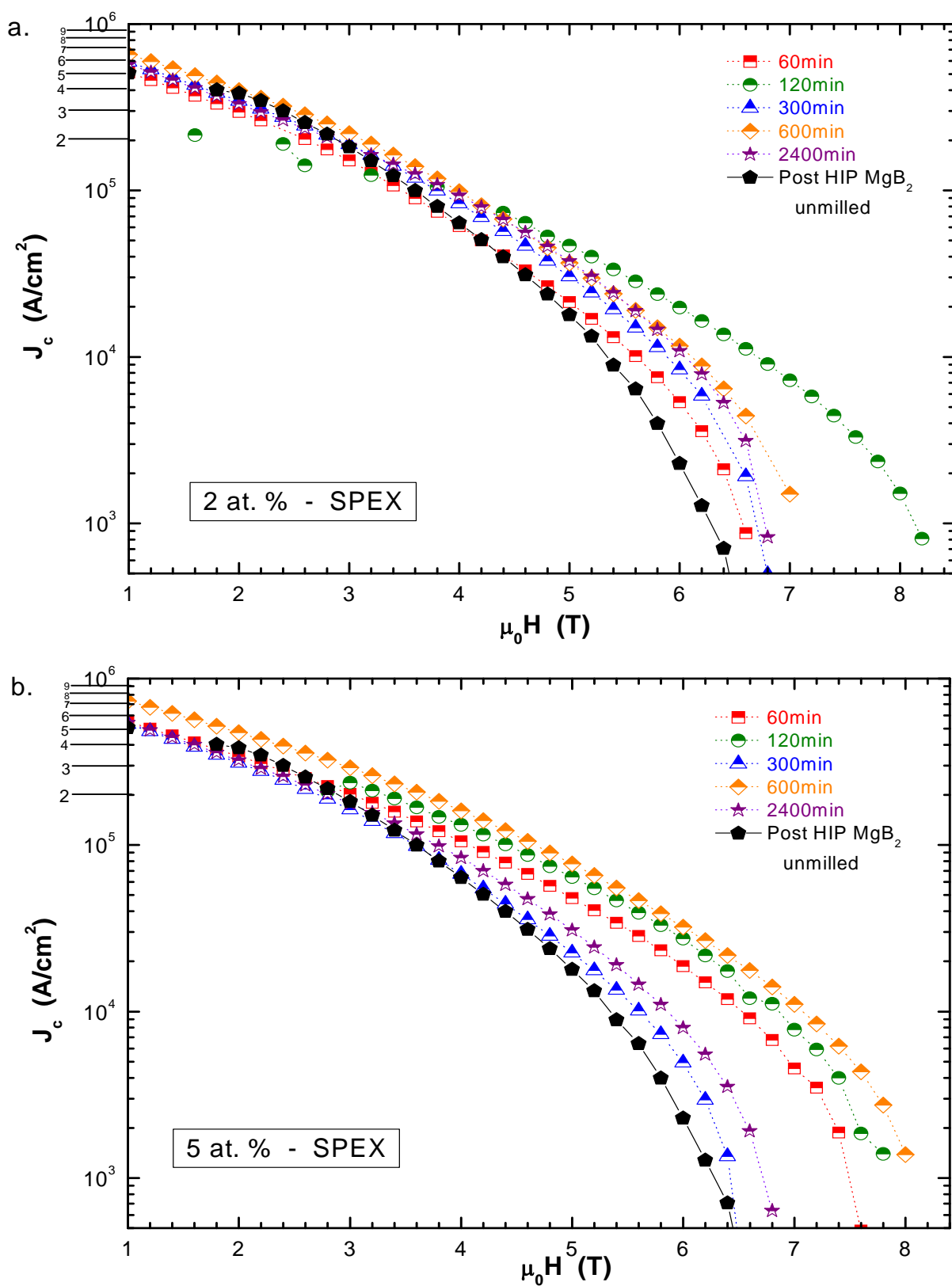


Figure 6.24 Critical current density ( $J_c$ ) as a function of applied magnetic field ( $\mu_0 H$ ) post HIP SPEX processed material. **a.** 2 at.% and **b** 5 at.%  $\text{TaB}_2$  doped  $\text{MgB}_2$ .

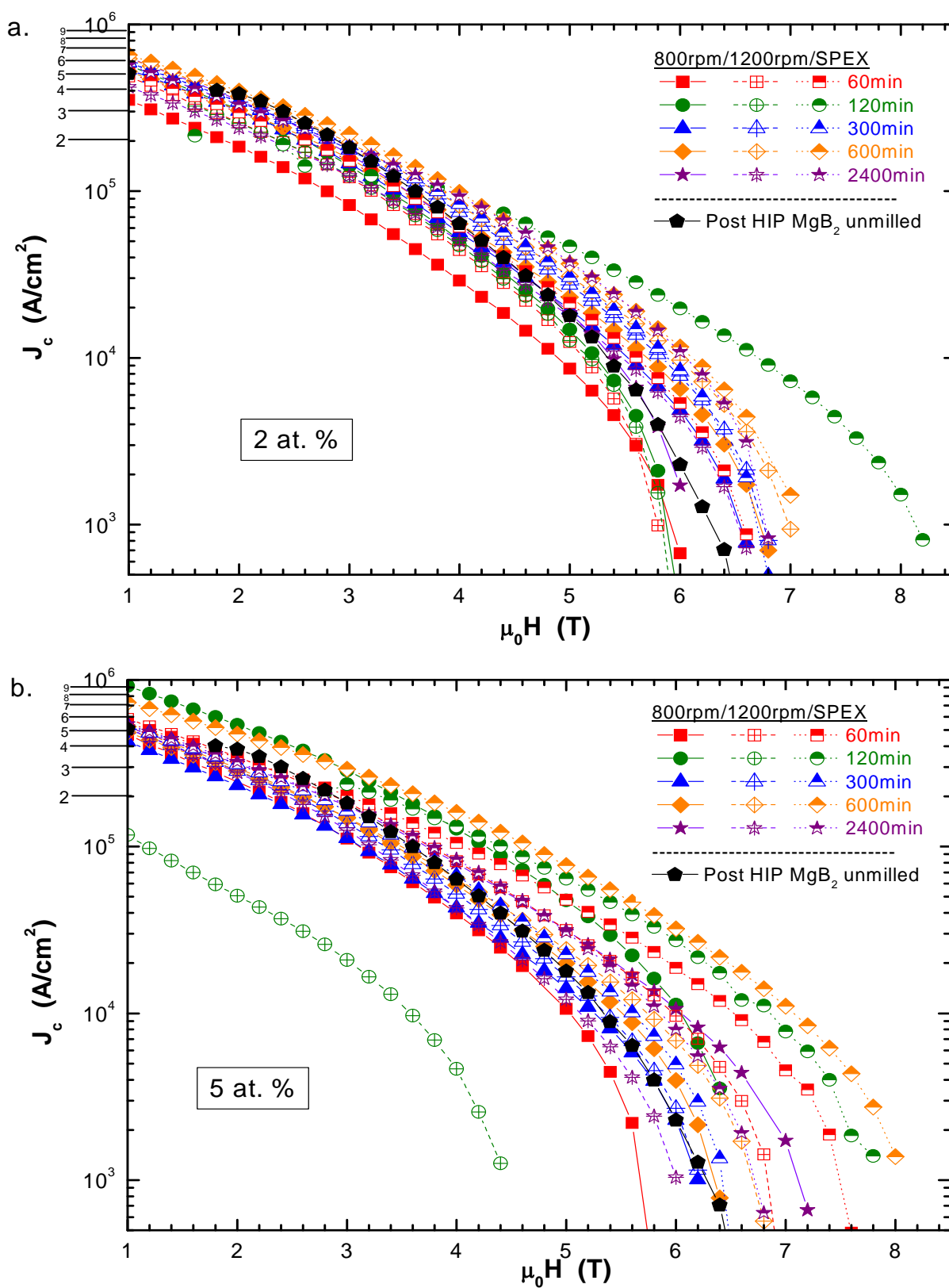


Figure 6.25 Overall comparison of critical current density ( $J_c$ ) as a function of applied magnetic field ( $\mu_0 H$ ) for post HIP  $TaB_2$  doped  $MgB_2$  SPEX and Pulverisette-4 ball millings for (a) 2 at.% and (b) 5 at.% doped levels.

Figure 6.25 (a) and 6.25 (b) shown the  $J_c$  as a function of applied magnetic field for the 2 at.% and 5 at.% TaB<sub>2</sub> doped MgB<sub>2</sub>, respectively, under the processing conditions outlined in the in-sets. The data in Figure 6.25 (a) and 6.25 (b) exhibited the same TaB<sub>2</sub> type of general trend. The 120 minutes processed material shown in Figure 6.25 (a) exhibited the  $J_c$  values in the highest applied magnetic field ( $\mu_0H = 8.2$  T) while the Pulverisette-4 processed material (corresponding to 1200 rpm for 120 minutes at 5 at.%), showed in Figure 6.25 (b), had the least  $J_c(4.2$  K, 4.4 T) = 1.26 kA/cm<sup>2</sup>. Compared to Figure 6.25 (b) it is evident that the 5 at.% TaB<sub>2</sub> doped MgB<sub>2</sub> exhibited high  $J_c$  at magnetic fields. From Figure 6.22 to 6.24, the higher  $J_c$  values are observed for SPEX processed materials compared with Pulverisette-4 processed materials. At this parameters, 5 at.% TaB<sub>2</sub> doped MgB<sub>2</sub> shows higher  $J_c$  values compared with 2 at.%, as shown in Table 6.8 and Table 6.9 at 5T, respectively. Figure 6.25 (b) shows, for SPEX processed material, that as the milling time increase, 60,120 and 600 minutes,  $J_c(4.2$  K, 5 T) = 48.1, 64.4 and 77.3 kA/cm<sup>2</sup> increase, respectively. It is not valid for 300 minutes and 2400 minutes in the SPEX at 5 at.%, in which  $J_c$  values reduce, shown in Table 6.9.

Pulverisette-4 processed material showed an increase in  $J_c$  values not at the range of SPEX processed material  $J_c$ . The highest  $J_c$  values is obtained at 800 rpm for 120 minutes at 5 at.%,  $J_c(4.2$  K, 5 T) = 47.7 kA/cm<sup>2</sup>, which average crystallite size of MgB<sub>2</sub> phase is the lower one reached for Pulverisette-4 processed material as shown in Figure 6.14. At 2 at.%, Figure 6.25 (a), 60 minutes ball milling shows the lower  $J_c$  values at 800 rpm, 1200 rpm and SPEX milling condition,  $J_c(4.2$  K, 5 T) = 8.6, 12.4 and 21.3 kA/cm<sup>2</sup>, respectively. Different behavior is found at 5 at.% for 1200 rpm in the Pulverisette-4, Figure 6.25 (b), which as the milling time increase  $J_c$  decrease. Figure 6.25 (b) is similar to Figure 6.25 (a), referred to the 5 at.% TaB<sub>2</sub> doped MgB<sub>2</sub> materials, showed comparable trend with respect to decreasing  $J_c$  with increasing  $\mu_0H$ . In marked contrast to the 2 at.% TaB<sub>2</sub> doped MgB<sub>2</sub>, the

extent of overlap between the SPEX-8000D and Pulverisette-4 processed materials was smaller for 5 at.% TaB<sub>2</sub> doped MgB<sub>2</sub> materials. According to Senkowicz [5], the correlation of the variation of  $J_c$  with the milling time was not well defined.

In general, the SPEX-8000D processed materials exhibited highest  $J_c$  values in the 6.5 T to 8.2 T  $\mu_0H$  ranges, which were higher than the corresponding Pulverisette-4 ball milled materials whose values ranged from 5.7 T to 7.2 T. In both cases, one noticed increased  $J_c$  for increased ball milling time. Additionally, the incorporation of 2 at.% compared with 5 at.% of TaB<sub>2</sub> in MgB<sub>2</sub> has an effect on  $J_c$ . The incorporation of TaB<sub>2</sub> doped MgB<sub>2</sub> will help in the introduction of magnetic flux in the material.

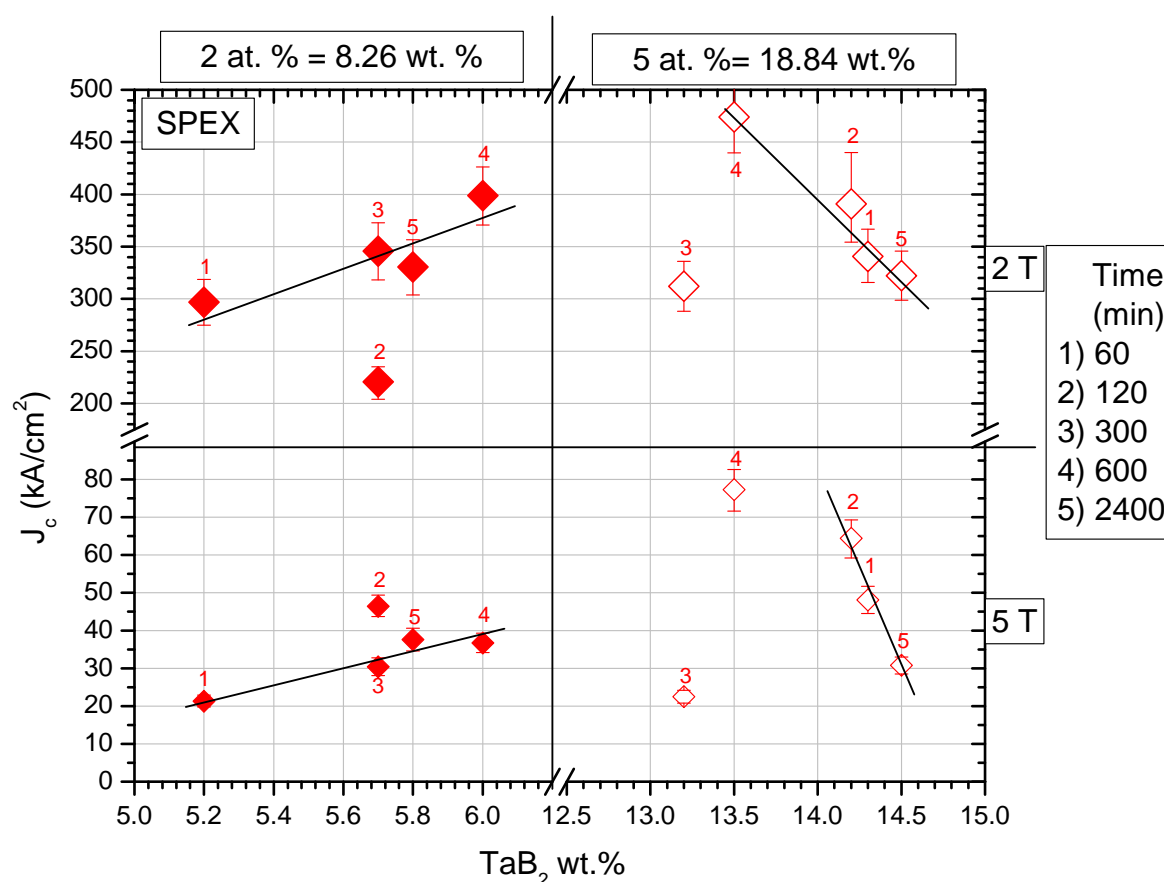


Figure 6.26  $J_c$  as a function of TaB<sub>2</sub> wt.% in the MgB<sub>2</sub> matrix. Data are extracted from  $J_c(4.2K)$  at 2 and 5 T from 2 and 5 at.% SPEX processed material.

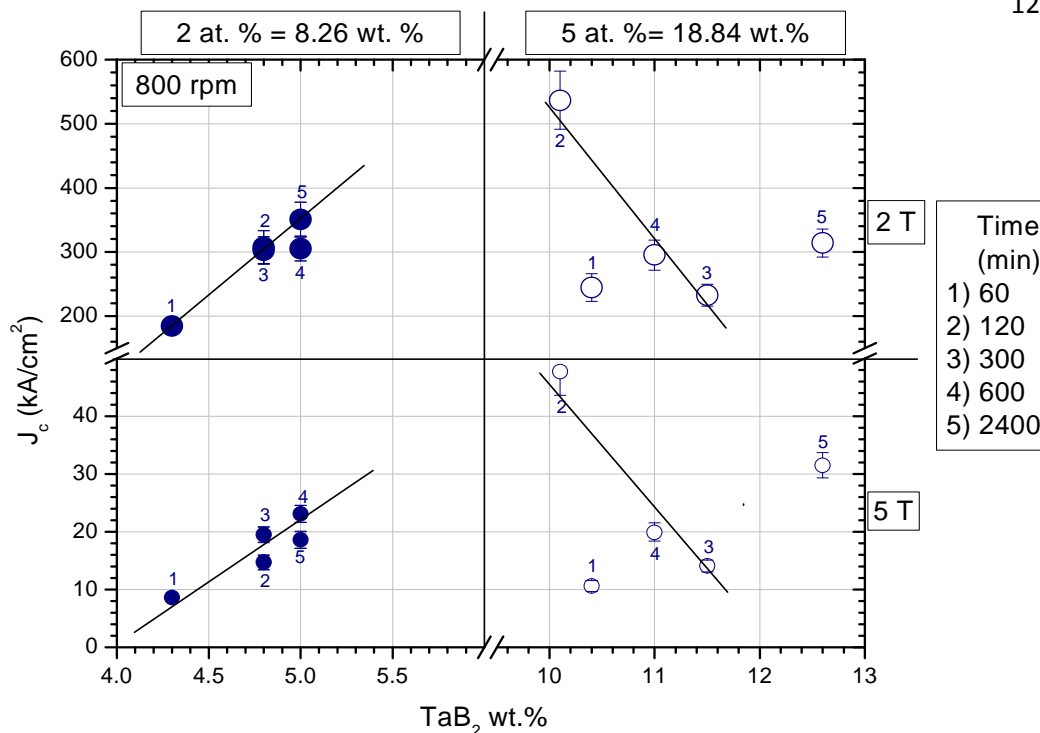


Figure 6.27  $J_c$  as a function of TaB<sub>2</sub> wt.% in the MgB<sub>2</sub> matrix. Data are extracted from  $J_c(4.2K)$  at 2 and 5 T from 2 and 5 at.% of Pulverisette-4 processed material at 800 rpm.

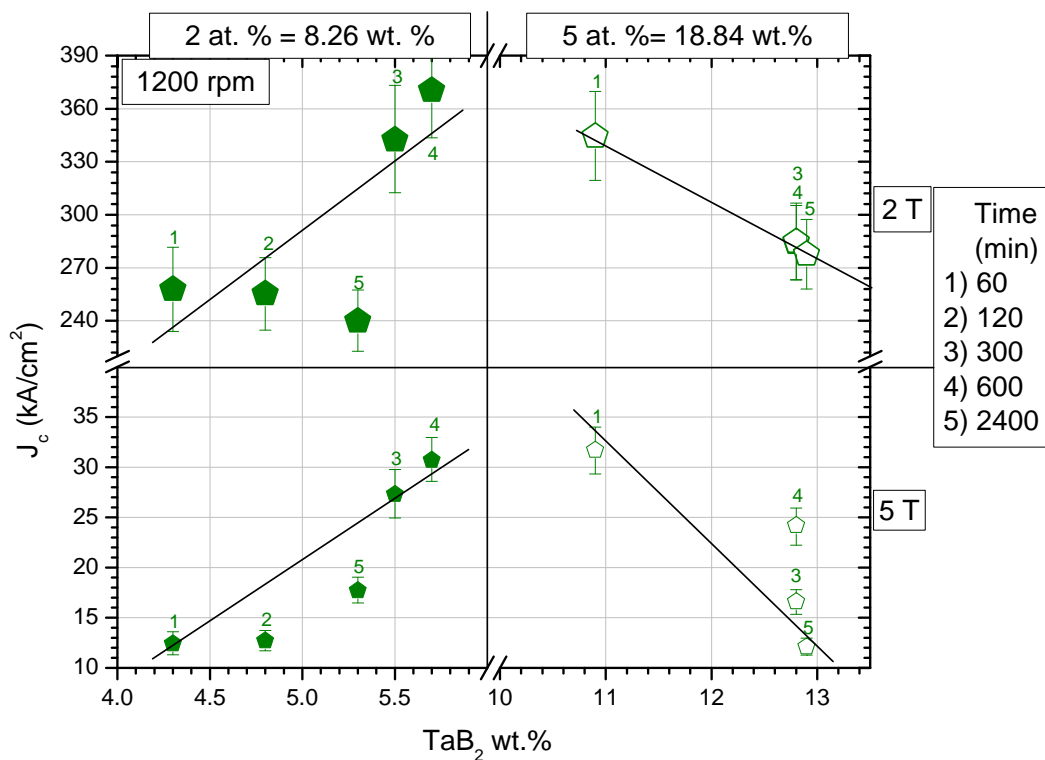
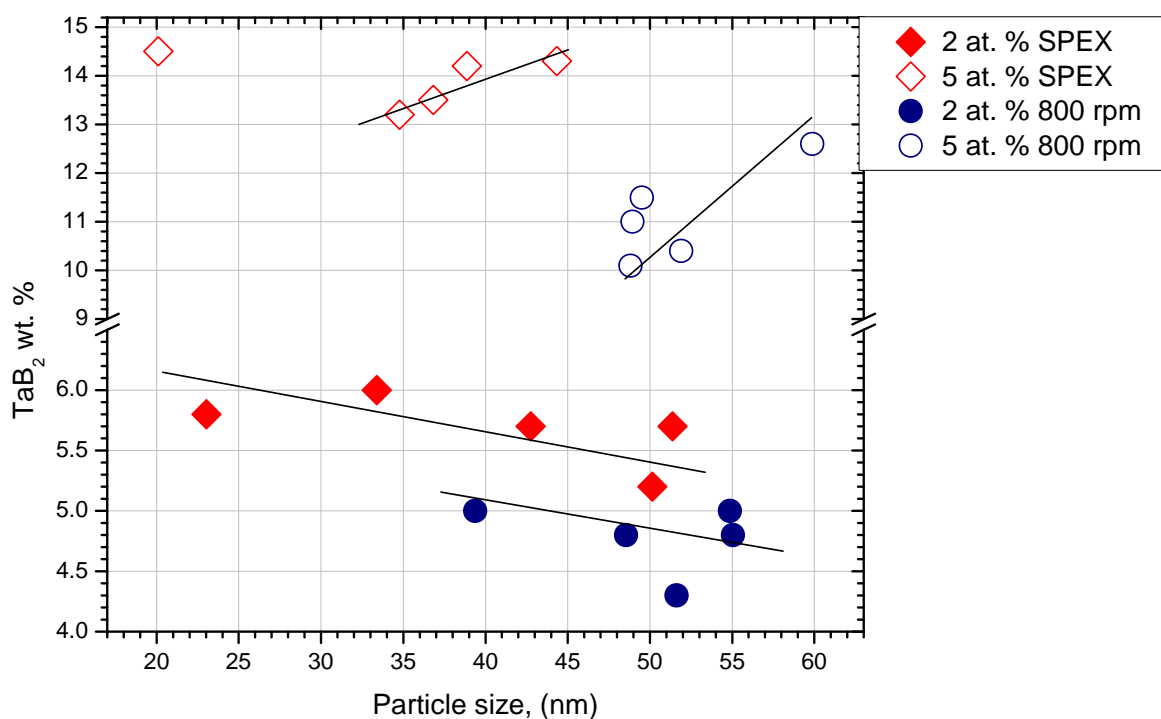


Figure 6.28  $J_c$  as a function of TaB<sub>2</sub> wt.% in the MgB<sub>2</sub> matrix found from Rietveld analyses. Data are extracted from  $J_c(4.2K)$  at 2 and 5 T from 2 and 5 at.% of Pulverisette-4 processed material at 1200 rpm.

From Figure 6.26 to Figure 6.28 the effect  $\text{TaB}_2$  wt. percent present in the matrix of  $\text{MgB}_2$  to the  $J_c$  values at 2 and 5 T is shown. The  $\text{TaB}_2$  values are tabulated in Tables 6.1 to 6.8 and are graphically shown in Figure 6.20. A close linear representation is observed of an increase of  $J_c$  as a function of  $\text{TaB}_2$  for all SPEX and Pulverisette-4 material processed in the 2 at. %. Inversely, a decrease is observed for the 5 at.%  $\text{TaB}_2$  doped  $\text{MgB}_2$ . Therefore, between 2 and 5 at.%  $\text{TaB}_2$  doped  $\text{MgB}_2$  a maximum of  $J_c$  values must be found. Then, the improvement of  $J_c$  can be related to the  $\text{TaB}_2$  incorporation. This incorporation, as was the suggestion is Chapter 2, must be around grain boundaries or inside them. TEM measurements need to be done to support this suggestion.



**Figure 6.29**  $\text{TaB}_2$  wt. % as a function of the  $\text{TaB}_2$  average crystallite size. Data plot for 2 and 5 at.% for SPEX and Pulverisette-4 at 800 rpm processed material.

In the SPEX processed material, the high  $J_c$  values with high TaB<sub>2</sub> wt.%, from Figure 6.26 and 6.27, correspond to the lower average crystallite size as shown in Figure 6.29. TaB<sub>2</sub> average crystallites decrease as the composition of TaB<sub>2</sub> wt. % increase, as is the case of 2 at. %. Inversely, for 5 at.%, which average crystallite size increase as the amount of TaB<sub>2</sub> in the material increase. The higher value of  $J_c(4.2k, 5 T) = 46.4 \text{ kA/cm}^2$  at 2 at. % in the SPEX processed material, correspond to 120 minutes which contain 5.7 TaB<sub>2</sub> wt.%, while at the same atomic level the lower  $J_c(4.2 K, 5 T) = 21.3$  correspond to 60 minutes which contain 5.2 TaB<sub>2</sub> wt.%. Therefore, TaB<sub>2</sub> average crystallites in the matrix of MgB<sub>2</sub> are better distributes in the SPEX than Pulverisette-4 processed material.

Different behavior was found to Pulverisette-4 processed material at 1200 rpm in which TaB<sub>2</sub> wt. % increase as the average crystallite size increase for 2 at. % TaB<sub>2</sub> doped MgB<sub>2</sub> and decrease at 5 at. %. Figure 6.31 shows this behavior, which is inversely compared to Figure 6.29.

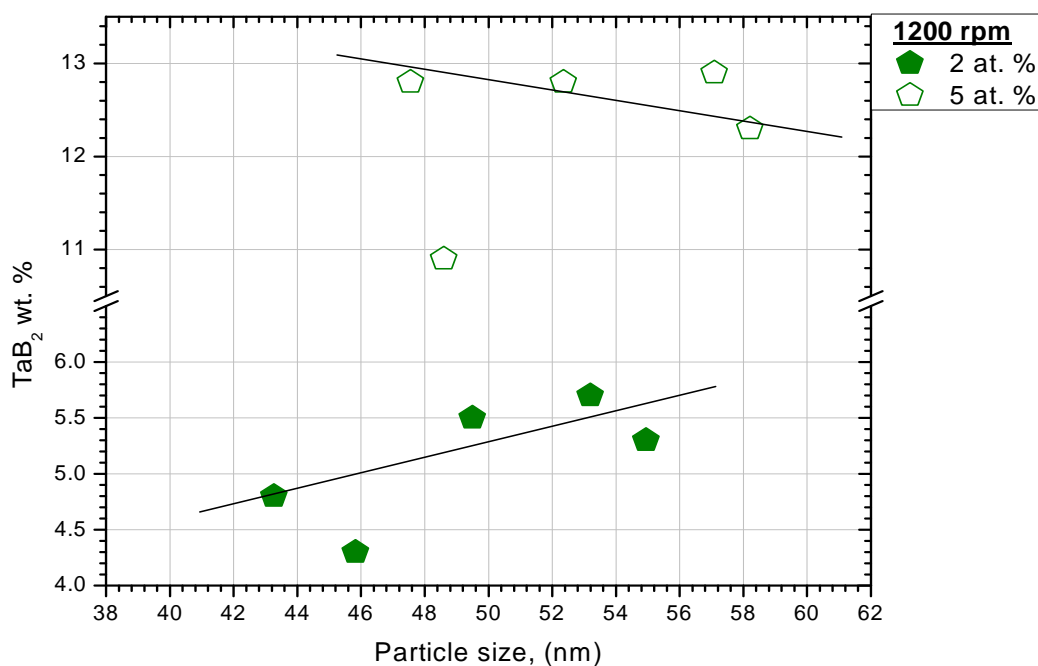


**Figure 6.30** TaB<sub>2</sub> wt. % as a function of the TaB<sub>2</sub> average crystallite size. Data plot for 2 and 5 at.% for Pulverisette-4 at 1200 rpm processed material.

At higher rotational speed the increase amount of TaB<sub>2</sub> wt.% found at 1200 rpm in the Pulverisette-4 at 2 at. % is possible understand by the highly distribution of TaB<sub>2</sub> average crystallites due to an increase of high energy impacts. Then, this average crystallites tends to agglomerate in the HIP process as a result of the sintering process. Inversely is observed to 5 at.% TaB<sub>2</sub> doped MgB<sub>2</sub> which TaB<sub>2</sub> wt.% decrease as the average crystallites size increase. In this case the amount of TaB<sub>2</sub> participate is more than 2 at. % and can be incorporated as other phase. Otherwise, no additional phase was observed in the x-ray spectra.

#### ***6.1.4 Pinning Force ( $F_p$ ) measurements as a function of applied magnetic field.***

The pinning force ( $F_p$ ) measurement can be obtained by multiplying  $J_c$  by the applied magnetic field  $\mu_0 H$ . Due to it, most of the comparison will be similar as  $J_c$  section. The plot of  $F_p$  as a function of  $\mu_0 H$  is characterized by a maximum, mostly in 2 T for this work, and a decreasing slow curve which tend to zero, as in Figure 6.31. The maximum  $F_p$  value can be related with well defined pinning centers while the slowly decreasing curve shows an increase in the magnetic flux lines going inside the sample. Figures 6.30 to Figure 6.33 compared the  $F_p$  for the post HIP processed material on the Pulverisette-4 and SPEX 8000D with the milling time condition tabulated at the upper right in-set.

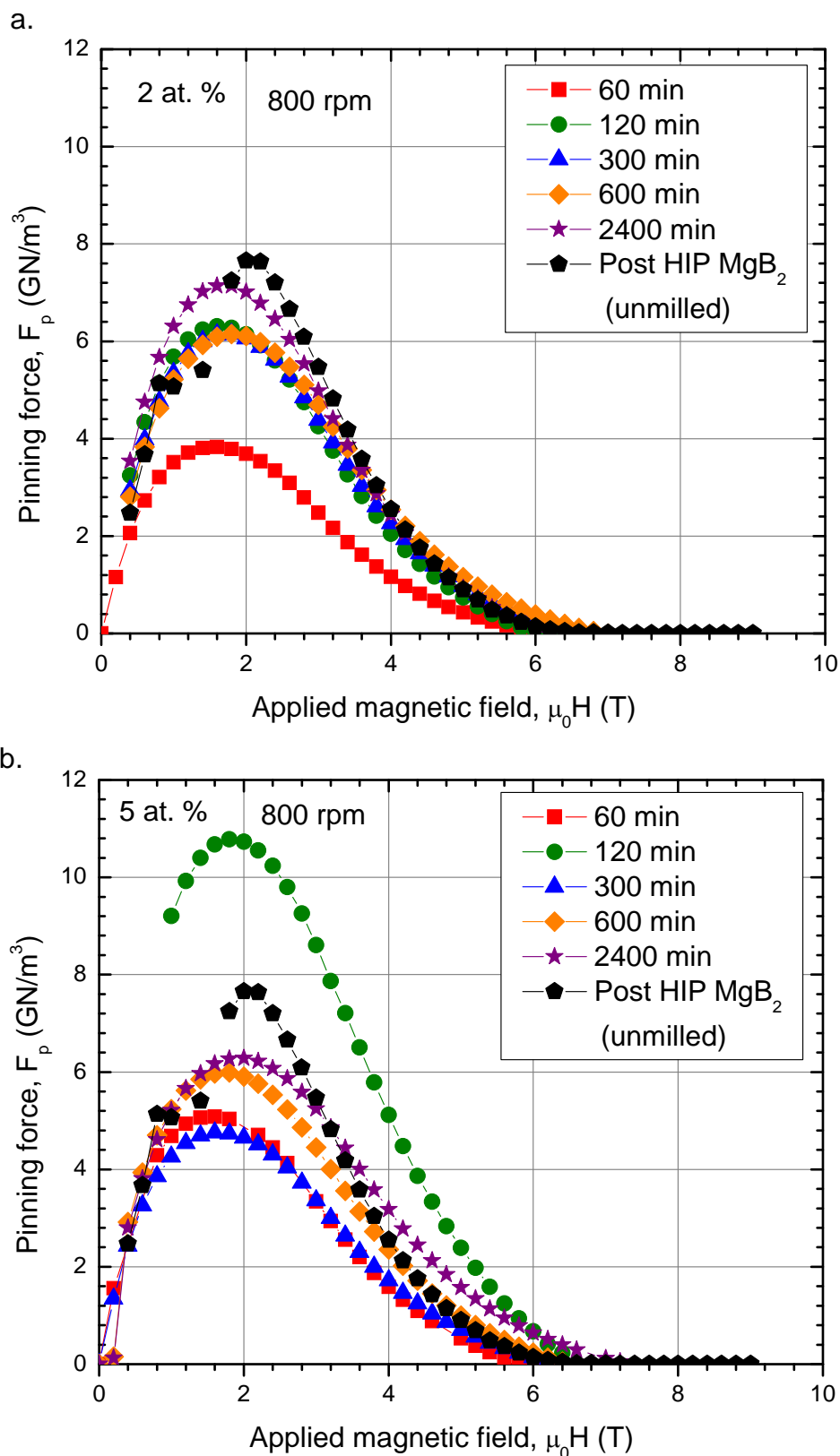
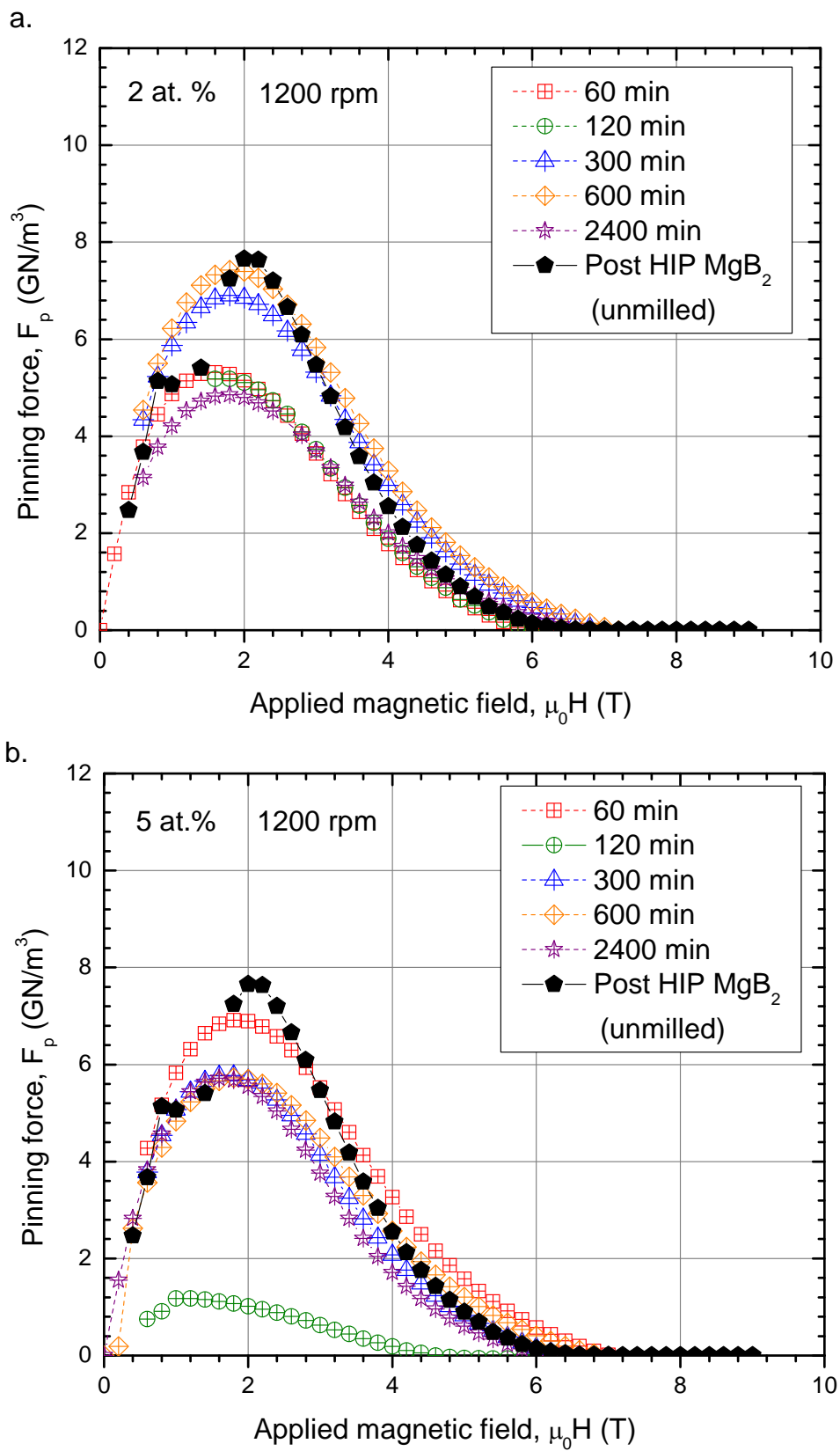


Figure 6.31 Pinning force ( $F_p$ ) values as a function of applied magnetic field ( $\mu_0 H$ ) for post HIP  $\text{TaB}_2$  doped  $\text{MgB}_2$  (a) 2 at.% and (b) 5 at.% based on Pulverisette-4 ball mill operated at 800 rpm for the times indicate in the in-set.



**Figure 6.32** Pinning force ( $F_p$ ) values as a function of applied magnetic field ( $\mu_0 H$ ) for post HIP  $\text{TaB}_2$  doped  $\text{MgB}_2$  (a) 2 at.% and (b) 5 at.% based on Pulverisette-4 ball mill operated at 1200 rpm for the times indicate in the in-set.

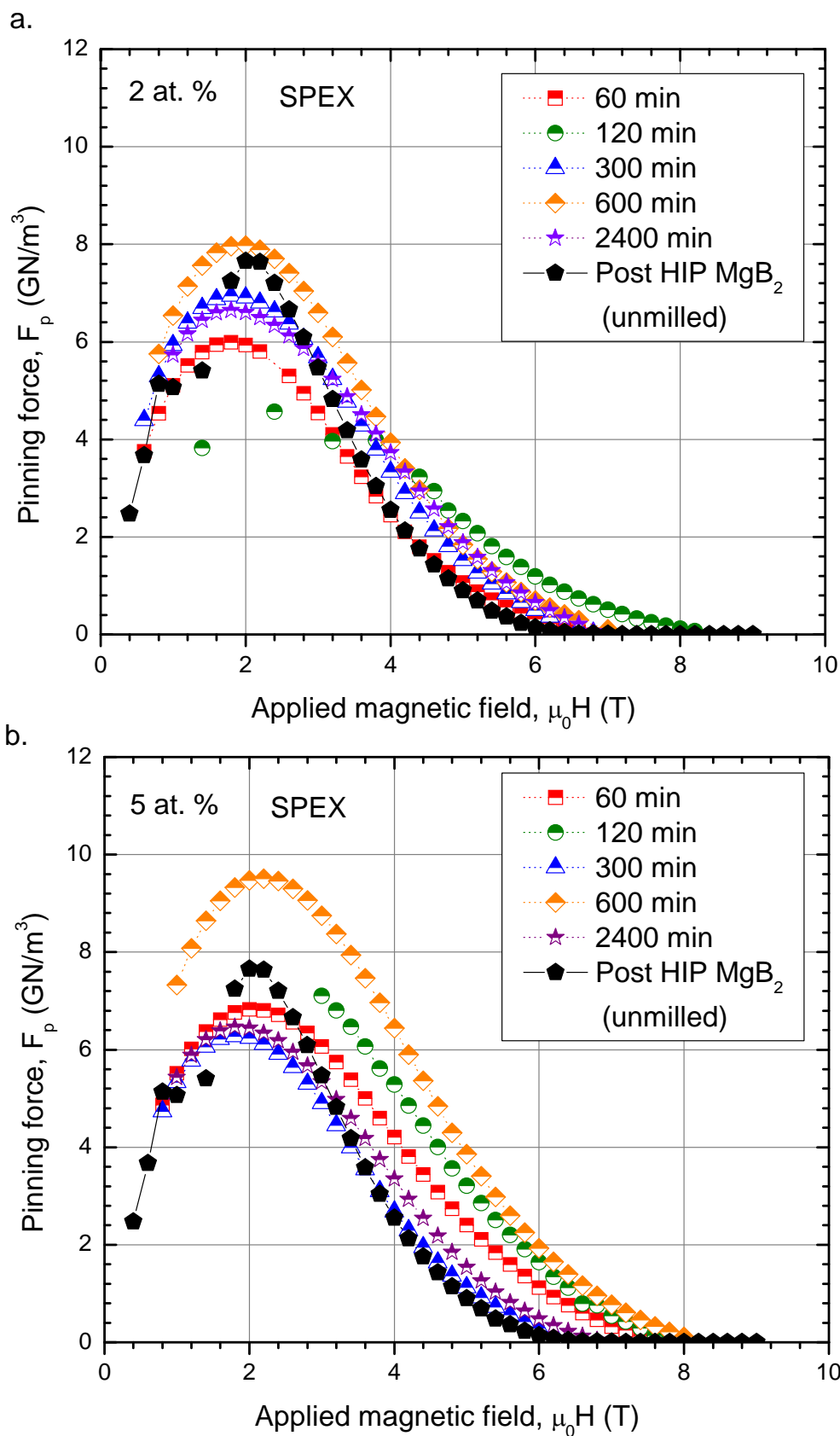


Figure 6.33 Pinning force ( $F_p$ ) values as a function of applied magnetic field ( $\mu_0 H$ ) for post HIP  $\text{TaB}_2$  doped  $\text{MgB}_2$  (a) 2 at.% and (b) 5 at.% based on SPEX-8000D ball mill for the times indicate in the in-set.

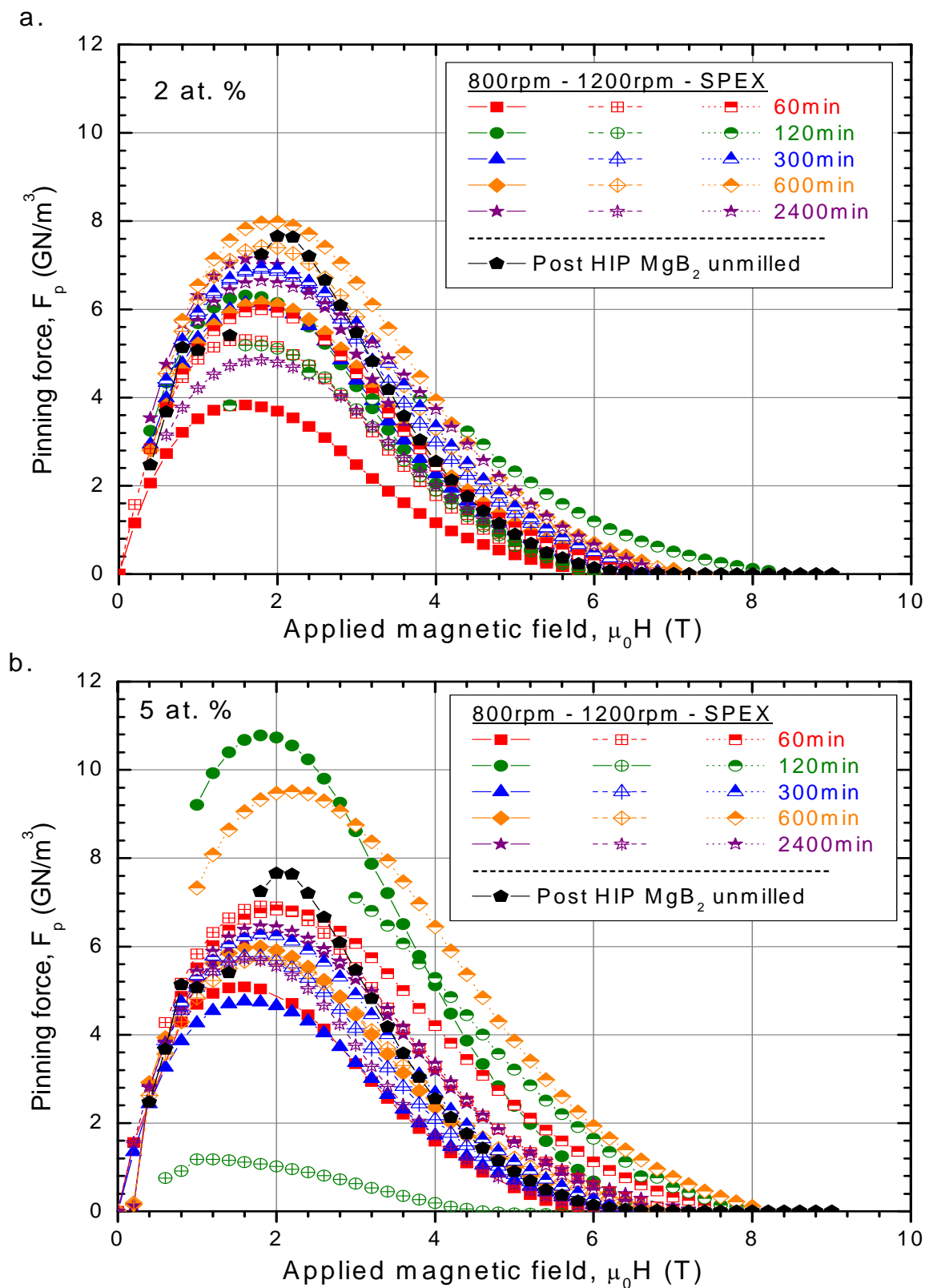


Figure 6.34 Pinning force ( $F_p$ ) values as a function of applied magnetic field ( $\mu_0 H$ ) for post HIP  $\text{TaB}_2$  doped  $\text{MgB}_2$  (a) 2 at.% and (b) 5 at.% based on Pulverisette-4, operated at 800 rpm and 1200 rpm, and SPEX-8000D ball mills for the times indicate in the in-set.

The pinning force ( $F_p$ ) measured as a function of applied magnetic field ( $\mu_0H$ ) for the 2 at.% and 5 at.% TaB<sub>2</sub> doped MgB<sub>2</sub> is shown in Figures 6.30 through 6.33. The post HIP MgB<sub>2</sub> for the no milling condition is included to aid comparison with the varying processing conditions. The variation trend of the pinning force ( $F_p$ ) with increasing applied magnetic field can be seen to be similar for both the 2 at.% and 5 at.% TaB<sub>2</sub> dopant levels. The SPEX processed materials recorded the highest peak values for  $F_p$  in both cases.

Proportional  $F_p$  values is observed, from  $J_c$  values on Section 6.1.3. As shown in Figure 6.33, the highest values for SPEX processed material at 60, 120 and 600 minutes are  $F_p(4.2 \text{ K}, 2 \text{ T}) = 6.83, 7.58$  and  $9.47 \text{ GN/m}^3$ , respectively. The highest  $F_p$  value is obtained for Pulverisette-4 processed material at 800 rpm using 5 at. % TaB<sub>2</sub> doped MgB<sub>2</sub>,  $F_p(4.2 \text{ K}, 2 \text{ T}) = 10.73 \text{ GN/m}^3$ .

During the decrease  $F_p$  transition, from 2 T to 8 T approximately, the  $F_p$  values decrease as a result of increase of magnetic flux through the material. For SPEX processed material  $F_p$  values is observed close to the end of the transition until 8 T compared with Pulverisette-4 processed material. From Figure 6.34 (a), is possible to observed that the highest  $J_c(4.2\text{K})$  at 8 T correspond to SPEX processed material at 120 minutes. This processed material contain smallest average crystallite size, as see in Figure 6.9, high strain (Figure 6.12) and high level of TaB<sub>2</sub> wt. %, observed in Figure 6.20.

The major difference between the pinning force values obtained was recorded between the 2 T and 5 T applied magnetic fields. The values at 5 T were consistently lower than the values for at 2 T field measurements. For the 2 at.% TaB<sub>2</sub> doped MgB<sub>2</sub>, the difference between the pinning force for the 1200 rpm processed material and the 800 rpm ones was very insignificant. The difference in the SPEX processed materials and the Pulverisette-4 ones, respect to the force pinning values, could be attributed to the higher defect

inducement associated with the SPEX mill. These higher defects inducement, reflected on the higher values of the force pinning,  $F_p$ , for SPEX post HIP processed material, can promote the superconductivity by creating magnetic flux pinning center in the sample. As reflected on  $F_p$  values, from Figure 6.31 through 6.33, this magnetic flux pinning center are well held or well pinning by SPEX post HIP processed material more than Pulverisette-4 ones. Magnetic flux pinning not well pin in the material could have the opportunity to move through it. Therefore, the electrons can be scattered by the motion of the flux pinning creating a resistance in the material.

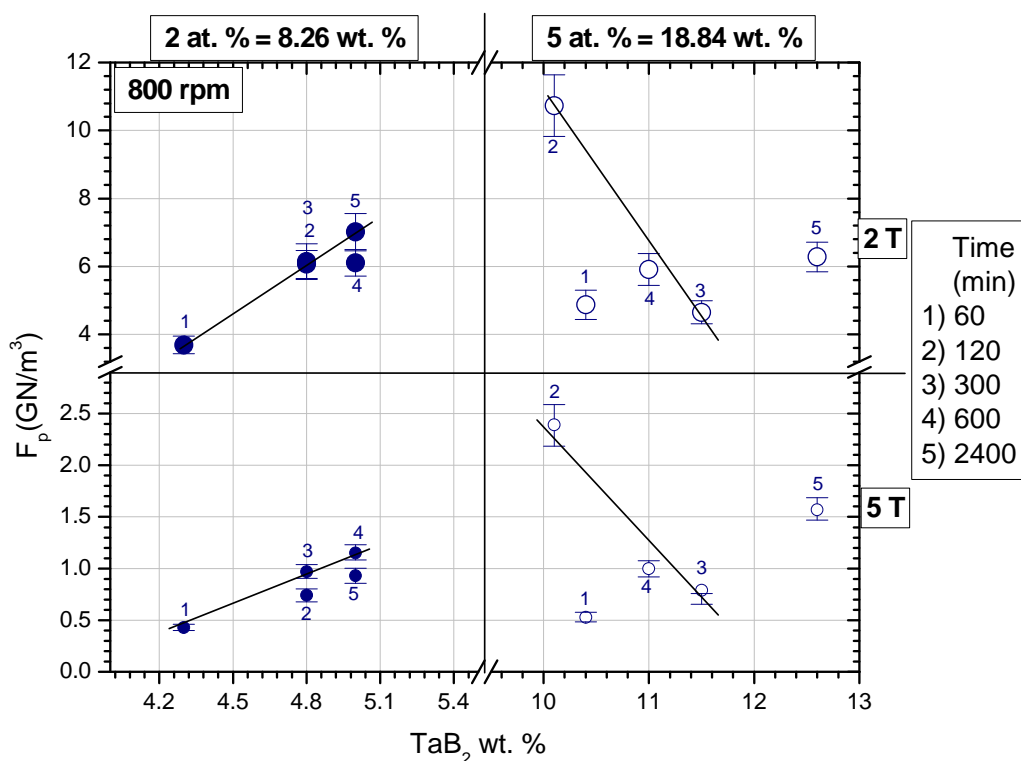


Figure 6.35  $F_p$  as a function of  $TaB_2$  wt.% in the  $MgB_2$  matrix. Data are extracted from  $F_p(4.2K)$  at 2 and 5 T from 2 and 5 at.% of Pulverisette-4 processed material at 800 rpm.

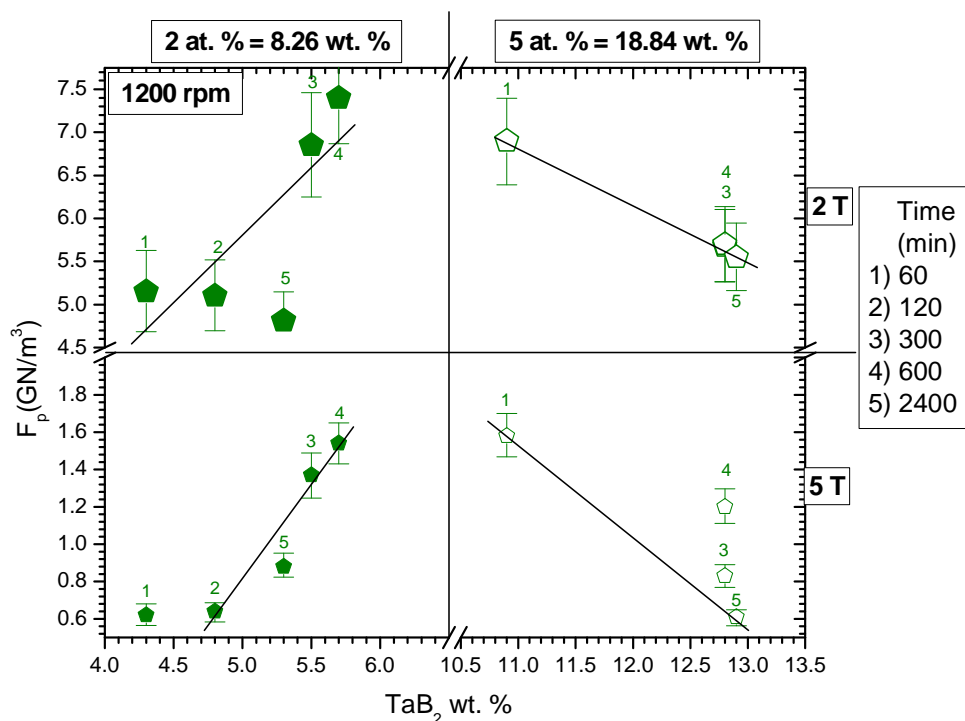


Figure 6.36  $F_p$  as a function of TaB<sub>2</sub> wt.% in the MgB<sub>2</sub> matrix. Data are extracted from  $F_p(4.2K)$  at 2 and 5 T from 2 and 5 at.% of Pulverisette-4 processed material at 1200 rpm.

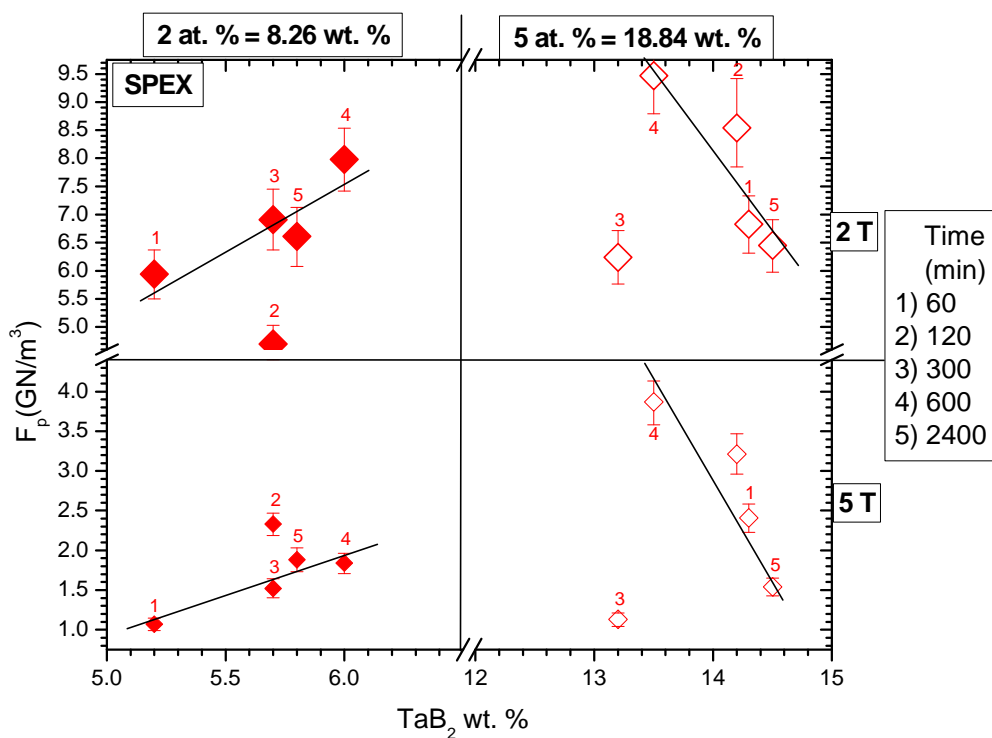


Figure 6.37  $F_p$  as a function of TaB<sub>2</sub> wt.% in the MgB<sub>2</sub> matrix. Data are extracted from  $F_p(4.2K)$  at 2 and 5 T from 2 and 5 at.% of SPEX processed material.

Figures 6.34 to Figure 6.37 reveal the same information as discussed for the  $J_c$ . From 2 to 5 at.% the values of  $F_p$  increase until some at. % unknown, possible 3.5 at.%, and decrease as the incorporation of  $TaB_2$  wt. % increase. The highest values of  $F_p$  was found at 13.5, 10.1 and 5.7 wt. % corresponding to SPEX 5 at.% for 600 minutes, Pulverisette-4 at 800 rpm 5 at.% for 120 minutes and at 1200 rpm 2 at.% for 600 minutes at 2 T, respectively. The trends of Figures 6.34 to 6.36 suggest that high  $F_p$  values can be found in the region of 5 to 11 wt.% corresponding to 1.17 to 2.72 at.%. It can explain why most of the high values for  $F_p$ , as well for  $J_c$ , correspond to the 5 at. %. The atomic percent found for material processed at 2 at. % was around 1 at. % while for material processed at 5 at.%, the amount of  $TaB_2$  phase in the material was around 3 at.%.

### ***6.1.5 Magnetization measurements: Zero field Cooled (ZFC)***

The magnetization measurements as a function of temperature are showed in Figure 6.38 (a) 2 at.% and (b) 5 at.%. These measurements were obtained cooling to 4.2 K in zero field and applied field of 50 Oe during heated with field from 4.2 K to 50 K. The  $\mu_0 H$  is turning off, while  $T = 4.2$  K is reached. Better explanation of the ZFC process is resumed in Chapter 3 section 3.2.1.1. At this point, before ZFC process, the superconductivity properties, meaning magnetization, of the material are maximized. The applied magnetic field is on while the temperature increases. A magnetic flux, coming from the applied magnetic field will interact with the material.

In the case of TaB<sub>2</sub> doped MgB<sub>2</sub>, TaB<sub>2</sub> will act as a pinning center after T = 9 K, behaving as non-superconducting regions. Other secondary phases such as MgO and MgB<sub>4</sub>, observed in the x-ray diffraction measurements of Pulverisette-4 and SPEX processed material and WC, for SPEX samples ones, will act as non-superconducting regions, too. Then, magnetic flux increase in the material as temperature increase, especially in the mixed superconducting state region, see Figure 2.4 (b) from Chapter 2, the superconducting properties of the material become weaker until they disappear at T<sub>c</sub>.

Figure 6.38 shows T<sub>c</sub> for all samples described in Tables 6.1 to 6.6. Lowest T<sub>c</sub>, at 2 and 5 at.%, for SPEX samples was observed. The amount of MgO and MgB<sub>4</sub> phases may be depressing T<sub>c</sub>. Tables 6.8 and 6.11 shows T<sub>c</sub>(10%) values for all the samples. Another factor that can help to reduction of T<sub>c</sub> is the increase in average crystallite size. As smallest the average crystallite size improvement in the superconducting properties, as T<sub>c</sub>, will be reflected. When an average crystallite can reach to a grain size, then the average crystallite will have the entire superconducting properties of the grain. As the milling time increases a variation on average crystallites is observed, Figure 6.9 for SPEX and 6.14 for Pulverisette-4 processed material. In both cases is observed a variation in average crystallite size as the milling time increases. Due to that a well defined trend for T<sub>c</sub> as a function of the reduction of average crystallite size will not reveal any information.

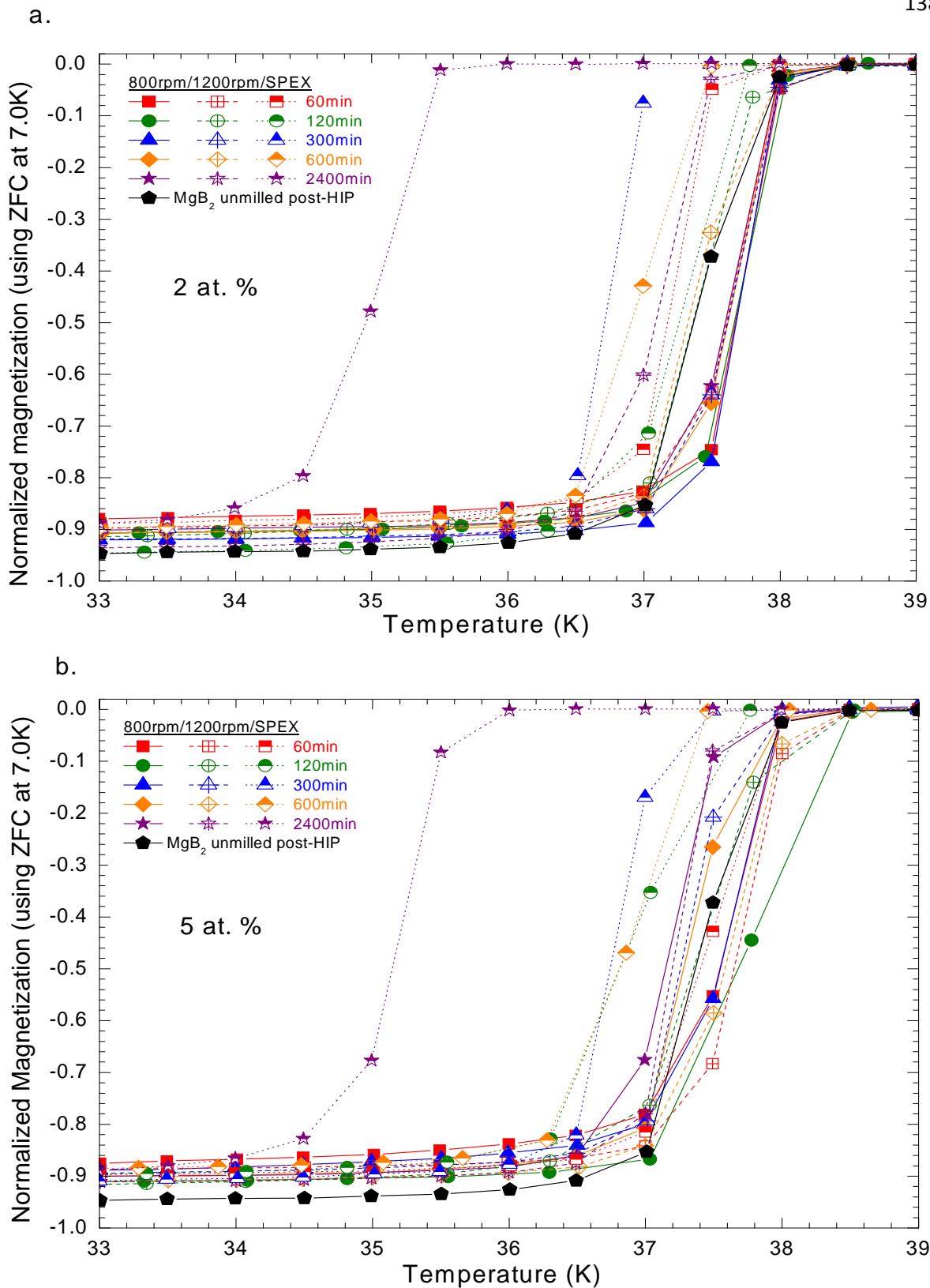


Figure 6.38 Magnetization measurement as a function of an applied magnetic field ( $\mu_0H$ ) for post HIP TaB<sub>2</sub> doped MgB<sub>2</sub> processed material at (a) 2 at.% and (b) 5 at.%. Pulverisette-4 at 800 and 1200 rpm, and SPEX 8000D for different milling times.

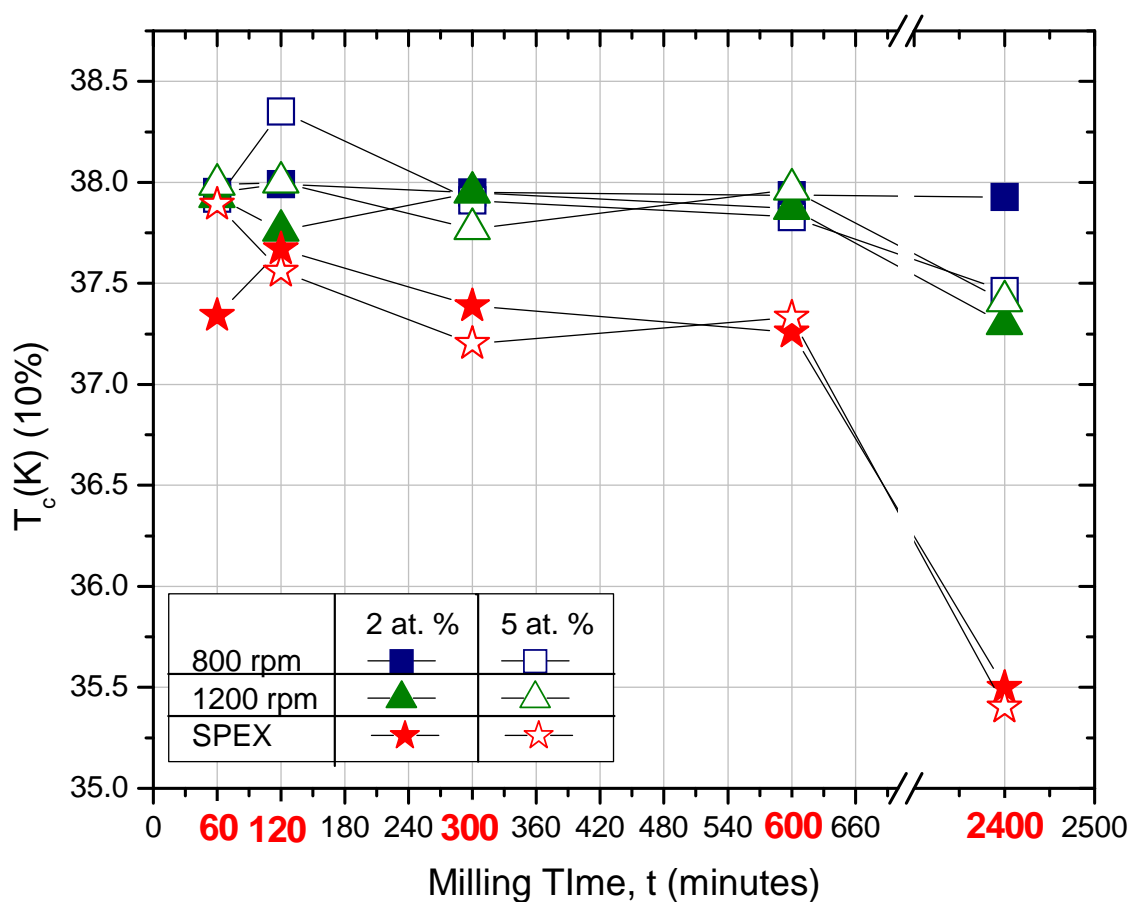


Figure 6.39  $T_c$  behavior at different milling time.  $T_c$  extract from the 10% criterion.

Figure 6.39 shows a decreasing in  $T_c$  as the milling time increase. Higher reduction is found for 2400 minutes. SPEX processed material shown the lower  $T_c$  for all milling time compared with Pulverisette-4 material processed. For Pulverisette-4 processed material at 800 rpm and 1200 rpm was observed similar values during the trend. The highest  $T_c$  was 38.35 K for the Pulverisette-4 800 rpm processed material corresponding to the 5 at.% TaB<sub>2</sub> doped MgB<sub>2</sub> during 120 minutes. SPEX processed material shows  $T_c$  values in the range of 35.49 K and 35.40 K, for 2400 minutes to 37, 67 K, 120 minutes, and 37.89 K, 60 minutes, for 2 and 5 at.% TaB<sub>2</sub> doped MgB<sub>2</sub>, respectively.

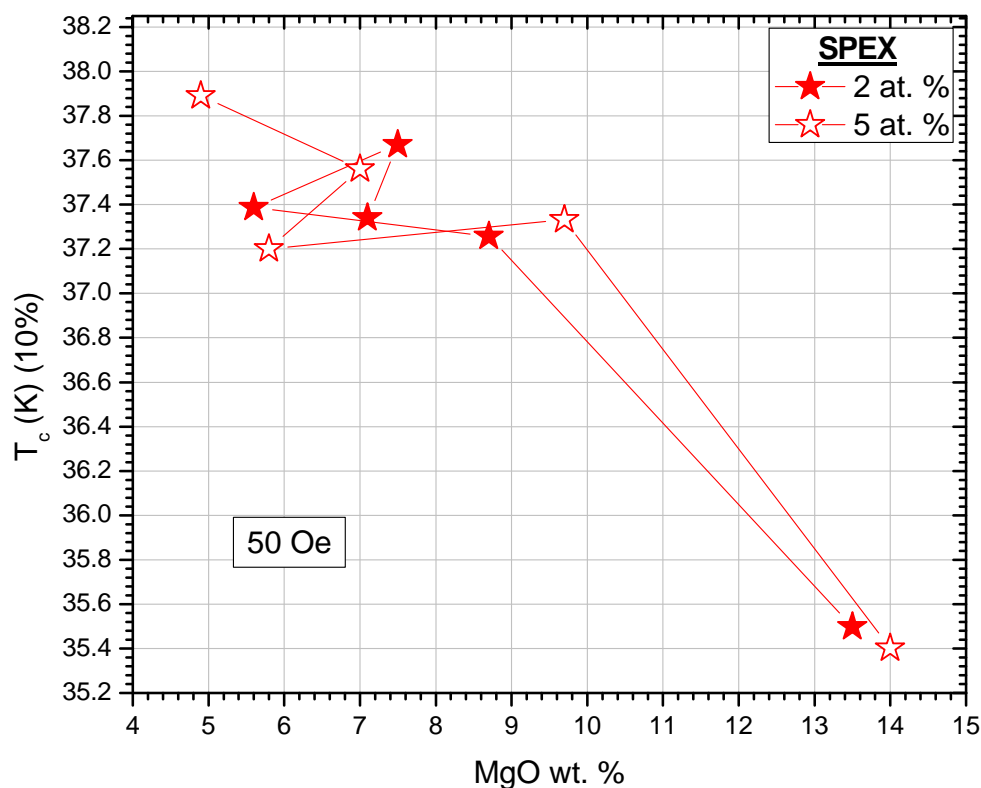
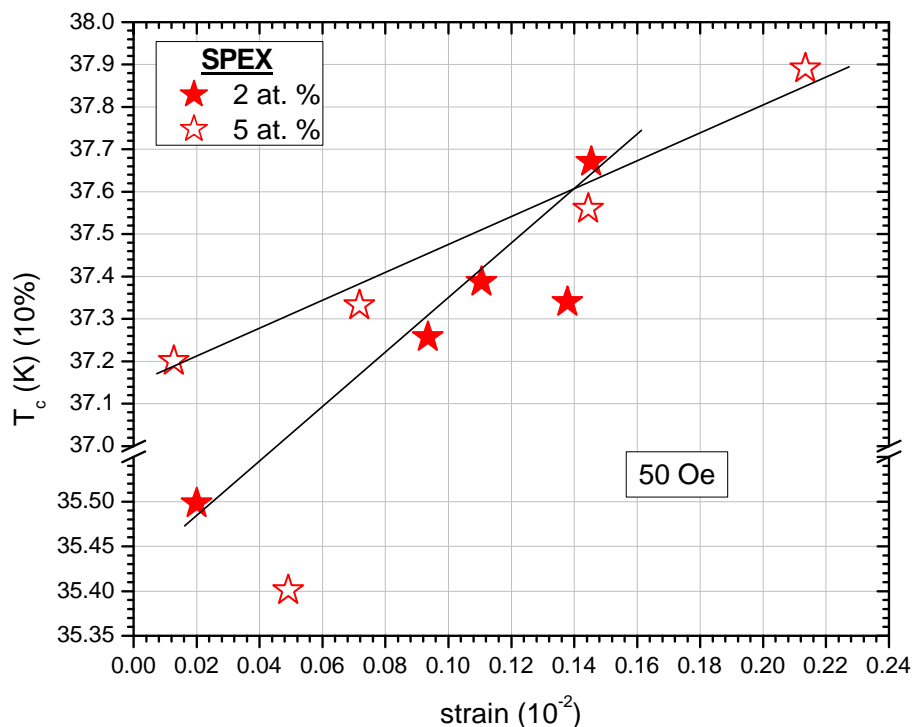


Figure 6.40  $T_c$  as a function of MgO wt. % for SPEX processed material at 2 and 5 at. % TaB<sub>2</sub> doped MgB<sub>2</sub>.  $T_c$  extract from the 10 % criterion

The reduction of average crystallite size as the milling time increase, Figure 6.10 for SPEX processed material for instance, is proportional to the effect of MgO contamination as the milling time increase showed in Figure 6.7. The increasing of MgO contamination as the milling time increase has the tendency to reduce the  $T_c$ , as shown in Figure 6.40. The lower values of  $T_c$  have the higher MgO wt.% values which correspond to 2400 minutes ball milling time. The higher  $T_c$  value, 37.891 K, belong to SPEX processed material at 5 at.% during the first 60 minutes which contain the lower MgO contamination of 4.9 wt. %. MgO as non-superconducting secondary phase in the MgB<sub>2</sub> matrix creates inhomogeneities surface in the material which tends to scatter the electrons.



**Figure 6.41**  $T_c$  as a function of MgO wt. % for SPEX processed material at 2 and 5 at. % TaB<sub>2</sub> doped MgB<sub>2</sub>.  $T_c$  extract from the 10 % criterion

In section 6.1.1.a, an increase in strain SPEX processed material is observed as the milling time increase, Figure 6.12. This behavior is proportional to  $T_c$  as shown in Figure 6.41 for SPEX processed material. Apart of the lower values of  $T_c$  at 2 and 5 at.% TaB<sub>2</sub> doped MgB<sub>2</sub> for SPEX processed material, which are related to the increase of MgO wt.% showed in Figure 6.40, a positive slope is found as the strain increase. The strain in the material, reveal changes in the lattice parameters. These changes correspond to an increase of  $T_c$  as shown Figure 6.41. Therefore, a force on the electron spins rotation, to change its magnetization properties as  $\mu_0 H$  increase, is increasing as the strain increase. For magnetization lower strain in the material which has the tendency to reduce  $T_c$ .

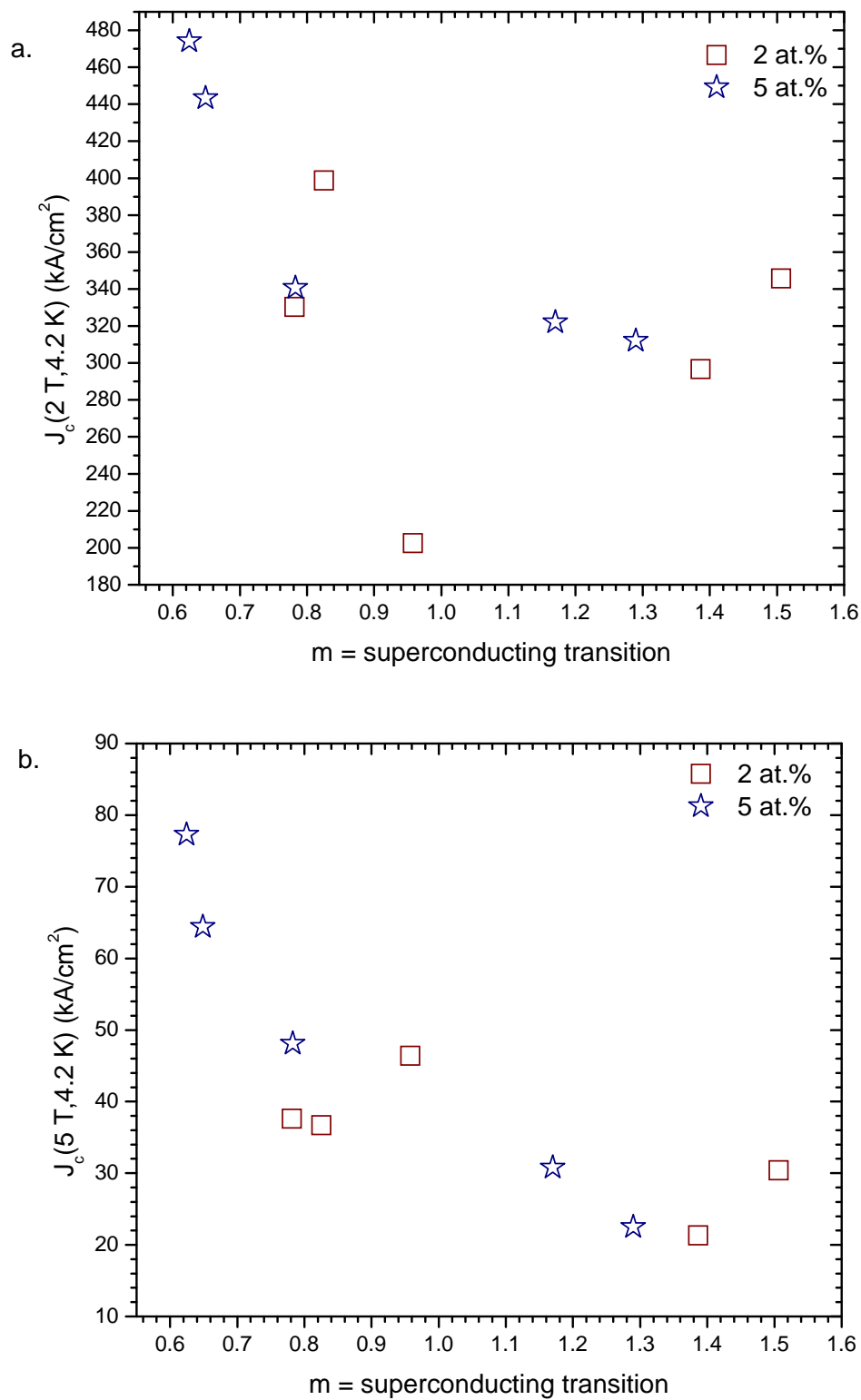


**Figure 6.42**  $J_c$  as a function of superconducting transition slope ( $m$ ) for SPEX processed material at 2 at.% and 5 at.%.  $J_c(4.2\text{ K})$  values at (a) 2 T and (b) 5 T are shown.

In Figure 6.42 it is possible to observe an increase of the superconducting transition slope ( $m$ ) showing a decrease in the critical current density ( $J_c$ ) for SPEX post HIP processed material. This behavior remains the same for values of  $J_c(2 \text{ T}, 4.2 \text{ K})$  and  $J_c(5 \text{ T}, 4.2 \text{ K})$ . The higher values of  $J_c$  in Figure 6.42 (a) and (b) is obtained for 5 at.% dopant levels processed materials which have the smallest  $m$ . Otherwise, smallest  $J_c$  values are observed for 2 at.% TaB<sub>2</sub> doped MgB<sub>2</sub> which shows the highest  $m$ .

The superconducting transition to the lower magnetization can have an interpretation of superconducting homogeneity as will be extracted from the results. The superconducting transition close to  $T_c$ , 2 at.% and 5 at.% of TaB<sub>2</sub> doped MgB<sub>2</sub> shows different behavior. The transition to a lower magnetization for 2 at.% processed material is slightly smooth compared with the transition of 5 at.% processed material which superconducting transition tends to be straight. For instance, SPEX processed material ball milled for 2400 minutes shows a slightly different transition when compared 2 at.% and 5 at.% in Figure 6.38 (a) and (b), respectively.

The superconducting transition ( $m$ ) in a material, see Figure 3.17 in Chapter 3, reveals the superconducting homogeneity of the material. This homogeneity is characteristic to the clean limit of the sample or with lack of impurities. Non-superconducting secondary phases in the material could reduce the homogeneity level. In this way, taking the sample of SPEX material ball milled for 2400 minutes, for 2 at.% the amount of MgO (10.5 wt.%) and TaB<sub>2</sub> (1.3 wt.%) is lower than 5 at.% processed material with MgO = 13.3 wt.% and TaB<sub>2</sub> = 3.5 wt.%, as shown Table 6.1 and 6.2, respectively. Therefore, this superconducting transition can be attributed to the amount of non-superconducting secondary phases in the material.

### ***6.1.6 Kramer function ( $F_k$ ) measurements as a function of applied magnetic field.***

The Kramer function ( $F_k$ ) is used to obtain the irreversibility field ( $H_{irr}=H^*$ ) of the material. To obtain  $H^*$ , using  $F_k$ , is necessary to extrapolate it, from a linear fit, to the applied magnetic field ( $\mu_0H$ ) axis in a plot of  $J_c^\alpha H^\beta$  against  $\mu_0H$ . Both coefficients,  $\alpha$  and  $\beta$ , have typically values of 0.5 and 0.25, in the case of a grain boundary pinner materials,  $Nb_3Sn$ , i.e., respectively. Therefore, from Figure 6.43 and 6.4, normalized to the  $F_k$  maximum ( $F_{k,max}$ ),  $H^*$  was determined for all processed materials. From the normalization, better comparison of the samples can be extract.

Figure 6.44 shows an enlarge view of Figure 6.43 close to the  $\mu_0H$  axis intercept. Figure 6.43, in other way, shows that the plot for each post HIP processed material can modulate a linear fit. In this way,  $\alpha$  and  $\beta$  values used were close enough to get a linear fit for  $TaB_2$  doped  $MgB_2$  processed material. Therefore, as wrote before,  $MgB_2$  is a good representation of a grain boundary pinner material.

The increase of  $H_{irr}$  in Figure 6.44, reveal that the improved pinning in field seems to be caused by the enhanced grain boundary pinning provide by the large number of grain boundaries as conclude X. Xu et. al [63]. Therefore  $TaB_2$  average crystallites are the precursors to the improvement of  $F_p$  by taking place in the inter and intra grain boundary spaces. SPEX processed material shows the higher  $H_{irr}$  values as shown in Figure 6.44 compared with Pulverisette-4 processed materials.

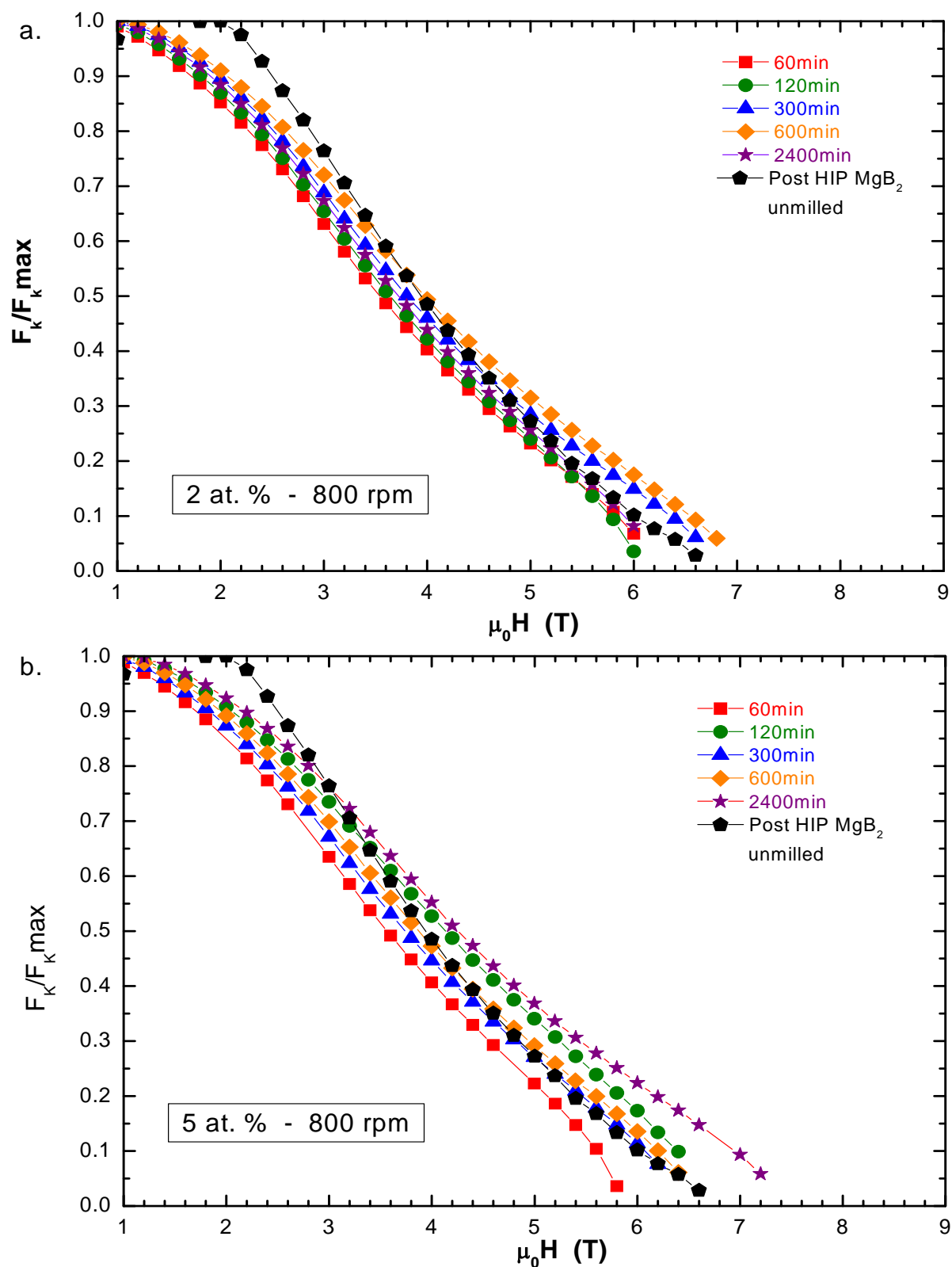


Figure 6.43 Normalized Kramer Function ( $F_k = J_c^{0.5} H^{0.25}$ ) as a function of applied field  $H$  at 4.2 K. **Pulverisette-4 at 800 rpm processed material. a. 2 at. % and b. 5 at. % TaB<sub>2</sub> doped MgB<sub>2</sub>.**

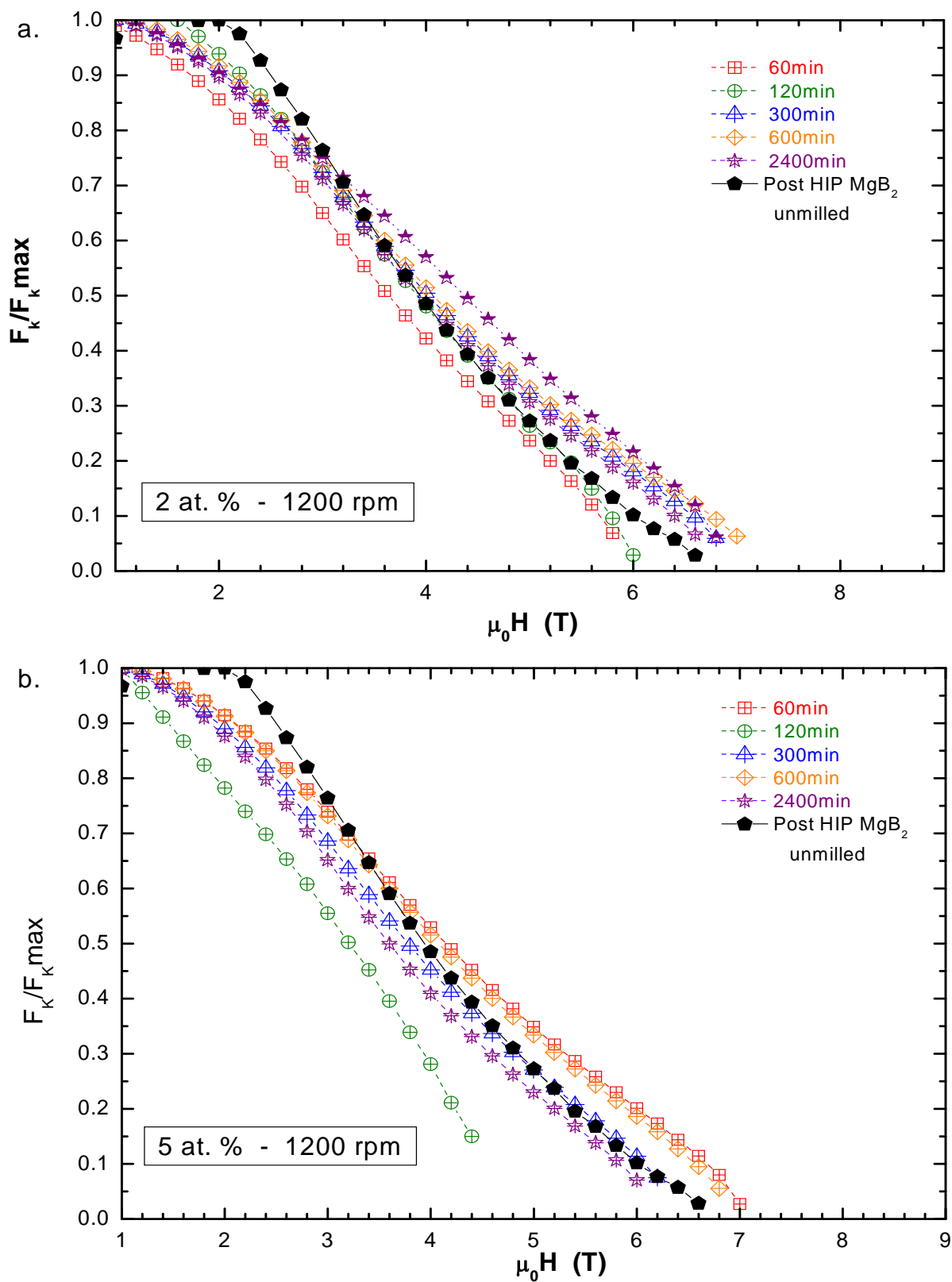


Figure 6.44 Normalized Kramer Function ( $F_k = J_c^{0.5} H^{0.25}$ ) as a function of applied field  $H$  at 4.2 K. **Pulverisette-4 at 1200 rpm processed material. a. 2 at. % and b. 5 at. %  $\text{TaB}_2$  doped  $\text{MgB}_2$ .**

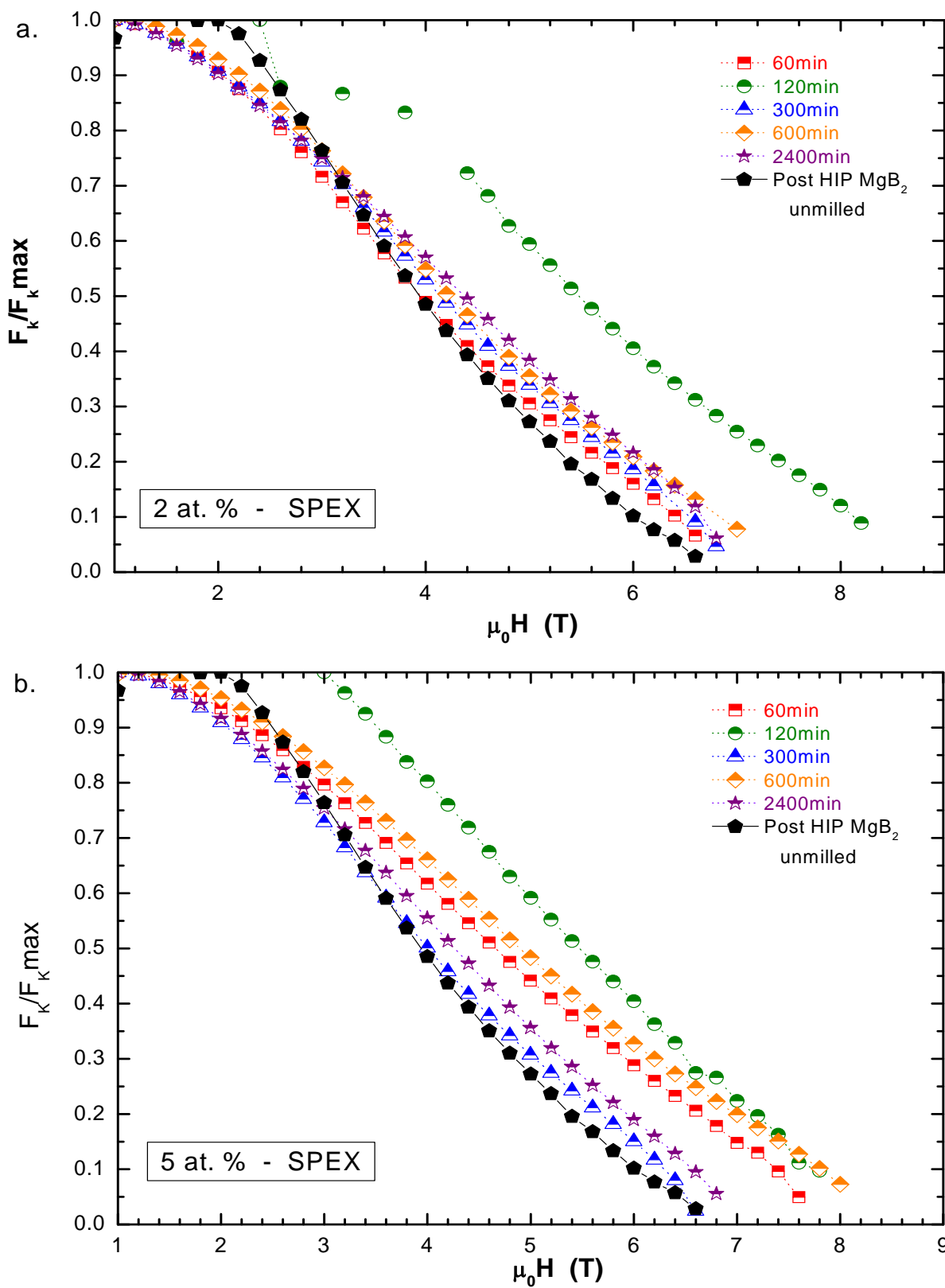


Figure 6.45 Normalized Kramer Function ( $F_k = J_c^{0.5} H^{0.25}$ ) as a function of applied field  $H$  at 4.2 K. **SPEX processed material. a. 2 at. % and b. 5 at. % TaB<sub>2</sub> doped MgB<sub>2</sub>.**

By the extrapolation of the Kramer function from a linear fit of the curves shown from Figures 6.43 to 6.45, the irreversibility field ( $H^*$ ) can be determined.  $H^*$  shows a better relationship with  $J_c$  as conclude by Senkowicz et al, in the increase of  $J_c$  with the penetration of Carbon in the lattice.  $H^*$  is shown in Table 6.8 to Table 6.11 for SPEX and Pulverisette-4 processed material, respectively. SPEX processed material, Figure 6.45 a and b, shows the larger  $H^*$  values. However, Pulverisette-4 stay closer to SPEX values as show material processed milled at 800 rpm for 2400 minutes in the Pulverisette-4 using 5 at.%  $TaB_2$ , Figure 6.43-b. The superconducting properties shown in Table 6.8, to Table 11, show us the proportionality between  $J_c$  and  $F_p$  making a contribution of granular superconductors.

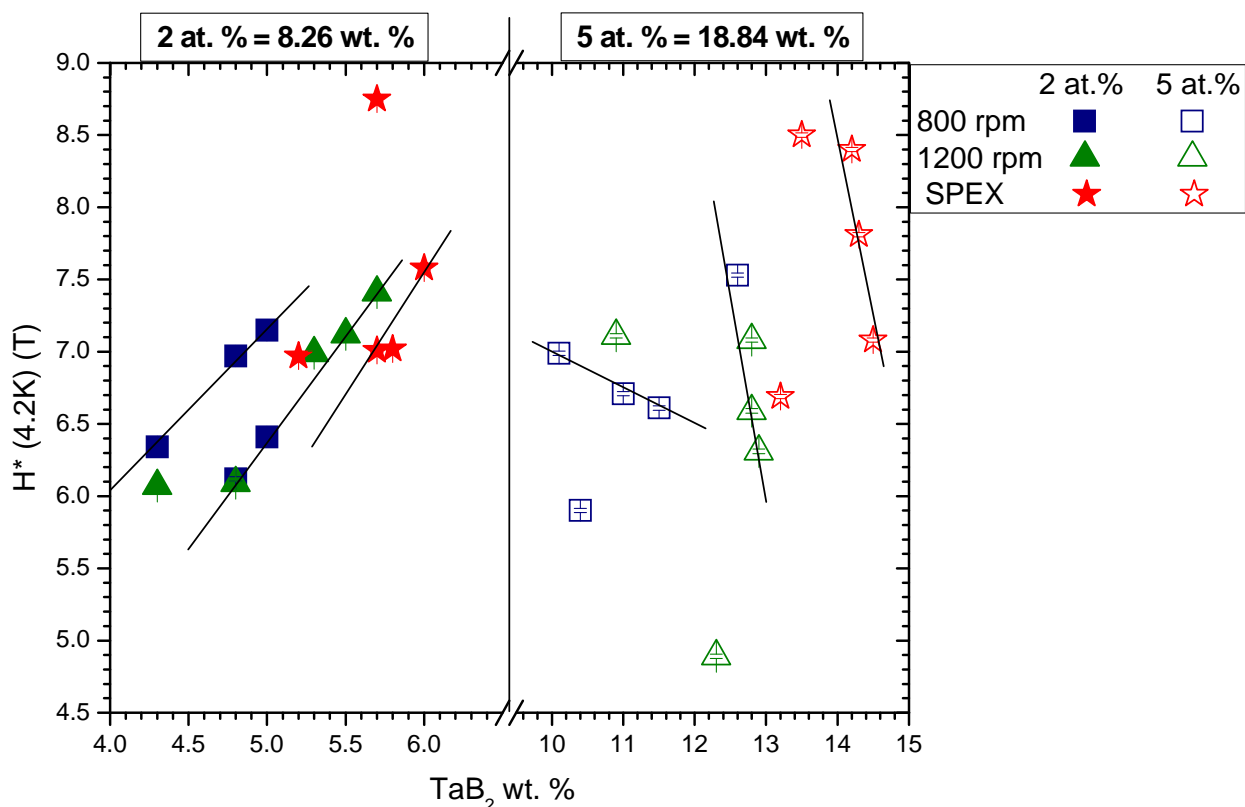


Figure 6.46 Irreversibility field ( $H^*$ ) as a function of  $TaB_2$  wt.% for the 2 and 5 at.%  $TaB_2$  doped  $MgB_2$ . Data plot for the material processed in the SPEX and Pulverisette-4 at 800 rpm, 1200 rpm at different milling time.

Figure 6.46 show practically the same trend as in  $J_c$  and  $F_p$  for the 2 and 5 at. % shown in Figures 6.26 to 6.28 and in Figure 6.35 to 6.37, respectively. As the amount of  $TaB_2$  wt.% increase in the material in the 2 at.%  $H^*$  increase. Different for the 5 at.% which  $H^*$  decrease as increase the amount of  $TaB_2$  wt.% in the material increase. It suggest that at some  $TaB_2$  wt.% between 2 and 5 at. %  $H^*$  is a maximum. This optimum  $TaB_2$  wt.% is the amount needed to maximized the improved of superconductivity shown in this work. Then  $TaB_2$  will be fully cover the intra an inter grain space without oversaturated the samples as seems to happen with the 5 at. %.

### *Superconducting Properties*

Table 6.8 Superconducting properties of the  $TaB_2$  doped  $MgB_2$  in the 2 at.% for the post HIP processed material in the **SPEX-8000D**.

Sample Description		Superconducting properties					
Time (minutes)	at.%	$J_c(2T,4.2K)$ (kA/cm <sup>2</sup> )	$J_c(5 T,4.2 K)$ (kA/cm <sup>2</sup> )	$F_p(2 T,4.2 K)$ (GN/m <sup>3</sup> )	$F_p(5 T,4.2 K)$ (GN/m <sup>3</sup> )	$H^*(4.2 K)$ (T)	$T_c(K)$ 10%
60	2	296.7	21.3	5.94	1.07	6.97	37.340
120	2	220.5	46.4	4.70	2.33	8.75	37.67
300	2	345.8	30.4	6.91	1.52	7.01	37.387
600	2	398.8	36.7	7.98	1.84	7.58	37.257
2400	2	330.4	37.6	6.61	1.88	7.02	35.498

**Table 6.9** Superconducting properties of the TaB<sub>2</sub> doped MgB<sub>2</sub> in the **5 at.%** for the post HIP processed material in the **SPEX-8000D**.

Sample Description		Superconducting properties					
time (minutes)	at.%	J <sub>c</sub> (2 T,4.2 K) (kA/cm <sup>2</sup> )	J <sub>c</sub> (5 T,4.2 K) (kA/cm <sup>2</sup> )	F <sub>p</sub> (2 T,4.2 K) (GN/m <sup>3</sup> )	F <sub>p</sub> (5 T,4.2 K) (GN/m <sup>3</sup> )	H*(4.2 K) (T)	T <sub>c</sub> (K) 10%
60	5	340.7	48.1	6.83	2.41	7.81	37.891
120	5	390.9	64.4	8.54	3.21	8.40	37.56
300	5	312.0	22.5	6.24	1.13	6.69	37.201
600	5	474.1	77.3	9.47	3.87	8.50	37.332
2400	5	322.0	30.8	6.45	1.54	7.08	35.401

**Table 6.10** Superconducting properties of the TaB<sub>2</sub> doped MgB<sub>2</sub> in the **2 at.%** for the post HIP processed material milled in the **Pulverisette -4**.

Sample Description			Superconducting properties					
Speed (rpm)	time (min)	at.%	J <sub>c</sub> (2T,4.2K) (kA/cm <sup>2</sup> )	J <sub>c</sub> (5T,4.2K) (kA/cm <sup>2</sup> )	F <sub>p</sub> (2T,4.2K) (GN/m <sup>3</sup> )	F <sub>p</sub> (5T,4.2K) (GN/m <sup>3</sup> )	H*(4.2K) (T)	T <sub>c</sub> (K) 10%
No milling Post-HIP			382.72	17.91	7.66	0.89	6.80	37.88
800	60	2	184.6	8.6	3.69	0.43	6.34	37.952
800	120	2	307.2	14.7	6.15	0.74	6.12	37.990
800	300	2	302.9	19.5	6.07	0.97	6.97	37.949
800	600	2	305.4	23.1	6.11	1.15	7.15	37.937
800	2400	2	350.5	18.6	7.02	0.93	6.41	37.929
1200	60	2	257.9	12.4	5.15	0.62	6.07	37.927
1200	120	2	255.4	12.7	5.10	0.64	6.09	37.76
1200	300	2	342.4	27.3	6.85	1.37	7.12	37.950
1200	600	2	370.4	30.7	7.40	1.54	7.41	37.869
1200	2400	2	239.8	17.7	4.81	0.88	6.99	37.298

Table 6.11 Superconducting properties of the TaB<sub>2</sub> doped MgB<sub>2</sub> in the 5 at.% for the post HIP processed material milled in the Pulverisette-4.

Sample Description			Superconducting properties					
speed (rpm)	Time (minutes)	at. %	J <sub>c</sub> (2 T,4.2 K) (kA/cm <sup>2</sup> )	J <sub>c</sub> (5 T,4.2 K) (kA/cm <sup>2</sup> )	F <sub>p</sub> (2 T,4.2 K) (GN/m <sup>3</sup> )	F <sub>p</sub> (5 T,4.2 K) (GN/m <sup>3</sup> )	H*(4.2K) (T)	T <sub>c</sub> (K) 10%
800	60	5	244.6	10.6	4.87	0.53	5.90	37.92
800	120	5	536.4	47.7	10.73	2.39	6.99	38.35
800	300	5	232.7	14.1	4.65	0.79	6.61	37.91
800	600	5	295.5	19.9	5.91	1.00	6.71	37.828
800	2400	5	314.4	31.5	6.28	1.57	7.53	37.462
1200	60	5	344.4	31.7	6.90	1.58	7.11	37.989
1200	120	5	50.7	0	N/A	N/A	4.89	38.00
1200	300	5	284.2	16.6	5.68	0.83	6.59	37.77
1200	600	5	284.9	24.2	5.70	1.20	7.08	37.965
1200	2400	5	277.6	12.1	5.55	0.61	6.31	37.412

## 6.2 Conclusions

Physical properties were study with the help of the Rietveld analysis of the x-ray diffraction spectra for material processed in the SPEX 8000D and Pulverisette-4 at 800 rpm and 1200 rpm. Milling time range from 60 to 2400 minutes at 2 an 5 at.% TaB<sub>2</sub> doped MgB<sub>2</sub>. Superconducting properties were measured to superconducting characteristic enhancement by the high energy ball milling process and HIP treatment.

- a. Material processed at 5 at.% shown higher superconducting properties compared with 2 at.% due to the higher amount of TaB<sub>2</sub> to penetrate in the material.
- b. In general, SPEX processed materials exhibited higher  $J_c$ ,  $F_p$ , and  $H_{irr}$  values than the Pulverisette-4 processed materials. For instance, material processed at 5 at.% for 600 minutes in the SPEX compared to Pulverisette-4 at 800 rpm these were  $J_c(2\text{ T}, 4.2\text{ K}) = 474.1$  to  $295.5\text{ kA/cm}^2$ ,  $F_p(2\text{ T}, 4.2\text{ K}) = 9.47$  to  $5.91\text{ GN/m}^3$ , and  $H_{irr}(4.2\text{ K}) = 8.50$  to  $6.71\text{ T}$ , respectively. However, the  $T_c$  value of 37.33 K for SPEX ball milled material was lower than 37.82 K for Pulverisette-4 ball milled material

# 7 CONCLUSIONS AND SUGGESTION FOR FUTURE WORKS

## 7.1 Conclusions

The goal of this study was to determine the conditions that would lead to the improvement of the superconducting properties of  $\text{MgB}_2$ . This was carried out by first conducting a study of how atmospheric effects (reflecting material handling) affected the superconducting behavior of  $\text{MgB}_2$  with high energy ball milling. Next, properties enhancement based on  $\text{TaB}_2$  doping were carried out. The levels of  $\text{TaB}_2$  used were 2 at.% and 5 at.% respectively. The two levels of  $\text{TaB}_2$  dopings studied were to permit increased amount of Ta substitution in  $\text{MgB}_2$ . Two types of ball mills, notably, SPEX 8000D and Pulverisette-4 were employed because their processing parameters were different, implying that different characteristics would be associated with their processed materials. The properties investigated were critical current densities, ( $J_c$ ), critical temperature, ( $T_c$ ), the upper critical field, ( $H_{c2}$ ), and the flux pinning force.

The processing conditions that were varied included the ball to powder ratio of the materials, the speed of disc rotation for Pulverisette-4 and the time of ball milling. In the SPEX-8000D processed materials, only one ball to powder ratio was employed (3:1) while it was varied for the pulverisette-4 mill. The milled materials were subsequently processed to obtain the superconducting wires whose properties were evaluated. From the totality of the study conducted, the following conclusions could be drawn:

1. On the effect of atmospheric condition: it was observed that the formation of MgO during ball milling and material handling resulted in the changes in  $T_c$  and  $H_{c2}$  values. The  $T_c$  for the materials of this study were 37.5 K, and 38 K compared to 39 K for pure  $MgB_2$ . Relative residual resistivity (RRR) measurements was the basis for this determination. The difference in  $T_c$  recorded for this study was attributed to variable sample connectivity with the distribution of MgO in the  $MgB_2$ .
2. The connectivity parameters,  $A_r$ , was determined to range from 0.19 to 0.33 from the sample studied.
3. The presence of atmospheric air exposure resulted in the formation of MgO and  $MgB_4$  while decomposition of  $CO_2$  resulted in the unintentional C-doping of the  $MgB_2$ .
4. On the strain inducement disorder effect:
  - a. In general, the SPEX processed materials were smaller in particle size than the Pulverisette-4 processed ones.
  - b. The SPEX processed materials in general showed distinct properties in comparison to the Pulverisette-4 processed ones because particle size reduction, and also defects introduction were higher in SPEX milling. The determined  $T_c$  for SPEX milled materials varied from 37.89 K (5 at.%, 60 minutes ball milling) to 35.4 K (5 at.%, 2400 minutes). For the Pulverisette-4 processed materials displayed  $T_c$  of 38.35 K (5 at.%, 120 minutes, at 800 rpm) to 37.29 K (2 at.%, 2400 minutes, 1200 rpm).
  - c. For the Pulverisette-4, though smaller particle sizes were obtained with 1200 rpm processed materials, however, better superconducting properties were realized with the 800 rpm processed ones. Further, it was observed that amount of MgO increased in the materials as the rotational speed increased

from 800 to 1200 rpm with a reduction on the  $T_c$  from 37.92 to 37.29 K (milled samples at 2400 minutes at 2 at.%), respectively.

- d. Change in the BPR did not result in comparable changes to the superconductivity properties as was the rotational speed. However, the BPR of 10:1 shows better superconducting properties. For instance, material processed at 800 rpm for 300 minutes in the Pulverisette-4 using BPR of 3:1 and 10:1, Chapter 5, show the following superconducting properties, respectively:  $J_c(2 \text{ T}, 4.2 \text{ K}) = 240.65$  to  $380.21 \text{ kA/cm}^2$ ,  $J_c(5 \text{ T}, 4.2 \text{ K}) = 11.52$  to  $12.61 \text{ kA/cm}^2$ ,  $F_p(2 \text{ T}, 4.2 \text{ K}) = 4.81$  to  $7.26 \text{ GN/m}^3$ ,  $H_{in}(4.2 \text{ K}) = 6.29$  to  $6.79 \text{ T}$  and  $T_c(50 \text{ Oe}) = 37.97$  to  $37.96 \text{ K}$  from M-T curve.

#### 5. TaB<sub>2</sub> doped MgB<sub>2</sub> effect at 2 and 5 at.%

- a. Material processed at 5 at.% shown higher superconducting properties compared with 2 at.% due to the higher amount of TaB<sub>2</sub> to penetrate in the material.
- b. In general, SPEX processed materials exhibited higher  $J_c$ ,  $F_p$ , and  $H_{in}$  values than the Pulverisette-4 processed materials. For instance, material processed at 5 at.% for 600 minutes in the SPEX compared to Pulverisette-4 at 800 rpm these were  $J_c(2 \text{ T}, 4.2 \text{ K}) = 474.1$  to  $295.5 \text{ kA/cm}^2$ ,  $F_p(2 \text{ T}, 4.2 \text{ K}) = 9.47$  to  $5.91 \text{ GN/m}^3$ , and  $H_{in}(4.2 \text{ K}) = 8.50$  to  $6.71 \text{ T}$ , respectively. However, the  $T_c$  value of 37.33 K for SPEX ball milled material was lower than 37.82 K for Pulverisette-4 ball milled material

## 7.2 Suggestions for Futures works

The following suggestions are made based on careful examination and analyses of the study carried out.

1. The Pulverisette-4 ball mill should be studied in order to determine milling conditions that are comparable to the SPEX-8000D milling machine. This could be done by carefully selecting a material that could be used as the basis for this study. The different processing parameters such as BPR, rotational speed, and times of milling should be varied in order to determine the outcome that closely matches with SPEX-8000D ball milling.
2. X-ray diffraction measurements of the as-ball-milled materials should be done before further processing necessary to generate superconducting wires. Similarly, detailed scanning electron microscopy (SEM) studied should be carried out. This should help distinguish between the effects of ball milling and that of the hot-isostatic pressing associated with the superconducting wires making.
3. Detailed TEM should be conducted to determine the extent of TaB<sub>2</sub> dispersion in MgB<sub>2</sub>, lattice parameters changes, and hence defects introduction in as-ball-milled materials, and on the superconducting wires.
4. Intermediate dopant levels of 2.5 at.% and 3.5 at.% should be studied in order to investigate properties evolution tendencies with dopings.
5. Efforts should be put on investigating the effects of shorter milling times-from 30 minutes to 180 minutes.
6. The suggestions of carrying out pre-milling of the dopant materials before milling the mixture of MgB<sub>2</sub> and the dopant is highly recommended. This measure should serve to investigate the most effective means of enhancing the doping action.

## References

- [1] J. Nagamatsu, N. Nakagawa, T. Muranaka, Y. Zenitani and J. Akimitsu, *Superconductivity at 39K in magnesium diboride*, Nature, vol. 410, March 2001, pp.63-64
- [2] C. Buzea, T. Yamashita, *Review of superconducting properties of MgB<sub>2</sub>*, Superconductors, Science & Technology, Vol. 14, No. 11, 2001, pp. 115-146
- [3] Larbalestier D C, Rikel M O, Cooley L D, Polyanskii A A, Jiang J Y, Patniak S, Cai X Y, Feldmann D M, Gurevich A, Squitieri A A, Naus M T, Eom C B, Hellstrom E E, Cava R J, Regan K A, Rodago N, Hayward M A, He T, Slusky J S, Khalifah P, Inumaru K and Haas M (2001) Strongly linked current flow in polycrystalline forms of the superconductor MgB<sub>2</sub> *Nature* **410** 186
- [4] J. Kortus, I. I. Mazin, K. D. Belashchenko, V.P. Antropov, and L. L. Boyer, Phys. Rev. Lett. 86, 4656-4659 (2001).
- [5] B J Senkowicz, R J Mungall, Y Zhu, J Jiang, P M Voyles, E E Hellstrom, and D C Larbalestier (2007) Nanoscale grains, high irreversibility field, and large critical current density as a function of high energy ball milling time in C-doped magnesium diboride.
- [6] Senkowicz B J, Polyanskii A, Mungall R J, Zhu Y, Giencke J E, Voyles P M, Eom C B, Hellstrom E E, and Larbalestier D C (2007) Understanding the route to high critical current density in mechanically alloyed Mg(B<sub>1</sub>-XCX)<sub>2</sub> *Supercond. Sci. Technol.* **20** 650
- [7] J. Bardeen, L. N. Cooper and J.R. Schrieffer, Phys. Rev. 108, 1175 - 1204 (1957)
- [8] M.J. Qin, X. L. Wang, H. K. Liu, S. X. Dou, Phys. Rev. B 65, 132508 (2002)
- [9] Introductory Solid State Physics Second Edition - H.P. Myers, 1997
- [10] D.Dimos, P.Chaudhari and J.Mannhart : *Phys. Rev.* **B41** (1990) 4038.
- [11] Bud'ko, S.L., Lapertot, G., Petrovic, C., Cunningham, C.E., Anderson, N., Canfield, P.C. *Phys. Rev. Lett.*, v. 86, p. 1877, 2001
- [12] Meng, R.L., Lorenz, B., Wang, Y.S., Cmaidalka, J., Sun, Y.Y., Xue, Y.Y., Meen, J.K., Chu, C.W. *Physica C: Superconductivity*, v. 382, p. 113-116, 2002.
- [13] V. Russell, R. Hirst, F. A. Kanda, and A. J. King, Acta Cryst. 6, 870 (1953).
- [14] K.D. Belashchenko, M. van Schilfhaarde, and V.P. Antropov, Phys. Rev. B 64, 092503 (2001).
- [15] A. Y. Liu, I. I. Mazin, J. Kortus, Phys. Rev. Lett. 87 (2001) 087005.
- [16] K.-P. Bohnen, R. Heid, and B. Renker, Phys. Rev. Lett. 86, 5771 (2001).

- [17] Y. Kong, O. V. Dolgov, O. Jepsen, and O. K. Andersen, Phys. Rev. B 64, o20501 (R) (2001).
- [18] Pablo de la Mora, Miguel Castro, Gustavo Tavizon, J. Phys.: Condens. Matter. 17, 965-978 (2005).
- [19] S. Kumashiro, H. Tanaka, Y. Kawamata, H. Yanagisawa, K. Momose, G. Nakamura, C. Oshima, S. Otani, *e-J. Surf. Sci. Nanotech. Vol. 4 (2006) 100-104*
- [20] B. Lönnberg, “*Thermal expansion studies on the group IV-VII transition metal diborides*” Journal of the Less-Common Metals, 141, 145-156 (1988).
- [21] N.V. Vekshina, L. Ya. Markavskii, Yu. D. Kondrashev and T. K. Voevodskaya, “*Double Borides of Aluminum and Magnesium.*” Journal of Applied Chemistry of the USSR, Translated from Zhurnal Prikladnoi Khimii, 44 (5), 970-974 (1971).
- [22] D. Kaczorowski, A.J. Zaleski, O.J. Zogal, J. Klamut, cond-matter/0103571 (2001)
- [23] H. Rosner, W.E. Pickett, S. –L. Drechsler et al., cond-matter/0106092 (2001).
- [24] P.P. Singh, cond-matter/0104580 (2001).
- [25] Yong-Jihn Kim, personal communication.
- [26] Rodrigues Jr., D. “*Study of the composition of phases in the contours of superconducting grains A-15 and its influence on the properties of transport*” Doctoral Thesis, Instituto de Fisica “Gleb Wataghin” – Unicamp, Campinas, 1997.
- [27] Larbalestier, D., Cooley, L.D., Rikel, M.O., Polyanskii, A.A., Jiang, J., Patnaik, S., Cai, X.Y., Feldmann, D.M., Gurevich, A., Squitieri, A.A., Naus, M.T., Eom, C.B., Hellstrom, E.E., Cava, R.J., Regan, K.A., Rogado, N., Hayward, M.A., He, T., Slusky, J.S., Khalifah, P., Inumaru, K., Haas, M. Nature, v. 410, p. 186-189, 2001a.
- [28] T. C. Shields, K. Kawano, D. Holdom, and J. S. Abell, “Microstructure and superconducting properties of hot isostatically pressed  $MgB_2$ ”, Superc. Sci. Tech., vol. 15, pp. 202-205, Feb. 2002.
- [29] L. Gozzelino, F. Laviano, D. Botta, A. Chiodoni, R. Gerbaldo, G. Ghigo, E. Mezzetti, G. Giunchi, S. Ceresara, G. Ripamonti, M. Poyer, “Critical state analysis in bulk  $MgB_2$  by means of a quantitative magneto-optical technique”, Phil. Mag. B-Phys. Cond. Matt., vol. 82, pp. 1-11, Jan 2002.
- [30] X. Z. Liao, A. Serquis, Y. T. Zhu, J. Y. Huang, L. Civale, D. E. Peterson, F. M. Mueller, H. F. Xu, cond-mat/0212571
- [31] M.J. Kramer, S.L. Bud'ko, P.C. Canfield, R.H.T. Wilke, D.K. Finnemore, R.J. Suplinskas, cond-mat/0302443
- [32] B J Senkowicz, “*Optimizing Critical Current Density through Composition and Microstructure in Mechanical Alloyed Magnesium Diboride*” Doctoral Thesis, University of Wisconsin-Madison, Madison 2007.

- [33] Room Temperature Superconductivity - Andrei Mourachkine, Cambridge International Science Publishing, 2004
- [34] Rodrigues Jr., D. "Improvement of intragranular and intergranular pinning in MgB<sub>2</sub> superconductors by mechanical alloying with AlB<sub>2</sub>-type compounds" Pos-Doctoral Thesis, Applied Superconductivity Center and Materials Science and Engineering Department, University of Wisconsin-Madison, 2006-2007.
- [35] Wilke R H T, Bud'ko S L, Canfield P C, Farmer J, Hannahs S T (2006) Systematic study of the superconducting and normal-state properties of neutron-irradiated MgB<sub>2</sub> *Physical Review B* **73**, 134512
- [36] Xu HL, Feng Y, Zhao Y, Xu Y D, Wu X J, Pu M H, Yan G, Lu Y F, Li C S, Ji P, Shen Z H and Xu Z (2006) Effects of polycarbosilane doping on the superconductivity and microstructure of MgB<sub>2</sub>. *Supercond. Sci. Technol.* **19** 68
- [37] Kitaguchi H, Matsumoto A, Kumakura H, Doi T, Yamamoto H, Saitoh K, Sosiati H, Hata S (2004) MgB<sub>2</sub> films with very high critical current densities due to strong grain boundary pinning. *Applied Physics Letters* **85** 14, 2842
- [38] Serquis, A., Civale, I., Hammon, D.L., Liao, X.Z., Coulter, J.Y., Zhu, Y.T., Jaime, M., Peterson, D.E., Mueller, F.M., Nesterenko, V.F., Gu, Y., *Appl. Phys. Lett.*, v. 82, p. 2847, 2003.
- [39] Senkowicz, B. J., Giencke, J. E., Patnaik, S., Eom, C. B., Hellstrom, E. E., Larbalestier, D. *Appl. Phys. Lett.*, v. 86, 202502, 2005.
- [40] Larbalestier, D., Gurevich, A., Feldmann, D.M., Polyanskii, A. *Nature*, v. 414, p. 368-377, 2001.
- [41] Suryanarayana, C. *Progress in Materials Science*, v. 46, p. 1-184, 2001.
- [42] Senkowicz, B.J., Pérez Moyet, R., Mungall, R.J., Hedstrom, J., Uwakweh, O. N. C., Hellstrom, E.E., Larbalestier, D.C. *Supercond. Sci. Technol.*, v. 19, p. 1173-1177, 2006.
- [43] High Temperature Superconductor Bulk Material - Gernot Krabbes, Günter Fuchs, Wolf-Rüdiger Canders, Hardo May, and Ryszard Palka, *Wiley-VCH Verlag GmbH & Co. KGaA, Weinheim, 2006.*
- [44] Bean, C.P., *Phys. Rev. Lett.*, v. 8, p. 250-3, 1962.
- [45] Rietveld, H. M. *J. Appl. Cryst.*, v. 2. P. 65-71, 1969.
- [46] W. Kraus and G. Nolze, *J. Appl. Cryst.* (1996). 29, 301-303.
- [47] Bhatia M, Sumption M D, Collings E W, Dregia S (2005) Increases in the irreversibility field and the upper critical field of bulk MgB<sub>2</sub> by ZrB<sub>2</sub> addition. *Applied Physics Letters* **87**, 042505
- [48] Dou S X, Wang X L, Hrovat J, Milliken D, Collings E W and Sumption M D Preprint cond-mat/0102320.

- [49] Handstein A, Hinz D, Fuchs G, Muller K H, Nenkov K and Gutfleisch O *Preprint cond-mat/0103408*.
- [50] Takano Y, Takeya H, Fujii H, Kumakura H, Hatano T, Togano K, Kito H and Ihara H, *Appl.Phys.Lett* 2001 **78** 2914.
- [51] Sung G Y, Kim S H, Kim J, Yoo D C, Lee J W, Lee J Y, Jung C U, Park M S, Kang W N, Zhonglian D and Lee S I *Preprint cond-mat/0102498*.
- [52] Serquis A, Civale L, Coulter J Y, Hammon D L, Liao X Z, Zhu Y T, Peterson D E, Mueller F M, Nesterenko V F and Indrakanti S S (2004) Large field generation with a hot isostatically pressed powder-in-tube MgB<sub>2</sub> coil at 25 K. *Supercond. Sci. Technol.* **17** L35
- [53] C. B. Eom, M. K. Lee, J. H. Choi, L. J. Belenky, X. Song, L. D. Cooley, M. T. Naus, S. Patnaik, J. Jiang, M. Rikel, A. Polyanskii, A. Gurevich, and X. Y. Cai, "High critical current density and enhanced irreversibility field in superconducting MgB<sub>2</sub> thin films", *Nature*, vol. 410, pp. 186-189, Mar. 2001.
- [54] X. Z. Liao, A. Serquis, Y. T. Zhu, J. Y. Huang, L. Civale, D. E. Peterson, F. M. Mueller, H. F. Xu, cond-mat/0212571
- [55] Serquis A, Civale L, Hammon D L, Coulter J Y, Liao X Z, Zhu Y T, Peterson D E and Mueller F M, 2003 *Appl. Phys. Lett.* **82** 1754
- [56] W. A. C. Passos<sup>1</sup>, P. N. Lisboa-Filho<sup>1</sup>, G. L. Fraga<sup>2</sup>, F. W. Fabris<sup>2</sup>, P. Pureur<sup>2</sup>, and W. A. Ortiz<sup>1</sup>, "Paramagnetic Meissner Effect and Magnetic Remanence in Granular MgB<sub>2</sub>", *Braz. J. Phys.* vol.32 no.3 São Paulo Sept. 2002
- [57] K. Nagasao, T. Masui, S. Tajima, cond-mat.supr-con/0802.0061v1
- [58] Jung C U, Park M S, Kang W N, Kim M S, Lee S Y and Lee S I 2001 Temperature- and magnetic-field-dependences of normal state resistivity of MgB<sub>2</sub> prepared at high temperature and high pressure condition *Physica C* **353** 162
- [59] Lee S, Mori H, Masui T, Eltsev Yu, Yamamoto A and Tajima S 2001 Growth, structure analysis and anisotropic superconducting properties of MgB<sub>2</sub> single crystals *Preprint cond-mat/0105545*
- [60] Xu M, Kitazawa H, Takano Y, Ye J, Nishida K, Abe H, Matsushita A and Kido G 2001 Single crystal MgB<sub>2</sub> with anisotropic superconducting properties *Preprint cond-mat/0105271*
- [61] Grant P 2001 Rehearsals for prime time *Nature* **411** 532
- [62] Charles P. Peole Jr., Horacio A. Farach, Richard J. Creswick, "Superconductivity" page 271, 1995.
- [63] X. Xu, J. H. Kim, M.S.A. Hossain, J. S. Park, Y. Zhao, and S. X. Dou "Phase transformation and superconducting properties of MgB<sub>2</sub> using ball-milled low purity boron" *J. Appl Phys* (2008), **103**, 023912.

[64] Senkowicz B J, Perez Moyet R, Mungall R J, Hedstrom J, Uwakweh O N C, Hellstrom E E and Larbalestier D C (2006) Atmospheric conditions and their effect on ball-milled magnesium diboride. *Supercond. Sci. Technol.* **19** 1173

[65] Wilke R H T, Bud'ko S L, Canfield P C, Finnemore D K, Suplinskas R J and Hannahs S T (2005) Synthesis and optimization of  $\text{Mg}(\text{B}_{1-x}\text{C}_x)_2$  wire segments *Physica C* **424** 1